FEASIBILITY STUDY II OF A MUON BASED NEUTRINO SOURCE

Executive Editors
S. Ozaki*, R. Palmer*, M. Zisman#
*BNL, Upton, NY 11973, USA
#LBNL, Berkeley, CA 94720, USA
Editor
J. Gallardo*

March 13, 2001

Contents

List of Figures

List of Tables

0.1 Authors

0.2 Executive Summary

S. Ozaki
B. Palmer
M. Zisman

0.3 Charge to the Study Group

0.4 Summary of Parameters and Performance

0.5 Acknowledgement

Chapter 1

Introduction and Overview

1.1 Scope and Context of Present Study

B. Palmer

1.2 Expected Performance

B. Palmer

1.3 Physics Motivation

R. Shrock

1.3.1 Neutrino Oscillation Experiments with a Muon Storage Ring/Neutrino Factory

Here we discuss the current evidence for neutrino oscillations, and hence neutrino masses and lepton mixing, from solar and atmospheric data. A review is given of some theoretical background including models for neutrino masses and relevant formulas for neutrino oscillation transitions. We next mention the near-term and mid-term experiments in this area and comment on what they hope to measure. We then discuss the physics potential of a muon storage ring as a neutrino factory in the long term.

1.3.2 Evidence for Neutrino Oscillations

In a modern theoretical context, one generally expects nonzero neutrino masses and associated lepton mixing. Experimentally, there has been accumulating evidence for such masses and mixing. All solar neutrino experiments (Homestake, Kamiokande, SuperKamiokande, SAGE, and GALLEX) show a significant deficit in the neutrino fluxes coming from the Sun [?]. This deficit can be explained by oscillations of the ν_e's into other weak eigenstate(s), with Δm^2_{sol} of the order 10^{-5} eV^2 for solutions involving the Mikheev-Smirnov-Wolfenstein (MSW) resonant matter oscillations [?, ?] or of the order of 10^{-10} eV^2 for vacuum oscillations. Accounting for the data with vacuum oscillations (VO) requires almost maximal mixing. The MSW solutions include one for small mixing angle (SMA) and one with essentially maximal mixing (LMA).

Another piece of evidence for neutrino oscillations is the atmospheric neutrino anomaly, observed by Kamiokande [?], IMB [?], SuperKamiokande [?] with the highest statistics, and by Soudan [?] and MACRO [?]. This data can be fit by the inference of $\nu_\mu \to \nu_x$ oscillations with $\Delta m^2_{atm} \sim 3.5 \times 10^{-3}$ eV^2 [?] and maximal mixing $\sin^2 2\theta_{atm} = 1$. The identification $\nu_x = \nu_\tau$ is preferred over $\nu_x = \nu_{sterile}$ at about the 2.5σ level [?], and the identification $\nu_x = \nu_e$ is excluded by both the Superkamiokande data and the Chooz experiment [?, ?].

In addition, the LSND experiment [?] has reported observing $\bar{\nu}_\mu \to \bar{\nu}_e$ and $\nu_\mu \to \nu_e$ oscillations with $\Delta m^2_{LSND} \sim 0.1 - 1$ eV^2 and a range of possible mixing angles, depending on Δm^2_{LSND}. This result is not confirmed, but also not completely ruled out, by a similar experiment, KARMEN [?]. The miniBOONE experiment at Fermilab is designed to resolve this issue, as

discussed below.

If one were to try to fit all of these experiments, then, since they involve three quite different values of $\Delta m^2_{ij} = m(\nu_i)^2 - m(\nu_j)^2$ which could not satisfy the identity for three neutrino speciies,

$$\Delta m^2_{32} + \Delta m^2_{21} + \Delta m^2_{13} = 0 \tag{1.1}$$

it would follow that one would have to introduce a fourth neutrino. Since one knows that there are only three leptonic weak doublets and associated light neutrinos with weak isosopin $T = 1$ and $T = 1/2$ from the measurement of the Z width, it follows that this fourth neutrino weak eigenstate would have to be an electroweak singlet ("sterile" neutrino). Because the LSND experiment has not been confirmed by the KARMEN experiment, we choose here to use only the (confirmed) solar and atmospheric neutrino data in our analysis, and hence to work in the context of three active neutrino weak eigenstates.

1.3.3 Neutrino Oscillation Formalism

In this simplest theoretical context, there are three electroweak doublet neutrinos. Although electroweak singlet neutrinos may be present in the theory, one expects that, since their bare mass terms are electroweak singlet operators, the associated masses should not have any close relation with the electroweak symmetry breaking scale and, from a top-down point of view such as a grand unified theory, should be much larger than this scale. If this is the case, then the neutrino mixing can be described by the matrix

$$U = R_{23} K R_{13} K^* R_{12} K' \tag{1.2}$$

where R_{ij} is a rotation matrix in the ij subsector. Writing this out gives

$$U = \begin{pmatrix} c_{12}c_{13} & c_{13}s_{12} & s_{13}e^{-i\delta} \\ -c_{23}s_{12} - s_{13}s_{23}c_{12}e^{i\delta} & c_{12}c_{23} - s_{12}s_{13}s_{23}e^{i\delta} & c_{13}s_{23} \\ s_{12}s_{23} - s_{13}c_{12}c_{23}e^{i\delta} & -s_{23}c_{12} - s_{12}c_{23}s_{13}e^{i\delta} & c_{13}c_{23} \end{pmatrix} K' \tag{1.3}$$

where R_{ij} is the rotation matrix in the ij subspace, $c_{ij} = \cos\theta_{ij}$, $s_{ij} = \sin\theta_{ij}$, $K = diag(e^{-i\delta}, 1, 1)$ and K' involves further possible phases due to Majorana mass terms that will not be important here. Thus, in this framework, the neutrino mixing depends on the four angles θ_{12}, θ_{13}, θ_{23}, and δ, and on

two independent differences of squared masses, $\Delta m^2_{atm.}$, which is $\Delta m^2_{32} = m(\nu_3)^2 - m(\nu_2)^2$ in the favored fit, and $\Delta m^2_{sol.}$, which may be taken to be $\Delta m^2_{21} = m(\nu_2)^2 - m(\nu_1)^2$. Note that these quantities involve both magnitude and sign; although in a two-species neutrino oscillation in vacuum the sign does not enter, in the three species oscillations relevant here, and including both matter effects and CP violation, the signs of the Δm^2 quantities do enter and can, in principle, be measured.

For our later discussion it will be useful to record the formulas for the various relevant neutrino oscillation transitions. In the absence of any matter effect, the probability that a (relativistic) weak neutrino eigenstate ν_a becomes ν_b after propagating a distance L is

$$\begin{aligned} P(\nu_a \to \nu_b) &= \delta_{ab} - 4 \sum_{i>j=1}^{3} Re(K_{ab,ij}) \sin^2\Big(\frac{\Delta m^2_{ij} L}{4E}\Big) + \\ &+ 4 \sum_{i>j=1}^{3} Im(K_{ab,ij}) \sin\Big(\frac{\Delta m^2_{ij} L}{4E}\Big) \cos\Big(\frac{\Delta m^2_{ij} L}{4E}\Big) \end{aligned} \tag{1.4}$$

where

$$K_{ab,ij} = U_{ai} U^*_{bi} U^*_{aj} U_{bj} \tag{1.5}$$

and

$$\Delta m^2_{ij} = m(\nu_i)^2 - m(\nu_j)^2 \tag{1.6}$$

Recall that in vacuum, CPT invariance implies $P(\bar\nu_b \to \bar\nu_a) = P(\nu_a \to \nu_b)$ and hence, for $b = a$, $P(\bar\nu_a \to \bar\nu_a) = P(\nu_a \to \nu_a)$. For the CP-transformed reaction $\bar\nu_a \to \bar\nu_b$ and the T-reversed reaction $\nu_b \to \nu_a$, the transition probabilities are given by the right-hand side of (1.4) with the sign of the imaginary term reversed. (Below we shall assume CPT invariance, so that CP violation is equivalent to T violation.)

In most cases there is only one mass scale relevant for long baseline neutrino oscillations, $\Delta m^2_{atm} \sim$ few $\times 10^{-3}$ eV^2 and one possible neutrino mass spectrum is the hierarchical one

$$\Delta m^2_{21} = \Delta m^2_{sol} \ll \Delta m^2_{31} \approx \Delta m^2_{32} = \Delta m^2_{atm} \tag{1.7}$$

In this case, CP (T) violation effects are negligibly small, so that in vacuum

$$P(\bar\nu_a \to \bar\nu_b) = P(\nu_a \to \nu_b) \tag{1.8}$$

$$P(\nu_b \to \nu_a) = P(\nu_a \to \nu_b) \tag{1.9}$$

In the absence of T violation, the second equality (1.9) would still hold in matter, but even in the absence of CP violation, the first equality (1.8) would not hold. With the hierarchy (1.7), the expressions for the specific oscillation transitions are

$$\begin{aligned} P(\nu_\mu \to \nu_\tau) &= 4|U_{33}|^2|U_{23}|^2 \sin^2\Big(\frac{\Delta m^2_{atm} L}{4E}\Big) \\ &= \sin^2(2\theta_{23}) \cos^4(\theta_{13}) \sin^2\Big(\frac{\Delta m^2_{atm} L}{4E}\Big) \end{aligned} \tag{1.10}$$

$$\begin{aligned} P(\nu_e \to \nu_\mu) &= 4|U_{13}|^2|U_{23}|^2 \sin^2\Big(\frac{\Delta m^2_{atm} L}{4E}\Big) \\ &= \sin^2(2\theta_{13}) \sin^2(\theta_{23}) \sin^2\Big(\frac{\Delta m^2_{atm} L}{4E}\Big) \end{aligned} \tag{1.11}$$

$$\begin{aligned} P(\nu_e \to \nu_\tau) &= 4|U_{33}|^2|U_{13}|^2 \sin^2\Big(\frac{\Delta m^2_{atm} L}{4E}\Big) \\ &= \sin^2(2\theta_{13}) \cos^2(\theta_{23}) \sin^2\Big(\frac{\Delta m^2_{atm} L}{4E}\Big) \end{aligned} \tag{1.12}$$

In neutrino oscillation searches using reactor antineutrinos, i.e. tests of $\bar{\nu}_e \to \bar{\nu}_e$, the two-species mixing hypothesis used to fit the data is

$$P(\nu_e \to \nu_e) = 1 - \sin^2(2\theta_{reactor}) \sin^2\Big(\frac{\Delta m^2_{reactor} L}{4E}\Big) \tag{1.13}$$

where $\Delta m^2_{reactor}$ is the squared mass difference relevant for $\bar{\nu}_e \to \bar{\nu}_x$. In particular, in the upper range of values of Δm^2_{atm}, since the transitions $\bar{\nu}_e \to \bar{\nu}_\mu$ and $\bar{\nu}_e \to \bar{\nu}_\tau$ contribute to $\bar{\nu}_e$ disappearance, one has

$$P(\nu_e \to \nu_e) = 1 - \sin^2(2\theta_{13}) \sin^2\Big(\frac{\Delta m^2_{atm} L}{4E}\Big) \tag{1.14}$$

i.e., $\theta_{reactor} = \theta_{13}$, and the Chooz reactor experiment yields the bound [**?**]

$$\sin^2(2\theta_{13}) < 0.1 \tag{1.15}$$

which is also consistent with conclusions from the SuperK data analysis [**?**].

Further, the quantity "$\sin^2(2\theta_{atm})$" often used to fit the data on atmospheric neutrinos with a simplified two-species mixing hypothesis, is, in the three-generation case,

$$\sin^2(2\theta_{atm}) \equiv \sin^2(2\theta_{23})\cos^4(\theta_{13}) \tag{1.16}$$

The SuperK experiment finds that the best fit to their data is to infer $\nu_\mu \to \nu_\tau$ oscillations with maximal mixing, and hence $\sin^2(2\theta_{23}) = 1$ and $|\theta_{13}| << 1$. For the value $\Delta m^2_{32} = 3.5 \times 10^{-3}$ obtained in this fit by the SuperK experiment, the CHOOZ experiment on $\bar{\nu}_e$ disappearance yields the upper limit $\sin^2(2\theta_{13}) < 0.1$. The various solutions of the solar neutrino problem involve quite different values of Δm^2_{21} and $\sin^2(2\theta_{21})$: (i) large mixing angle solution, LMA: $\Delta m^2_{21} \simeq$ few$\times 10^{-5}$ eV^2 and $\sin^2(2\theta_{21}) \simeq 0.8$; (ii) small mixing angle solution, SMA: $\Delta m^2_{21} \sim 10^{-5}$ and $\sin^2(2\theta_{21}) \sim 10^{-2}$, (iii) LOW: $\Delta m^2_{21} \sim 10^{-7}$, $\sin^2(2\theta_{21}) \sim 1$, and (iv) "just-so": $\Delta m^2_{21} \sim 10^{-10}$, $\sin^2(2\theta_{21}) \sim 1$. Currently, there are preliminary reports from SuperK that their data favors the LMA and LOW solutions and disfavors the SMA and just-so solutions [**?**].

1.3.4 Types of Neutrino Masses, Seesaw Mechanism

We review here the theoretical background concerning neutrino masses and mixing. In the standard SU(3) $\times$ SU(2)$_L\times$ U(1)$_Y$ model (SM) neutrinos occur in SU(2)$_L$ doublets with $Y = -1$:

$$\mathcal{L}_{L\ell} = \begin{pmatrix} \nu_\ell \\ \ell \end{pmatrix}, \quad \ell = e,\ \mu,\ \tau \tag{1.17}$$

There are no electroweak-singlet neutrinos (often called right-handed neutrinos) $\chi_{R,j}$, $j = 1, ..., n_s$. Equivalently, these could be written as $\overline{\chi^c}_{L,j}$. There are three types of possible Lorentz-invariant bilinear operator products that can be formed from two two Weyl fermions ψ_L and χ_R:

- Dirac: $m_D\bar{\psi}_L\chi_R + h.c.$ This connects opposite-chirality fields and conserves fermion number.
- Left-handed Majorana: $m_L\psi_L^T C\psi_L + h.c.$ where $C = i\gamma_2\gamma_0$ is the charge conjugation matrix.
- Right-handed Majorana: $M_R\chi_R^T C\chi_R + h.c.$

The Majorana mass terms connect fermion fields of the same chirality and violate fermion number (by two units). Using the anticommutativity of fermion fields and the property $C^T = -C$, it follows that a Majorana mass matrix appearing as

$$\psi_i^T C (M_{maj})_{ij} \psi_j \tag{1.18}$$

is symmetric in flavor indices:

$$M_{maj}^T = M_{maj} \tag{1.19}$$

Thus, in the SM, there is no Dirac neutrino mass term because (i) it is forbidden as a bare mass term by the gauge invariance, (ii) it cannot occur, as do the quark and charged lepton mass terms, via spontaneous symmetry breaking (SSB) of the electroweak (EW) symmetry starting from a Yukawa term because there are no EW-singlet neutrinos $\chi_{R,j}$. There is also no left-handed Majorana mass term because (i) it is forbidden as a bare mass term and (ii) it would require a $I = 1$, $Y = 2$ Higgs field, but the SM has no such Higgs field. Finally, there is no right-handed Majorana mass term because there is no $\chi_{R,j}$. The same holds the minimal supersymmetric standard model (MSSM) and the minimal SU(5) grand unified theory (GUT), both for the original and supersymmetric versions.

However, it is easy to add electroweak-singlet neutrinos χ_R to the SM, MSSM, or SU(5) GUT; these are gauge-singlets under the SM gauge group and SU(5), respectively. Denote these theories as the extended SM, etc. This gives rise to both Dirac and Majorana mass terms, the former via Yukawa terms and the latter as bare mass terms. In the extended SM:

$$-\mathcal{L}_{Yuk} = \sum_{i=1}^{3} \sum_{j=1}^{n_s} h_{ij}^{(D)} \bar{\mathcal{L}}_{L,i} \chi_{R,j} \phi + h.c. \tag{1.20}$$

The electroweak symmetry breaking (EWSB), with

$$\langle \phi \rangle_0 = \begin{pmatrix} 0 \\ v/\sqrt{2} \end{pmatrix} \tag{1.21}$$

where $v = 2^{-1/4} G_F^{-1/2} \simeq 250$ GeV, yields the Dirac mass term

$$\sum_{i=1}^{3} \sum_{j=1}^{n_s} \bar{\nu}_{L,i} (M_D)_{ij} \chi_{Rj} + h.c. \tag{1.22}$$

with

$$(M_D)_{ij} = h_{ij}^{(D)} \frac{v}{\sqrt{2}} \tag{1.23}$$

The Majorana bare mass terms are

$$\sum_{i,j=1}^{n_s} \chi_{Ri}^T C (M_R)_{ij} \chi_{Rj} + h.c. \tag{1.24}$$

For compact notation, define the flavor vectors $\nu = (\nu_e, \nu_\mu, \nu_\tau)$ and $\chi = (\chi_1, .., \chi_{n_s})$ and observe that one can equivalently write ν_L or ν_R^c and χ_R or χ_L^c, where $\psi^c = C\overline{\psi}^T$, $\overline{\psi} = \psi^\dagger \gamma^0$. One can write the full set of Dirac and Majorana mass terms in the compact matrix form

$$-\mathcal{L}_m = \frac{1}{2} (\bar{\nu}_L \ \overline{\chi^c}_L) \begin{pmatrix} M_L & M_D \\ (M_D)^T & M_R \end{pmatrix} \begin{pmatrix} \nu_R^c \\ \chi_R \end{pmatrix} + h.c. \tag{1.25}$$

where M_L is the 3×3 left-handed Majorana mass matrix, M_R is a $n_s \times n_s$ right-handed Majorana mass matrix, and M_D is the 3-row by n_s-column Dirac mass matrix. In general, all of these are complex, and $(M_L)^T = M_L$, $(M_R)^T = M_R$. Because the extension of the SM to include χ_R does not include a $I = 1$, $Y = 2$ Higgs field allowing a renormalizable, dimension-4 Yukawa term that would yield a left-handed Majorana mass, one may take $M_L = 0$ at this level (but see below for dimension-5 contributions). The diagonalization of this mass matrix yields the neutrino masses and corresponding transformation relating the neutrino weak eigenstates to the mass eigenstates.

The same comments apply to the extended MSSM and SU(5) GUT. In the extended SU(5) GUT, the Dirac neutrino mass term arises most simply from the Yukawa couplings of the 5_R with a 5-dimensional Higgs representation H^α (in terms of component fields):

$$\bar{\psi}_{R\alpha} M_D \chi_L^c H^\alpha + h.c. \tag{1.26}$$

and the bare Majorana mass term $\chi_R^T M_R \chi_R + h.c.$.

In the extended SM, MSSM, or SU(5) GUT, one could consider the addition of the χ_R fields as *ad hoc*. However, a more complete grand unification is achieved with the (SUSY) SO(10) GUT, since all of the fermions of a given generation fit into a single representation of SO(10), namely, the 16-dimensional spinor representation ψ_L. In this theory the states χ_R are not *ad*

hoc additions, but are guaranteed to exist. In terms of SU(5) representations (recall, SO(10) $\supset$ SU(5) $\times$ U(1))

$$16_L = 10_L + \bar{5}_L + 1_L \tag{1.27}$$

so for each generation, in addition to the usual 15 Weyl fermions comprising the 10_L and 5_R, (equivalently $\bar{5}_L$) of SU(5), there is also an SU(5)-singlet, χ^c_L (equivalently, χ_R). So in SO(10) GUT, electroweak-singlet neutrinos are guaranteed to occur, with number equal to the number of SM generations, inferred to be $n_s = 3$. Furthermore, the generic scale for the coefficients in M_R is expected to be the GUT scale, $M_{GUT} \sim 10^{16}$ GeV.

There is an important mechanism, which originally arose in the context of GUT's, but is more general, that naturally predicts light neutrinos. This is the seesaw mechanism [**?**]. The basic point is that because the Majorana mass term $\chi_R^T C M_R \chi_R$ is an electroweak singlet, the associated Majorana mass matrix M_R should not be related to the electroweak mass scale v, and from a top-down point of view, it should be much larger than this scale. Denote this generically as m_R. This has the very important consequence that when we diagonalize the joint Dirac-Majorana mass matrix above, the eigenvalues (masses) will be comprised of two different sets: n_s heavy masses, of order m_R, and 3 light masses. We illustrate this in the simplest case of a single generation and $n_s = 1$. Then the mass matrix is simply

$$-\mathcal{L}_m = \frac{1}{2}(\bar{\nu}_L \ \bar{\chi^c}_L) \begin{pmatrix} 0 & m_D \\ m_D & m_R \end{pmatrix} \begin{pmatrix} \nu^c_R \\ \chi_R \end{pmatrix} + h.c. \tag{1.28}$$

The diagonalization yields the eigenvalues

$$\lambda = \frac{1}{2}\Big[m_R \pm \sqrt{m_R^2 + 4m_D^2} \ \Big] \tag{1.29}$$

Since $m_D \sim h^{(D)} v$ while m_R is naturally $>> v$ and hence $m_R >> m_D$, we can expand to get

$$\lambda_> \simeq m_R \tag{1.30}$$

and

$$\lambda_< \simeq -\frac{m_D^2}{m_R}\Big[1 + O\big(\frac{m_D^2}{m_R^2}\big)\Big] \tag{1.31}$$

(The $-$ sign is not physically important.) The largeness of m_R then naturally explains the smallness of the masses (or, most conservatively, upper bounds

on masses) of the known neutrinos. This appealing mechanism also applies in the physical case of three generations and for $n_s \geq 2$.

However, at a phenomenological level, without further theoretical assumptions, there is a large range of values for the light m_ν, since (1) the actual scale of m_R is theory-dependent, and (2) it is, *a priori*, not clear what to take for m_D since the known (Dirac) masses range over 5 orders of magnitude, from $m_e, m_u \sim$ MeV to $m_t = 174$ GeV, and this uncertainty gets squared.

For the full case with 3 generations and $n_s > 1$, and assuming, as is generic, that $det(M_R) \neq 0$ so that M_R^{-1} exists, the set of 3 light neutrino mass eigenstates is determined by the matrix analogue of eq. (1.31):

$$M_\nu = -M_D M_R^{-1} M_D^T \tag{1.32}$$

The seesaw mechanism is appealing, but detailed predictions are rather model-dependent.

A different way to get neutrino masses is to interpret the SM as a low-energy effective field theory, as is common in modern quantum field theory. One thus allows (nonrenormalizable) operators $\mathcal{O}$ in the Lagrangian of mass dimension $d_\mathcal{O} > 4$, provided that their coefficients, of dimension $4 - d_\mathcal{O}$ in mass units, are sufficiently small. Then one observes that the dimension-5 operator [**?**]

$$\mathcal{O} = \frac{1}{M_X} \sum_{a,b} h_{L,ab} (\epsilon_{ik}\epsilon_{jm} + \epsilon_{im}\epsilon_{jk}) \Big[\mathcal{L}_{aL}^{Ti} C \mathcal{L}_{bL}^{j}\Big] \phi^k \phi^m + h.c. \tag{1.33}$$

(where a, b are flavor indices, i, j, k, m are SU(2) indices) is an electroweak singlet. Upon electroweak symmetry breaking (EWSB), this operator yields a left-handed Majorana mass term

$$\sum_{a,b=1}^{3} \nu_{L,a}^T C (M_L)_{ab} \nu_{L,j} + h.c. \tag{1.34}$$

with

$$(M_L)_{ab} = \frac{(h_L)_{ab}(v/\sqrt{2})^2}{M_X} \tag{1.35}$$

Since the SM is phenomenologically very successful, one should have $M_X >> v$, so again these dimension-5 operators lead naturally to light neutrinos. The

diagonalization of the above operator determines the unitary transformation relating the mass eigenstates to the weak eigenstates,

$$\nu_{\ell_a} = \sum_{i=1}^{3} U_{ai}\nu_i \ , \quad \ell_1 = e,\ \ell_2 = \mu,\ \ell_3 = \tau \tag{1.36}$$

i.e.,

$$\begin{pmatrix} \nu_e & \nu_\mu & \nu_\tau \end{pmatrix} = \begin{pmatrix} U_{11} & U_{12} & U_{13} \\ U_{21} & U_{22} & U_{23} \\ U_{31} & U_{32} & U_{33} \end{pmatrix} \begin{pmatrix} \nu_1 \\ \nu_2 \\ \nu_3 \end{pmatrix} \tag{1.37}$$

One often denotes $U_{1i} = U_{ei}$, etc.

For the case of electroweak-singlet neutrinos and resultant seesaw, because of the splitting of the masses into the light set and the heavy set, the observed weak eigenstates of neutrinos are again, to a very good approximation, linear combinations of the three light mass eigenstates, so that the full $(3 + n_s) \times (3 + n_s)$ mixing matrix breaks into block diagonal form involving the 3×3 U matrix and an analogous $n_s \times n_s$ matrix for the heavy sector. In terms of the flavor vectors, this is

$$\begin{pmatrix} \nu_\ell \\ \chi^c \end{pmatrix} = \begin{pmatrix} U & 0 \\ 0 & U_{heavy} \end{pmatrix} \begin{pmatrix} \nu_i \\ \chi^c_{i,m} \end{pmatrix} \tag{1.38}$$

If one accepts all of the data indicating neutrino masses, including the solar neutrino deficiency, atmospheric neutrinos, and LSND experiments, then one needs light sterile (electroweak-singlet) neutrinos with masses of $\sim$ eV or smaller. These are usually considered unnatural, because electroweak-singlet neutrinos naturally have masses $\sim m_R >> M_{ew} = v$. If such light χ_R's exist, this tends to undermine the reasoning on which the seesaw mechanism is based.

1.3.5 Tests for Neutrino Masses in Decays

Given the focus of this booklet, we shall not review the well-known kinematic tests for neutrino masses except to mention that these are of three main types. There are direct tests, which search for the masses of the dominantly couipled neutrino mass eigenstates emitted in particle and nuclear decays; these yield the current upper bounds on these eigenstates for the three dominantly coupled mass components in ν_e, ν_μ, and ν_τ. Second, there

are tests for rather massive neutrinos emitted, via lepton mixing, in particle and nuclear decays. Third, there are searches for neutrinoless double beta decay, which would occur if there are massive Majorana neutrinos. The quantity on which one puts limits in searches for neutrinoless double beta decay is $\langle m_\nu \rangle = |U_{ei}^2 m(\nu_i)|$. Note that since U_{ei} is complex, destructive interference can occur in this sum. At present, the best published upper limit on this quantity is $\langle m_\nu \rangle < 0.4$ eV [**?**] from the Heidelberg-Moscow experiment with ^{76}Ge. A number of new proposals for more sensitive experiments have been put forward, including GENIUS, EXO, MOON, and MAJORANA, among others, which hope to search down to a sensitivity below 0.01 eV in $\langle m_\nu \rangle$ [**?**].

1.3.6 Models for Neutrino Masses and Mixing

We discuss the seesaw mechanism in further detail here. In the SM, a single Higgs field ϕ breaks the gauge symmetry and gives masses to the fermions. In the MSSM, one needs two $T = 1/2$ Higgs fields H_1 and H_2 with opposite hypercharges $Y = 1$ and $Y = -1$ to do this. GUT theories may have more complicated Higgs sectors; one typically uses different Higgs to break the gauge symmetry and give masses to fermions. In the context of the weakly coupled heterotic string, there is a connection between the Kac-Moody levels for the factor groups SU(3), SU(2), U(1)'s, and the corresponding representations of the chiral matter superfields. Indeed, for GUT's in a string context, this connection has yielded a tight constraint on the Higgs chiral superfields. Starting first by allowing the full range of Higgs fields in SO(10); then for the Clebsch-Gordan decomposition of the representations in the fermion mass term

$$16 \times 16 = 10_s + 120_a + 126_s \tag{1.39}$$

Hence, *a priori*, one considers using Higgs of dimension 10, 120, and 126. The coupling to the 10-dimensional Higgs fields yields Yukawa terms of the following form (suppressing generation indices).

$$\psi_L^T C \psi_L \bar{\phi}_{10} = (\bar{d}_R d_L + \bar{e}_R e_L)\phi_{10}(\bar{5}) + (\bar{u}_R u_L + \bar{\nu}_R \nu_L)\phi_{10}(5) \tag{1.40}$$

The coupling to the 126-dimensional Higgs yields a term

$$\chi_R^T C \chi_R \phi_{126}(1) \tag{1.41}$$

together with other linear combinations of $\bar{u}_R u_L$, $\bar{\nu}_R \nu_L$, $\bar{d}_R d_L$, and $\bar{e}_R e_L$ times appropriate SU(5)-Higgs; these four types of terms are also produced by the

coupling to a 120-dimensional Higgs. Hence, in this approach, one expects some similarity in Yukawa matrices, and thus Dirac mass matrices, for $T_3 = +1/2$ fermions, i.e. the up-type quarks u, c, t and the neutrinos:

$$M^{(u)} \sim M_D^{(\nu)} \ , \quad M^{(d)} \sim M_D^{(\ell)} \tag{1.42}$$

However, in many string-inspired models, one avoids high-dimension Higgs representations such as the 120- and 126-dimensional representations in SO(10). Instead, one constructs the neutrino mass terms from nonrenormalizable higher-dimension operators. A review with references to a large number of papers with theoretical models is [?].

To get a rough idea of the predictions, one may pretend that M_D and M_R are diagonal and let m_R denote a typical entry in M_R. Denote $m_{u,1} = m_u$, $m_{u,2} = m_c$, $m_{u,3} = m_t$. Then, (neglecting physically irrelevant minus signs)

$$m(\nu_i) \simeq \frac{m_{u,i}^2}{m_R} \tag{1.43}$$

This is the quadratic seesaw. For $m(\nu_3)$, one gets

$$m(\nu_3) \sim \frac{m_t^2}{m_R} \simeq \left(\frac{175 \text{ GeV}}{10^{16} \text{ GeV}}\right)(1.75 \times 10^{11} \text{ eV}) \sim 10^{-3} \text{ eV} \tag{1.44}$$

which, given the uncertainties in the inputs, is comparable to the value

$$m(\nu_3) \simeq \sqrt{\Delta m_{32}^2} = \simeq 0.05 \text{ eV} \tag{1.45}$$

inferred from the SuperK data with the assumption $\nu_\mu \to \nu_\tau$ and $m(\nu_2) << m(\nu_3)$. This gives an idea of how the seesaw mechanism could provide a neutrino mass in a region relevant to the SuperKamiokande data.

In passing, we note that string theories allow a low string scale, perhaps as low as 100 TeV. These models have somewhat different phenomenological implications for neutrinos than conventional models with a string scale comparable to the Planck mass.

1.3.7 Lepton Mixing

We proceed to consider off-diagonal structure in M_R, as part of the more general topic of lepton mixing. Neutrino mass terms naturally couple different generations and hence violate lepton family number; the Majorana mass

terms also violate total lepton number. Lepton mixing angles are determined by diagonalizing the charged lepton and neutrino mass matrices, just as the quark mixing angles in the CKM (Cabibbo-Kobayashi-Maskawa) matrix are determined by diagonalizing the up-type and down-type quark mass matrices. Before the atmospheric neutrino anomaly was reported, a common expectation was that lepton mixing angles would be small, like the known quark mixing angles. This was one reason why theorists favored the MSW mechanism over vacuum oscillations as an explanation of the solar neutrino deficiency – MSW could produce the deficiency with small lepton mixing angles, whereas vacuum oscillations needed nearly maximal mixing. It was long recognized that an explanation of the atmospheric neutrino anomaly requires maximal mixing, and while neutrino masses are not surprising or unnatural to most theorists, the maximal mixing has been something of a challenge for theoretical models to explain.

Denoting the lepton flavor vectors as $\ell = (e, \mu, \tau)$ and $\nu = (\nu_e, \nu_\mu, \nu_\tau)$, we have, for the leptonic weak charged current,

$$J^\lambda = \bar{\ell}_L \gamma^\lambda \nu_L \tag{1.46}$$

The mass terms are

$$\bar{\ell}_L M_\ell \ell_R + \bar{\nu}_L M_\nu \nu_R^c + h.c. \tag{1.47}$$

where, as above, $M_\nu = -M_D M_R^{-1} M_D^T$ and we have used the splitting of the neutrino eigenvalues into a light sector and a very heavy sector. We diagonalize these so that, in terms of the associated unitary transformations, with the notation $\ell_m = (e_m, \mu_m, \tau_m)$ and $\nu_m = (\nu_1, \nu_2, \nu_3)$, for charged lepton and neutrino mass eigenstates, the the charged current is

$$J^\lambda = \bar{\nu}_{mL} U_L^{(\nu)} \gamma^\lambda U_L^{(\ell)\dagger} \ell_{mL} = \bar{\nu}_{mL} U \gamma^\lambda \ell_{mL} \tag{1.48}$$

where the lepton mixing matrix is

$$U = U_L^{(\nu)} U_L^{(\ell)\dagger} \tag{1.49}$$

Although many theorists expected before the SuperK results indicating that $\sin^2(2\theta_{23}) = 1$ that leptonic mixing angles would be small, like the quark mixing angles, after being confronted with the SuperK results, they have constructed models that can accomodate large mixing angles. Of course, θ_{13} must be small to fit experiment. Models are able to yield either $\sin^2(2\theta_{12}) \sim 1$ for the LMA, LOW, and just-so solutions, or $\sin^2(2\theta_{12}) << 1$ for the SMA solution.

1.3.8 Relevant Near- and Mid-Term Experiments

There are currently intense efforts to confirm and extend the evidence for neutrino oscillations in all of the various sectors – solar, atmospheric, and accelerator. Some of these experiments are running; in addition to SuperKamiokande and Soudan-2, these include the Sudbury Neutrino Observatory, SNO, and the K2K long baseline experiment between KEK and Kamioka. Others are in development and testing phases, such as BOONE, MINOS, the CERN - Gran Sasso program, KAMLAND, and Borexino [**?**]. Among the long baseline neutrino oscillation experiments, the approximate distances are $L \simeq 250$ km for K2K, 730 km for both MINOS, from Fermilab to Soudan and the proposed CERN-Gran Sasso experiments. K2K is a ν_μ disappearence experiment with a conventional neutrino beam having a mean energy of about 1.4 GeV, going from KEK 250 km to the SuperK detector. It has a near detector for beam calibration. It has obtained results consistent with the SuperK experiment, and has reported that its data disagrees by 2σ with the no-oscillation hypothesis [**?**]. MINOS is another conventional neutrino beam experiment that takes a beam from Fermilab 730 km to a detector in the Soudan mine in Minnesota. It again uses a near detector for beam flux measurements and has opted for a low-energy configuration, with the flux peaking at about 3 GeV. This experiment expects to start taking data in early 2004 and, after some years of running, to obtain higher statistics than the K2K experiment and to achieve a sensitivity down to roughly to the level $\Delta m^2_{32} \sim 10^{-3}\mathrm{eV}^2$. The CERN - Gran Sasso program will come on later, around 2005. It will involve taking a higher energy neutrino beam from CERN to the Gran Sasso deep underground laboratory in Italy. This program will emphasize detection of the τ's produced by the ν_τ's that result from the inferred neutrino oscillation transition $\nu_\mu \to \nu_\tau$. The OPERA experiment will do this using emulsions [**?**], while the ICARUS proposal uses a liquid argon chamber [**?**]. Moreover, at Fermilab, the miniBOONE experiment plans to run in the next few years and to confirm or refute the LSND claim after a few years of running.

There are also several relevant solar neutrino experiments. The SNO experiment is currently running and should report their first results in spring, 2001. These will involve measurement of the solar neutrino flux and energy distribution using the charged current reation on heavy water, $\nu_e + d \to e{+}p{+}p$. Subsequently, they will measure the neutral current reaction $\nu_e{+}d \to \nu_e + n + p$. The KamLAND experiment in Japan expects to begin taking

data in late 2001. This is a very long baseline reactor experiment, looking for $\bar{\nu}_e$ disappearance. On a similar time scale, the Borexino experiment in Gran Sasso expects to turn on and hopes to measure the ^{7}Be neutrinos from the sun. These experiments should help to decide which of the various solutions to the solar neutrino problem is preferred, and hence the corresponding values of Δm^2_{21} and $\sin^2(2\theta_{12})$.

This, then, is the program of relevant experiments during the period 2000-2010. By the end of this period, we may expect that much will be learned about neutrino masses and mixing. However, there will remain several quantities that will not be well measured and which can be measured by a neutrino factory.

1.3.9 Oscillation Experiments at a Neutrino Factory

Although a neutrino factory based on a muon storage ring will turn on several years after this near-term period in which K2K, MINOS, and the CERN-Gran Sasso experiments will run, we believe that it has a valuable role to play, given the very high-intensity neutrino beams of fixed flavor-pure content, including, in particular, ν_e and $\bar{\nu}_e$ beams as well as the conventional ν_μ and $\bar{\nu}_\mu$ beams. The potential of the neutrino beams from a muon storage ring is that, in contrast to a conventional neutrino beam, which, say, from π^+ decay, is primarily ν_μ with some admixture of ν_e's and other flavors from K decays, the neutrino beams from the muon storage ring would high extremely high purity: μ^- beams would yield 50 % ν_μ and 50 % $\bar{\nu}_e$, and so forth for the charge conjugate case of μ^+ beams. Furthermore, these could be produced with extremely high intensities; we shall take the BNL design value of 2×10^{20} μ decays per Snowmass year, 10^7 sec.

The types of neutrino oscillations that can be searched for with the neutrino factory based on a muon storage ring are listed below for the case of μ^-, decaying as $\mu^- \to \nu_\mu e^- \bar{\nu}_e$:

1. $\nu_\mu \to \nu_\mu$, $\nu_\mu \to \mu^-$ (survival)
2. $\nu_\mu \to \nu_e$, $\nu_e \to e^-$ (appearance)
3. $\nu_\mu \to \nu_\tau$, $\nu_\tau \to \tau^-$; $\tau^- \to (e^-, \mu^-)$... (appearance*)
4. $\bar{\nu}_e \to \bar{\nu}_e$, $\bar{\nu}_e \to e$ (survival)
5. $\bar{\nu}_e \to \bar{\nu}_\mu$, $\bar{\nu}_\mu \to \mu^+$ (appearance)

6. $\bar{\nu}_e \to \bar{\nu}_\tau$, $\bar{\nu}_\tau \to \tau^+$; $\tau^+ \to (e^+, \mu^+)$... (appearance*)

It is clear from the list of processes above that since the beam contains both neutrinos and antineutrinos, the only way to determine what the parent neutrino was is to determine the identity of the final state charged lepton and measure its charge. One aspect of the experiments will involve the measurement of $\nu_\mu \to \nu_\mu$ as a disappearance experiment. A unique aspect for the neutrino factory will be the measurement of the oscillation $\bar{\nu}_e \to \bar{\nu}_\mu$, giving a wrong-sign μ^+. Of greater difficulty would be the measurement of the transition $\bar{\nu}_e \to \bar{\nu}_\tau$, giving a τ^+ which will decay part of the time to μ^+. These physics goals mean that a detector must have excellent capability to identify muons and measure their charges. The oscillation $\nu_\mu \to \nu_e$ would be difficult to observe, since it would be difficult to identify an electron shower from a hadron shower. From the above formulas for oscillations, one can see that, given a knowledge of Δm^2_{32} and $\sin^2(2\theta_{23})$ that one will have by the time a neutrino factory is built, the measurement of the $\bar{\nu}_e \to \bar{\nu}_\mu$ transition yields the value of θ_{13}.

To get a rough idea of how the sensitivity of an oscillation experiment would scale with energy and baseline length, recall that the event rate in the absence of oscillations is simply the neutrino flux times the cross section. First of all, neutrino cross sections in the region above about 10 GeV (and slightly higher, for τ production) grow linearly with the neutrino energy. Secondly, the beam divergence is a function of the initial muon storage ring energy; this divergence yields a flux, as a function of θ_d, the angle of deviation from the forward direction, that goes like $1/\theta_d^2 \sim E^2$. Combining this with the linear E dependence of the neutrino cross section and the overall $1/L^2$ dependence of the flux far from the production region, one finds that the event rate goes like

$$\frac{dN}{dt} \sim \frac{E^3}{L^2} \tag{1.50}$$

Event rates have been given in the Fermilab Neutrino Factory Working Group. For a stored muon energy of 20 GeV, as in the BNL plans, and a distance of $L = 2900$ to the WIPP Carlsbad site in New Mexico, these event rates amount to several thousand events per kton of detector per year, i.e. they are satisfactory for the physics program.

One could estimate that at a time when the neutrino factory turns on, Δm^2_{32} and $\sin^2(2\theta_{23})$ would be known at perhaps a 30% level. The neutrino factory should improve the precision on those two parameters, and can

contribute to three important measurements: (i) measurement of θ_{13}, as discussed above; (ii) measurement of the sign of Δm^2_{32} using matter effects; and (iii) possibly a measurement of CP violation in the leptonic sector, if Δm^2_{21} and $\sin^2(2\theta_{21}$ are sufficiently large. To measure the sign of Δm^2_{32}, one uses the fact that matter effects reverse sign when one switches from neutrinos to antineutrinos, and carries out this switch in the charges of the stored $\mu^{\pm}$. We elaborate on this next.

1.3.10 Matter Effects

With the advent of the muon storage ring, the distances one can place detectors are large enough so that for the first time matter effects can be exploited in accelerator-based oscillation experiments. Simply put, matter effects are the matter-induced oscillations which neutrinos undergo along their flight path through the Earth from the source to the detector. Given the typical density of the earth, matter effects are important for the neutrino energy range $E \sim O(10)$ GeV and $\Delta m^2_{atm} \sim 10^{-3}$ eV^2 values relevant for the long baseline experiments. After the initial discussion of matter-induced resonant neutrino oscillations in [**?**], an early study of these effects including three generations was carried out in [**?**]. The sensitivity of an atmospheric neutrino experiment to small Δm^2 due to the long baselines and the necessity of taking into account matter effects was discussed e.g., in [**?**]. After Ref. [**?**], many analyses were performed in the 1980's of the effects of resonant neutrino oscillations on the solar neutrino flux, and matter effects in the Earth were studied, e.g., [**?**] and [**?**], which also discussed the effect on atmospheric neutrinos (see also the review [**?**]). Recent papers on matter effects relevant to atmospheric neutrinos include [**?**, **?**]. Early studies of matter effects on long baseline neutrino oscillation experiments were carried out in Early studies of matter effects on long baseline neutrino oscillation experiments were carried out in [**?**]. More recent analyses relevant to neutrino factories include [**?**, **?**], [**?**]-[**?**]. In recent papers by one of the authors (RS) and I. Mocioiu, calculations were presented of the matter effect for parameters relevant to possible long baseline neutrino experiments envisioned for the muon storage ring/neutrino factory [**?**]. In particular, these authors compared the results obtained with constant density along the neutrino path versus results obtained by incorporating the actual density profiles. They studied the dependence of the oscillation signal on both $E/\Delta m^2_{atm.}$ and on the angles in the leptonic mixing matrix, and commented on the influence of $\Delta m^2_{sol.}$

1.3.11 CP Violation

Because of the large angle θ_{23}, leptonic CP violation, which involves all of the angles in combination with the CP-violating angle δ, could be considerably larger than CP violation in the quark sector. However, it will be very challenging to measure. The reason for this is that to do so one would compare $\nu_e \to \nu_\mu$ with $\bar{\nu}_e \to \bar{\nu}_\mu$. However, matter effects already skew these rates, even in the absence of any CP violation, since these matter effects have the opposite sign for neutrinos and antineutrinos. Alternatively, one might think of comparing $\nu_e \to \nu_\mu$ with the time-reversed reaction $\nu_\mu \to \nu_e$. Although this would be equivalent if CPT is valid, as we assume, and although the matter effects are the same here, the detector response is completely different and, in particular, it is quite difficult to identify $e^\pm$.

1.3.12 Detector Considerations

We have commented on the requisite properties of detectors. These should be quite massive, O(10) - O(100) ktons. Possibilities include magnetized steel calorimeters, water Cherenkov detectors, and liquid Argon chambers.

1.3.13 Conclusions

In conclusion, neutrino masses and mixing are generic theoretical expectations. The seesaw mechanism naturally yields light neutrinos, although its detailed predictions are model-dependent and may require a lower mass scale than the GUT mass scale. One of the most interesting findings from the atmospheric data has been the maximal mixing in the relevant channel, which at present is favored to be $\nu_\mu \to \nu_\tau$. Even after the near-term program of experiments by K2K, MINOS, the CERN-Gran Sasso experiments, and mini-BOONE, a high-intensity neutrino factory at BNL with 2×10^{20} μ decays per Snowmass year and a stored $\mu^\pm$ energy of 20 GeV coupled with a long-baseline neutrino oscillation experiment, say with $L = 2900$ km to the WIPP facility in Carlsbad would make a valuable contribution to the physics of neutrino masses and lepton mixing. (An alternative $L = 1700$ to Soudan is also being considered.) In particular, the neutrino factory should be able to improve the accuracy of the measurement of $\sin^2(2\theta_{23})$ and Δm^2_{32} and to measure $\sin^2(2\theta_{13})$ and the sign of $\Delta m^2_{atm.}$. It might also be able to measure leptonis CP violation. BNL can build on its longstanding expertise in ac-

celerator design and construction, its pioneering role with muon colliders, to proceed with the requisite R+D to build the muon storage ring and neutrino factory on the BNL site. The physics potential of this facility is excellent.

Bibliography

[1] Fits and references to the Homestake, Kamiokande, GALLEX, SAGE, and Super Kamiokande data include N. Hata and P. Langacker, Phys. Rev. **D56** 6107 (1997); J. Bahcall, P. Krastev, and A. Smirnov, Phys. Rev. **D58**, 096016 (1998); J. Bahcall and P. Krastev, Phys. Lett. **B436**, 243 (1998); J. Bahcall, P. Krastev, and A. Smirnov, Phys. Rev. **D60**, 093001 (1999); M. Gonzalez-Garcia, P. de Holanda, C. Pena-Garay, and J. W. F. Valle, Nucl. Phys. B, in press (hep-ph/9906469). Recent discussions of flux calculations are in J. Bahcall, Phys. Rept. **333**, 47 (2000), talk at Neutrino-2000, and http://www.sns.ias.edu/ jnb/. Super Kamiokande data is reported in Super Kamiokande Collab., Y.Fukuda et al., Phys. Rev. Lett. **82**, 1810, 243 (1999). For recent reviews, see e.g., Y. Suzuki, talk at Neutrino-2000, Int'l Conf. on Neutrino Physics and Astrophysics, http://www.nrc.ca/confserv/nu2000/, Y. Takeuchi at ICHEP-2000, Int'l Conf. on High Energy Physics, Osaka, http://ichep2000.hep.sci.osaka-u.ac.jp.

[2] L. Wolfenstein, Phys. Rev. **D17**, 2369 (1978).

[3] S. P. Mikheyev and A. Smirnov, Yad. Fiz. **42**, 1441 (1985) [Sov.J. Nucl. Phys. **42**, 913 (1986)], Nuovo Cim., **C9**, 17 (1986).

[4] Kamiokande Collab., K. S. Hirata, Phys. Lett. **B205**, 416; *ibid.* **280**, 146 (1992); Y.Fukuda et al., Phys. Lett. **B335**, 237 (1994); S. Hatakeyama et al. Phys. Rev. Lett. **81**, 2016 (1998).

[5] IMB Collab., D. Casper et al., Phys. Rev. Lett. **66**, 2561 (1991); R.Becker-Szendy et al., Phys. Rev. **D46**, 3720 (1992); Phys. Rev. Lett. **69**, 1010 (1992).

[6] Y. Fukuda et al., Phys. Lett. **B433**, 9 (1998); Phys. Rev. Lett. **81**,1562 (1998); *ibid.*, **82**, 2644 (1999); Phys. Lett. **B467**, 185 (1999); H. Sobel, in Neutrino-2000, T. Toshito, in ICHEP-2000. Recent discussions of flux calculations are T. Gaisser, Nucl. Phys. (Proc. Suppl.) **87**, 145 (2000) and P. Lipari, Astropart. Phys. **14**, 153 (2000).

[7] W. Allison et al., Phys. Lett. **B449**, 137 (1999), A. Mann, talk at Neutrino-2000, hep-ex/0007031.

[8] M. Ambrosio et al., Phys. Lett. **B478**, 5 (2000); B. Barish, talk at Neutrino-2000.

[9] M. Sakuda and K. Nishikawa, talks at ICHEP-2000, Osaka.

[10] M. Apollonio et al., Phys. Lett. **B420**, 397 (1998); Phys. Lett. **B466**, 415 (1999).

[11] LSND Collab., C. Athanassopoulous et al., Phys. Rev. Lett. **77**, 3082 (1996), LSND Collab., C. Athanassopoulous et al., Phys. Rev. Lett. **81**, 1774 (1998); K. Eitel, in Neutrino-2000.

[12] For a recent general review, see J. Ellis, in Neutrino-2000.

[13] M. Gell-Mann, P. Ramond, R. Slansky, in *Supergravity*, edited by P. van Nieuwenhuizen and D. Freedman (North Holland, Amsterdam, 1979), p. 315; T. Yanagida in proceedings of *Workshop on Unified Theory and Baryon Number in the Universe*, KEK, 1979.

[14] References and websites for these experiments and future projects can be found, e.g., at http://www.hep.anl.gov/ndk/hypertext/nu_industry.html.

[15] Some relevant websites at BNL, FNAL, and CERN containing further information are http://www.cap.bnl.gov/mumu/ http://www.fnal.gov/projects/muon_collider/nu/study/study.html. http://www.cern.ch/~ autin/nufact99/whitepap.ps. See, in particular, the report of the Fermilab Working Group, C. Albright et al., *FNAL Feasibility Study on a Neutrino Source Based on a Neutrino Storage Ring* (March 30, 2000), available at the above FNAL web site.

[16] Neutrino Factory and Muon Collider Collaboration, Expression of Interest for R+D towards a Neutrino Factory Based

on a Storage Ring and Muon Collider, physics/9911009, http://puhep1.princeton.edu/mumu/NSFLetter/nsfmain.ps. This site also contains further references to the relevant literature.

[17] ICANOE Collab. F. Cavanna et al., LNGS-P21-99-ADD-1,2, Nov 1999; A. Rubbia, hep-ex/0001052.

[18] OPERA Collab., CERN-SPSC-97-24, hep-ex/9812015.

[19] S. Geer, Phys. Rev. **D57**, 6989 (1998).

[20] De Rujula, M. B. Gavela, and P. Hernandez, Nucl. Phys. **B547**, 21 (1999).

[21] V. Barger, K. Whisnant, S. Pakvasa, and R. J. N. Phillips, Phys. Rev. **D22**, 2718 (1980). See also V. Barger, K. Whisnant, and R. J. N. Phillips, Rev. Rev. Lett. **45**, 2084 (1980).

[22] D. Ayres, T. Gaisser, A. K. Mann, and R. Shrock, in *Proceedings of the 1982 DPF Summer Study on Elementary Particles and Future Facilities*, Snowmass, p. 590; D. Ayres, B. Cortez, T. Gaisser, A. K. Mann, R. Shrock, and L. Sulak, Phys. Rev. **D29**, 902 (1984).

[23] P. Krastev, S. Petcov, Phys. Lett. **B205**, 8 (1988). A. J. Baltz, J. Weneser, Phys. Rev. **D37**, 3364 (1988).

[24] S. Petcov, Phys. Lett. **B434**, 321 (1998). M. Chizhov, M. Maris, S. Petcov, hep-ph/9810501; M. Chizhov, S. Petcov, hep-ph/9903424; M.Chizhov, S.Petcov, Phys. Rev. Lett. **83**, 1096 (1999).

[25] E. Akhmedov, A. Dighe, P. Lipari, A. Smirnov, Nucl. Phys. **B542**, 3 (1999); E. Akhmedov, Nucl.Phys. **B538**, 25 (1999); hep-ph/0001264.

[26] P. Krastev, Nuovo Cimento **103A**, 361 (1990); R. H. Bernstein an d S. J. Parke, Phys. Rev. **D44**, 2069 (1991); M. Campanelli, A. Bueno, A. Rubbia, hep-ph/9905240; P. Lipari, hep-ph/9903481; D. Dooling, C. Giunti, K. Kang, C. W. Kim, hep-ph/9908513.

[27] V. Barger, S. Geer, K. Whisnant, Phys.Rev. **D61**, 053004 (2000).

[28] I. Mocioiu, R. Shrock, Phys. Rev. **D62**, 053017 (2000); *Proceedings of NNN99*, A.I.P. Conf. Proc. 533, pp. 74-79 (A.I.P., New York, 1999).

[29] S.M. Bilenky, C. Giunti, W.Grimus, Phys.Rev.**D58**, 033001 (1998); K. Dick, M. Freund, M. Lindner, A. Romanino, Nucl. Phys. **B562**, 29 (1999); M. Tanimoto, Phys. Lett. **B462**, 115 (1999); A. Donini, M.B. Gavela, P. Hernandez, S. Rigolin, hep-ph/9909254; M. Koike, J. Sato, hep-ph/9909469; P.F. Harrison, W.G. Scott, hep-ph/9912435.

[30] V. Barger, S. Geer, R. Raja, K. Whisnant, hep-ph/9911524; M. Freund, T. Ohlsson, hep-ph/9909501; T. Ohlsson, H. Snellman, hep-ph/9910546, hep-ph/9912295. M. Freund, M. Lindner, S.T. Petcov, A. Romanino, hep-ph/9912457; A. Cervera, A. Donini, M.B. Gavela, J. Gomez Cadenas, P. Hernandez, O. Mena, and S. Rigolin, hep-ph/0002108.

1.4 Parameters of Major Components

B. Palmer

Chapter 2

Proton Driver

T. Roser

M.J Brennan, I. Marneris, T. Roser, A.G. Ruggiero, D. Trbojevic, S.Y. Zhang

ColliderAccelerator Department
Brookhaven National Laboratory
Upton, N.Y. 117935000

2.1 Introduction

After more the 40 years of operation the AGS is still at the heart of the Brookhaven hadron accelerator complex which presently consists of a 200 MeV Linac for the preacceleration of high intensity and polarized protons, two Tandems for the preacceleration of heavy ion beams, a versatile Booster, that allows for efficient injection of all three types of beams into the AGS and most recently the two RHIC collider rings that produce high luminosity heavy ion and polarized proton collisions. For several years now the AGS is holding the world intensity record with more than $7x10^{13}$ protons accelerated in a single pulse.

We are examining here the possible upgrades to the AGS complex that would meet the requirements for the proton beam for neutrino factory operation. Those requirements are summarized in Table 1 and a layout of the upgraded AGS is shown in Figure 1. Since the present number of protons per fill is already close to the required number, the upgrade will focus on increasing the repetition rate and on reducing beam losses to avoid excessive shielding requirements and to maintain the machine components serviceable by hand. It is also important to maintain all the present capabilities of the AGS, in particular its role as injector to RHIC.

The AGS Booster was built to allow the injection of any species of heavy ion into the AGS but also allowed a fourfold increase of the AGS intensity since it is one quarter the size of the AGS with the same aperture. However, the accumulation of four Booster loads in the AGS take precious time and is not well suited for high average beam power operation. We are proposing here to built a superconducting upgrade to the existing 200 MeV Linac to an energy of 1.2 GeV for direct H minus injection into the AGS. This will be

Table 2.1: AGS proton driver parameters

labeltb1-proton

Total beam power	1 MW
Beam energy	24 GeV
Average beam current	42 A
Cycle time	400 ms
Number of protons per fill	1×10^{14}
Average cicrculating current	5.3 A
Number of bunches per fill	6
Number of protons per bunch	1.7×10^{13}
Time between extracted bunches	20 ms
Rms bunch length at extraction	3 ns
Peak bunch current	400 A
Total bunch area	5 eVs
Rms bunch emittance	0.4 eVs
Rms momentum spread	0.5 %

discussed in section 2. The minimum ramp time to full energy is presently 0.5 s, which will have to be upgraded to reach the required repetition rate of 2.5 Hz. Since the six bunches have to extracted one bunch at a time, as is presently done for the operation of the g2 experiment, a 100 ms flattop has to be included which leaves in fact only 150 ms for the ramp up or ramp down cycle. The required a threefold upgrade of the AGS power supply will be described in section 3. Finally, the increased ramp rate and the final bunch compression requires a substantial upgrade to the AGS rf system. This will be discussed in section 4. The final section describes possible upgrade paths towards a 4 MW operation.

TABLE 1. AGS proton driver parameters

The front end consists of the existing high intensity negativeion source, followed by the 750 keV RFQ, and the first 5 tanks of the existing room temperature DriftTube Linac (DTL) to accelerate protons to 116 MeV. The SCL is made of three sections, each with its own energy range, and different cavitycryostat arrangement.

The frontend of the Linac is made of an ion source operating with a 0.25% duty cycle at the repetition rate of 2.5 Hz. The beam current within a pulse is 37.5 mA of negativehydrogen ions. The ion source seats on a platform at 35 kVolt. The beam is prechopped by a chopper located between the ion source and the RFQ. The beam chopping extends over 65% of the beam length, at a

Figure 2.1: AGS proton driver layout

Table 2.2: Comparison of H minus injection parameters

	AGS Booster	SNS	1 MW AGS
Beam power, Linac exit, kW	N/A	1000	54
Kinetic Energy, MeV	200	1000	1200
Number of Protons N_P, 10^{12}	15	200	100
Vertical Acceptance A, mmmrad	192	480	108
$\gamma^2 beta^3$	0.57		9.56
N_P /$\gamma^2\beta^3$ A), 10^{12} mmmrad	0.136		0.097
Total Beam Losses, %	5		2

frequency matching the accelerating rf at injection into the AGS. Moreover, the transmission efficiency through the RFQ is taken conservatively to be 80%, so that the average current of the beam pulse in the Linac, where we assume no further beam loss, is 25 mA. The combination of the chopper and of the RFQ pre bunches the beam with a sufficiently small longitudinal extension so that each of the beam bunches can be entirely fitted in the accelerating rf buckets of the following DTL that operates at 201.25 MHz. The DTL is a room temperature conventional Linac that accelerates to 116 MeV.

The proposed new injector for the AGS is a 1.2 GeV superconducting linac upgrade with an average output beam power of about 50 kW. The injection energy is still low enough to control beam losses due to stripping of the negative ions that are used for multiturn injection into the AGS. The duty cycle is about 0.25 %. The injection into the AGS is modeled after the SNS. However, the repetition rate and consequently the average beam power is much lower. The larger circumference of the AGS also reduces the number of foil traversals. Beam losses at the injection into AGS are estimated to be about 2% of controlled losses and 0.2 % of uncontrolled losses. This is based on a comparison with the actual experience in the AGS Booster and the predicted losses at the SNS using the quantity N_P /^{23} A), which is proportional to the Laslett tune shift, as a scaling factor. This is summarized in Table 2. As can be seen the predicted 2% beam loss is consistent with both the AGS Booster experience and the SNS prediction.

The AGS injection parameter are summarized in TB. 2.3. The result of a simulation of the 360 turn injection process with a twoharmonic rf system is shown in Fig. 2.2 resulting in a longitudinal emittance of 4.2 eVs per bunch. Such a small emittance is important to limit beam losses during transition

Table 2.3: AGS injection parameter

Injection turns	360
Repetition rate	2.5 Hz
Pulse length	1.05 ms
Chopping rate	0.65
Linac peak current	25 mA
Momentum spread	$\pm 0.2\%$
Norm. 95% emittance	$12\pi\mu m$
RF voltage	100 kV
Bunch length	324 ns
Longitudinal emittance	4.2 eVs
Momentum spread	$\pm 0.44\%$
Norm. 95% emittance	100m

crossing and to allow for effective bunch compression before extraction from the AGS.

Since the intensity of 1×10^{14} is only marginally higher than the present intensity of 7×10^{13} no new instabilities are expected during acceleration and transition crossing. However, significant more rf voltage per turn and rf power will be required. This will be addressed in section 4.

2.2 Superconducting Linac

The superconducting linacs accelerate the proton beam from 116 MeV to 1.2 GeV. The presented configuration follows a similar design described in detail in [1]. All three linacs are built up from a sequence of identical periods as shown in Figure 2. Each period is made of a cryomodule and a roomtemperature insertion that is needed for the placement of focusing quadrupoles, vacuum pumps, steering magnets, beam diagnostic devices, bellows and flanges. The cryomodule includes 4 identical cavities, each with 4 or 8 identical cells.

Figure 3. Configuration of the cavities within the cryomodules (cryostats)

The choice of cryomodules with identical geometry, and with the same cavity/cell configuration, is economical and convenient for construction. But there is,

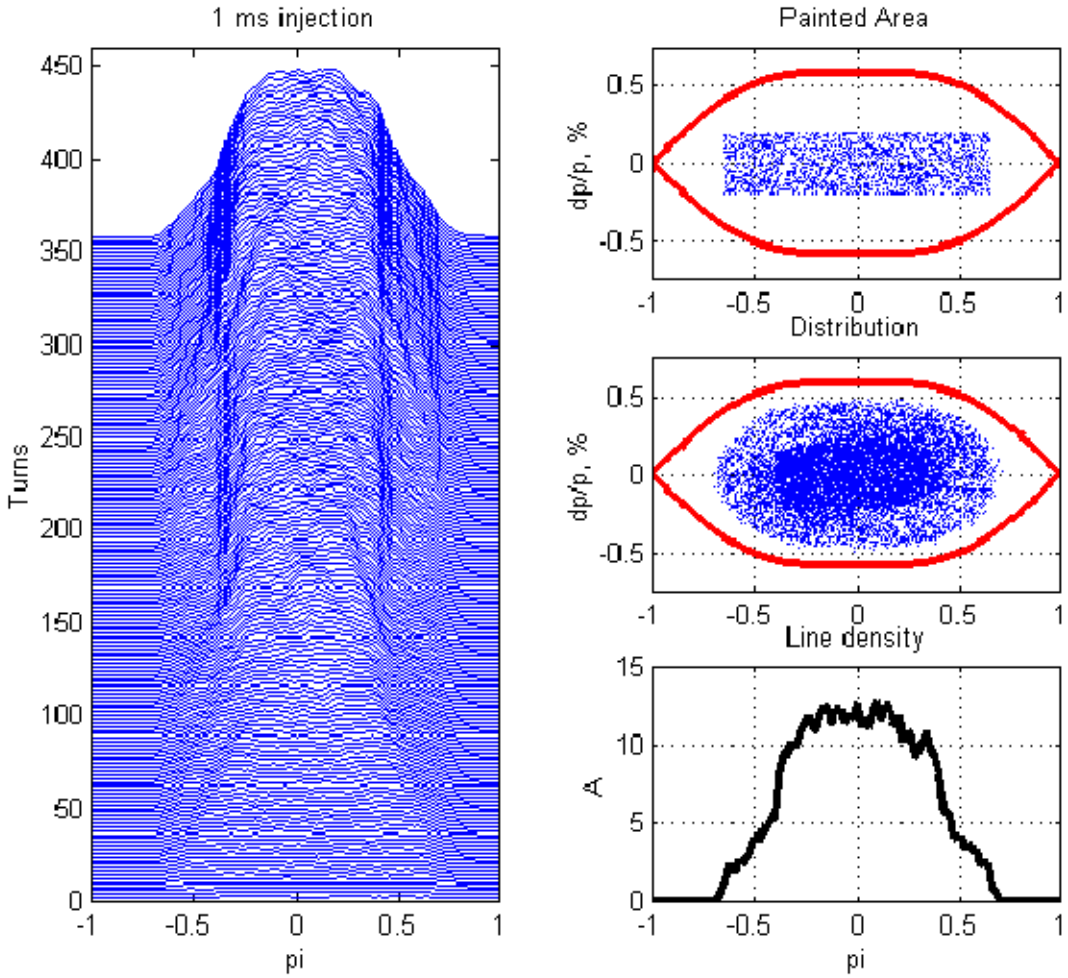

Figure 2.2: AGS injection with double RF

nonetheless, a penalty due to the reduced transittimefactors when a particle crosses cavity cells, with lengths adjusted to a common central value $_0$ that does not correspond to the particle's instantaneous velocity. This is the main reason to divided the superconducting linac into three sections, each designed around a different central value $_0$, and, therefore, with different cavity/cell configurations. The cell length in a section is fixed to be

where l is the rf wavelength.

The major parameters of the three sections of the SCL are given in Table 2. Transverse focussing is done with a sequence of FODO cells with halflength equal to that of a period. The phase advance per cell is 90 degrees . The rms normalized betatron emittance is 0.3 mmmrad. The rms bunch area is 0.5 degree MeV. The rf phase angle is 30 degrees .

The length of the Linac depends on the average accelerating gradient. The local gradient has a maximum value that is limited by three causes: (1) The surface field limit is taken to be 26 MV/m. For a realistic cavity shape, we set a limit of a 13 MV/m on the axial electric field. (2) There is a limit on the power provided by rf couplers that we take here not to exceed 400 kW, including a contingency of 50% to avoid saturation effects. (3) To make the longitudinal motion stable, we can only apply an energy gain per cryomodule that is a relatively small fraction of the beam energy in exit of the cryomodule. The conditions for stability of motion have been derived in ref. [1].

The proposed mode of operation is to operate each section of the SCL with the same rf input power per cryomodule. This will result in some variation of the actual axial field from one cryomodule to the next. If one requires also a constant value of the axial field, this could be obtained by adjusting locally the value of the rf phase.

For the pulsedmode of operation of the superconducting cavities the Lorentz forces could deform the cavity cells enough to detune them off resonance. This has to be controlled with a thick cavity wall and additional supports. Also, a significant time to fill the cavities with rf power is required before the maximum gradient is reached and beam can be injected. The expected fill time is short compared to the beam pulse length of 1 ms.

TABLE 4. Parameters of the superconducting linacs

	Low energy	Medium energy	High
Beam power, Linac exit, kW	18	36	54
Kinetic Energy Range, MeV	116 ... 400	400 ... 800	800 ... 1200

Velocity Range, c	
	0.4560...0.7131
	0.7131...0.8418
	0.8418...0.9017
Frequency, MHz	
	805
	1610
	1610
Protons / Bunch, 10^8	
	2.33
	2.33
	2.33
Temperature, K	
	2.0
	2.0
	2.0

Cells / Cavity

4

8

8

Cavities / CryoModule

4

4

4

Cell Length, cm

9.68

6.98

8.05

Cell reference velocity, c

0.865

Cavity internal diameter, cm

	5
Cavity Separation, cm	
	32
	16
	16
ColdtoWarm transition, cm	
	30
Accelerating Gradient, MeV/m	
	21.5
Cavities / Klystron	

No. of Klystrons (or periods)	4
Klystron Power, kW	9
Energy Gain / Period, MeV	2160
Length of a period, m	48.0

	4.7
Total length, m	
	42.6

3. AGS main power supply upgrade

Present Mode of Operation

The present AGS Main Magnet Power Supply (MMPS) is a fully programmable 6000 A , ±9000 V SCR power supply. A 9MW Motor Generator, made by Siemens, is a part of the main magnet power supply of the accelerator, which allows to pulse the main magnets up to 50 MW electric peak power, while the input power of the motor generator remains constant. The maximum power into the motor ever utilized is 7 MW, that is the maximum average power dissipated in the AGS magnets did never exceed 5 MW.

The AGS ring consists of 240 magnets hooked up in series. The total resistance R is 0.27 ohm and the total inductance L is 0.75 henry. There are 12 superperiods, A through L, of 20 magnets each, divided in two identical sets of 10 magnets per superperiod.

Two stations of power supplies are each capable of delivering up to 4500V and 6000 A. The two stations are connected in series and the magnet coils are arranged to have a total resistance R/2 and a total inductance of L/2. The grounding of the power supply is done only in one place, in the middle of station 1or 2 through a resistive network. With this grounding configuration, the maximum voltage to ground in the magnets will not exceed 2500 Volt. The magnets are hipotted to 3000 Volt to ground, prior of each starting of the AGS MMPS after long maintenance periods.

To cycle the AGS ring to 24 GeV at 2.5 pulses per second and with ramp time of 150 ms the magnet peak current is 4300 Amp and the peak voltage is 25 kV. Figure 3 displays the magnet current, voltage of a 2.5Hz cycle. The cycle includes a 100 ms flattop for the six singlebunch extractions. The total average power dissipated in the AGS magnets has been estimated to be 3.7 MW. To limit the AGS coil voltage to ground to 2.5 kV the AGS magnets will need to be divided into three identical sections, each powered similarly to the present whole AGS except that now the magnet loads is 1/6 of the total resistance and inductance. Every section will have to be powered separately with its own feed to the ring magnets and an identical system of power supplies, as shown in Figure 4**.**

Figure of AGS mmps cycle

Figure 3. Current and voltage cycle for 2.5 Hz operation. Also shown are the AGS dipole field and average power.

Although the average power is not higher than now the peak power required is approximately 100 MW exceeding the 50 MW rating of the existing motor generator. The new motorgenerator should also operate with 6 or 12 phases to limit or even eliminate phaseshifting transformers so that every power supply system generates 24 pulses. The generator voltage will have to be around 30 kV linetoline. In this case the generator current is approximately equal to the magnet current as it is presently the case. Also, the generator needs to be rated at a slip frequency of 2.5 Hz.

Figure of power supply connection to AGS magnets

Figure 4. Schematic of power supply connections to the AGS magnets for the 2.5 Hz operation

Running the AGS at 2.5 Hz requires that the acceleration ramp period decreases from 0.5 sec down to 0.15 sec. That is, the magnet current variation dI/dt is about 3.3 times larger than the present rate. Eddycurrent losses on the vacuum chamber are proportional to the square of dI/dt, that is 10 times larger. However, this still significantly smaller than the present ramp rate of the AGS Booster and does not require active cooling. Also, the increased eddycurrents will increase the sextupole fields during the ramp and will add about 20 units of chromaticity. The present chromaticity sextupoles will probably have to upgraded to correct this.

4. AGS rf system upgrade

5. Upgrade to 4 MW

An upgrade to 4 MW beam power is possible by increasing the linac energy to 1.5 GeV, which allows for doubling the number of protons per pulse to 210^{14}, and upgrading the AGS repetition rate to 5 Hz. To achieve the required bunch length compression a separate "compressor ring" will be needed.

Compressor ring parameter

Circumference

200

m

Bending field

42

4.15

Tesla

Kinetic energy

24

GeV

Transition gamma

38.4

eta

0.00074

Betatron tune, x/y

14.8/9.2

Maximum beta function, x/y

12.9/19.8

m

Dispersion function

0.12

m

Chamber radius

25

mm

Maximum beam radius, x/y

7.0/8.6

mm

Acceptance, x/y

48.5/31.6

m

Beam emittance, x/y

3.8/3.8

m

Accp./emit. ratio, x/y

12.8/8.3

Natural chromaticity, x/y

2.5/1.7

(norm)

Operated below transition.

Very small slippage factor, quasiisochronous ring.

Very small dispersion.

Acceptance/emittance ratio ¿ 8, with the consideration of extremely tight beam loss limit.

Chromaticity needs to be corrected.

RF parameter

RF frequency

5.94

MHz

Harmonic number

4

RF Voltage

200

KV

Bucket height, in dp/p

4.2

%

Bucket area

222

eVs

Bunch area

10

eVs

Synchrotron frequency, center

46

91.5

Hz

Synchrotron frequency, edge

82.6

Hz

Bunch is injected from the AGS, unmatched. It is extracted immediately after a bunch rotation.

Very low RF voltage required, because of the very small slippage. For the same bucket height, RF voltage in the AGS needs to be 5.3 MV.

Bunch rotation takes a quarter of synchrotron period, i.e. 3 ms, or 4500 turns.

Longitudinal aspect

Inj.

Ext.

Particle per bunch

0.17

0.17

10^{14}

Bunch rms length

5/17

0.9/3

m/ns

Peak current

65

363

A

Beam momentum spread

0.4

2.24

%

Longitudinal emittance

10.5

10.5

48

eVs

Broadband impedance

5

5

j

Long. space charge imp.

1.66

1.66

j

KeilSchnell threshold

3.75

25.5

Effective RF voltage

200

248

KV

49

Longitudinal microwave instability threshold is low at the injection, because of the small slippage factor and low dp/p.

Bellows will not be shielded, in order to avoid finger contact arcing, but the chamber steps will be tapered. Broadband impedance of j 5 is reasonable to achieve.

Combination of the broadband and space charge impedance is j3.34 , slightly lower than the KS threshold. Since it is below the transition, beam instability is not expected.

The overall inductive impedance below the transition has a focusing effect, which is shown as the increase of the effective RF voltage in the bunch rotation.

Transverse aspect

Inj.

Ext.

Broadband impedance

0.51

0.51

jM/m

BB imp. induced tune shift

0.0003

0.0017

Space charge inc. tune spread

0.003

0.016

Chromatic tune spread,

0.22

1.32

Chromatic frequency,

59.4

51

59.4

GHz

Transverse impedance is low for compressor ring, .

Strong focusing also helps for less tune shift.

Comparing to the AGS, the beam is transversely more stable. This is just opposite to the longitudinal instability.

Space charge incoherent tune spread is small.

But if the chromaticity is not corrected, the chromatic tune spread is large.

Chromatic frequency is very large, because of the small slippage factor, the high revolution frequency, and the high tune.

Normalized chromaticity may need to be controlled within the range of 1%.

Conclusion

The scheme of 1 MW proton driver is feasible.

AGS beam intensity is modestly higher than the normal high intensity proton operation. Since the proposed beam emittance is larger, the beam instability is not expected to be a problem.

Beam loss limit is tight at the AGS, which may require some upgrade.

Compressor ring design requires very low RF voltage. Also the potential well effect helps for the short bunch production.

Required impedance is reasonable to achieve.

Acceptance/emittance ratio of 8 is much larger than the existing and proposed high intensity proton accelerators. Together with the large momentum aperture, the beam loss can be controlled.

Chromaticity control at the compressor ring is tight, and may need some study.

References

1. A. Ruggiero, "Design Considerations on a Proton Superconducting Linac" BNL Internal Report 62312, 1995.

Chapter 3

Target System and Support Facility

K. McDonald, P. Spampinato

Figure 3.1: The overall target support facility.

3.1 Target System, Proton Beam Absorber, and Support Facility

(P. Spampinato/ORNL:3/11/01)

3.1.1 Introduction

The Target Support Facility consists of the target region and decay channel, a crane hall over the length of the facility, a maintenance cell at the ground floor elevation for magnet components, a hot cell at the tunnel level for mercury target system components, and various remote handling equipment used for maintenance tasks. The facility is bounded by the proton beam window at the upstream end and the first induction linear accelerator at the downstream end. It contains the equipment for the freejet mercury target, high field and low field superconducting solenoids, watercooled shielding to limit radiation dose and neutron heating to the coils, biological shielding to protect personnel and the environment, and a 50 ton crane used for the initial assembly and installation of major components and for subsequent maintenance activities. The target support facility is 11 meters wide, and approximately 40 meters long. Figure 3.1 shows the overall facility.

3.1.2 Target System and Proton Beam Absorber

The mercuryjet target system consists of a process flow loop, a replaceable nozzle assembly mounted in the bore of the iron plug magnet, a containment vessel that is part of the decay channel, and a dedicated hot cell that contains most of the flow loop components. Figure 3.2 is a schematic diagram of the overall system.

Figure 3.2: Target system and beam absorber schematic layout.

3.1.3 Process Flow Loop

The process flow loop contains 85 liters of mercury distributed as follows: 30 l in the beam absorber pool, 6 l in the heat exchanger, 35 l in the sump tank, and 14 l in miscellaneous piping and valves. A 200 liter tank provides storage of the mercury when the system is shutdown or undergoing maintenance. Various valves are used to isolate portions of the system for storage, flow, or drainage into the storage tank by means of gravity. The pumps are centrifugal magnetic drive. The low capacity, selfpriming pump (36 gpm) transfers mercury from the storage tank into the flow loop, and the high capacity pump (3550 gpm) is a sumppump that circulates the mercury though the nozzle assembly at 30 m/s. The heat exchanger is a welded tube, closed loop water system; the inlet temperature of the Hg is 122C, outlet temperature is __C; water inlet temperature is 20C, outlet temperature is __C. (The heat exchanger calculations need to be redone ...)

In addition to the gravity drain lines from the sump pump and beam absorber pool, a secondary drain/vent is located at Z = 6.0 m. Its purpose is to extract and condense mercury vapor prior to a maintenance operations that requires opening the mercury containment in the capture/decay channel. The vent line is connected in series to a mercury trap (condenser) and a vacuum scroll pump. The condensate is returned to the storage tank by means of a bypass line, and the vacuum exhaust passes through a bank of sulfurtreated charcoal filters before entering the facility ventilation exhaust.

The average beam power deposited in the jet is 400 W/g (128 kW) and the remainder of the 1 MW proton beam is assumed to end up in the absorber. The bulk temperature rise of the mercury in the absorber pool is 102C, well below the boiling point. However, this assumes there is no local heating in the pool, and that homogeneous mixing occurs because of the mercury jet (if it remains intact) that streams into the pool at a rate of 2.4 l/s.

The storage tank is located in the pit area under the first cryostat at an

vskip 2cm

Figure 3.3: Arrangement of components in the target hot cell.

vskip 2cm

Figure 3.4: Side elevation of the facility geometry.

elevation below the bottom of the sumppump tank. All other components are located in the target hot cell ...

... throughthewall manipulator and shield window ... Figure 3.3 is a view of the target hot cell.

More to be added:

3.1.4 Target System Operation

3.1.5 Mercury Containment

3.1.6 Target System Replacement and Remote Handling

(100 mrad, nozzle)

3.2 Target Support Facility

The geometry for the target support facility is defined around the intersection of the mercury jet, the proton beam, and the magnetic axis of the coils. The proton beam interacts with the jet over a 30 cm region so that the downstream interaction point is at Z = 0 cm (where the proton beam intersects the magnetic axis), and the upstream interaction point is at Z = 30 cm. The location of the coils and other components are measured from Z = 0. The decay channel extends to Z = 35.60 m, which is the facility interface with the first induction linear accelerator. Figures 3.4 and 3.5 show the basic geometry of the facility and its boundaries.

The proton beam window is located at Z = 330 cm and is connected to the core vacuum vessel with a removable section of beam pipe. This

vskip 2cm

Figure 3.5: Side elevation of the target region.

design permits the window assembly to be close to the target region, yet readily removable to replace the window or the mercury jet nozzle, or provide clearance for the replacement of the inner solenoid module should that ever become necessary.

It is important to keep in mind that virtually all of the components that make up the target and capture facility will be highly radioactive; hence, handling and replacement after start up operations must be done using remote handling equipment and tools. Therefore, development of the facility arrangement was based on considering the initial assembly and installation of the various components, and also on modularization of components to simplify remote handling and have minimal impact on operating availability.

3.3 Solenoid Magnets

The solenoid magnets are located in the capture and decay tunnel of the support facility, and although they are considered to be lifetime components, the facility design is based on their remote replacement. The tunnel begins in the target region upstream of the proton beam window and extends to Z = 35.6 m. The first five solenoids (SC15) are contained in a common cryostat that extends to Z = 6.1 m, and is designed so that its inner cryostat shell is the outer shell of part of the tungstencarbide shield. Therefore, there is a shield cylinder attached to the cryostat that is 12 cm thick and contains inner rib supports to stiffen this cylindrical beam. The ribs are also partitions for the cooling flow channels of the shield. Figure 6 is a section through the first cryostat that shows the magnet arrangement and the shieldbeam. The end view shows the rib structure of the shield beam and the other inner shield modules.

There is a separate module for the resistive magnets and shielding contained within the bore of SC1. It consists of an iron plug, three resistive, watercooled magnets (HC13), and tungstencarbide shielding. The combination of these coils and SC1 provide the 20 Tesla fieldonaxis in the target region. Figure 7 shows the resistive coil module along with the nozzle insert

Figure 3.6: Main cryostat and shield support beam.

Figure 3.7: The resistive coils/shield module.

for the mercury jet.

The magnets downstream of the first cryostat are single coil solenoids contained in 2meter long cryostats, except for SC6 which has a 0.5 m cryostat. These extend from Z = 6.117.6 m and make up the rest of the transition coils (SC612). In this region, the fieldonaxis decreases to 1.25 T. (see Figs. 1 and 4)

Coil SC6 is smaller and is designed to be the mounting support for a beryllium window that is located at Z = 6.1 m. The window is the downstream containment boundary for mercury target vessel. The window is periodically replaced by removing SC6 and installing a spare SC6 with a replacement window already installed. Figure 8 is a view that shows SC6 removed from the transition region, with the upstream isolation valve closed.

The coils from the transition region to the end of the decay channel are contained in 3meter long cryostats, three coil pairs to a cryostat. (see Figs. 1 and 4) ...

The overall dimensions of the coil modules and their respective component weights are given in Table 1.

Figure 3.8: SC6 is the support structure for the mercury containment Be window.

Table 3.1: Solenoid coil sizes and weights, and shield module weights.

Component	Outer Diam (cm)	Length (cm)	Module Wt.(lbs)
Resist. Module			47,500
Iron Plug	n/a	n/a	
HC1	n/a	n/a	
HC2	n/a	n/a	
HC3	n/a	n/a	
WC Shield			
First Cryostat	270	740	TBD
+Shield Beam			
SC1	256	178	61,000
SC23	202	183	21,700
34 Shield	128	183	59,600
SC45	176	351	17,900
45 Shield	148	351	86,400
SC6+Shield	104	50	TBD
SC7+Shield	104	185	TBD
SC8+Shield	104	185	TBD
SC9+Shield	104	185	TBD
SC10+Shield	104	185	TBD
SC11+Shield	104	185	TBD
SC12+Shield	104	185	TBD
Decay Coils + Shield (6)	TBD	296	TBD

3.4 High Field Region

The high field coils provide a 20 Tesla field in the target region and consist of three resistive coils and an iron plug surrounded by a water cooled tungstencarbide shield and an outer superconducting coil (SC 1). The three coils and the shield are a single module that is separate from, but inserted into the cryostat of the high a field superconducting coil. The inner radius of the cryostat for this coil is __ cm.

3.4.1 CoiltoCoil Forces/Method of Support/Method of Assembly

The net force between SC112 is near zero, meaning it is a balanced system. However, the coiltocoil forces between individual magnets are significant. SC1 reacts the accumulated forces of the downstream coils which total 23 million pounds (102.5 kN), with an equal but opposite force. The forces from SC25 are, respectively, 10.3E6 lbs, 6.6E6 lbs, 3.4E6 lbs, 2.3E6 lbs. (The force contributions from SC612 are ignored here since they are small by comparison). In order to minimize heat leaks into the cryostat caused by largearea coldtowarmtocold supports, use of a common cryostat was chosen by the solenoid coil designers. Hence, the coiltocoil supports are cold, but the cryostat structure must support the total gravity load of coils SC15. This is accomplished by making a cylindrical portion of the radiation shield part of the cryostat.

3.4.2 Transition Field Coils

The cryostat is assembled from two sections onto a continuous cylindrical beam that is part of the radiation shield. The cryostat/beam assembly is lowered into the target region of the tunnel, onto a pair of trunnion supports. The trunnion is located midway along the cryostat to minimize the depth of pit area under SC15, and to minimize the elevation of the crane for installing SC45. The cryostat is rotated so that the upstream end points up and SC1 is lowered into position. The weight of the SC1, the heaviest coil module is 61,000 lbs. (At this time, the remainder of the high field magnets, i.e. the iron plug, HC13, and shielding) may be installed into the inner bore of the shieldbeam. Figure 3.9 shows the installation sequence of the high field coils.

Figure 3.9: Installation sequence of the high field coils SC1, HC13.

Figure 3.10: Installation sequence of the transition coils SC45.

The cryostat is then rotated so that the downstream end points up and the coil module consisting of SC23 is installed, followed by its protective inner shield; then module SC45 is installed followed by its inner shield. Figure 10 shows the installation sequence of SC45.

3.4.3 Decay Channel Coils

Each of the remaining cryostat modules contains a 5 cm thick radiation shield beam mounted to the inner diameter of the cryostat shell. For the coils downstream from Z = 6.1 m, the shield material is (Cu?? SS?? TBD). Preassembled to the inner shell of the shield is another shell which is the vacuum boundary for the muon decay channel. These are assembled into each cryostat so that the outer flange of the vacuum boundary shell is sealwelded to the flange of adjacent modules. Figure 11 is a typical side view and end view of the decay channel magnets showing the vacuum flange attachments and clearance for coolant lines.

3.4.4 Coil Replacement and Remote Handling

The solenoid magnets are considered to be lifetime components, i.e. Class 2. However, they must be designed to be remotely replaced in the event

Figure 3.11: Muon channel vacuum flanges and coolant line clearance.

of a failure since they are critical to the operation of the facility, and since they will become highly activated. The assembly procedure described above would be ...

3.4.5 Facility Shielding

The facility shielding is designed for the 4 MW (upgrade) proton beam power and permits unlimited access to radiation workers in the crane hall. The shield material and thickness is sized to limit the dose rate at the crane hall floor to 0.25 mrem/h (0.0025 mSv). A Monte Carlo neutron, photon, charged particle transport code (MCNPX) using cylindrical geometry was prepared for neutronic calculations. The results show that the shield over the target region and the decay channel requires a thickness of 5.5 m, consisting of 5.2 meters of steel to attenuate fast neutrons and 0.3 meters of concrete to attenuate slow neutrons. The model was carried out downstream to Z = 3600 cm, but it is clear that beyond the decay channel, into the first induction linear accelerator and beyond, the modular solenoid components will have dose rates too high to permit hands on maintenance. Therefore, the crane hall and the remote handling access that it provides to the tunnel magnets is envisioned to go well beyond the end of the decay channel. It is assumed at this time that the same crane system could be used to service the linear accelerator regions downstream, several hundred meters to the storage ring.

Figure 3.12 is a typical cross section in the decay channel showing the arrangement of removable shield slabs. The shields are sized to a weight limit of 45 tons. Each layer is 46 cm thick, and the successive slabs are slightly shorter (tunnel) in length because of the increasing width, so each slab layer has offset joints that avoid a streaming path to the crane hall. It should be noted that the width of the tunnel decreases from 7 meters in the target region to 5.2 meters at approximately Z = 700 cm because of the

Figure 3.12: Facility shield over the decay channel.

smaller diameter of the magnets downstream from SC7.

3.4.6 Upstream shielding requirements, He containment vessel and air activation

TBAdded.

3.4.7 Proton Beam Window

The proton beam window is contained in the helium vessel upstream of the target located at Z = 330 cm. It is attached to the beam pipe feedthrough with a Grayloc or Reflange remote connector. (The beam pipe diameter is assumed to be 25 cm.) **MORE TO BE ADDED + FIGURE**

3.4.8 Crane Hall TBA

3.4.9 Maintenance Operations

3.4.10 Component lifetimes

The components in the target facility fall into three categories: Class 1 are lifelimited components that require frequently scheduled remote replacements during the life of the facility; they are designed for remote handling and minimal impact on operating availability, and remote handling tools and equipment are included in the cost estimate. Class 2 are lifetime components with activation levels that preclude hands on replacement, and whose failure shuts down the facility. They have a finite probability of at least failure. They are designed for remote handling, but remote handling tools and equipment are not provided or costed (unless they are used during the initial installation). Their replacement will impact operating availability since spare components

Table 3.2: Component Lifetimes.

Component	Replacement
Class 1	
Proton Beam Window	
Be Mercury Vapor Window	
Mercury Jet Nozzle	
??	
Class 2	
All Solenoid Magnets	
??	
Class 3	
Hot Cell (at crane hall level for waste disposal and Class 2 components ...)	
Remote Handling Equipment	
Cost	
Design Issues and Near Term R&D	

are not on hand. Class 3 are components that are not expected to fail during the facility lifetime. Examples of each are: Class 1 proton beam window; Class 2 any of the solenoid magnets; Class 3 shield window, piping. Component lifetimes are listed in Table 2.

Chapter 4

Front End

4.1 Decay and Phase Rotation Sections

H. Kirk

4.1.1 Conceptual Overview THIS IS MISSING

4.2 Buncher and Ionization Cooling Section

R. Fernow, P. Lebrun

E. Black[1], D. Elvira[1], D. Kaplan[2], R. Fernow*, J. Gallardo*,
M. A. Green#, P. Lebrun[1], A. Moretti[1], D. Neuffer[1], J. Norem[3],
D. Li#, R. Palmer*, R. Rimmer#, A. Tollestrup[1],
[1]Fermilab, Batavia, Ill 60150,USA
[2]IIT, Chicago, Ill, USA
[3]Argone Natl. Lab., Ill, USA
*BNL, Upton, NY 11973, USA
#LBNL, Berkeley, CA 94720, USA

The Buncher and SFOFO cooling channel are introduced and described. Performance, systematic errors and tolerances are discussed. These are the section 12 and 13, respectively, in the Feasibility II study document.

4.3 The Buncher and Matching section from the Induction Linac

After the energy spread of the beam has been reduced in the induction linacs the muons are distributed continuously over a distance of around 100 m. It is then necessary to form the muons into a train of bunches prior to cooling and subsequent acceleration. First an 11 m long magnetic lattice section is used to gently transform the beam from the approximately uniform solenoidal field used in the induction linacs to the so called "super-FOFO", or SFOFO, lattice used in the remainder of the front end. This is followed by the 55 m long *rf* buncher itself, which consists of *rf* cavity sections interspersed with drift regions. The two functions of this section are perfomed sequentially for design simplicity. There is a significant advantage in using the same lattice in the buncher section as in the following cooling region since it avoids adding another complicated 6-dimensional matching section.

Two distinct computer codes were used to simulate this buncher and the cooling channel: ICOOL[**?**] and Geant4[**?**]. There is no shared code between the two programming environments, FORTRAN for ICOOL and C++ for Geant4. The Geant4 implementation was based solely on the parameters listed below. After optimization of the matching sections and minor clarifications, good agreement was obtained, as shown in the performance section. Based on this successful comparison, the more demanding magnet alignment tolerance study was done in the generic 3D code, i.e. Geant4.

4.3.1 Matching section

The goal of the matching section is to smoothly transform the muon beam from the 1.25 T approximately uniform focusing field to the 2 T alternating polarity s-FOFO lattice. The 4 % rms momentum spread entering the matching section is relatively small, so chromatic corrections are less critical than in the mini-cooling field reversal. Table 4.1 gives coil dimensions and current densities for the solenoid magnets used in the match.

Table 4.1: Matching section magnets

z	dz	r	dr	j
m	m	m	m	A/mm^2
0.358	1.375	0.300	0.100	-9.99
1.733	0.330	0.300	0.110	-15.57
2.446	0.187	0.330	0.330	-33.40
2.963	0.187	0.330	0.330	35.19
4.008	0.330	0.770	0.110	67.41
5.146	0.187	0.330	0.330	43.75
5.663	0.187	0.330	0.330	-43.75
6.708	0.330	0.770	0.110	-66.12
7.896	0.187	0.330	0.330	-43.75
8.413	0.187	0.330	0.330	43.75
9.458	0.330	0.770	0.110	66.12
10.646	0.187	0.330	0.330	43.75

The magnet configuration at the beginning of the section, the axial magnetic field on-axis, and the beta function for three momenta are shown in Fig. 4.1. The magnetic lattice goes from a series of constant radius solenoids to a s-FOFO cell structure consisting of small radius coils at each end of a cell and a large radius coil in the middle. Four magnets in the transition region have non-standard current densities. The axial magnetic field in a cell peaks symmetrically near the two ends and has a smaller secondary peak in the middle. The beta function across the match is similar for the three particles shown, which vary in momentum in steps of 7.5 % from 185 to 215 MeV/c.

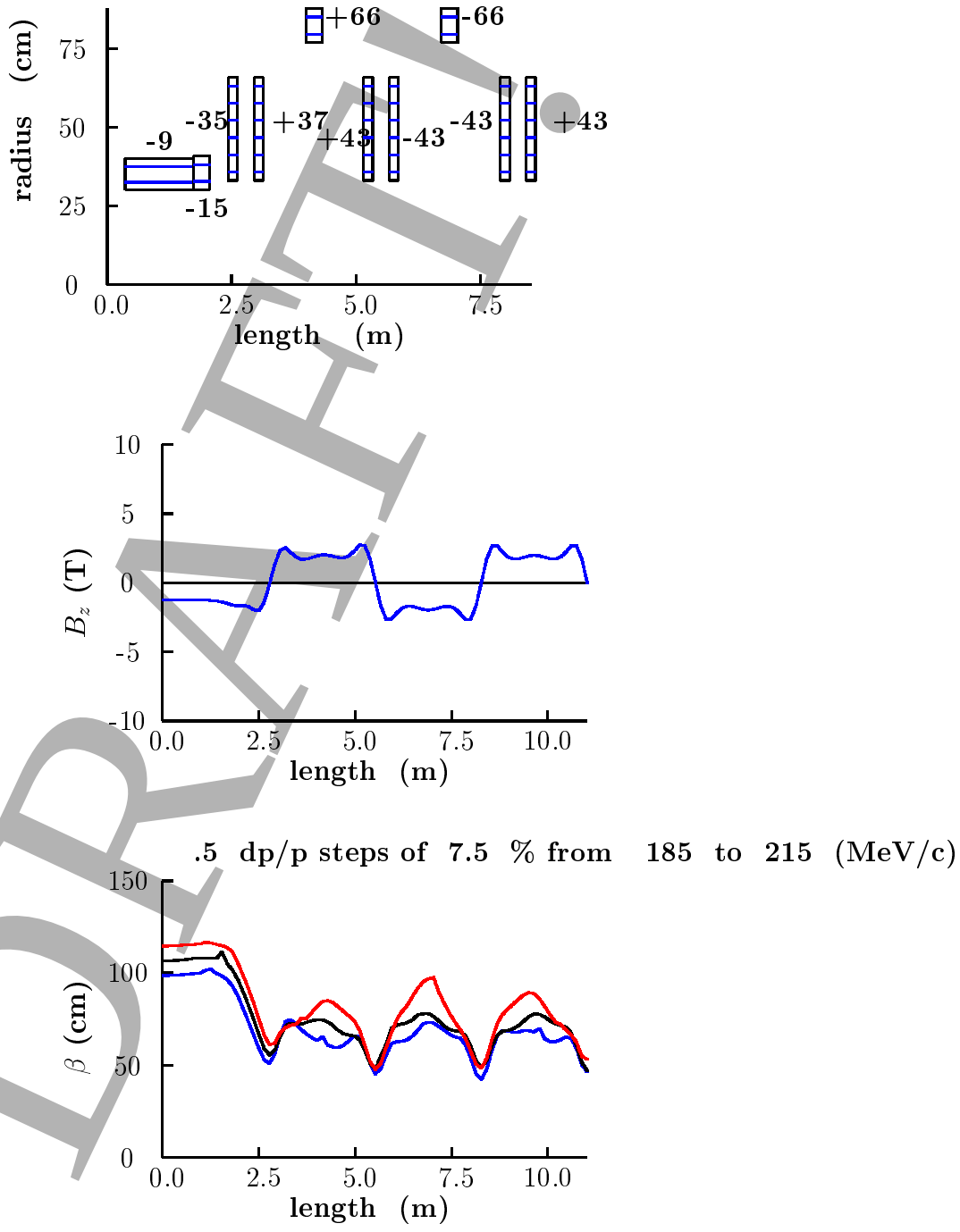

Figure 4.1: Magnet configuration; axial magnetic field; beta function.

4.3.2 Buncher section

The design principles for the lattice and details concerning the *rf* and other technical components for the buncher section will be described later. Only the beam dynamics and performance will be described here. The buncher magnetic lattice is identical to that used in the first cooling section. It contains *rf* cavities in selected lattice cells and no absorbers. The main *rf* frequency was chosen to be 201.25 MHz in the front end, so that the beam would fit radially inside the cavity aperture and because power sources and other technical components are available at this frequency. The 201.25 MHz cavities are placed at the high beta locations in the lattice, just as in the cooling section. Harmonic cavities running at 402.5 MHz are placed at beta minimum locations, where hydrogen absorbers are located in the cooling section.

The buncher encompasses 20 lattice cells, each 2.75 m long. Maximum bunching efficiency was obtained by breaking the region into three *rf* stages separated by drift regions. The locations and lengths of the buncher components are given in Table 4.2.

Second harmonic (402.5 MHz) cavities are used at the entrance and exit of the first and second stages to linearize the shape of the *rf* pulse. All cavities are assumed to have thin Be windows at each end. They are modelled in the simulation codes as perfect TM_{010} pillboxes. The window radii and thicknesses are given in Table (REFER TO TABLE 18.D HERE).

The electric field gradient is gradually raised in the buncher from 6 to 8 MV/m. A long drift is provided after the first stage to allow the particles to begin overlapping in space.

The following Fig. **??** shows the momentum-time distributions at the start, and after each of the three buncher stages. Distributions are also shown at the ends of the first and second cooling stages. In the last three distributions, ellipses are drawn indicating the approximate acceptance of the cooling channel.

It can be seen that at the end of the buncher, most, but not all, particles are within the approximately elliptical bucket. About 25 % are outside the bucket and are lost relatively rapidly, and another 25 % are lost more slowly

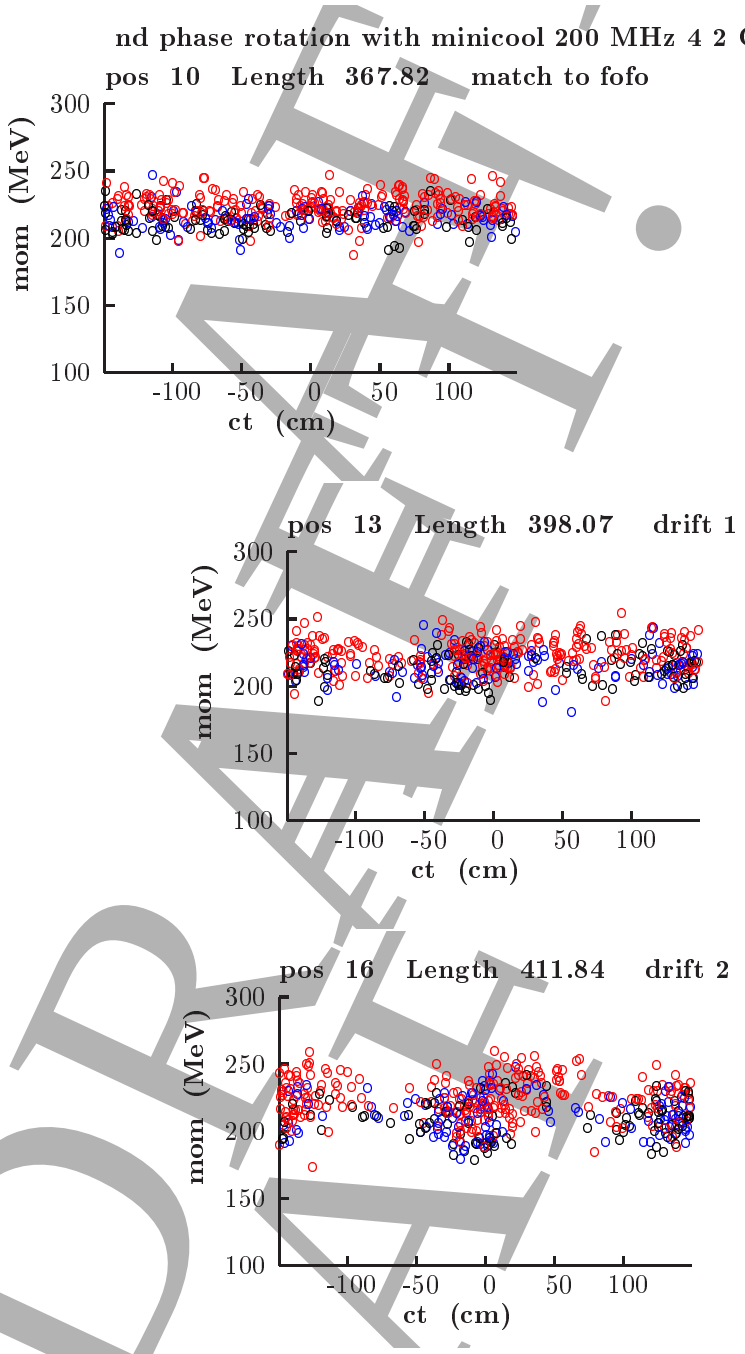

Figure 4.2: Momentum-time distributions through the buncher.

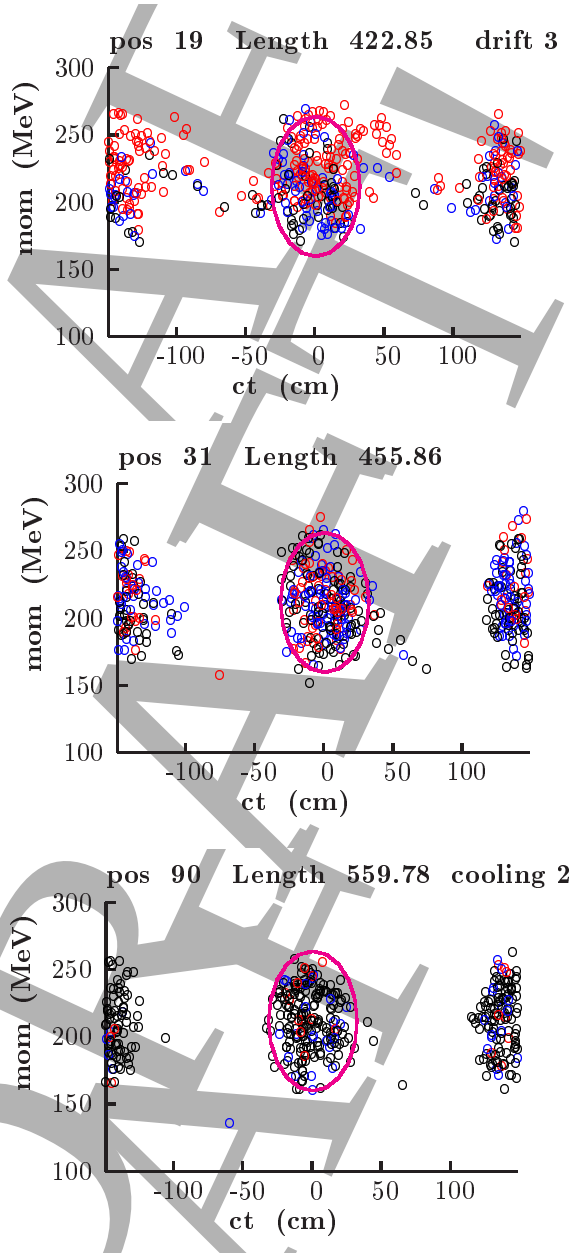

Figure 4.3: Momentum-time distributions through the buncher.

Table 4.2: *rf* buncher component locations

	length m	frequency MHz	phase degree	gradient MV/m
harmonic *rf*	.186	402.5	180	6.4
space	.443			
rf	4 × .373	201.25	0	6.4
space	.443			
harmonic *rf*	.186	402.5	180	6.4
drift 1	10 × 2.75			
harmonic *rf*	.186	402.5	180	6
space	.443			
rf	4 × .373	201.25	0	6
space	.443			
harmonic *rf*	2 × .186	402.5	180	6
space	.443			
rf	4 × .373	201.25	0	6
space	.443			
harmonic *rf*	.186	402.5	180	6
drift 2	3 × 2.75			
space	.629			
rf	4 × .373	201.25	12	8
space	.629			
space	.629			
rf	4 × .373	201.25	12	8
space	.629			
drift 3	2 × 2.75			

as the longitudinal emittance rises from straggling and the negative slope of the energy loss with energy.

4.3.3 Longitudinal-transverse correlation

A significant coupling develops in this front end lattice, including the induction linac, between a particle's longitudinal and transverse motions. This coupling develops because particles with different transverse displacements or angular divergences take different amounts of time to move axially down the solenoidal lattice. They thus arrive at the cavities at different points in the *rf* cycle, thereby obtaining different acceleration and different longitudinal and transverse focusing.

The correlation can be expressed as

$$p = p_o + C A^2 \tag{4.1}$$

where C is the correlation coefficient and the transverse amplitude is

$$A^2 = \frac{r^2}{\beta_\perp^2} + \theta^2 \tag{4.2}$$

Figure 4.4 shows that there is little correlation between momentum and angular momentum after the induction linacs, indicating that the field reversal is correctly located.

The magnitude of the momentum-amplitude correlation is seen to be 0.7. This is a higher value than the correlation of 0.45 that would be obtained without the mini-cooler. Ideally the correlation should be such that forward velocity in the following lattice is independent of transverse amplitude. A value of approximately 1.1 would be required for this.

4.4 The Ionization Cooling Channel

The *rms* transverse emittance of the muon beam emerging from the induction linac must be reduced to at least $\approx$ 2 mm rad (normalized) in order to fit in the downstream accelerators, and be contained in the storage rings. Ionization cooling is currently our only feasible option[**?**]. The cooling channel described below, as well as the one described in the appendix, are based on extensive theoretical studies and computer simulations performed in the same context of our previous studies[**?**, **?**, **?**, **?**].

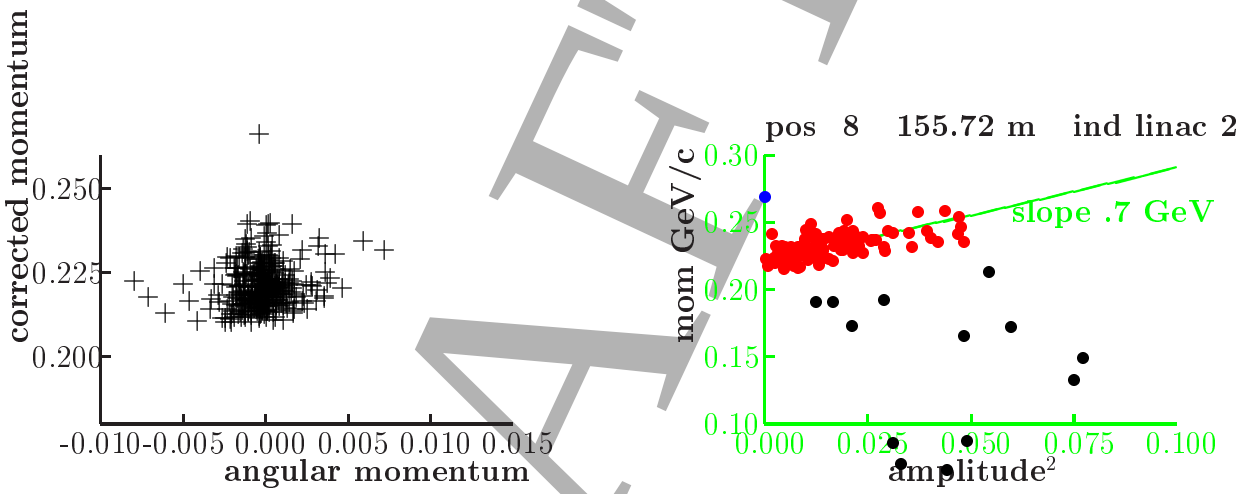

Figure 4.4: (a) Correlation between momentum and angular momentum; (b) correlation between longitudinal momentum and transverse amplitude.

4.4.1 Principle of ionization cooling

In ionization cooling the beam loses both transverse and longitudinal momentum by ionization energy loss while passing through the absorber. The longitudinal momentum is then restored to the beam in accelerating cavities. This sequence, repeated many times, results in a reduction of the angular spread and thereby reduces the transverse emittance. Ionization cooling is limited by multiple Coulomb scattering (MSC) in these absorbers. To minimize this effect, one must have rather strong focusing at the absorber, with $\beta_{\perp,min} \approx 0.4$ to 0.2 m at a momentum of 200 MeV/c .

Strong solenoidal fields are used for this purpose. Weak focusing at the absorber, i.e. too large $\beta_\perp$ at the absorbers, leads to excessive emittance growth due to MSC. Too strong focusing is not only hard to achieve for such large aperture beam transports, but can also be detrimental to the 6D beam dynamics. As the angles, or beam divergence, get too large, the longitudinal velocity decreases too much, leading to the wrong longitudinal-transverse correlation factor and thereby resulting in unacceptable growth of the longitudinal emittance. Choosing the right range of $\beta_{\perp,min}$ and the operating momentum is the key to a successful design[**?**, **?**].

The approximate equation for transverse cooling in a step ds along the particle's orbit is [**?**]

$$\frac{d\epsilon_N}{ds} = -\frac{1}{\beta^2}\frac{dE_\mu}{ds}\frac{\epsilon_N}{E_\mu} + \frac{\beta_\perp (0.014GeV)^2}{2\beta^3 E_\mu m_\mu L_R}, \tag{4.3}$$

where β is the normalized velocity, E_μ is the total energy, m_μ is the muon mass, ϵ_N is the normalized transverse emittance, $\beta_\perp$ is the betatron function at the absorber, dE_μ/ds is the energy loss per unit length, and L_R is the radiation length of the material. The betatron function is determined by the strengths of the elements in the focusing lattice. Together with the beam emittance this function determines the local size and divergence of the beam. Note that the energy loss dE_μ/ds is defined here as a positive quantity, unlike the convention often used in particle physics. The first term in this equation is the cooling term, and the second describes the heating due to multiple scattering. The heating term is minimized if $\beta_\perp$ is small (strong-focusing) and L_R is large (a low-Z absorber).

The minimum, normalized transverse emittance that can be achieved for a given absorber in a given focusing field is reached when the cooling rate

equals the heating rate in Eq. 4.12

$$\epsilon_{N,min} = \frac{\beta_\perp (14MeV)^2}{2\beta m_\mu \frac{dE_\mu}{ds} L_R} \tag{4.4}$$

For a relativistic muon in liquid hydrogen with a betatron focusing value of 8 cm, which corresponds roughly to confinement in a 15 T solenoidal field, the minimum achievable emittance is about 340 mm-mrad.

The equation for energy spread is

$$\frac{d(\Delta E_\mu)^2}{ds} = -2\frac{d\left(\frac{dE_\mu}{ds}\right)}{dE_\mu}\langle(\Delta E_\mu)^2\rangle + \frac{d(\Delta E_\mu)^2_{\text{stragg.}}}{ds} \tag{4.5}$$

where the first term describes the cooling (or heating) due to energy loss, and the second term describes the heating due to straggling. ΔE_μ is the rms spread in the energy of the beam.

Ionization cooling of muons seems relatively straightforward in theory, but will require simulation studies and hardware development for its optimization. There are practical problems in designing lattices that can transport and focus the large emittance beam. There will also be effects from space charge and wake fields.

We have developed a number of tools for studying the ionization cooling process. First, the basic theory was used to identify the most promising beam properties, material type and focusing arrangements for cooling. Given the practical limits on magnetic field strengths, this gives an estimate of the minimum achievable emittance for a given configuration. Next several tracking codes were either written or modified to study the cooling process in detail. These codes use Monte Carlo techniques to track particles one at a time through the cooling system. The codes attempt to include all relevant physical processes to some degree, (e.g. energy loss, straggling, multiple scattering) and use Maxwellian models of the focusing fields.

4.4.2 The concept of the tapered SFOFO cooling Channel

.

The solenoidal field should not be kept constant during the entire cooling stage. The transverse momentum of each particle will decrease, while the position of the Larmor center will not, causing the net total angular momentum of the beam to grow. One must flip the field, while maintaining good focusing throughout the beam transport and low $\beta_\perp$ at the absorbers. One of the simplest solutions, based on the FOFO lattice, is to vary the field sinusoidally. The transverse motion in such a lattice can be characterized by the betatron resonances, near which the motion is unstable. The operating, stable, region is between the 2π and π phase advance per half-period.

The SFOFO lattice[**?**] is also based on the use on alternating solenoids, but is a bit more complicated. We add a second harmonic to the simple sinusoidal field, producing the axial field shown in figure 4.6. As in the FOFO case, the longitudinal field vanishes at the $\beta_{\perp,min}$ position, located at the center of the absorber. This is accomplished by two short "focusing" coils running in opposite polarity. However, unlike in the FOFO case, the field decreases and flattens at $\beta_{\perp,max}$, due to a "coupling" coil located around the Linac. Thus, the transverse beam dynamics is strongly influenced by the solenoidal field profile on-axis and by the desired range of momentum acceptance. It is important to note that a geometrical cell in this lattice occupies a half period of the solenoidal magnetic field.

This SFOFO lattice has several advantages over the FOFO:

- The betatron resonances are usually considered a nuisance, since they inevitably induce an unstable motion. However, in this case they give us strong, equal focusing strength across the relevant momentum range, if we operate between the two 2π (low momentum) and π (high momentum) resonances. This is illustrated in Fig. 4.7 and Fig. 4.5. Within this (albeit limited) momentum range transverse motion is stable.

- For a given $\beta_{\perp,min}$, the SFOFO period length is longer than in the FOFO case, allowing longer absorbers and linac regions per lattice cell, thereby reducing the relative multiple scattering from the windows. It also gives us a bit more room for all the components for a fixed absorber length.

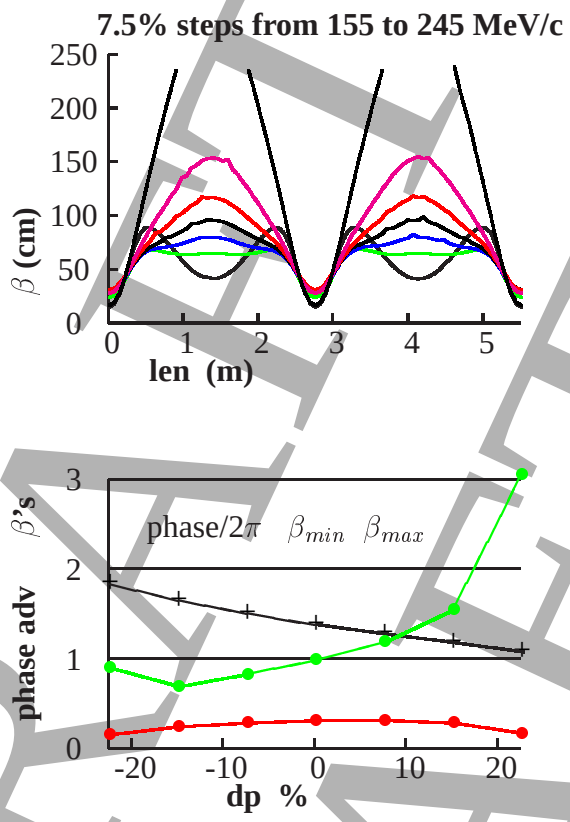

Figure 4.5: (a) Beta functions in the (1,3) cooling lattice section; (b) phase advance as function of momentum spread.

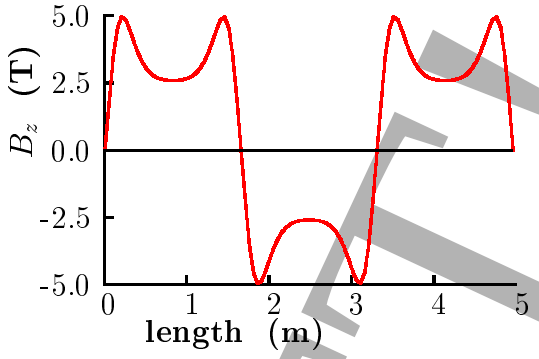

Figure 4.6: The longitudinal component of the magnetic field, B_z, on axis, for the SFOFO lattice.

- The focusing coils can be located above the absorbers, right next to the linac. Since the *rf* cavities have a much larger outer diameter than the absorbers, this arrangement allows us to reduce considerably the diameter of these high field magnets and thereby reduce their cost.

For a given lattice period length, one can adjust independently the location of the two betatron resonances, or, conversely, the nominal operating momentum and the $\beta_{\perp,min}$ at that momentum. By adjusting these two parameters, we can keep the $\beta_\perp$ symmetric about the required nominal momentum, and independently reduce the central $\beta_\perp$ value. However, this is true only over a limited momentum range. As we decrease the coupling field, the momentum acceptance will shrink as the π and 2π resonance move closer to the nominal momentum. At this point, we are forced to change the lattice period.

This brings us to the second improvement over the FOFO channel used in the previous feasibility study: $\beta_{\perp,min}$ can be "tapered" down. One can slowly increase the focusing strength at a fixed operating momentum, keeping a reasonable momentum acceptance. At a fixed $\beta_{\perp,min}$, as the cooling progresses, the *rms* angle would decrease. The cooling rate would then also decrease because the heating term due to multiple scattering becomes relatively significant. By slowly increasing the focusing strength, (decreasing $\beta_{\perp,min}$), one tends to maintain large *rms* angles at the absorbers ($\sigma_{x'} = \sigma_{y'} \approx 0.1$ rad.).

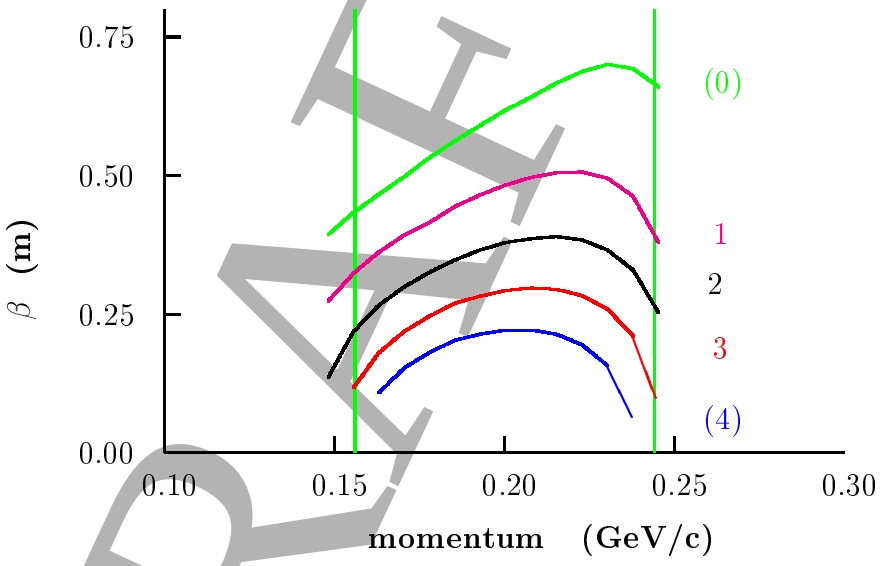

Figure 4.7: The $\beta_\perp$ function, versus momentum, for the six SFOFO lattices described below.

4.4.3 Description of the SFOFO cooling channel

In this subsection, we describe the cooling channel from the perspective of the beam physicist writing the corresponding computer simulation package. Engineering details will be given later.

The lattices

The channel operates at a nominal momentum of 200 MeV/c. There are six sections with steadily decreasing $\beta_{\perp,min}$. In the first three lattices, labeled (1,i), i=1,3, the lattice half period length is 2.75 m, and in the last three lattices, (2,i), i=1,3, this half period length is 1.65 m. The matching sections between these sections also consist of cooling cells, which differ from the regular cooling sections only by the current circulating in the coils, with one exception. A different coil length must be used in the matching section where the lattice period length decreases from 2.75 m to 1.65 m, and the absorber has been removed. The length of these lattices are specified in Table 4.3.

Specific coil dimensions, current densities are specified on Table 4.4 . It is assumed that the current density is uniform across the thickness of the coil.

Table 4.3: Length of the sections and integrated length from the start of the cooling channel.

section	**Length (m.)**	**Total length (m.)**
cool 1,1	$4 \times 2.75 = 11$	11
match 1,1-2	$2 \times 2.75 = 5.5$	16.5
cool 1,2	$4 \times 2.75 = 11$	27.5
match 1,2-3	$2 \times 2.75 = 5.5$	33
cool 1,3	$4 \times 2.75 = 11$	44
match 1,3-2,1	4.4	48.4
cool 2,1	$12 \times 1.65 = 19.8$	68.2
match 2,1-2	$2 \times 1.65 = 3.3$	71.5
cool 2,2	$8 \times 1.65 = 13.2$	84.7
match 2,2-3	$2 \times 1.65 = 3.3$	88
cool 2,3	$12 \times 1.65 = 19.8$	107.8

The design of the matching sections between regular sections with the same lattice cell length goes as follow. In all cases a matching section is

Table 4.4: Geometry and current densities for the solenoids. The first (last) three coil types refer to the 2.75 (1.65) m long cell (half period), respectively. The position refers to the upstream edge of the coil and start from the beginning of half period cell. The radius refers to the inner radius of the coil. Dimension are in m and A/mm^2. The current indices refer to the nomenclature used in the previous table.

Type	**Position**	**Length**	**Radius**	**Thickness**	j(1,1)	j(1,2)	j(1,3)
focusing	0.175	0.167	0.330	0.175	75.20	84.17	91.46
coupling	1.210	0.330	0.770	0.080	98.25	92.42	84.75
focusing	2.408	0.167	0.330	0.175	75.20	84.17	91.46
					j(2,1)	j(2,2)	j(2,3)
focusing	0.066	0.145	0.198	0.330	68.87	75.13	83.48
coupling	0.627	0.396	0.792	0.099	95.65	88.00	76.52
focusing	1.439	0.145	0.198	0.330	68.87	75.13	83.48

inserted and consists of two lattice cells: the first as in the previous cells, the second as in the following cells, except that the currents in the central pair of focus coils are set to an average of the currents in the previous and following focusing coils. For instance, Table 4.5 describes the match between the (1,1) and (1,2) lattices.

The match where the lattice period changes from 2.75 down to 1.65 m requires further attention. Although the proposed solution is not a perfect match, its mechanical simplicity and relatively short length might actually outweigh the benefit we could get with a slow, adiabatic match from one lattice period to an other. Note that the absorber in the matching cell is removed, allowing us to run the upstream and downstream linac closer to the bunching condition, giving us a slight increase of the r.f. bucket size, and ease of mechanical assembly. Coils and current are listed on table 4.6. The magnetic field on axis for the entire cooling channel is shown on figure 4.8.

Cooling *rf*

The lengths of the linacs are constrained by the lattices themselves, as the focusing coils have a bore radius smaller than the *rf* cavities, and by the *rf* cell length, which must be optimized to give the high Q required to reach

Table 4.5: Geometry and current densities for the solenoids in the first matching section. Coil locations are given with respect to the start of the channel. Dimension are in m and A/mm^2. The coil dimensions are specified in Table 4.4.

Type	**Location [m]**	**j(1,i)**
last 1,1		
focusing	11.175	75.20
coupling	12.210	98.25
focusing	13.408	75.20
match		
focusing	13.925	-75.20
coupling	14.960	-98.25
focusing	16.158	-80.07
focusing	16.675	80.07
coupling	17.710	92.42
focusing	18.908	84.17
first 1,2		
focusing	19.425	-84.17
coupling	20.460	-92.42
focusing	21.658	-84.17

high gradient. These linacs are always placed in the middle of the half-period lattice cell. Each cell can be phased separately. In order to improve the Q of the cavity, the iris of the cell must be covered with a foil or a grid.

Our baseline design calls for thin, pre-stressed beryllium windows with thicknesses that increase with radius. This arrangement is justified on two separate grounds. (i) The power dissipated on the iris or foil goes like the 4th power of the radius (at relatively small radius). We therefore need more thickness at higher radius to remove the heat. (ii) The particles at large radius tend to have large transverse amplitude and are "warmer" than the central core. One can therefore afford a bit more multiple scattering at such large radius. Note also that the windows on each end of the linacs dissipate half the power than the windows at the boundary between two adjacent cells. Thus, these edge windows are thinner than those in the center of the linac. The parameters of these linacs are listed on Table 4.7 and the *rf* window parameters are in Table (REFER TO TABLE 18.D HERE).

Table 4.6: Geometry and current densities for the solenoids in the matching section between the (1,3) and (2,1) lattices. Coil locations are given with respect to the start of the channel. Distances are given in meters.

Type	**Location**	**Length**	**Radius**	**Thickness**	j (A/mm^2)
last 1,3					
focusing	41.425	0.167	0.330	0.175	91.46
coupling	42.460	0.330	0.770	0.080	84.75
focusing	43.658	0.167	0.330	0.175	91.46
match					
focusing	44.175	0.167	0.330	0.175	-91.46
coupling	45.210	0.330	0.770	0.080	-84.75
focusing, match	46.393	0.198	0.330	0.175	-95.24
focusing	46.816	0.145	0.198	0.330	56.39
coupling	47.377	0.396	0.792	0.099	95.65
focusing	48.189	0.145	0.198	0.330	68.87
first 2,1					
focusing	48.466	0.145	0.198	0.330	-68.87
coupling	49.027	0.396	0.792	0.099	-95.65
focusing	49.839	0.145	0.198	0.330	-68.87

The use of thin aluminum tubes arranged in a Cartesian grid can also be considered, as briefly discussed in the engineering section.

The absorbers

The absorber material is liquid hydrogen (LH2). The density is approximately 0.071 g/cm^3. The energy loss, as given by the Bethe-Bloch formula[**?**] with a mean excitation energy of 21.9 eV, is 4.6 MeV cm^2/g. The length of these absorbers is 35 cm for the (1,i), i=1,3 lattices and 21 cm for the (2,i) lattices, respectively. The muons therefore lose $\approx$ 12 MeV per lattice cell for the (1,i) lattices and $\approx$ 7 MeV for the (2,i) lattices. This includes the energy loss in the windows. The LH2 vessels must also be equipped with thin aluminum windows. Their thickness is 360 μm (220), with a radius of 18 (11) cm, for the (1,i) and (2,i) lattices, respectively.

Table 4.7: Geometry and *rf* parameters for the linac in the cooling channel.

Lattice type	**# of cells**	**Cell length (m)**	**Peak Voltage (MV/m)**	**Phase (deg)**
(1,i), i=1,3	4	0.466	15.48	40.
(1,3 match)	4	0.466	15.48	18.8
(2,1 match)	2	0.559	16.72	18.8
(2,i), i=1,3	2	0.559	16.72	40

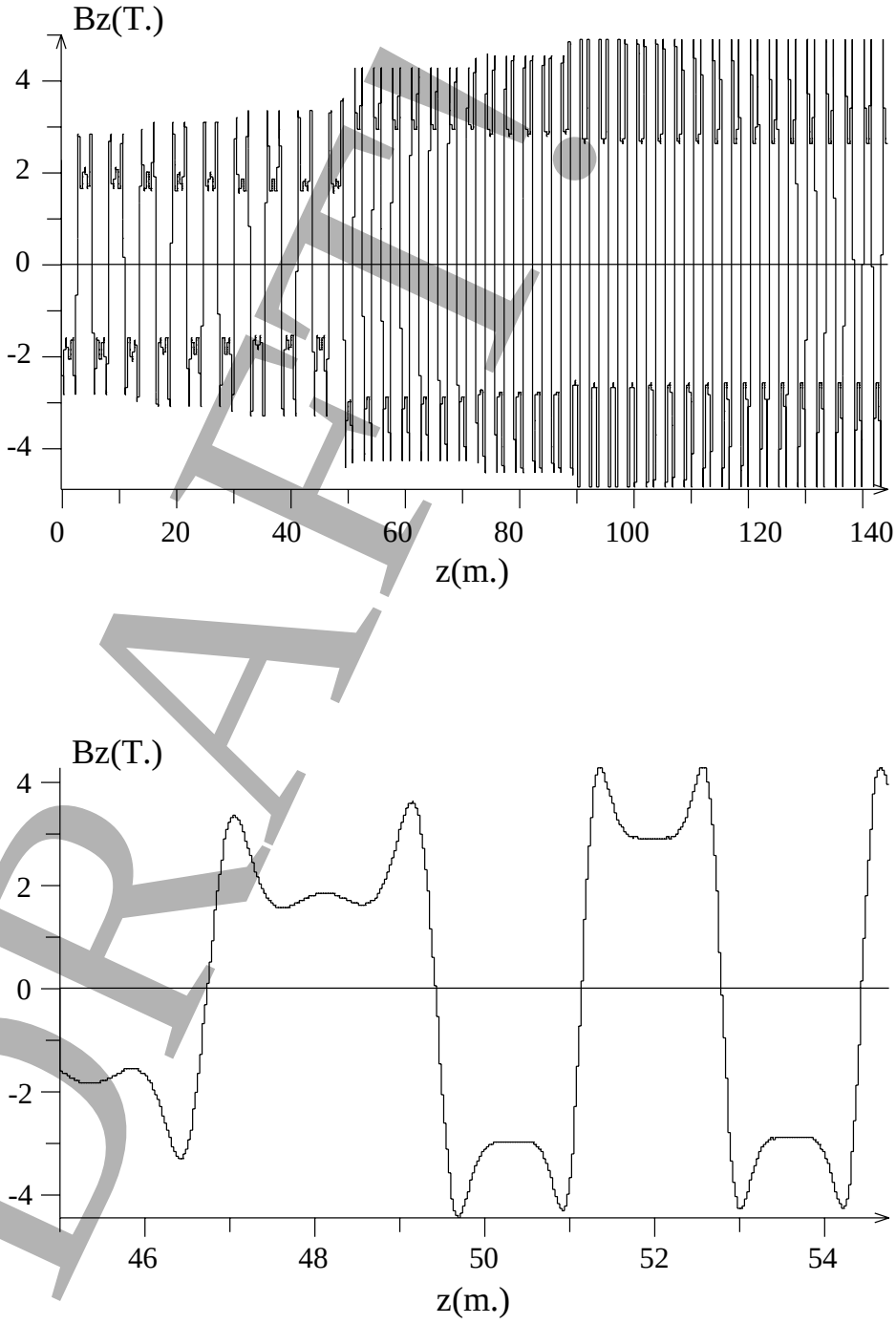

Figure 4.8: Bz on axis for the entire SFOFO cooling channel (top) and for the matching section between (1,3) - (2,1) lattices.

4.4.4 Performance

Fig. 4.9 shows the beta functions and radii, which step down with each new section of the cooling lattice (ICOOL result) . The *rms* angular size is kept substantially constant in order to minimize the effects of multiple scattering. The $\beta_{\perp,min}$ function, derived from the beam second order moments estimated at the absorber's center using Geant4, is shown on Figure 4.10.

The transverse and longitudinal emittances through the cooling system are shown in Fig. 4.11. They were obtained based on the ICOOL simulation code and calculated using the code ECALC9 [**?**]. Emittances are computed in this code using diagonalized covariance matrices. The emittance values are corrected for correlations between the variables, including the strong momentum-transverse amplitude correlation. The transverse and longitudinal emittances obtained in the Geant4 version are shown in Figure 4.12. At equilibrium a transverse emittance of 2.2 mm rad is reached, consistent with the ICOOL result.

The transverse emittance cools from 12 to 2 mm rad. The longitudinal emittance shows an initial rise as particles not within the *rf* bucket are lost, and then an approach to an asymptotic value set by the bucket size. Naturally, this longitudinal emittance should rise due to straggling and the negative slope of energy loss with energy. However, since the *rf* bucket is already full, instead of an emittance growth we have a steady loss of particles, as seen in Fig. 4.13.

Despite this overall loss, the numbers of particles within the accelerator acceptance increases. The lower two curves give the number of particles within the baseline longitudinal and transverse acceptances. The middle line represents the values for the accelerator parameters in this study. The lower line, given for comparison, gives the values for the acceptances used in Feasibility Study 1 [**?**].

- Longitudinal (FS1 & FS2): $(dz^2)/\beta_s \ + \ (dp/p)^2 \ \beta_s \ < \ 150$ (mm)
- Transverse (FS2): $(x^2 + y^2)/\beta_\perp \ + \ (x'^2 + y'^2)\beta_\perp \ < \ 15$ (mm rad)
- Transverse (FS1): $(x^2 + y^2)/\beta_\perp \ + \ (x'^2 + y'^2)\beta_\perp \ < \ 9.75$ (mm rad)

where β_s is the synchrotron beta function ($\beta_s = \sigma_{dz}/\sigma_{dp/p}$), and $\beta_\perp$ is the transverse β function.

It is seen that the gain in muons within the accelerator acceptance due to cooling is 3.1 $\times$ (or 5 $\times$ if the study 1 acceptances were used). If the particle

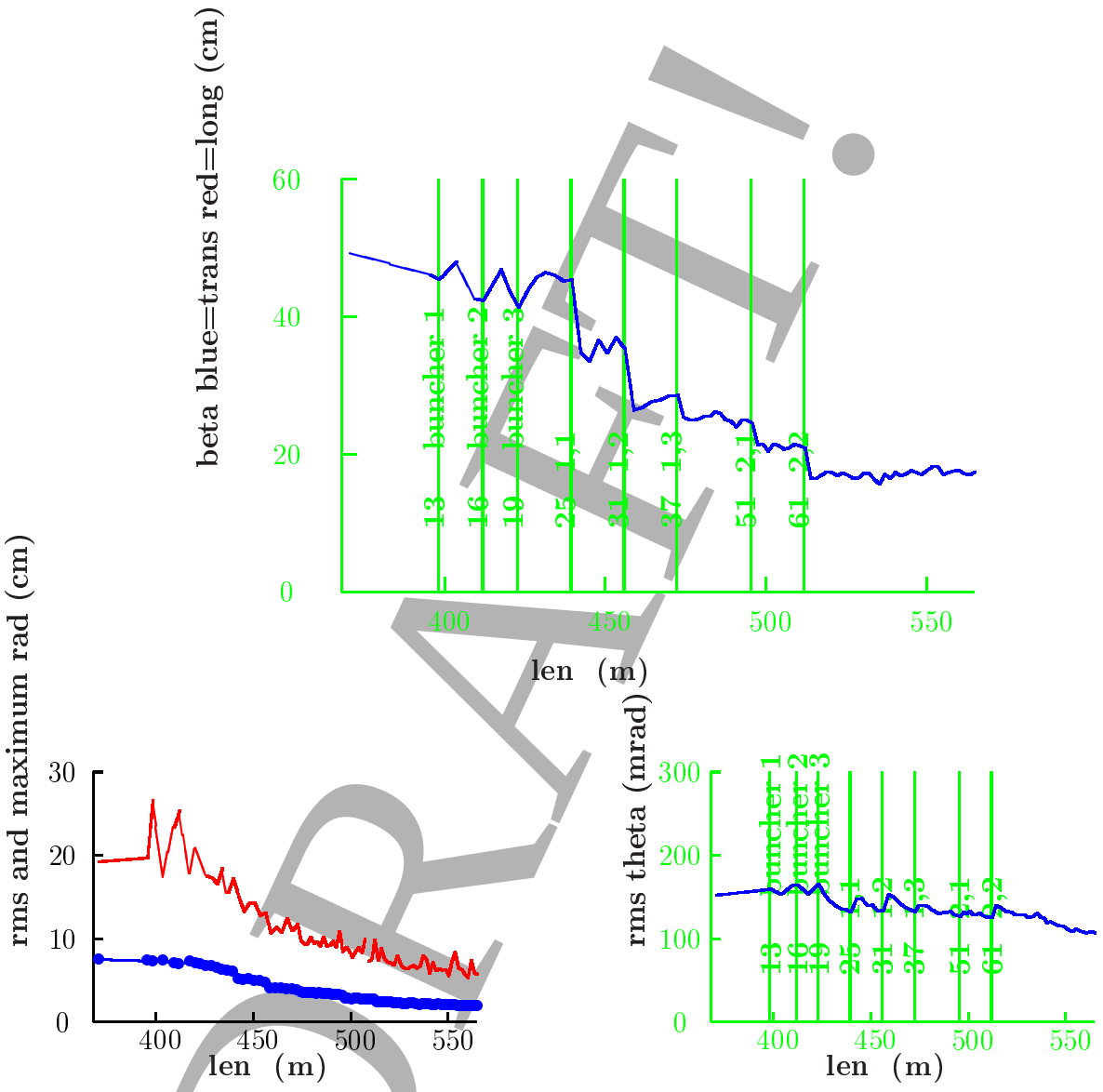

Figure 4.9: Beta function in the buncher and cooling sections; *rms* beam radius; *rms* divergence.

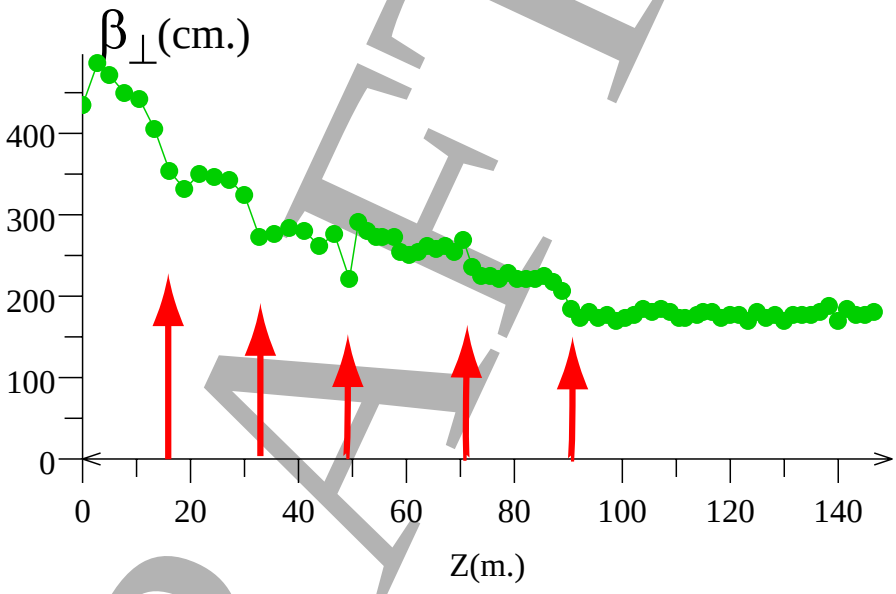

Figure 4.10: The $\beta_\perp$ function, average over the relevant momentum bite, and measured from the second order moments of the beam itself, as the cooling progresses, for the entire SFOFO cooling channel. The 5 arrows indicate the beginning of the (1,2), (1,3), (2,i), i=1,3 lattice sections

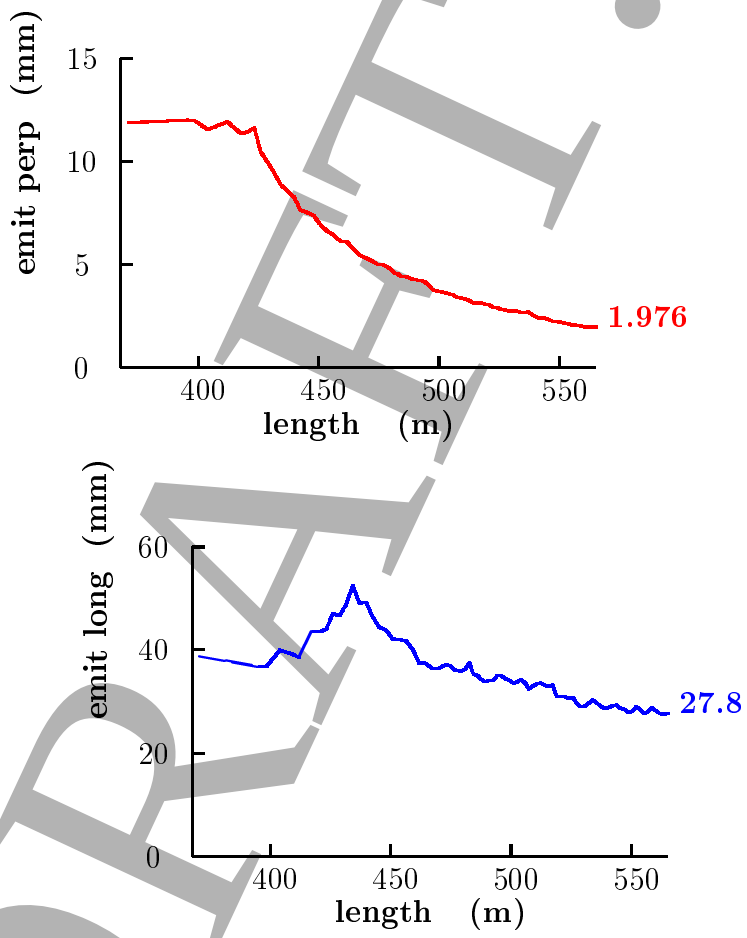

Figure 4.11: Transverse and longitudinal emittances in the buncher and cooling sections.

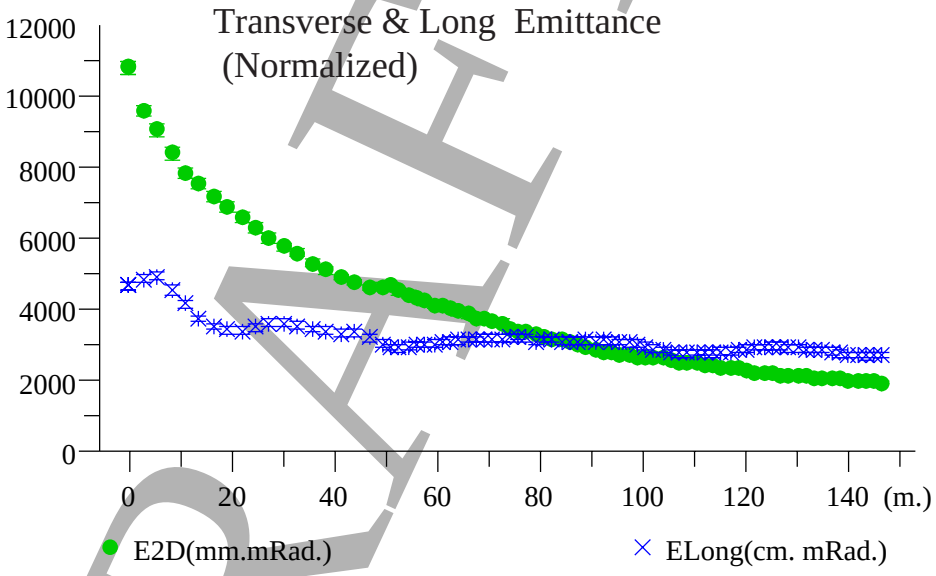

Figure 4.12: The longitudinal and transverse emittances.

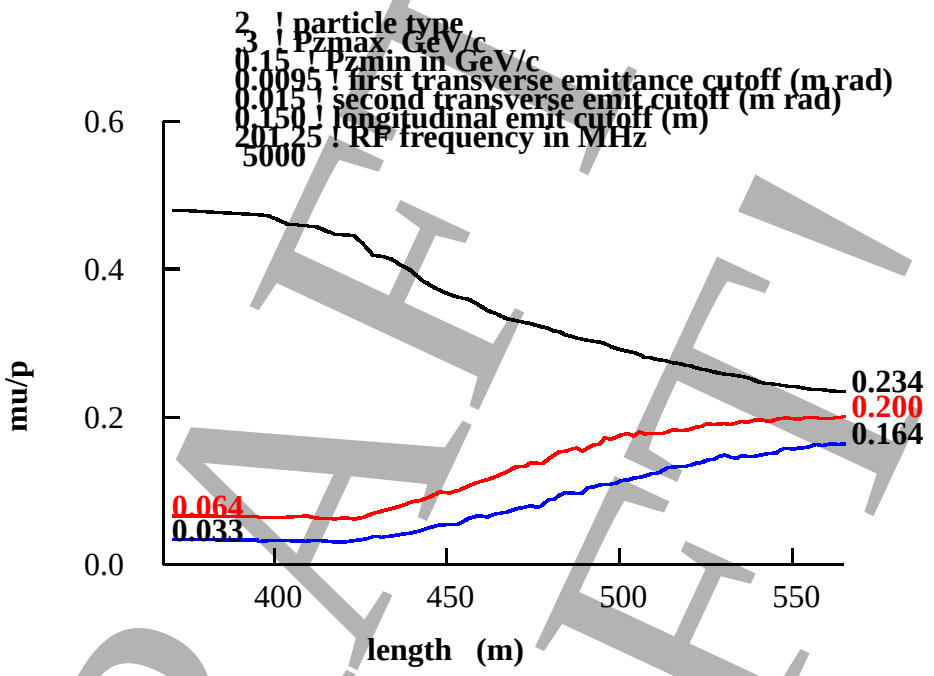

Figure 4.13: Particle transmission in the buncher and cooling sections; top curve is overall muons per incident proton; middle curve is acceptance into 15 mm transverse acceptance; lower curve is acceptance into 9.5 mm transverse acceptance.

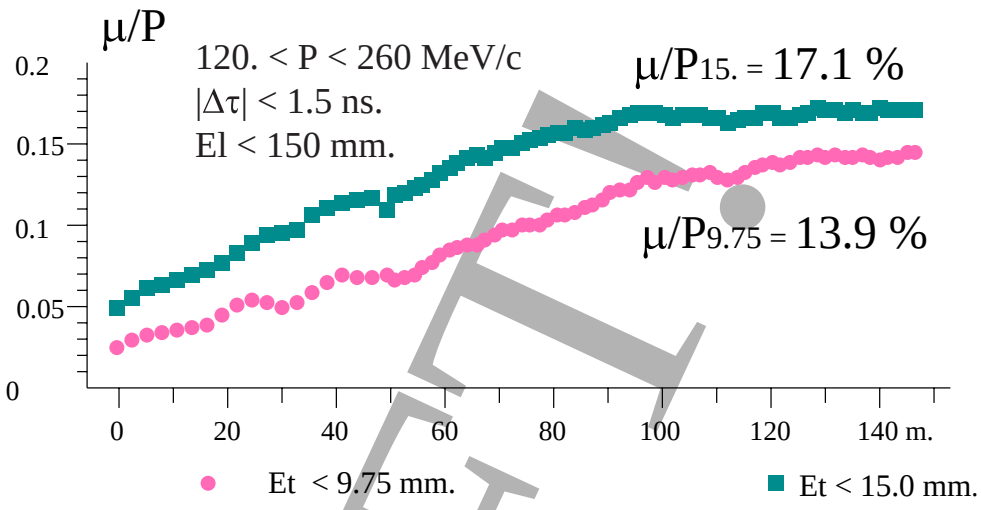

Figure 4.14: The muon to proton yield ratio for the two transverse emittance cuts, clearly showing that the channel cools as the density in the center of the phase space increases.

loss from longitudinal emittance growth could be eliminated, as should be the case if emittance exchange were used, then these gains would double. Similar performance is obtained with the Geant4 code, as shown in Figure 4.14

Table 4.8: Beam characteristics summary

location (end of)	σ_x (cm)	$\sigma_{x'}$ (mrad)	σ_p (MeV/c)	σ_t (ns)	$\langle p \rangle$ (MeV/c)
induction linac	8.6	95	113		260
matching section	5.8	114	113		260
buncher	5.3	107	111	0.84	256
2.75 m cooler	3.0	91	70	0.55	226
1.65 m cooler	1.8	102	30	0.51	207

The beam characteristics in the buncher and cooler sections are summarized in Table 4.8. The beam is symmetric in this lattice, so the y properties are similar to those in x. We see that the size steadily decreases as we proceed down the channel. The angular divergence is kept constant for max-

imum cooling efficiency. The momentum spread of the entire beam is still large after the induction linac, but this includes very low and high energy muons that do not get transmitted through the subsequent SFOFO lattice. The decrease in energy spread is due to particle losses since there is no longitudinal cooling or emittance exchange in this lattice. Likewise, the average momentum of the beam decreases until it matches the acceptance of the SFOFO lattice. The time spread refers to a single bunch in the bunch train.

The longitudinal emittance remains more or less stable, at around 30 mm. This is in part deceptive. Straggling and imperfections in the longitudinal to transverse correlation[1] cause particles to fall out of the *rf* bucket and to be scraped away due to the strong π betatron resonances. In fact, the buncher delivers a full *rf* bucket to the cooling section and the longitudinal emittance cannot grow any larger. This scraping occurs on the combined time scale of a synchrotron period, about 20 m, and on the growth time of the betatron resonance instability.

The performance of the cooling channel is limited by both multiple scattering and the limited momentum acceptance. While the latter is difficult to estimate based on computer simulations, it is straightforward to estimate the former contribution by simply turining off multiple scattering in the code. If so, the relative μ/P_{15} and $\mu/P_{9.75}$ yields would increase by 11 % and 19 %, respectively.

[1] described in the bunching section

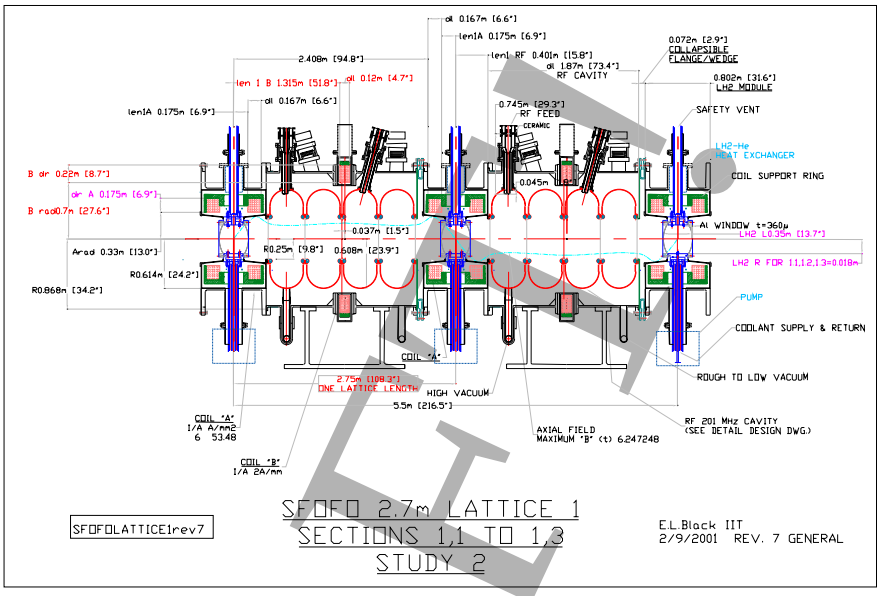

Figure 4.15: Engineering detail of the 2.75 m cooling lattice cell.

4.4.5 Engineering details

DESCIPTIVE TEXT IS NEEDED HERE

A detailed layout of a 2.75 m lattice cell is shown in Fig. 4.15.

A detailed layout of a 1.65 m lattice cell is shown in Fig. 4.16.

4.4.6 rf systems

The *rf* systems for the buncher and the cooler are required to match the muon beam into the longitudinal acceptance of the cooling channel and replenish the beam energy lost during ionization cooling. Since they must operate inside the strong solenoid fields, they cannot be superconducting. These systems require a large number of *rf* cavities operating at high gradient, and a large amount of pulsed *rf* power. They are technically challenging and expensive and have therefore been the focus of continued development during study II. The cooling channel layout has continued to evolve since

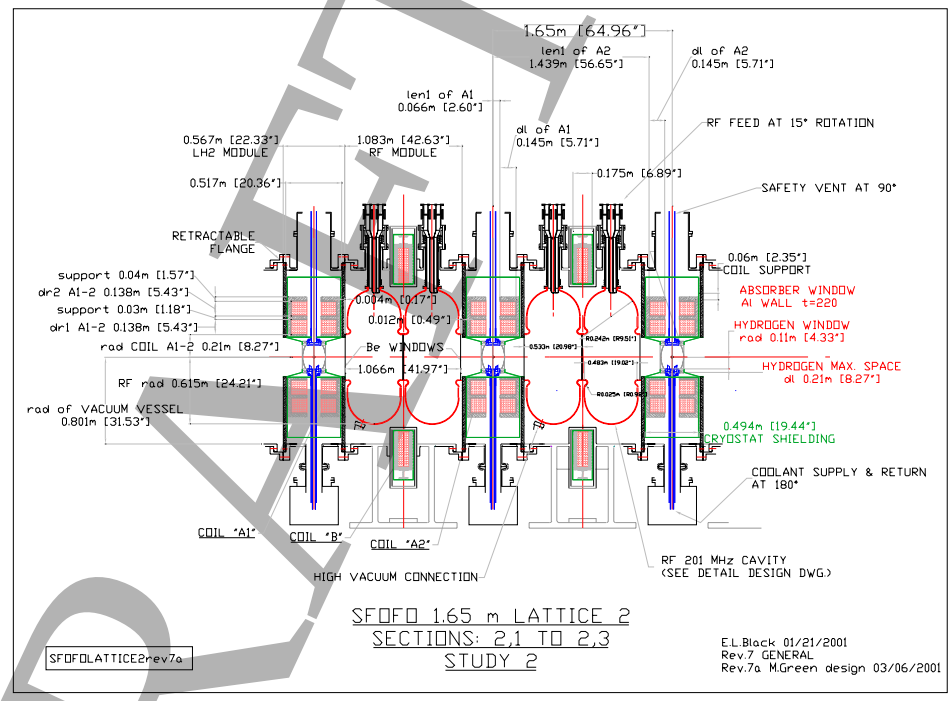

Figure 4.16: Engineering detail of the 1.65 m cooling lattice cell.

study I with emphasis on integration of realistic components into the available space along with optimization of the channel performance. The buncher and cooling channel systems must accommodate liquid hydrogen absorbers, high gradient *rf* cavities, windows, tuners, superconducting solenoids, diagnostics, pumping, harmonic cavities and other equipment. The system must be designed in such a way as to allow assembly and access for maintenance.

The buncher and cooling channel will be made of a large number of modules. Each module contains two or four 201.25 MHz closed-cell cavities and is powered by one or two high power klystrons. The density of equipment in the building is therefore high and the systems must be carefully laid out to allow access for installation and maintenance.

The proposed buncher and cooling channel is approximately 163 m long and requires 162 cavities and 73 klystrons. The total installed power is approximately 690 MW. (REFER TO SECTION 18 FOR DETAILS)

Power sources

The ionization cooling channel requires high peak *rf* power sources at 201.25 MHz and 402.5 MHz to efficiently cool the muon beam. There are 162, 201.25 MHz cavities in the channel that require 687 MW of *rf* power for a pulse length of 115 ms at 15 Hz and 6, 402.5 MHz cavities that require 1.8 MW at 15 Hz. An examination of the requirements shows that an *rf* source of about 5 to 12 MW would be ideal for the 201.25 MHz cavities and a source of 500 to 750 kW for the 402.5 MHz cavities.

The *rf* for the 201.25 MHz cavities could be supplied by existing gridded tubes at about the 5 MW level. However, the low gain and lifetime of gridded tubes make the R&D effort to develop an alternative most attractive. Preliminary calculations at SLAC have shown that a 201.25 MHz klystron could be built with a reasonable amount of R&D. SLAC has examined two designs: a single gun diode design, and the multibeam klystron. The multibeam klystron is the most attractive in that it reduces the overall length of the tube from 7.5 m to between 3.5 and 4.0 m. The length reduction factor of the multibeam klystron and its potential for higher efficiency make it the optimum candidate for the neutrino factory. The length of the multibeam klystron is, also, consistent with the manufacturing capabilities of current tube manufacturers. However the manufacture of a 7.5 m diode tube would be a big step and would require new and costly facility upgrades. To provide *rf* power overhead for dynamic regulation of the *rf* phase and amplitude, a

12 MW multibeam klystron has been selected as the high power *rf* source for the neutrino factory. This provides an *rf* power overhead margin of about 20 % for regulation.

The 12 MW multibeam klystron design should be a fully integrated horizontal package incorporating the tube, solenoid, and high voltage terminal, as pioneered at CERN for LEP. This would facilitate the replacement and installation of tubes in the facility. Another advantage, besides the ease of handling, is the reduced cost of the *rf* building because of the lower building height requirement. The transmission lines from the tubes to the cavities will be large coaxial lines because of the large size and costs of waveguide . Power splitters would divide the *rf* power from each tube to supply the appropriate *rf* power to the cavities. Splitters with proper built in phase delays would divide the power to each cell or cavity section of the cooling channel. (REFER TO SECTION 18 FOR DETAILS)

Cavities

The 201.25 MHz normal-conducting cavities in the cooling sections must operate at very high accelerating gradients. This would be impractical with conventional open iris structures because of the large size of the beam iris required. A great improvement can be made in the shunt impedance of the cavity by closing the iris with a thin conducting barrier. This barrier must use the smallest amount of material to minimize scattering of the muon beam. It is proposed to close the irises with thin beryllium foils. Other methods of closure, such as grids of thin-walled tubes, will be evaluated in the future. The foils must be thick enough to conduct away the heat from the *rf* currents and keep the temperature to a predetermined level. The foils will be pre-stressed in tension during manufacture in order to keep them flat. This method had been tested experimentally and works well up to the point where the thermal expansion exceeds the pre-stress and the foils begin to move. Foil thicknesses have been chosen for study II which should keep the temperatures below this critical level. The use of tapered foils or foils with stepped thickness can reduce the amount of material intercepted by the core of the beam, reducing the amount of scattering significantly.

The normal-conducting cavities in the buncher can be of the same design as those in the first cooling section, except that they would be operated at lower gradient. This will allow the use of thinner foils to minimize the scattering. The buncher section also contains a small number of harmonic

cavities operating at 402.5 MHz. These fit into the spaces normally occupied by the hydrogen absorbers in the cooling cells. For these cavities the foils occupy most of the diameter of the end walls, but the gradients are much lower, so the losses in the foils are manageable.

The normal conducting cells must have some cooling to remove the average power losses in the walls and to stabilize the frequency. The study II design has been evaluated for room temperature operation although the option of operating at reduced temperature has been kept open. This would lower the wall resistance and reduce the peak power requirements at the expense of adding a potentially large refrigeration system. (REFER TO SECTION 18 FOR DETAILS)

4.4.7 Superconducting Solenoids for the Muon Cooling Cells

Layout and parameters

The matching section consists of two 2.75-meter long cells and about 2.5 meters of solenoids that have a warm bore diameter of 600 mm. These solenoids must be designed to withstand longitudinal forces of up to 60 metric tons that are imparted on them by the two matching cells downstream. The solenoids in the matching section cells are the same as in the cells in the beam bunching section. The twenty 2.75-meter long bunching cells are the same as the 2.75-meter long cooling cells. The warm bore aperture of the of the A coils for a 2.75-meter long cooling cell must be about 650 mm in order to accommodate a liquid hydrogen absorber (See Figure 4.17. The A coils described in this section were refered to as focusing coils earlier. The B coils desribed here were refered to as coupling coils). The warm bore aperture for the beam bunching cell flux reversal coils must be the same in order to accommodate a 402.5 MHz *rf* cavity. Room temperature service ports to the 402.5 MHz *rf* cavity can go out through the flux reversal magnet cryostat between the flux reversal coils. Table 4.9 shows the number of cells of each type, the minimum aperture requirements for the magnets and the maximum coil current densities for the coils in each cell type. Included in Table 4.9 is the magnetic field 9.9 meters from the beam axis. Because the bunching and cooling cell solenoids are constantly changing polarity, there is almost no stray field from these solenoids at R = 10 meters.

Magnet parameters and a magnet cross-section for the 2.75-meter long bunching and cooling cell magnets are shown in Table 4.10 and Figure 4.17. Note: the solenoids in the 2.75-meter long cells are the same for both bunching and cooling cells. Magnet parameters and a magnet cross-section for the 1.65-meter long cooling cell magnets are shown in Table 4.11 and Figure 4.18. The solenoid magnet cross-sections shown in Figures 4.18 and 4.19 are through the longitudinal supports. The penetration of the hydrogen absorber plumbing through the space between the A coils is not shown in Figures 4.17 and 4.18.

Figures 4.17 and 4.18 show a cross-section of the bunching and cooling cell solenoids. The plane for the cross-sections is taken through the warm to cold supports that carry axial forces. The cross-sections in Figures 4.17 and 4.18 show the magnet cryostats, the coils, the coil support structure,

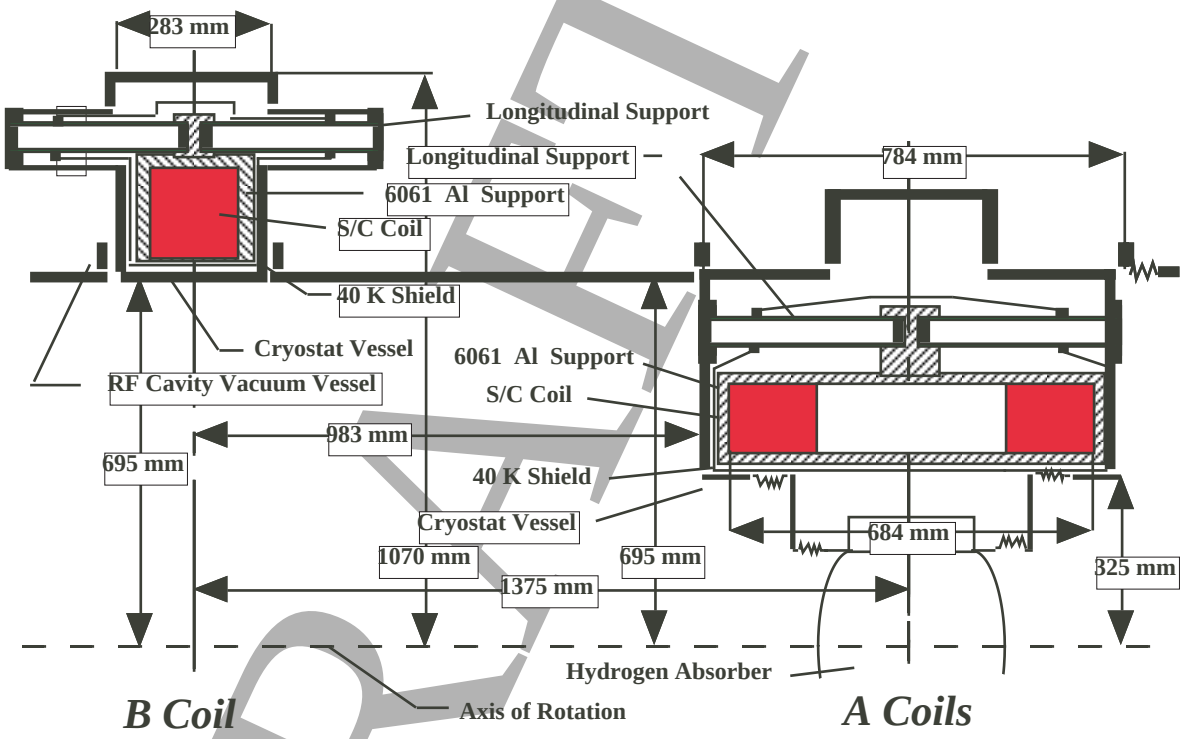

Figure 4.17: Magnet Cross-section for the 2.75-meter Long Cooling Cell.

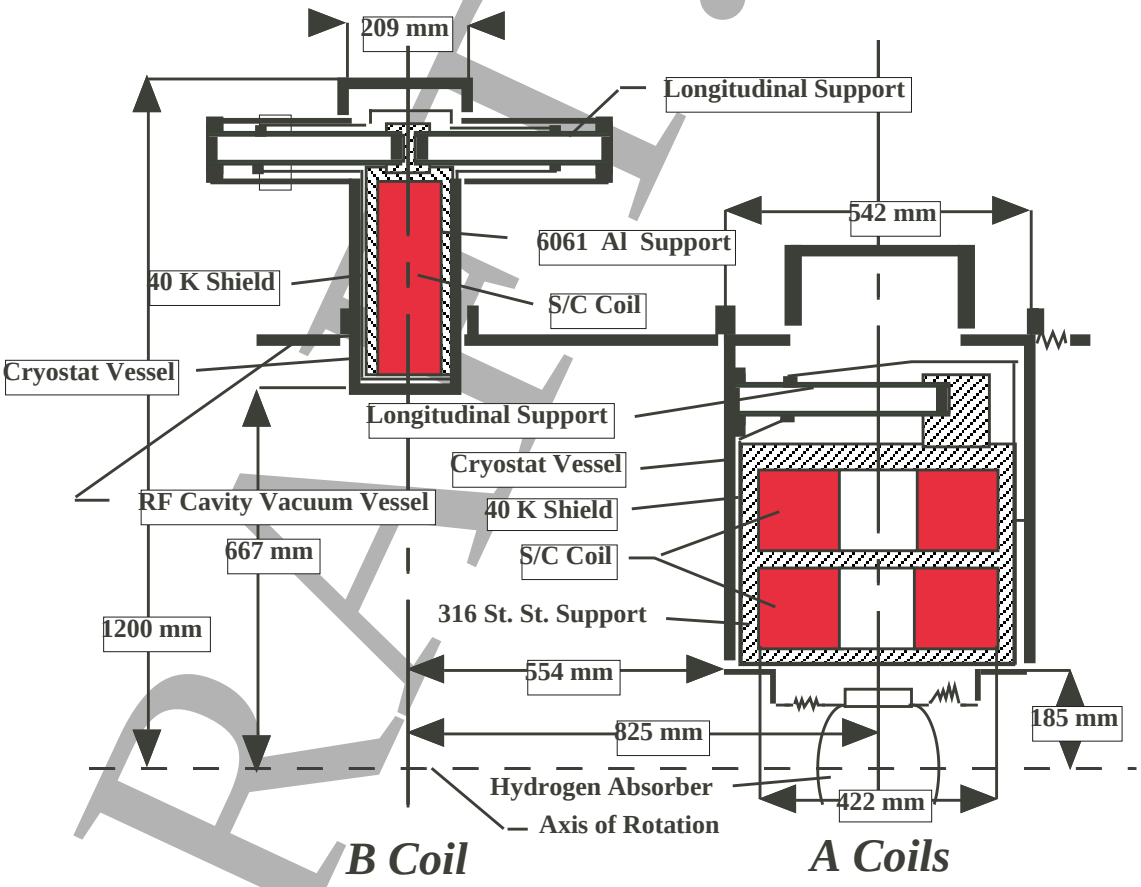

Figure 4.18: Magnet Cross-section for the 1.65-meter Long Cooling Cell.

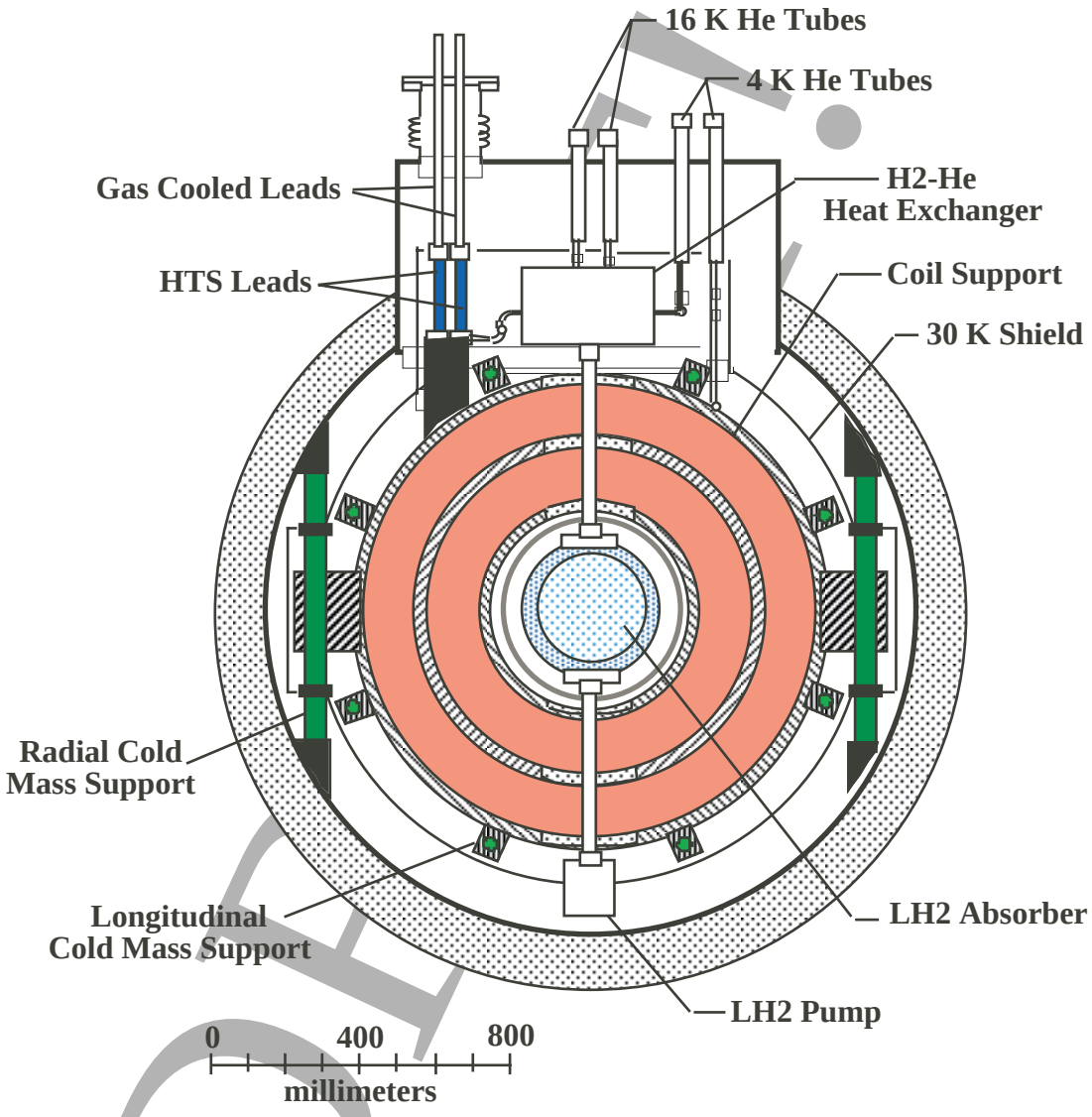

Figure 4.19: Cross-section of the 1.65 m Cell A Magnet Perpendicular to the Beam.

Table 4.9: Basic cell parameters for the beam bunching and cooling cell

Parameter	2.75 m Cell	1.65 m Cell
Number of Cells of This Type	39	37
Cell Length (mm)	2750	1650
Maximum Space for the *rf* Cavity	1966	1108
Number of 201.25 MHz *rf* Cavities per Cell	4	2
Number of 402,5 MHz *rf* Cavities per Bunching Cell	1	NA
A Magnet Cryostat Length (mm)	784	542
B Magnet Cryostat Length (mm)	283	209
Aperture for the A Magnet (mm)	650	370
Aperture for the B Magnet (mm)	1390	1334
Maximum A Coil Current Density (A mm^{-2})	128.04	99.65
Maximum B Coil Current Density (A mm^{-2})	99.24	109.45
Maximum Cell Stored Energy (MJ)	13.2	17.6
Maximum Longitudinal Warm to Cold Force (MN)	0.74	1.20
Number of Longitudinal Supports per Coil	4	6 to 8
Peak Induction 9.9 m from the Cell axis (T)	1.18x10^{-5}	2.62x10^{-5}

the 30 K shields, and the vacuum vessel around the *rf* cavities. The cryostat vacuum systems are separated from the vacuum around the *rf* cavities and the beam vacuum.

Figure 4.19 shows a cross-section through the center of the 1.65-meter long cell A coil pair. Note the location of the longitudinal cold mass supports and the cold mass supports that carry forces in both directions perpendicular to the solenoid axis. The figure illustrates how magnet electrical leads, and helium refrigeration can be brought into the cryostat. Figure 4.19 is a typical cross-section that can be applied to all of the bunching and cooling cell solenoids.

Figures 4.17 and 4.18 show the location of the hydrogen absorbers within the bore of the A coil pair. The hydrogen absorber will share the same cryostat with the A coils. The hydrogen absorber and the A magnet will have a common vacuum and the hydrogen absorber will be supported from the A coil package by a low thermal conductivity support system made from a titanium tube. Figure 4.19 illustrates schematically that connections to the hydrogen absorber can be made between the A coils through the support

Table 4.10: Solenoid parameters for the 2.75-meter long bunching and cooling cell

	A Magnets	B Magnets
Physical Parameters		
Magnet Cryostat Length (mm)	784	283
Magnet Cryostat Bore Diameter (mm)	650	1390
S/C Coil Length (mm)	167	162
Inner Radius of the Coil (mm)	355	729
S/C Coil Thickness (mm)	125	162
Distance Between Coils in Z Direction (mm)	350	NA
Inner Support Structure Thickness (mm)	15	0
Outer Support Structure Thickness (mm)	20	25
Number of Turns per Magnet	2304	1472
Magnet Cold Mass (kg)	1430	1245
Magnet Overall Mass (kg)	1870	1570
Electrical Parameters and Magnetic Forces		
Maximum Magnet Design Current (A)	2320.2	1779.9
Peak Induction in the Windings (T)	7.5	6.5
Magnet Stored Energy at Design Current (MJ)	≈7.9	≈7.7
Magnet Self Inductance per Cell (H)	≈2.9	≈4.9
Superconductor Matrix J (A mm^{-2})	155	119
E J2 Limit per Magnet Cell (J A^2 m^{-4})	$1.89x10^{23}$	$1.09x10^{23}$
Force Pushing the A Coils Apart (metric tons)	329	NA
Peak Fault Force on a the Coil (metric tons)	75.3	75.3

structure that carries the magnetic large forces generated by the two A coils that operate at opposing polarities.

Forces

Forces in the longitudinal direction are a serious concern for the bunching and cooling solenoids. The field flip coils (the A coils) generate large forces (up to 1950 metric tons) pushing them apart. These forces must be carried by a 4.4 K metallic structure between the two coils. The magnitude of the forces pushing the A coils apart depends on the spacing between the coils,

Table 4.11: Solenoid parameters for the 1.65-meter long cooling cell

	A Magnets	B Magnets
Physical Parameters		
Magnet Cryostat Length (mm)	542	209
Magnet Cryostat Warm Bore Diameter (mm)	380	1334
S/C Coil Length (mm)	145	109
Inner Radius of Inner Coil	210	687
S/C Coil Thickness (mm)	138	326
Distance Between Coils in Z Direction (mm)	132	NA
Inner Support Structure Thickness (mm)	20	0
Center Support Structure Thickness (mm)	30	NA
Outer Support Structure Thickness (mm)	40	25
Number of Turns per Magnet	4480	1974
Magnet Cold Mass (kg)	1995	1750
Magnet Overall Mass (kg)	2430	2290
Electrical Parameters and Magnetic Forces		
Maximum Magnet Design Current (A)	1780.5	1896.7
Peak Induction in the Windings (T)	8.4	6.5
Magnet Stored Energy at Design Current (MJ)	≈10.7	≈11.0
Magnet Self Inductance per Cell (H)	≈6.8	≈6.1
Superconductor Matrix J (A mm^{-2})	119	126
E J2 Limit per Magnet Cell (J A^2 m^{-4})	$1.51x10^{23}$	$1.74x10^{23}$
Force Pushing the A Coils Apart (metric tons)	1980	NA
Peak Fault Force on a the Coil (metric tons)	122	122

the average coil diameter and the current carried in each coil. The inter-coil forces are carried by either aluminum of stainless steel shells on the inside and the outside of the coils. The forces are transmitted to the coil end plates, which are put in bending. Large stresses are developed at the point where the end plates meet the shells inside and outside the coils. Since the force between the A coils in the 1.65-meter long cooling cells is so large (about 1950 metric tons), the A coils had to be divided in the radial direction in order to reduce the bending stress in the end plates. The large stress in the end plates of the A coils in the 1.65-meter long cooling cell dictate that the end plates and shells around the A coils must be made from 316 stainless

steel.

If the currents in all of the A coils and all of the B coils were the same from cooling cell to cooling cell, there would be no net longitudinal force on any of the coils. The currents in the cooling cell coils vary as one goes down the bunching and cooling channel. This generates a longitudinal force in various magnet coils. The largest longitudinal forces will be generated at the ends of the string or when one coil quenches and adjacent coils do not quench. One can attach all of the coils together with cold members, but further examination suggests that this approach does not make sense if one wants to be able to assemble and disassemble the muon cooling system. As a result, every magnet is assumed to have cold to warm longitudinal supports. The cold to warm supports in the magnets in the 2.75-meter long cells are designed to carry 80 metric tons (the maximum force during a magnet fault). These forces can be carried by four oriented glass fiber epoxy cylindrical supports that are 50-mm in diameter with a 4-mm thick wall. Oriented glass fiber rods can carry stresses up to 600 MPa in either tension or compression.

The 1.65-meter long cell magnets have longitudinal cold to warm supports that are designed to carry 120 metric tons. Figure 4.19 shows the location of eight of these supports on the 1.65-meter long cell A magnet. A six support longitudinal support system would also be practical. The support shown for the A coil in Figure 4.18 is designed to operate in both tension and compression. Further engineering can define an optimum cold mass support system for these magnets. Compared to other heat loads into the magnets, the longitudinal cold mass supports represent about one quarter of the total heat leak into the magnet cryostat.

Conductor

The magnet conductor that is assumed for the all of the B solenoids is a conductor that is 7 parts copper and 1 part niobium-titanium. This conductor consists of strands with a copper to superconductor ratio of 1 to 1.3. The twist pitch in the superconductor is about 10 mm. The strands of this conductor are attached to a pure copper matrix. The overall dimensions for the finished conductor is 3 mm by 5 mm. The proposed conductor will carry 5100 A at 5 T and 4.2 K. At 7.5 T the proposed conductor will carry about 2500 A at 4.4 K. This conductor could be used in the 2.75-meter cell A coils, but the margin is rather tight. The problem occurs in the 1.65-meter long cell A magnet where the peak field at the high field point in the magnet is

8.4 T. This coil must be operated at reduced temperature (say 2.5 K) when the proposed conductor is used. A re-optimization of the short cooling cell that moves the A coils further apart may be a better solution to the high field problem in the short cell A coils. It is proposed that the A coils in the both types of cells use a conductor with a 4 to 1 copper to superconductor ratio.

The conductor is assumed to have a varnish insulation that is 0.05 mm thick. The layer to layer fiber glass epoxy insulation is assumed to be 0.4 mm thick. The ground plane insulation around the coils is assumed to be 1.6 mm thick. This permits the superconducting coils to be discharged with a voltage across the leads of up to 1200 volts. Each A coil set and each B coil is assumed to be powered separately. A quench protection voltage of 1200 V is adequate to protect any of the coils in the cooling cells. Because the conductor current density is high, the A coils in the 2.75-meter long cells have the smallest safety margin when it comes to quench protection. Re-optimization of these coils can improve their quench protection.

The conductor current and current density given for the A and B coils in Tables 4.10 and 4.11 are the peak values that would occur in the cells operating at the highest current. The estimated stored energy occurs at the peak design current in the coils. In general, when the current density is high in the A coil, the current density in the B coil is low. The stored energy for the cooling cells changes very little as one moves down the cooling channel. The cell stored-energy shown in Table 4.9 is the average stored energy for that type of cell. Table 4.12 shows the average coil current density and coil current for the A and B coils in the various regions of the bunching and cooling channel.

Figure 4.20 is a schematic representation of the matching section of a 2.75-meter long cell to a 1.65-meter long cell. The forces between the coils in the A magnet are quite large. It is assumed that the structure around the A coils is stainless steel. The A coil set shown in Figure 4.20 is the only unique magnet is the muon cooling channel. There are 39 A and B coils that make up the 2.75-meter long bunching and cooling cells. There are 37 A and B coils that make up the 1.65-meter long cooling cells.

The last two meters of the induction linac channel must have thicker coils with a separate power supply on each coil. The 1.25 T solenoids at the end of the induction cells must have separate longitudinal warm to cold supports to carry forces (up to 60 metric tons) generated by the magnets in the first cells of the bunching section.

Table 4.12: Coil average J and I for various sections of the bunching and cooling channel

Section	No. Cells	A Coil J A mm^{-2}	A Coil I A	B Coil J A mm^{-2}	B Coil I A
Bunching Cells	22	106.34	1927.0	99.24	1779.9
Cooling 1-1	5	106.34	1927.0	99.24	1779.9
Cooling 1-2	6	117.83	2135.3	92.42	1657.8
Cooling 1-3	6	128.04	2320.2	84.75	1520.0
Cooling 2-1	14	82.21	1468.8	109.45	1896.7
Cooling 2-2	10	89.68	1602.3	101.93	1766.4
Cooling 2-3	13	99.65	1780.5	93.47	1619.8

Figure 4.20: Cross-section of the Matching Region between 2.75 m Cells and 1.65 m Cells.

Refrigeration

Refrigeration to the muon cooling magnets and hydrogen absorbers is supplied at 16 K and 4.4 K. The 4.4 K refrigeration is used to cool the superconducting coils except for coil A in the 1.65-meter long cell, which is cooled to 2.5 K. The 2.5 K cooling requires an additional heat exchanger and a vacuum pump to produce nearly 0.3 W of cooling at 2.5 K. Most of the heat into the 1.65-meter cell A coil package is intercepted at 4.4 K. The hydrogen absorbers are cooled from the same refrigerator as the solenoid magnets. Refrigeration for the hydrogen absorbers is drawn off at 16 K. The 16 K helium used to cool the liquid hydrogen returns to the helium cold box at 19 K. The absorbers in the 2.75-meter long cell contain 9 liters of liquid hydrogen. The 1.65-meter long cell absorbers contain about 4 liters of liquid hydrogen. The estimated heat load to the absorbers is between 120 and 130 W. Table 4.13 shows the refrigeration requirements for the 2.75-meter long cells and the 1.65-meter long cells with hydrogen absorbers. The equivalent 4.4 K refrigeration reflects the Carnot ratios from 4.4 K to 16 K and the refrigeration lost when helium returns to the compressor by bypassing the refrigerator heat exchangers. The equivalent 4.4 K refrigeration for each of

the 22 bunching cells is 21.1 W per cell. About 10.4 W of equivalent 4.4 K refrigeration is used to cool two pairs of 2000 A gas-cooled leads from 40 K to 300 K.

Figure 4.21 shows a schematic representation of the refrigeration for a pair of A coils with a hydrogen absorber. Two-phase helium at 4.4 K is used to cool the superconducting coils. If nineteen magnets are cooled from a single flow circuit, the mass flow of two-phase helium should be 8 to 10 grams per second. The flow circuit can have up to 20 magnet coils in series before the helium is returned to the control cryostat. The shields, intercepts, current leads, and hydrogen absorbers are cooled by helium that comes from the refrigerator at 16 K. The helium used to cool the shields and the leads is returned to the refrigerator compress warm. The rest of the 16 K helium returns to the refrigerator at 19 K.

The helium used to cool the magnet shield intercepts heat from the cold mass support, the bayonet tubes, the instrumentation wires and radiation heating through the multi-layer insulation before it is used to cool the gas cooled current leads for the A and B magnet. For the flow circuit shown in Figure 4.21, the flow of helium gas in the shield cooling circuit is dictated by the needs of the gas cooled current-leads. For the current leads in the cooling and bunching magnets this flow varies from 0.15 to 0.23 grams per second. Depending on the needs of the current leads, the temperature rise in the shield gas flow circuit will vary from 14 K to 23 K. If one could optimize the magnets, the lead current might be as low as 1200 A. With 1200 A current leads the temperature at the top of the high Tc superconducting leads would be about 50 K. It is proposed that both the A and the B magnet shields be cooled using the same 16 K source of gas from the helium refrigerator, but this is not optimum from the standpoint of overall refrigeration system efficiency. When the helium refrigerator cools both the hydrogen absorber and the magnets, there will be enough excess refrigeration capacity available to cool down the magnet coils down in a reasonable time.

The flow in the 16 K circuit to the hydrogen absorber is dictated by the heat load in the absorber. Without a muon beam, the heat load could be as low as 22 W. With beam heating and the circulation heater operating the heat load into the absorbers can approach 130 W. The temperature rise in the absorber cooling helium circuit should be limited to about 2 K. As a result, the helium flow circuit used to cool the hydrogen absorbers should be designed to provide 12.5 grams per second of 16 K helium. This gas will be returned to the refrigerator cold box at around 19 K (including heating in

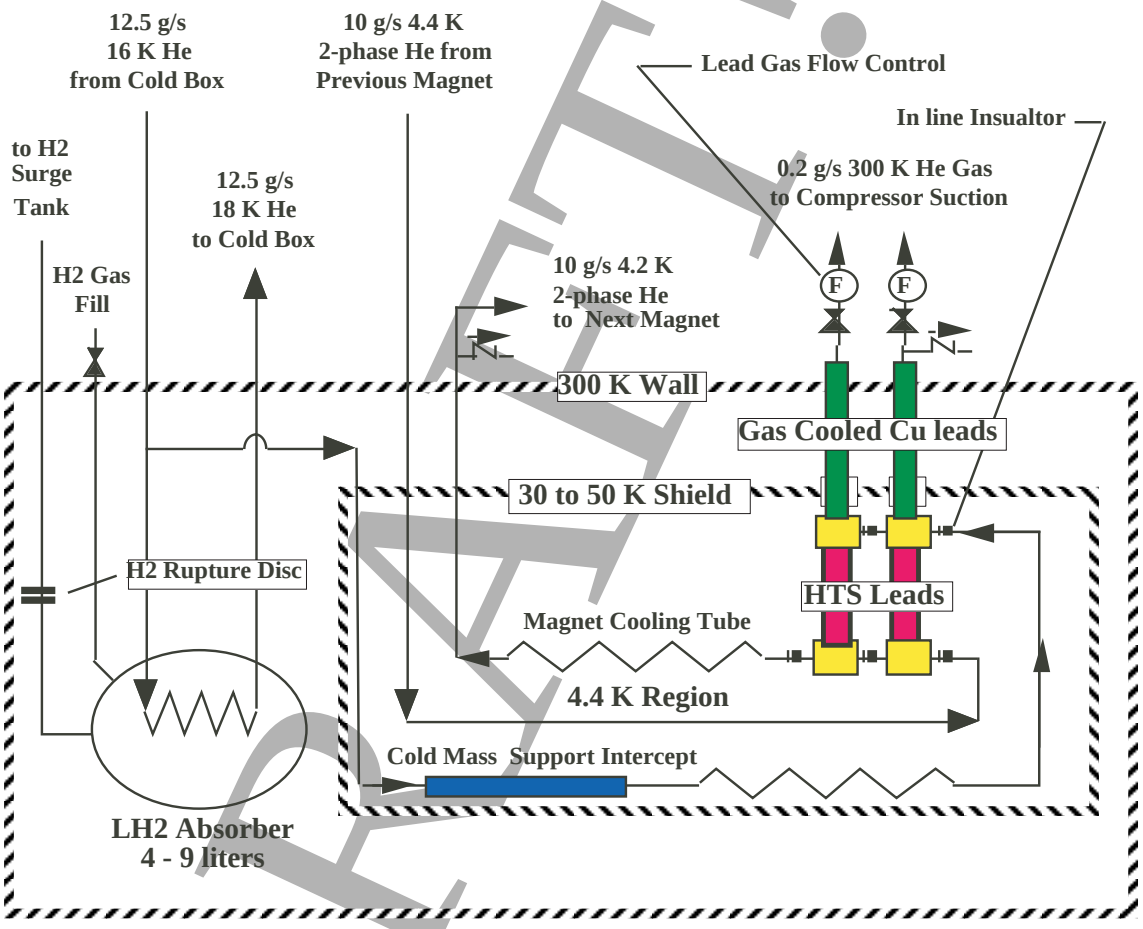

Figure 4.21: Cryogenic Cooling System within a Typical Cooling A Coil Cryostat

the return transfer line).

Quench protection

The bunching section has twenty magnets and twenty-one B magnets that have the same current in the coils. The number of cooling section cells where magnets carry the same current is up to thirteen. It is assumed that each magnet in the bunching and cooling sections has its own leads. The magnets can be powered individually or in strings of magnets that carry the same current. Powering magnets as a string of magnets requires a more complicated quench protection system that uses diodes and resistors to cause the string current to by-pass the quenching magnet. For simplicity sake, it is assumed that each magnet has its own power supply and quench protection system. A 2500 A power supply for charging and discharging a single magnet coil (either an A coil or a B coil) should be capable of developing 7 volts. The magnet quench protection consists of a dump resistor across the magnet leads. When a quench is detected, a fast switch disconnects the power supply from the magnet. In all cases, the power supply control system should permit one to control the current and the voltage across the coils as the magnet is charged and discharged. The power supply is not required to operate at both positive and negative currents. A controller is used to control the charging and discharging voltages across each coil and regulate the current once the coil has reached its set current.

Alignment

The B coils can be aligned so that the solenoid axis is correct to 0.3 m-radians. The magnetic center of the B coil can be maintained to about 0.3 mm. The alignment of the A coils can probably be maintained to about 0.5 or 0.6 m-radians. Correction dipoles can be installed in the bore of the A coils that will permit the apparent solenoid axis to be corrected by $\pm$ 1.5 m-radians.

4.4.8 Liquid hydrogen absorbers

Power handling

We estimate the maximum power dissipation per absorber to be about 300 W, dominated by the ionization energy loss of the muons. The main technical

Table 4.13: Sources of heat at 4.4 K, 20 K and 35 K in the bunching and cooling cell magnets

Source of Heat	2.75 m Cell(W)		1.65 m Cell(W)	
	A Coil	B Coil	A Coil	B Coil
Magnet Heat Loads at 4.4 K				
Vertical Cold Mass Supports	0.24	0.24	0.40	0.24
Longitudinal Cold Mass Supports	0.36	0.36	0.74	0.54
Thermal Radiation through MLI	0.16	0.14	0.01	0.19
Bayonet Joints and Piping	0.03	0.03	0.03	0.03
Instrumentation Wires	0.02	0.02	0.02	0.02
HTS Current Leads	0.60	0.60	0.60	0.60
Total 4.4 K Heat Load per Coil	1.41	1.39	1.80	1.62
Magnet Heat Loads at 2.5 K				
Vertical Cold Mass Supports	—	—	0.05	—
Longitudinal Cold Mass Supports	—	—	0.10	—
Thermal Radiation through MLI	—	—	0.11	—
Bayonet Joints and Piping	—	—	0.01	—
Instrumentation Wires	—	—	0.00	—
HTS Current Leads	—	—	0.02	—
Total 2.5 K Heat Load per Coil	0.0	0.0	0.29	0.0
Magnet Shield and Intercept Heat Loads at 16 to 40 K				
Vertical Cold Mass Supports	3.8	3.8	3.8	3.8
Longitudinal Cold Mass Supports	7.2	7.2	10.8	10.8
Thermal Radiation through MLI	2.7	2.9	1.9	3.2
Bayonet Joints and Piping	1.3	1.3	1.3	1.3
Instrumentation Wires	0.1	0.1	0.1	0.1
Gas Cooled Current Leads	—	—	—	—
Total 16 to 40 K Heat Load per Coil	15.1	15.3	17.9	19.2
Hydrogen Absorber (16 K Cooling)				
Cold Mass Supports	1.5	—	1.0	—
Thermal Radiation through MLI	0.3	—	0.2	—
Bayonet Joints and Piping	1.3	—	1.3	—
Instrumentation Wires	0.1	—	0.1	—
Thermal Radiation to Windows($\epsilon = 0.2$)	18.4	—	6.9	—
Beam Absorption Heating	77.0	—	81.0	—
Circulation Heater	≈30	—	≈30	—
Total 16 K Heat Load per Coil	128.6	0.0	121.5	0.0
Equivalent 4.4 K Refrigeration per Cell	54.6		57.6	

challenge in the absorber design is to prevent boiling of the hydrogen near the beam axis, where the power density is greatest. This requires that the hydrogen flow have a significant component transverse to the beam. We are investigating two ways to achieve this: a design in which the absorber connects to an external heat-exchange and temperature-control loop, and a design in which the absorber vessel is itself the heat exchanger, and heat transfer within the absorber is accomplished dominantly by convection.

The flow-through design resembles previous high-power liquid-hydrogen targets [?, ?], which have been operated successfully at power dissipations as high as 200 W [?] and proposed for operation at dissipations in excess of 500 W [?, ?]. In this aproach the hydrogen is pumped around a loop that includes the absorber vessel as well as a heat exchanger and a heater. In the heat exchanger, which runs at a constant power level, the hydrogen is cooled by counterflowing cold helium gas. The heater is used in feedback to regulate the hydrogen temperature and compensate for changes in beam intensity.

Given the small emittance of conventional particle beams, liquid-hydrogen targets tend to be narrow transverse to the beam, leading to designs in which the natural direction of hydrogen flow is parallel to the beam. To avoid boiling the liquid in the high-intensity beam core, various design strategems are then necessary to assure transverse flow of the liquid [?, ?]. In contrast, in our flow-through design the hydrogen enters the absorber vessel from below and exits at the top, assuring that the flow is transverse to the beam. The flow pattern is controlled by means of nozzles, which must be configured so as to avoid dead regions or eddies and ensure adequate flushing of the windows.

In the convection design (Fig. 4.22), the interior wall of the vessel is equipped with cooling tubes through which cold helium gas circulates. A heater located at the bottom of the vessel is used to compensate for changes in beam intensity. The design of the convection-cooled absorber is being guided by two-dimensional fluid-flow calculations carried out at IIT. The flow-through approach is less amenable to calculation but will be tested on the bench to verify the efficacy of the nozzle design, first in a room-temperature model and later at cryogenic temperature. Prototype construction and testing programs for both designs are now underway and will lead to high-power beam tests, currently envisioned for 2002.

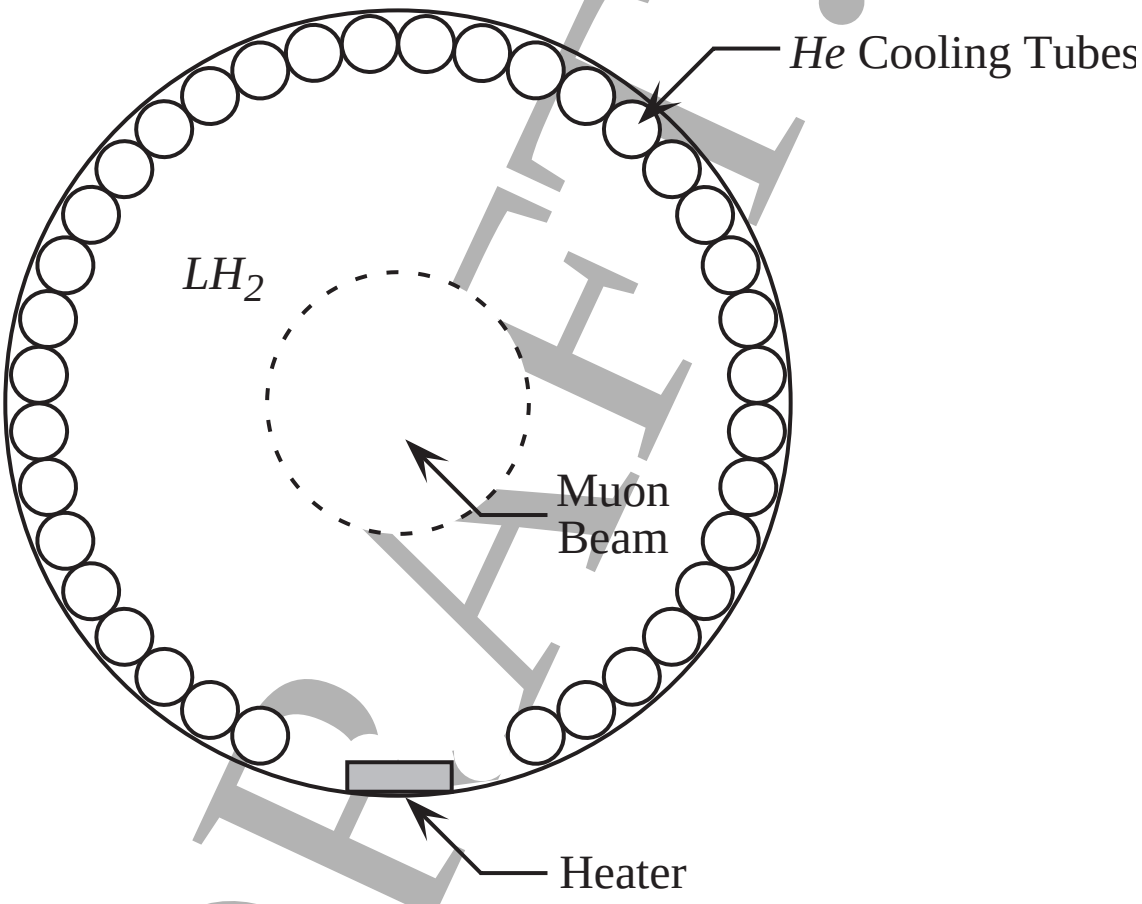

Figure 4.22: Schematic of convection cooled liquid hydrogen absorber.

Window design

To minimize heating of the beam due to multiple scatering, the absorbers must be equipped with thin, low-Z windows. Yet the windows must be strong enough to withstand the pressure of the liquid hydrogen. We have devised a window design that satisfies these requirements and also allows quite thin absorbers to be built. While a hemispherical window shape minimizes the window thickness for a given strength, the desire to build absorbers that are thinner relative to their diameter than a sphere leads to the "torispherical" shape. In the version specified by the American Society of Mechanical Engineers (ASME) [**?**], the torispherical head for pressure vessels is composed of a central portion having a radius of curvature (the "crown radius") equal to the diameter of the cylindrical portion of the vessel, joined to the cylindrical portion by a section of a toroidal surface with a radius of curvature 6% of the crown radius (see Fig. 4.23).

ASME specifies the minimum acceptable thickness of the torispherical head as

$$t = \frac{0.885PD}{SE - 0.1P}\,, \tag{4.6}$$

where P is the differential pressure across the window, D the vessel diameter, S the maximum allowable stress, and E the weld efficiency. Although previous high-power liquid-hydrogen targets have operated at 2 atm [**?**, **?**], to keep the windows as thin as possible we have designed for 1.2 atm. For S we follow ASME recommendations and use the smaller of 1/4 of the ultimate strength S_u or 2/3 of the yield strength S_y (in practice, for aluminum alloys it is the ultimate strength that matters). We have decided to machine the window with an integral flange out of a single disk of material (Fig. 4.24), with the flange fastened to the assembly by bolts (Fig. 18.11), thus there are no welds and so we take $E = 1$. For 1.2-atm operation, and given the ASME specification for 6061-T6 aluminum alloy $S_u = 289$ MPa, we obtain $t = 530\,\mu$m for the "lattice 1" absorbers ($D = 0.36$ m) and $t = 330\,\mu$m for the "lattice 2" absorbers ($D = 0.22$ m). However, the windows can be made thinner than this by tapering their thickness as described below. In addition, less easily-machinable, but stronger, aluminum alloys (such as 2090-T81) may allow further reduction in thickness.

In addition to eliminating the weld, machining the window out of a single disk allows detailed control of the window shape and thickness profile. We have used the ANSYS finite-element-analysis program to optimize the

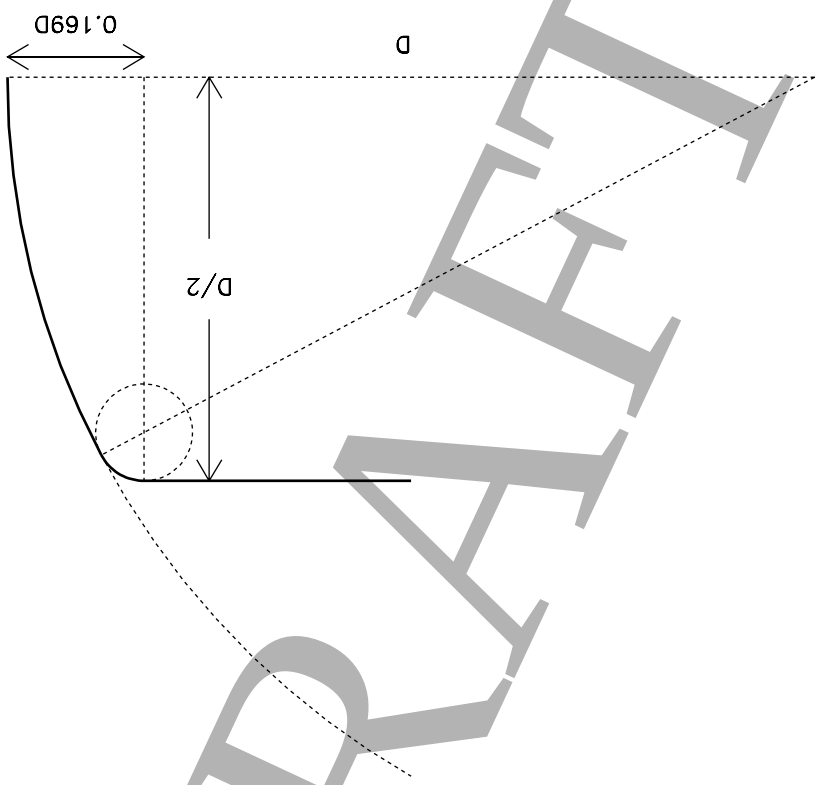

Figure 4.23: Schematic of ASME torispherical head on cylindrical vessel of diameter D: solid curve shows upper half section, with dashed lines and curves indicating the spherical and toric surfaces from which it is composed.

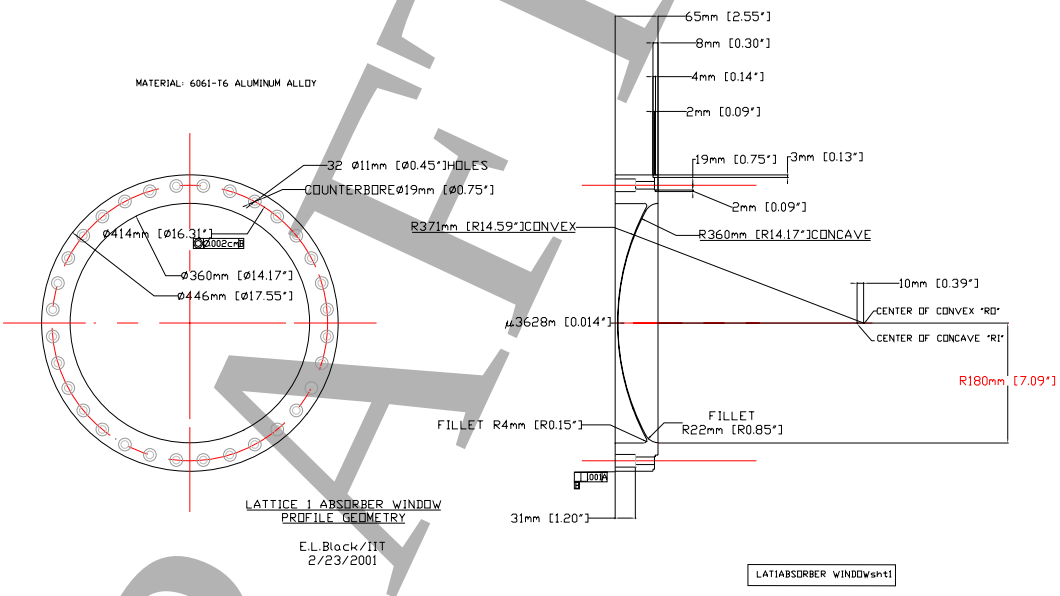

Figure 4.24: Window design for the SFOFO Lattice 1 absorbers.

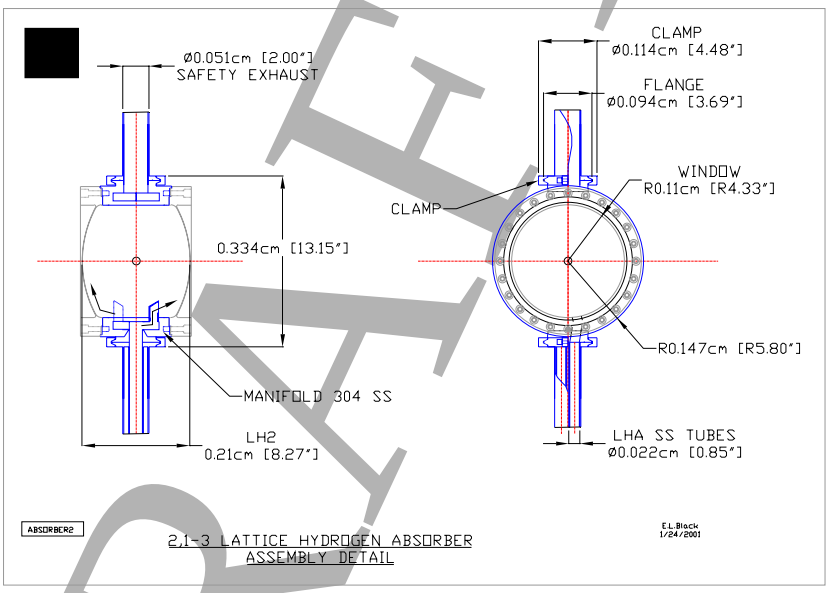

Figure 4.25: Absorber assembly for SFOFO Lattice 2 (flow-through design shown).

window shape and profile so as to minimize the window's thickness in its central portion, where most of the muons traverse it. The resulting shape and thickness profile are shown in Figs. 4.24.

4.4.9 Instrumentation issues in the Cooling Line

There are a number of unique instrumentation problems involved in optimizing and monitoring the performance the cooling line. The beams will be large and intense, and a variety of precise measurements will be required which are both novel and difficult.

There will be significant backgrounds in all detectors, both due to other particles from the target coming down the line with the muons, and x-rays and dark currents generated by the *rf* cavities. We must consider the angular momentum of the beam, perhaps for the first time any high energy physics beam. The beams will be intense enough so that thermal heating of the detectors will be significant. The environment will have high magnetic fields, a large range of temperatures, and high power *rf* cavities. In addition, under normal circumstances the access will be very limited, since the *rf* cavities and liquid hydrogen absorbers would occupy most of the available space. Loss monitors will not be useful for the low energy muons because the ranges of these particles are so short (6 cm in Cu) and they produce no secondaries.

On the other hand, there are a number of issues that would argue that the tune up and operation could be fairly straightforward. The cooling line has been, and will continue to be, very thoroughly simulated by the time of initial construction. In addition, there are a relatively small number of variables which control the behavior of the beam, such as currents in coils, *rf* parameters and liquid hydrogen target parameters, and these can be measured independently with high precision. While the change in transverse beam emittance, $\epsilon_\perp$, between individual modules may be difficult to measure, $\Delta\epsilon_\perp/\epsilon_\perp < 0.01$, the overall size and profile of a beam with $\sim 10^{12}$ particles is a comparatively straightforward measurement. The high power muon beam considered here makes measurements much easier than for the muon cooling demonstration experiment, which might operate with intensities of only $10^6 - 10^7$ muons.

Tolerances

The sensitivity of the system to alignment errors has been described above. Other concerns are transverse and longitudinal mismatches between the cooling line and the bunching section, arcdown and temporary loss of an *rf* cavity, boiling or loss of hydrogen in the absorber section, or inadvertent introduction of a collimator or thick diagnostic. An R & D program is underway to look at the sensitivity and usefulness of different diagnostic techniques and evaluate them in the environment of *rf* backgrounds and high magnetic fields.

Angular Momentum

Angular momentum plays an important role in solenoid ionization cooling channels, unlike the quadrupole channels used everywhere else in high energy physics. Due to the rotational symmetry of the solenoid focusing field, the canonical angular momentum is a conserved quantity when the cooling material is absent. When absorbers are present, however, the beam angular momentum can change, thereby yielding a residual angular momentum at the end of a cooling channel. Non-zero beam angular momentum creates coupling between the two transverse degrees of freedom and causes problems for matching the beam into a following quadrupole channel. Furthermore, the angular momentum intrinsically couples with the beam emittance in the cooling dynamics. For efficient cooling in a periodic channel, it is necessary to keep the change in the net angular momentum to be zero. This requirement becomes the following condition[**?**]

$$\int_0^\lambda \eta(s)\beta(s)B(s)ds = 0 \tag{4.7}$$

where λ is one period, $B(s)$ is the on-axis magnetic field, $\beta(s)$ is the envelope function, and $\eta(s)$ is the ionization energy loss rate.

Measurement of beam angular momentum is a new subject. A beam profile monitor, which measures beam distribution in x and y, can measure the beam emittance, but does not provide sufficient information to directly determine the angular momentum in a solenoid cooling channel. Based on beam emittance measurements, one may indirectly measure the angular momentum by identifying the two components that have different damping rates in the emittance damping curve. However, such measurements are difficult. Novel ideas are being explored to directly measure the correlation terms $\langle xPy \rangle$ etc.[**?**]

Since the energy loss rate, absorber thickness, and magnetic field are known, or can be measured with an accuracy much better than one percent, and an envelope function measurement is likely to be accurate to a few percent, it should be easy to determine whether the above requirement is approximately satisfied. Thus for machine operation purposes, beam angular momentum measurement is helpful, but not absolutely necessary. For cooling demonstration experiments, however, good angular momentum measurement can provide further evidence for the cooling behavior. The ability to adjust the amount of material in absorbers is useful for correcting any residual angular momentum at the end of a cooling channel.

Backgrounds

There are a number of distinct backgrounds which will impact beam diagnostics. These backgrounds come primarily from three sources: 1) backgrounds produced by the incident protons at the target, 2) backgrounds produced in the cooling line, primarily from *rf* cavities, and 3) backgrounds from decay electrons. We assume that the decay electrons can be simulated and subtracted from all measurements.

Beam Backgrounds The solenoidal beam transport channel for muons will also transport all other particles whose transverse momentum is less than $\sim$ 100 MeV/c. Thus hadronic showers from 3 GeV protons, for example, can be expected in the liquid hydrogen targets well down the cooling line. A large number of species are produced: K, D, n, γ, $e^{\pm}$, He^3, He^4, and other nuclear fragments should be seen in detectible quantities. Most low energy backgrounds from the target would be stopped in the first hydrogen absorbers, but the high energy particles which were left would be comparatively uneffected by the *rf* in the line. Timing should be very effective for identifying and discriminating against these particles.

***rf* Backgrounds** X ray production from *rf* cavities results from dark current electrons hitting the body of the cavity and nearby solid components. The bremsstrahlung x-ray flux produced is then scattered and attenuated by both the production material and by transmission through any external structure. While the dark current electron orbits would be influenced by magnetic fields along the beam axis, the x-rays, particularly those around 1-2 MeV, would scatter and diffuse freely up and down the cooling line. The

dark current electrons from single gap cavities, and the x-rays they produce would be expected to be in the 1 -10 MeV range. The electron and x-ray fluxes produced in this environment have been recently measured in a 1.3 GHz high gradient cavity[?]. Other experiments are planned using an 805 MHz cavity. Data taken from a variety of pulsed cavities seem to imply that *rf* breakdown limits the total dark current and thus the x ray flux that can be produced, somewhat independent of frequency.

Fluxes of dark current electrons and x-rays measured in a 1.3 GHz cavity were on the order of 10^{10} -10^{11} electrons / *rf* pulse, or 10^7 - 10^8 electrons/bucket, a more relevant parameter. The number of bremsstrahlung electrons is of the order $n_e r/L_R$ where r is the dark current electron range, which is usually a few mm, and L_R is the radiation length for the material, 1.44 cm for Cu. Because the energies are low, complex showers do not develop. The photons do, however, diffuse through the system.

There seems to be three ways of altering the flux of dark current electrons and the x-ray flux seen by the beam diagnostics: 1) the geometry of the system can be changed so that dark current electrons do not appear near the beam axis (the single flip cooling channel option does this); 2) the *rf* electric field, E_{rf}, can be reduced since $I_{dark} \propto E_{rf}^{10}$; and 3) the cavity can be coated with an insulating material. All of these are methods are to some extent applicable to the cooling line, so it is difficult at this point to make precise estimates of the radiation flux expected in the beam diagnostics.

Access in the Cooling Line

We assume it will be desirable to be able to insert, park, and also remove any instrumentation in the line without disrupting the beam vacuum. There are a number of options for insertion of diagnostics into the cooling line.

Analogous to FODO accelerator structures, it seems desirable to insert diagnostics at every major focusing element. While there is limited space in the cooling line, it seems that instrumentation modules may be compatible with the 5 - 7 cm expansion section that may be a part of every module, and we have assumed this. Figure 4.26 shows a possible location for inserting diagnostics in the cooling cell.

Special SFOFO sections, without hydrogen absorbers and with only enough *rf* voltage to contain the bunch, can also be used for specific Cherenkov counters or other devices which require more access than would be available in expansion sections. The expense of these special sections implies that maxi-

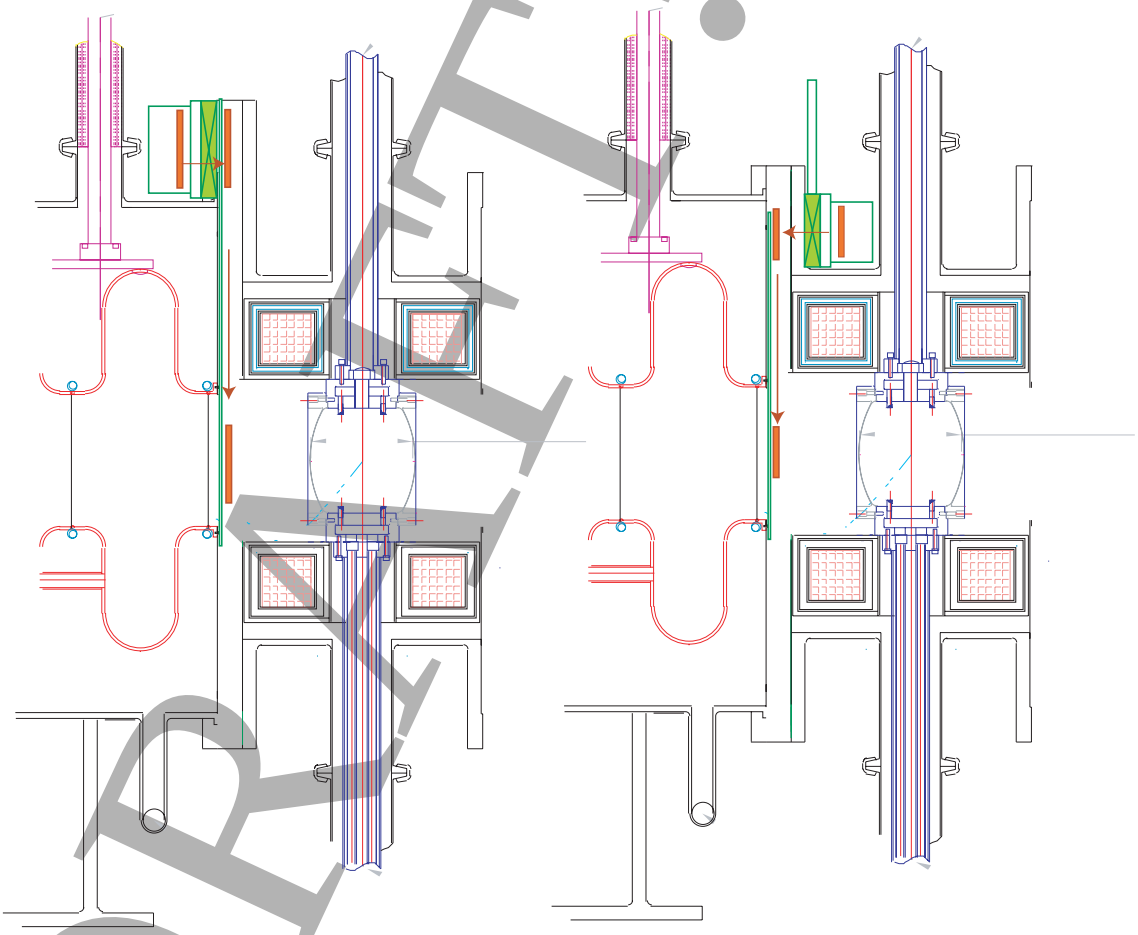

Figure 4.26: Options for insertion of instrumentation into the cooling line.

mum use should be made of the available space in expansion sections.

Making and Using Pencil Beams

We anticipate that pencil beams will be very useful in assessing the alignment of all cooling, accelerator, and storage ring components. Since the range of the 180 MeV/c muons in the cooling line is only about 6 cm in Cu and scattering angles are large, collimation works very well. Thus a variety of collimators could be used at locations in the bunching and cooling lines to produce low transverse emittance beams, on or off axis.

Producing a 6D "pencil" may be even more useful, since this could be used to track the longitudinal evolution of the bunch through all the whole acceleration and storage ring optics. In principle the 6D bunch can be produced from a 4D bunch by reducing the *rf* voltage in the cooling line so that only the center of the longitidinal phase space is transmitted down the line. While the intensities would be reduced, muon beams in the range of 10^{10} to 10^{11}, should be quite easily measured and useful.

Instrumentation Options

Although high energy particles, dark current electrons and x-rays will be present, the primary muon beam should dominate these backgrounds. It seems desirable, however, to look first at instrumentation options which offer very fast time response, so they would be comparatively less sensitive to these backgrounds. From this perspective, Segmented Secondary Emission Monitors (SSEMs) and Faraday cups seem to offer a significant advantage. These devices have been shown to have a useful resolution time of the order of 150 - 200 ps. Since the time response is significantly less than the bucket length, these devices would be able to provide some information on the bunch shape and thus the longitudinal emittance of the beam. Faraday cups could be used essentially interchangibly with the SSEMs. However, they would provide about two orders of magnitude more sensitivity, and the possiblilty of some particle discrimination, using range.

These devices can be used both to measure the beam parameters, but also provide consistency checks for evaluating measurements by other methods. Scintillating fibers, scintillation in the liquid hydrogen, and scintillation counters would also be useful particularly for measurement of the angular momentum of the beam at the end of the cooling line.

Semiconductor arrays of polycrystalline CdTe would be able to provide high precision x and y beam profiles in a single self consistent measurement[**?**]. The detector consists of an array of charge sensitive elements each providing a signal with amplitude proportional to the intercepted muon beam density.

Likewise bolometers are being developed which can measure xy profiles from the heating in the metallic windows of the liquid hydrogen absorbers. We are also looking at high rate ion chambers, which would be generally useful for a wide range of measurements. Transition radiation, which would detect dark current electrons much more efficiently than muons, may not be useful.

4.4.10 Tolerances & systematics

The performance of the cooling channel is based on computer simulations using two distinct codes. Yet, some parameters or assumptions in the calculation are identical. As no such channel has been built yet, it is fair to question if the estimation of the cooling performance are robust against small changes in these parameter values. In addition, what are the tolerances on the mechanical alignment in such a long, linear beam transport system? Do we need corrector coils, and if so, where do they need to be placed?

Sensitivity to Multiple Scattering model

ICOOL uses a straightforward Moliere model, imported from the Geant3 package. Geant4 uses an improved version of the Moliere model, but has a tunable parameter. We have studied the sensitivity of the *rms* value of the scattering angle to this parameter, in relation to the known uncertainties in the measured values for these r.m.s. scattering angle for light Z materials. The sensitivity of the μ/P_{15} yield in the relevant range of this tunable parameter has been measured. The systematic error due this uncertainty is approximately 10%.

Control of the energy loss in LH2 and energy gain in the Linac

Because of the relatively narrow momentum acceptance of the channel with respect to the momentum spread due to the large longitudinal emittance, the energy loss and the energy gain, on average, must be known in the channel to better than $\approx 0.25\%$ percent. This tolerance can be achieved in conventional linacs, where the peak voltage and acceleration voltage can be controlled to better than a few tenths of a percent.

The fluctuation in the LH2 density must also be controlled. In order to get a feel for this effect, the LH2 density was randomly set in each absorber, based on a Gaussian model, with a relative σ of 10 % and 20%. The relative μ/P_{15} yield decreased by 5% and 10%, respectively. However, we think that we will be able to keep the density uniform to better than a few percent, based on the experience of the Bates group[**?**].

The cooling channel will require about 72 12-MW klystrons. It is likely that one, (or more), will fail. One then would empty the most upstream LH2 vessel, and rephase the downstream linacs to keep the beam on the nominal momentum. If a (1,1) or a (1,3) cooling cell has an empty vessel and no

rf power, after proper rephasing, the performance of the channel degrades by about 5% (relative), allowing us to keep the cooling channel running productively.

Magnet alignments

The design of the cooling channel is being optimized using ideal magnetic fields from cylindrical current sheets[?]-[?]. In an actual magnetic channel, imprecisions that occur in the fabrication and assembly of the solenoids result in magnetic fields that deviate from the ideal used in the simulations by some small error field $\delta\vec{B}(x, y, z)$. Typical state-of-the-art magnet construction results in field errors of $\frac{\delta B}{B} \leq 0.1\%$. These field errors produce effects, in general detrimental, that tend to increase with the length of the channel. If left uncorrected, these errors lead to mismatching and betatron oscillations, which in turn result in degradation of the cooling performance of the channel and to a decrease of the channel transmission.

We have considered the following analytical treatment of the detrimental effects of magnet alignment errors. As the muon beam propagates along the periodic channel with a prescribed beta function, it encounters a series of errors of various origins which are assumed to be described by an stochastic function $\delta B(\vec{s})$ (we neglect the transverse coordinate dependence). The muons experience a series of random forces or *kicks*, which result in a random walk of the centroid of the beam. Statistically, the *rms* magnitude of the transverse deviation $\sqrt{< (\delta x(s))^2 >}$ is a function of the length of the channel s. In principle, it should be possible to develop a correction algorithm such that strategically located correction coils bring the centroid back to the ideal trajectory, thereby stopping the deterioration of the cooling process.

A first look at the effects of errors and sensitivity of the present design of the cooling channel has been carried out in references [?] and [?]. Studies of the error fields due to misalignment of individual coils and current sheets are found in references [?],[?].

There are several sources of magnet imperfections that may contribute to the overall deviation from the ideal fields of the channel:

- Geometric survey errors

    1. transverse misalignment of solenoids, characterized by a vector $\vec{d} = d\,(\cos\theta, \sin\theta, 0)$ of magnitude d and direction θ. In the sim-

ulations the values of d are chosen from a Gaussian stochastic function.

2. transverse tilt of full sections of the solenoid characterized by two angles; θ direction with respect to the x-axis, and the tilt by the magnitude ψ with respect to the z-axis.

The Cartesian coordinates $\vec{r} = (x, y, s)$ transform as

$$\vec{r'} = \vec{r} - \vec{d} \tag{4.8}$$

for a translation in the transverse plane and

$$x'_i = \mathcal{M}_{ij} x_j \tag{4.9}$$

for a tilted magnet.

The magnetic fields are calculated as

$$\vec{B}(x, y, s) = \vec{B'}(x', y, s') \qquad B_i(\vec{r}) = \mathcal{M}^{-1}_{ij} B'_j(\mathcal{M}\vec{r}) \tag{4.10}$$

for a translation and tilt respectively. The transformation matrix is

$$\mathcal{M} = \begin{bmatrix} \cos\psi + \cos^2\theta(1-\cos\psi) & \sin\theta\cos\theta(1-\cos\psi) & \sin\theta\sin\psi \\ \sin\theta\cos\theta(1-\cos\psi) & \cos\psi + \sin^2\theta(1-\cos\psi) & \cos\theta\sin\psi \\ \sin\theta\sin\psi & -\cos\theta\sin\psi & \cos\psi \end{bmatrix} \tag{4.11}$$

- Power supply fluctuations resulting in current fluctuations
- Geometric conductor positioning which leads to random *microscopic* field errors

In this work we only consider the first type, *i.e.*, geometric *macroscopic* field errors introduced by mis-positioning of entire cryostat magnets.

We have performed two studies with ICOOL[**?**]. The front end baseline has been simulated with independent Gaussian random tilt angles and translation spaced approximately every 5 m. The results are shown in Fig. 4.27 and Fig. 4.28.

An independent analysis of this alignment tolerance issue has been done using the generic, 3D Geant4 package. We ran the simulation of the buncher and cooling channels in the following mode:

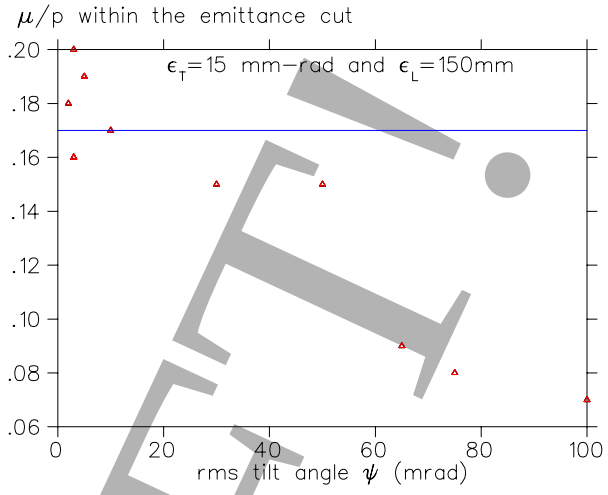

Figure 4.27: Transmission of the front end for different *rms* tilt angles.

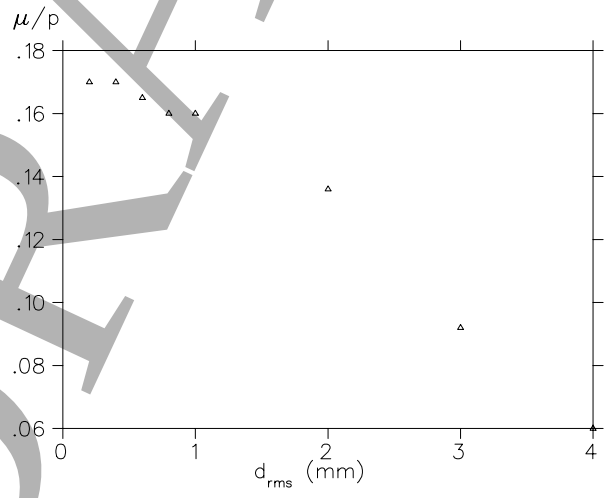

Figure 4.28: Transmission of the front end for different *rms* translation distance d.

- Random polar tilts. A Gaussian model was used to generate the "tilts", polar angles ψ, for each coil. This distribution was truncated: θ angles at more than $2\sigma_\theta$ away were resampled. The azimuthal angles were chosen randomly, between zero and 2π (no systematic bias). The μ/p_{15} yield was measured for tens of such simulated channel assemblies. The histogram shown on Figure 4.29 tells us that a σ_θ of 0.5 mrad gives no statistically significant degradation of the channel performance. However $\sigma_\theta \approx 2.5 mrad$ is unacceptable.

- Random transverse displacements. Since the coils are about 15 cm. long, a tilt of 0.5 mrad gives a lateral displacement at one end of about 75 μm. Evidently, the coil could also shift laterally by about the same amount. We verified that a 2 σ-truncated displacement of 100 μm has no significant impact on the channel performance.

Since the typical tolerance on accelerator magnet's alignment is about 25 to 50 μm, we believe that such a channel can be assembled to the required accuracy. Corrector coils seems to be unnecessary at this point.

Space Charge

The nominal number of muons per bunch is $N_\mu \approx 4/80 \times 10^{12}$, which corresponds to $Q \approx 8$ nC. An estimate of the deleterious effect on the beam dynamics can be found by calculating the self-electric field of a Gaussian distribution of charge represented by the Basetti-Erskine-Kheifts formula [**?**]

$$\Phi(r,z,s) = \frac{2Q}{\epsilon_o\sqrt{\pi}} \int_0^\infty dt \frac{e^{-\frac{r^2}{2{\sigma_\perp}^2+t}}}{(2{\sigma_\perp}^2+t)} \frac{e^{-\frac{z^2}{2{\sigma_3}^2+t}}}{\sqrt{(2{\sigma_3}^2+t)}} \tag{4.12}$$

The variable z is defined as $z = s - c\beta t$ with s the longitudinal coordinate, assuming that the centroid of the bunch is at $s = 0$ at time $t = 0$. The argument s in $\Phi(r,z,s)$ is there to indicate that the *rms* transverse size $\sigma_\perp$ and longitudinal size σ_3 of the beam are functions of s. This is important because the beta function varies from moderate to small values at the absorbers.

From Eq. 4.12 and the corresponding expression for the vector potential $A_s(r,z,s) = \beta\Phi(r,z,s)$ we can calculate the electric field components $E_r(r,s,t)$ and $E_s(r,s,t)$. [**?**]

ICOOL contains this formulation and systematic studies have been carried out. The results are shown in Fig. 4.30, where it can be seen that the

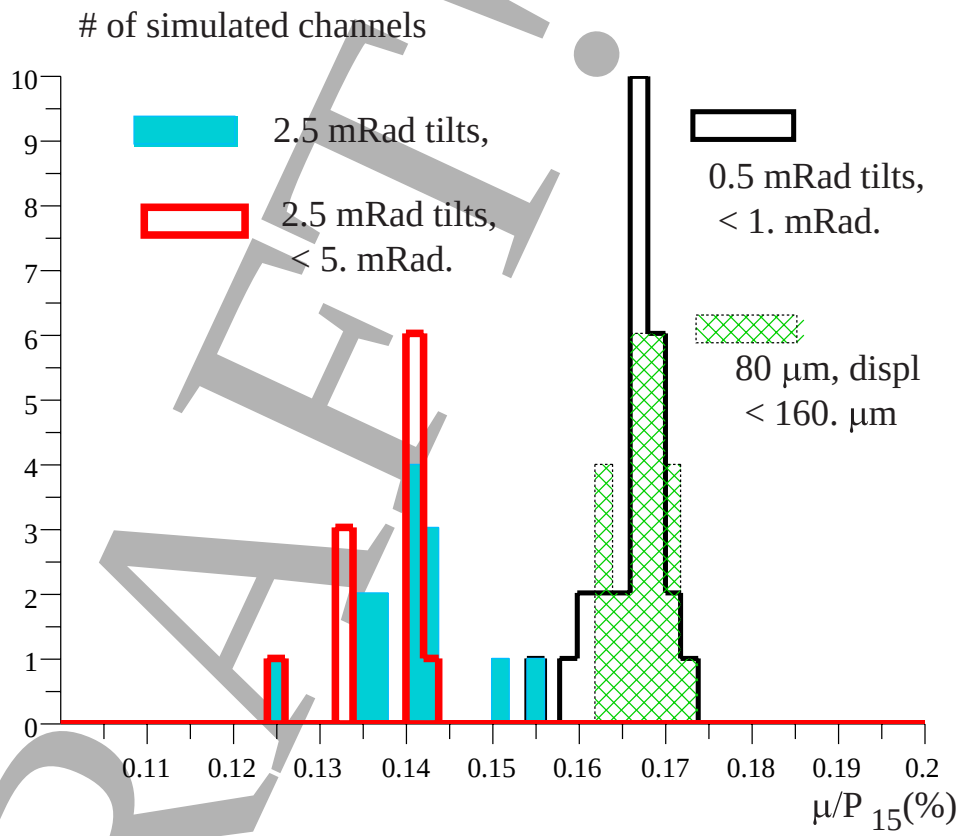

Figure 4.29: A histogram of the performance of 35 SFOFO cooling channels build with a tolerance of 0.5 mrad tilts. Note that muon decays have been turned off, which explains why the nominal performance is 20.7 %. I'll correct this by rescaling the performance in each run. (PAUL, DOES THIS STILL APPLY?)

number of muon per proton μ/p is rather insensitive to the number of muons in the bunch up to values $N_\mu \approx$ ....

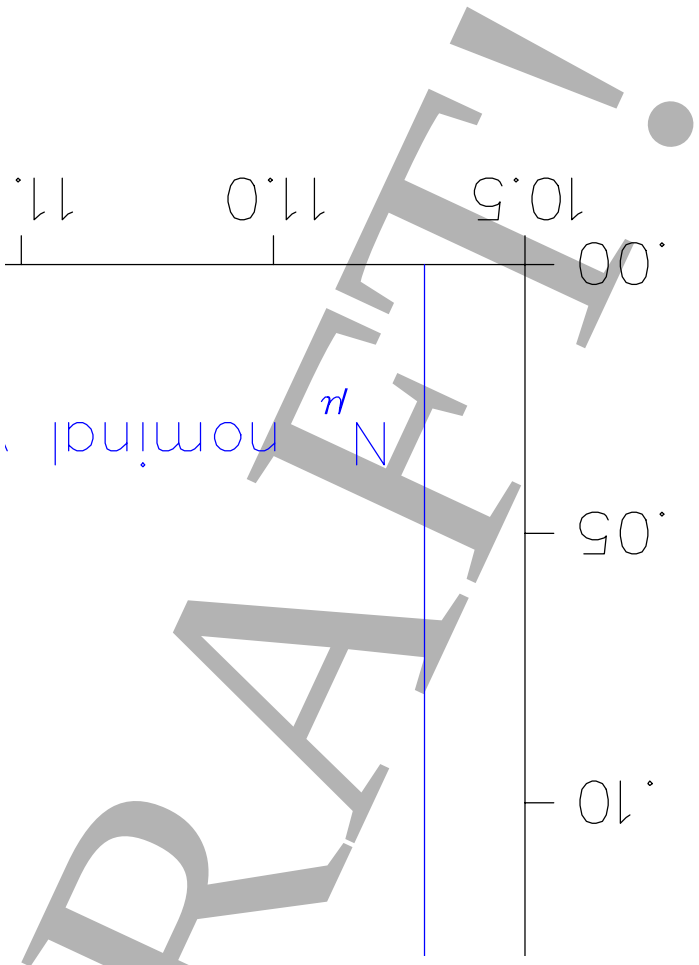

Figure 4.30: μ/p vs. N_μ in a bunch assuming a Gaussian self-field.

This approach is approximate and leaves aside potentially important phenomena: first the effects of induced charge in the walls of the beam pipe and in the metallic (Be) *rf* windows; second the short range wake potential created by the $\beta < 1$ muon beam inside of the cavities.

The effect of the walls of a cylindrical beam pipe on a bunch of charged particles has been computed with ICOOL. Results are shown in Fig. 4.31. We can see that for the nominal charge no noticeable effects are detected.

Figure 4.31: $/mu/$p vs. $N_{/mu}$ in a bunch including the wall effects

The presence of Be windows will mitigate any space charge effects. However, it is rather difficult to calculate this with precision. Recently, in Ref. [?] it has been shown that MAFIA [?] reproduces the theoretical short range wake potentials extremely well for the case of a single particle with $\beta < 1$ in a pill-box cavity. This gives us confidence that MAFIA solutions of the wave equation in the presence of boundary conditions and subluminal particles are correct. Using these fields in ICOOL or GEANT runs will allow a much better evaluation of the space charge problem. In any case, wake fields tend to decrease the effective transverse field seen by the bunch and consequently to reduce the space charge effects.

Next we give some simple arguments to validate the above assertion. The self field E_r causes the beam to expand radially and the corresponding magnetic field focuses the beam. The radial component of the Lorentz force is

$$r'' \approx \frac{qE_r}{mc^2\gamma\beta^2}(1-\beta^2) \tag{4.13}$$

A long cylinder of radius a and uniform charge density ρ_o creates a field

$$E_r^o \approx \frac{\rho_o}{2\epsilon_o} r \qquad (r < a) \tag{4.14}$$

Define $\Delta = \frac{<E_r>}{E_r^o}$ with $< E_r >= \int E_r(a,s)ds$ the average of the transverse field at r=a. We can write

$$r'' \approx \frac{qE_r^o}{mc^2\gamma\beta^2}(\Delta-\beta^2) \tag{4.15}$$

This equation shows that if $\Delta - \beta^2 << 1$ the radial electric field can be reduced by introducing charges in the system, such that their E_r opposes E_r^o and furthermore produces no magnetic field. Indeed, that is the case because of the induced charges in the surface of the metallic windows, which are created to insure that there is no electric field in the bulk of the Be window (perfect conductor approximation) [?]

Engineering *change orders*

Deviation from the design driven by engineering or cost considerations will unavoidably occur. The list below is probably far from complete. We simply mention a few items for the reader to gauge the feasibility aspects of this study:

- Coupling coil configuration. The engineering drawings in Figures 4.15 and 4.16 show coils which are shorter and thicker than those described in Table 4.4. This modification was motivated by ease of assembly and space constraints coming from the *rf* feeds. We verified that such coils perform adequately because they provide a field strength at the center of the half period length consistent with the field shown on Figure 4.6

- In the design described above, the beryllium *rf* window are "stepped", as their thickness suddenly increases at the radius $r1$ in Table (REFER TO TABLE 18.D HERE?). A practical implementation could require a smoother distribution of the mass at $r1$ (by chemical etching, for instance). We have verified that a smooth transition would not affect the performance, as expected.

- Absorber shape: The absorbers are not exactly cylindrical, as assumed in the ICOOL simulation. A hyperboloid shape has recently been implemented in Geant4, with no adverse effect to the performance.

- *rf* window shape or configuration. Grids made of aluminum tubes instead of beryllium foils have been proposed. Two concerns come to mind: (i) aluminum has a higher Z than beryllium, and particles can graze the tube surface, (ii) non-uniformity of the electric field around the grid could cause an increase of the beam emittance. We have shown that it is the effective, average radiation length seen by the beam that counts. In particular, if the grid has sufficiently small tube ($\approx$ 2 cm diameter), with large opening between the tubes ($\approx$ 5 to 10 cm), the cooling channel has the same performance as the one equipped with the beryllium foils specified above. The small transverse or longitudinal kicks caused by the grid does not significantly increase the emittance.

- If the downstream accelerator system can really take the 15 mm rad transverse acceptance with no loss, there might not be a strong incentive to cool beyond $\approx$ 100 m, as demonstrated on Fig. 4.14.

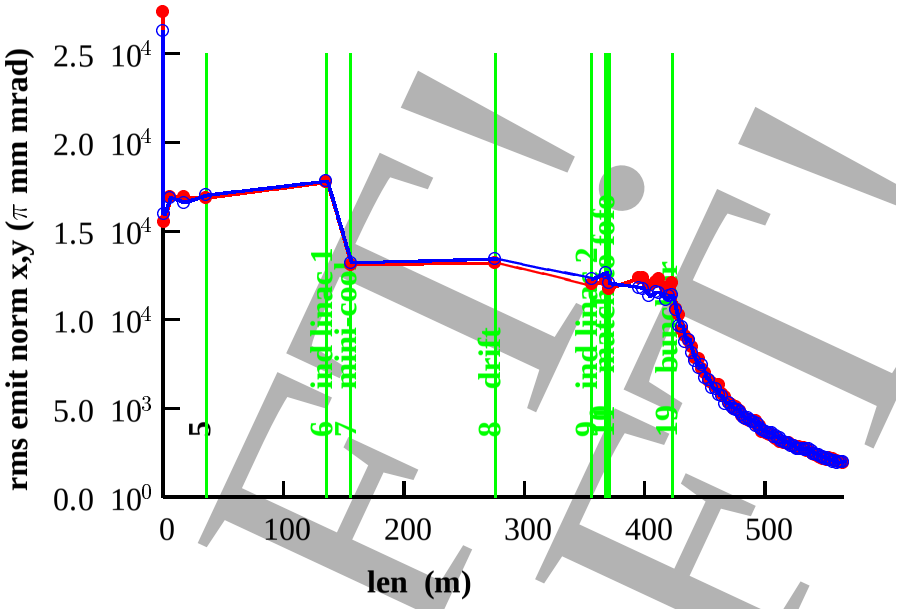

Figure 4.32: Emittance as a function of distance along the front end.

4.4.11 Conclusion: performance of the entire front-end

The transverse emittance along the entire front-end is plotted in Fig. 4.32. The emittance is seen to be reduced in the mini cooling at 150 m (from 18 to 13 mm rad), falls a little more as large amplitude particles are lost in the induction linac, and falls fast in the final cooling (from 12 to 2.2 mm rad).

The muons per proton along the full system are given in Fig. 4.33. The particle losses prior to the buncher come primarily from the loss of very high and very low momenta (about 30 %), plus (approx 20 %) loss from muon decay . The losses in the cooling come ≈25% from bunching inefficiency and ≈25% from loss of particles from the *rf* bucket as the longitudinal emittance grows in the cooling.

Fig. 4.34 shows the distributions of initial pion energies for (upper curve) all pions exiting the target and (lower curve) those pions that decayed to muons and exited the cooling. The second figure gives the ratios of these two

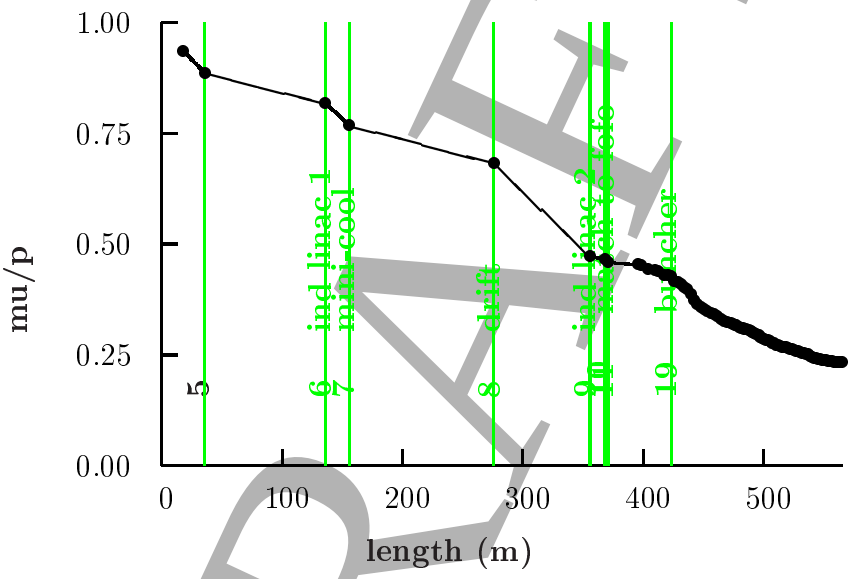

Figure 4.33: Muons per incident proton as a function of distance along the front end.

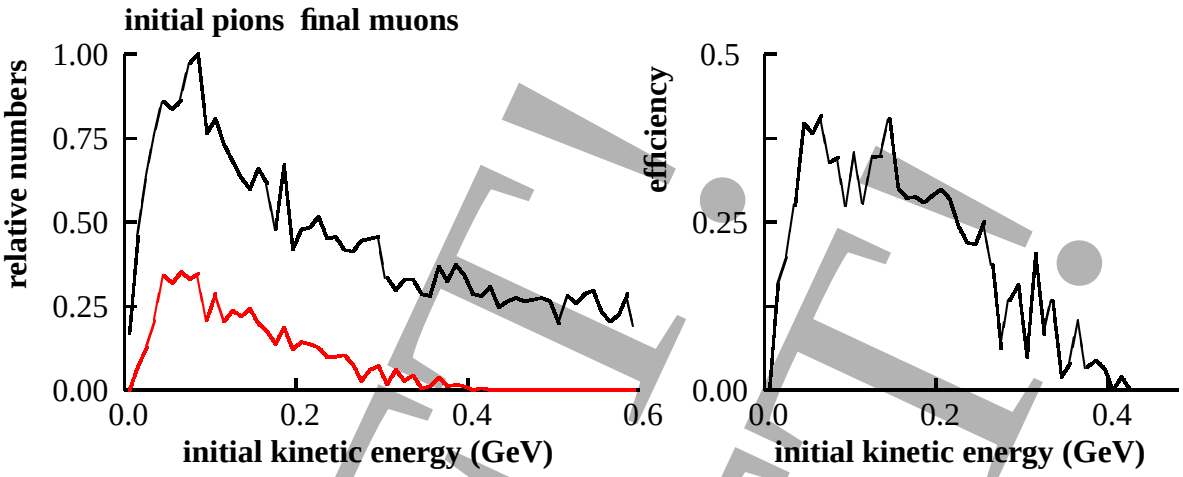

Figure 4.34: Initial kinetic energy of produced pions and muons exiting the cooling section.

and indicates that at the peak about 35 % of the pions yield muons at the end. Note the falling efficiency for higher energy pions.

The SFOFO cooling channel increases the number of muons per proton in the 15 mm rad transverse aperture by a factor 3.5, or a factor 5.75 in the 9.75 mm rad aperture (Geant4 estimate, ICOOL numbers listed above are a bit lower, consistent with systematic errors in the calculations). The corresponding number for the FOFO channel used in Feasibility Study I was approximately 2 to 2.5 [**?**]. Engineering and mechanical tolerances have been studied. We now know that such a channel can be assembled and aligned with known techniques. Finally, no new R& D programs beyond those defined a year ago[**?**] are required.

Bibliography

[1] "A Neutrino Source Based on an Intense Muon Storage Ring", ed. N. Holtkamp and D. Finley, submitted to Phys Rev. ST Accel. Beams (2000), available at http://www.fnal.gov/projects/muon_collider/nu-factory/nu-factory.html

[2] C.M. Ankenbrandt *et al* Phys. Rev. ST Accel. Beams 2, 081001 (1999)

[3] G. Penn *et al* Phys. Rev. Lett. 85 (4) pp. 764-767. July, 2000.

[4] J. Monroe *et al Design and Simulation of Muon Ionization Cooling Channels for the Fermilab Neutrino Factory Feasibility Study*, submitted to Phys. Rev. ST Accel. Beams.

[5] R. Fernow *et al*, "ICOOL, A Simulation Code for Ionization Cooling of Muons Beams", Proceedings of the 1999 Particle Accelerator Conference, A. Lucio and W. MacKay, eds. (IEEE, Piscataway, NJ, 1999) p. 3020.

[6] The Geant4 Tool Kit is available at *http://wwwinfo.cern.ch/asd/geant4/geant4.html*

[7] This code was written by G. Penn, LBNL.

[8] The Particle Data Group, *Review of Particle Physics*, EPJ C **15** p. 163 (2000)

[9] B. Palmer, *Neutrino Factory Draft Parameters* http://www-mucool.fnal.gov/mcnotes/muc0046.ps

[10] Jocelyn Monroe, Paul Lebrun, Panagiotis Spentzouris, *DPGeant and Icool Code Comparison* http://www-mucool.fnal.gov/mcnotes/muc0072.ps

[11] R. Fernow, *Effect of a dipole error on the performance of the alternating solenoid lattice*
http://www-mucool.fnal.gov/mcnotes/muc0035.pdf

[12] Paul Lebrun, *Sensitivity of the 15 T. Alternate Solenoid Cooling Channel to Dipole Errors caused by misalignment of the Solenoids*
http://www-mucool.fnal.gov/mcnotes/muc0073.ps

[13] Juan C. Gallardo, *Errors in a continuous solenoid* ,
http://www-mucool.fnal.gov/mcnotes/muc0041.ps; *Errors in a discrete solenoid*
http://www-mucool.fnal.gov/mcnotes/muc0037.ps

[14] Juan C. Gallardo, *Note on Vector potential for a Solenoid and Errors*, unpublished.

[15] First suggested by A. Sessler, LBNL.

[16] Semertzdis and Morse, Unpublished Note BNL 2000

[17] [Kwang-Je Kim and Chun-xi Wang, PRL 85 (760) 2000]:

[18] J. W. Mark, SLAC-PUB-3169 (1984) and references therein.

[19] E. J. Beise *et al.*, Nucl. Instrum. Meth. **A378** (1996) 383.

[20] R. W. Carr *et al.*, SLAC-Proposal-E-158, July 1997.

[21] R. W. Carr *et al.*, *E158 Liquid Hydrogen Target Milestone Report,* April 21, 1999, http://www.slac.stanford.edu/exp/e158/documents/target.ps.gz.

[22] D. J. Margaziotis, in *Proc. CEBAF Summer 1992 Workshop*, F. Gross and R. Holt, eds., AIP Conf. Proc. **269**, American Institute of Physics, New York (1993), p. 531.

[23] *ASME Boiler and Pressure Vessel Code,* ANSI/ASME BPV-VIII-1 (American Society of Mechanical Engineers, New York, 1980), part UG-32.

[24] A. Blondel is working to develop a system based on a ring imaging Cerenkov technique.

[25] M. Placidi *et al.*, *A CdTe Detector for Muon Transverse Profile Measurements*, CERN-NUFACT-Note 068, Contributed to the MuCool Instrumentation Workshop, IIT, Chicago, Nov,10-11, 2000.

[26] X-RAY STUDIES REFERENCE HERE

[27] SPACE CHARGE REFERENCE HERE

[28] SPACE CHARGE REFERENCE HERE

[29] SPACE CHARGE REFERENCE HERE

[30] SPACE CHARGE REFERENCE HERE

[31] SPACE CHARGE REFERENCE HERE

Chapter 5

Acceleration: Recirculating Linear Accelerator

V. Lebedev

5.1 Introduction

Acceleration of a muon beam is a challenging task because of the large source phase space and the short muon lifetime. In the design concept presented here, acceleration starts after ionization cooling at a momentum of 210 MeV/c and proceeds to 20 GeV/c where the beam is injected into a storage ring. The basic parameters for the system are given in Table 5.1. The key technical issues, beyond these basic parameters, are

- Choice of acceleration technology: superconducting versus normal conducting cavities, and related to that the choice of RF frequency
- Choice of acceleration scheme
- Capture, acceleration, transport, and preservation of the large source phase space and the rapidly decaying muons
- Acceleration performance issues such as potential collective effects (e.g., cumulative beam breakup) resulting from the high peak current.

To counteract muon decay, the highest possible accelerating gradient is required. That is the major driver for the proposed scheme. The acceleration system consists of a 2.83 GeV linac followed by a four-pass recirculating linear accelerator as shown in Figure 5.1.

Table 5.1: Main parameters relevant to acceleration.

Initial momentum	210 MeV/c
Initial kinetic energy	129.4 MeV
Initial normalized acceptance	15π mm
Initial longitudinal acceptance, $\Delta p L_b/m_\mu$	203π mm
Initial full momentum spread, $\Delta p/p$	± 0.275
Initial full bunch length, L_b	± 372 mm
Bunches per pulse	67
Particles per pulse	3×10^{12}
Bunch frequency	201.25 MHz
Acceleration RF frequency	201.25 MHz
Time structure of beam	6 pulses separated by 20 ms, repeating every 400 ms
Average beam power	150 kW

Very large transverse and longitudinal accelerator acceptances drive the design to low RF frequency. Were normal-conducting cavities used, the required high gradients of the order of 15 MV/m would demand unachievably high peak power of RF sources. Superconducting RF (SRF) cavities are a much more attractive solution. RF power can then be delivered to the cavities over and extended time, and thus RF source peak power can be reduced. Another important advantage of SRF cavities is that their design is not limited by a requirement of low shunt impedance and therefore their aperture can be significantly larger. Taking into account the required longitudinal and transverse acceptances and that the beam is already bunched at 201.25 MHz at the source (ionization cooling) the 201.25 MHz RF-frequency has been chosen for both the linear accelerator and the recirculator. This choice also provides adequate stored energy to accelerate multiple passes of a single-pulse bunch train without need to refill the extracted energy between turns.

Muon survival demands either a high-gradient conventional or recirculating linac. While recirculation provides significant cost savings over a single linac, it cannot be utilized at low energy for two reasons. First, at low energy the beam is not sufficiently relativistic and will therefore cause a phase slip for beams in higher passes, thus significantly reducing acceleration efficiency for subsequent passes. Secondly, there are major difficulties associated with injection of a beam with the large emittance and energy spread associated with a muon source. Beam pre-acceleration in a linear accelerator to about 2.3 GeV makes the beam sufficiently relativistic and adiabatically decreases the phase space volume so that further acceleration in recirculating linacs is possible.

Cost considerations favor multiple passes per stage, but practical experience commissioning and operating recirculating linacs dictates prudence.

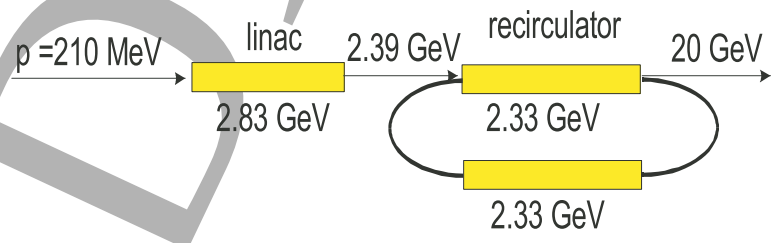

Figure 5.1: Layout of the acceleration systems.

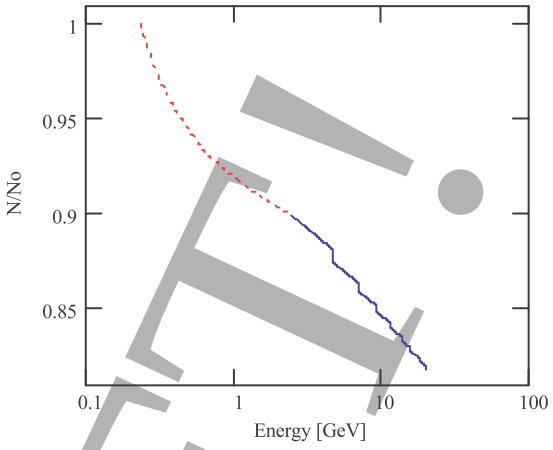

Figure 5.2: Decay of muons in the course of acceleration. The dotted line is the decay in the linac, the solid line in the RLA. Vertical drops correspond to the beam transport in the RLA arcs.

Experience at Jefferson Lab suggests that for given large initial emittance and energy spread, a ratio of final-to-injected energy below 10-to-1 is prudent and the number of passes should be limited to about five. We therefore propose a machine architecture (see Figure 5.1) featuring a 0.13 to 2.39 GeV straight "preaccelerator" linac, and 2.39 to 20 GeV four pass recirculating linac (RLA). Figure 2 shows loss of muons in the course of acceleration. One can see that although RLA gives significant contribution, the major fraction comes from the linac. One can also see that arcs (vertical drops in Figure 2) do not contribute much in the decay, which justifies the choice of normal conducting bends, and triplet focusing discussed below.

5.2 Linear Preaccelerator

5.2.1 Linac general parameters and lattice period layout

Initial large acceptance of the accelerator requires large aperture and tight focusing at its front-end. Because of the large aperture, tight space, moderate energy, and necessity of strong focusing in both planes, solenoidal focusing is

Table 5.2: Main parameters of the linear preaccelerator

	Initial	Final
Momentum	210 MeV	2453 MeV
Kinetic energy	129.4 MeV	2350 MeV
Acceptance	7.5π mm	0.674π mm
Momentum spread	± 0.275	± 0.1
Total bunch length	745 mm/180°	220 mm/41°
Total linac length	450 m	
Total installed accelerating voltage	2.83 GV	

Table 5.3: Parameters of the long and short periods of the linear preaccelerator

	Short	Long
Number of periods	26	23
Period length	6 m	12.5 m
Cavities per period	1	4
Cells per cavity	4	2
Couplers per cavity	2	2
Gradient in cavity	10 MV/m	15 MV/m
Cavity aperture (diameter)	460 mm	300 mm
Spacing between cavities within one period	N/A	1 m
Spacing between cavities in different periods	3 m	3 m
Aperture in solenoids (diameter)	460 mm	360 mm
Solenoid length	1 m	1.5 m
Solenoid maximum field	1.8 T	4.2 T

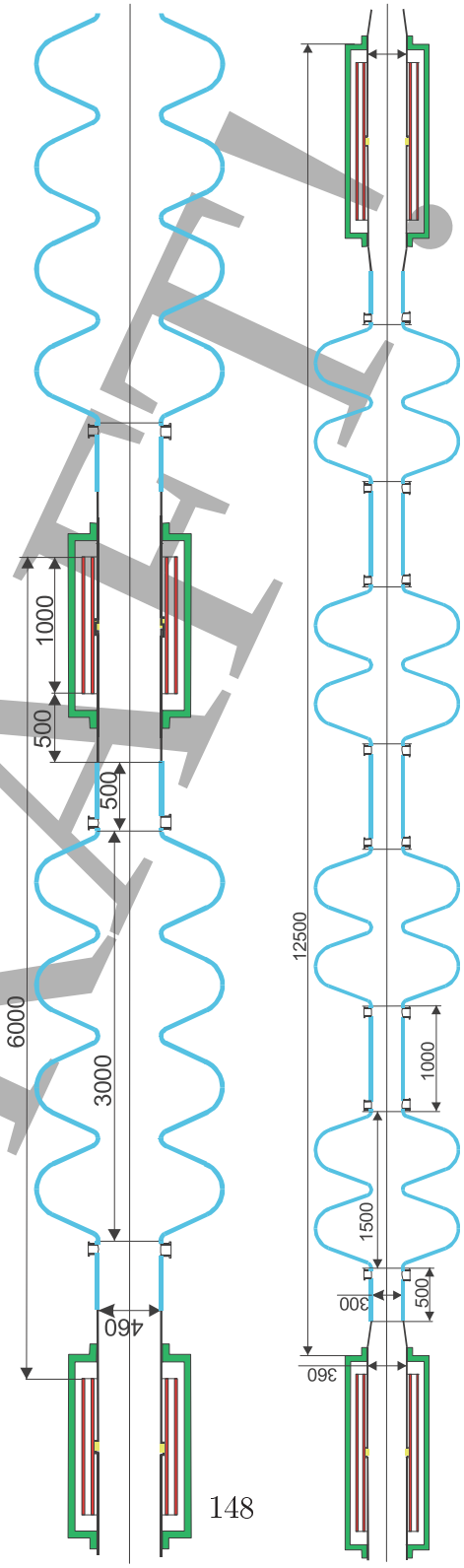

Figure 5.3: Short (left) and long (right) cryomodule layouts. Blue lines are the SC walls of cavities, solenoid coils are red, and BPMs are yellow.

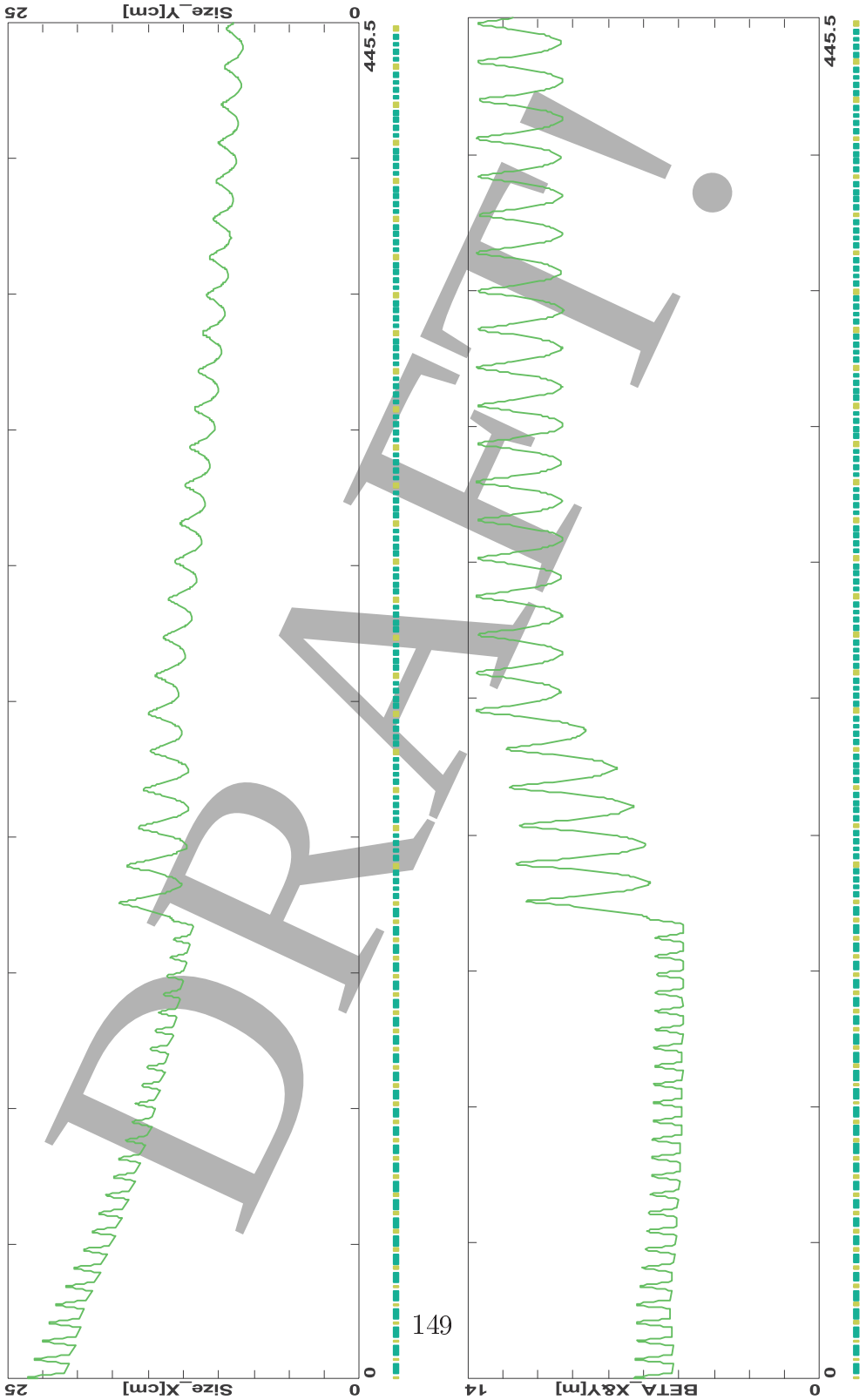

Figure 5.4: Beam envelope (left, 2.5σ) and beta function (right) along the linear accelerator. The beta functions are computed in the reference frame rotating with angular frequency $eB_s/2pc$.

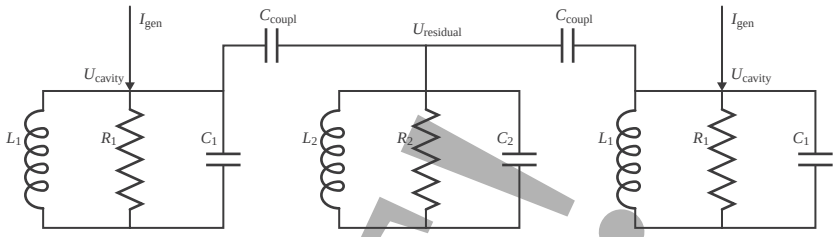

Figure 5.5: Electrical circuit model for computation of cavity coupling

superior to the triplet focusing and has been chosen for the entire linac. To achieve manageable beam size the first third of the linac uses short focusing cells and, consequently, short cryomodules. In comparison with the standard 10 m cryomodules in the rest of the system, these cryomodules have increased aperture and, consequently, reduced accelerating gradient. Since the beam size is adiabatically damped with acceleration, long cryomodules are used for the rest of the linac. The main parameters of the linac and its periods are presented in Tables 5.2 and 5.3. Figures 5.3 and 5.4 depict the layouts of short and long cryomodules, beam envelope and beta-function along the linac.

5.2.2 Cavity Layout Considerations

The layout of cryomodules and the arrangement of SC cavities are determined by the requirement to have cavities sufficiently decoupled and to keep power of the fundamental coupler at acceptable level (below 1 MW). The coupling coefficient $\delta = C_2/C_1$ (see Figure 5.5) should be at most $1/(10Q)$ to have a possibility to bypass malfunctioning cavities. Figure 8 demonstrates effects of cavity coupling and detuning on the cavity voltage. Thus for loaded Q of 5×10^5 the required cavity decoupling should be below 2×10^{-6}.

A two-cell cavity with power couplers at both ends is optimal from the power coupler point of view. But in the case of short cryomodules the required aperture is so large that the length of vacuum chamber between adjacent cavities should be more than about 1.7 m to decouple cavities (see Figure 5.7). That causes a significant reduction of the real estate gradient. In this case a four-cell cavity with gradient reduced due to power coupler limitations is a better choice. In the case of long cryomodules the aperture is already sufficiently small so that the distance of about 0.75 m is sufficient to decouple cavities. Here we additionally took into account that for zero length

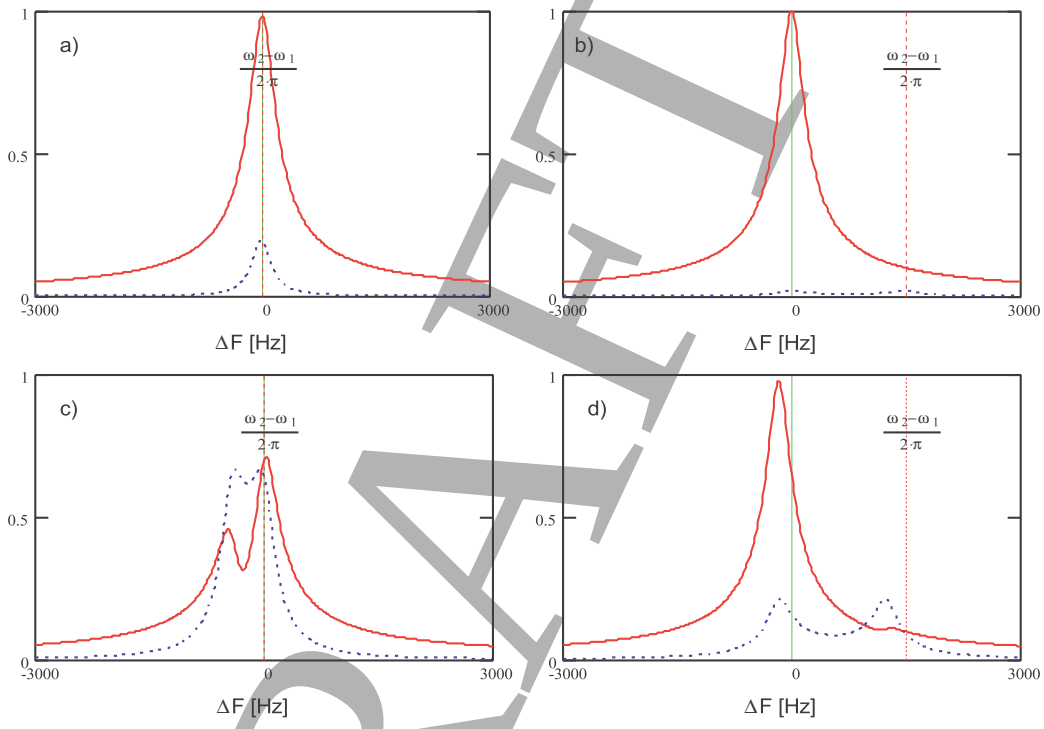

Figure 5.6: Dependence of cavity voltage on frequency. Solid lines: voltage for normally powered cavity; dashed lines: voltage for malfunctioning cavity with corresponding power generator off. For a) and c), the cavity is not detuned; for b) and d), the cavity is detuned by five bandwidths. For a) and b), $\delta = 0.1/Q$, for c) and d), $\delta = 1/Q$. $Q = 5 \times 10^5$.

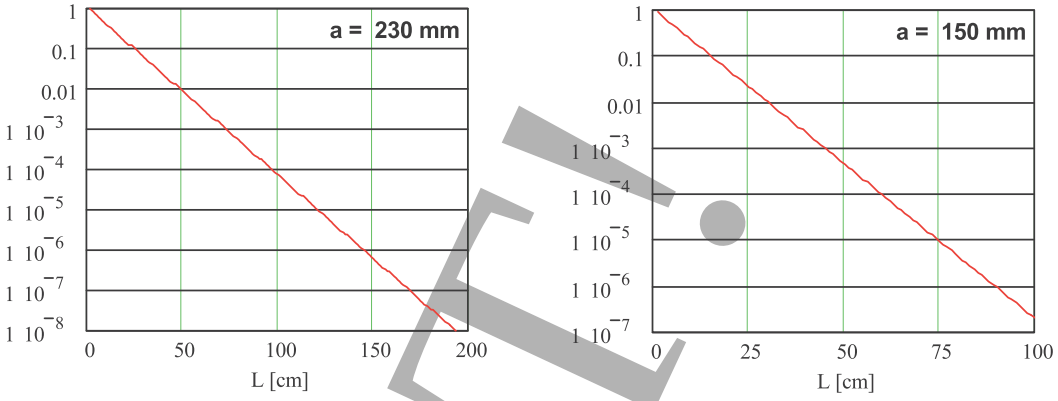

Figure 5.7: Attenuation of the electromagnetic wave between two cavities for short (left) and long (right) cryomodules. The attenuation is estimated by the formula $\delta = L\sqrt{(\mu_0/a)^2 - (2\pi/\lambda)^2}$.

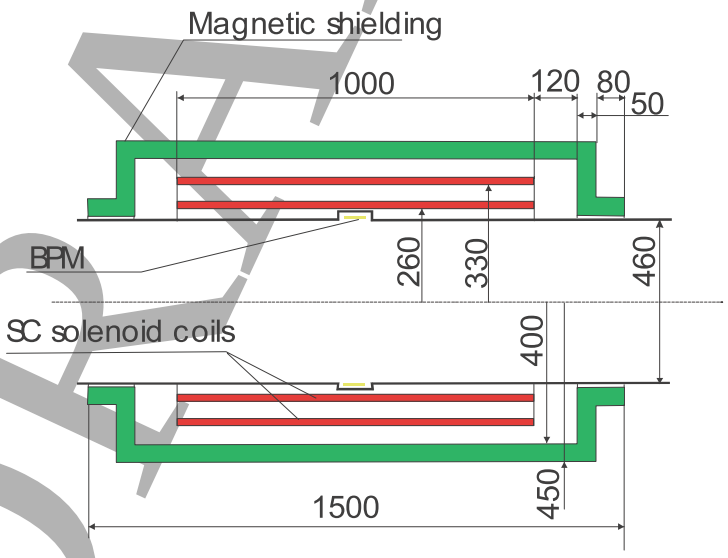

Figure 5.8: Layout of the short solenoid.

coupling depends on aperture and usually does not exceed a few percent.

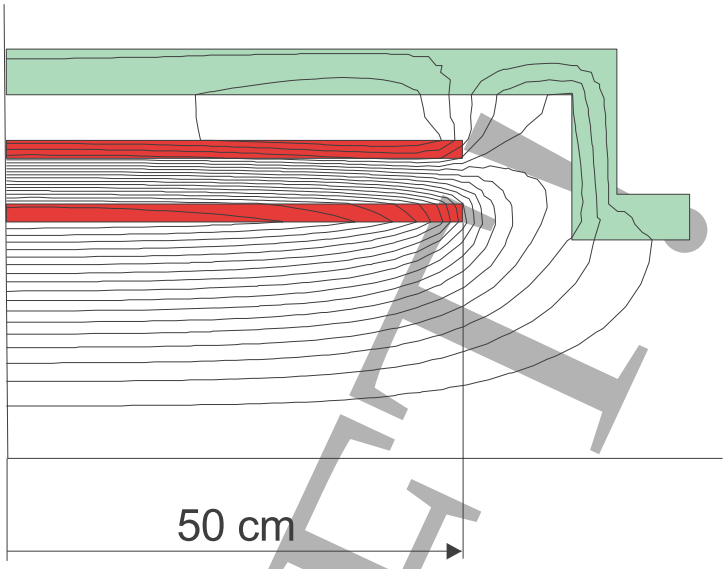

Figure 5.9: Magnetic field lines for the short solenoid.

5.2.3 Solenoid Design

The beam focusing is performed by solenoids. Considering the large aperture required by the beam size, the question of focusing linearity has to be addressed. The dependence of solenoid focusing strength on radius can be approximated by the following expression:

$$\Phi \equiv \frac{1}{F} \approx \left(\frac{e}{2pc}\right)^2 \left(\int B^2 ds + \frac{r^2}{2}\int B'^2 ds\right) \approx L\left(\frac{eB_0}{2pc}\right)^2 \left(1 + \frac{r^2}{3aL}\right), \quad (5.1)$$

where L and a are the solenoid length and radius respectively. As one sees from this equation, to reduce the nonlinearity one needs to increase the solenoid length and aperture. Increasing length directly decreases the real estate gradient, while increasing aperture requires larger distance between the solenoid and cavity to shield magnetic field which as a result also decreases real-estate gradient. Furthermore, aperture increase makes solenoids more expensive and less reliable. The layout of the short solenoid and plots of magnetic lines are shown in Figures 5.8 and ??.

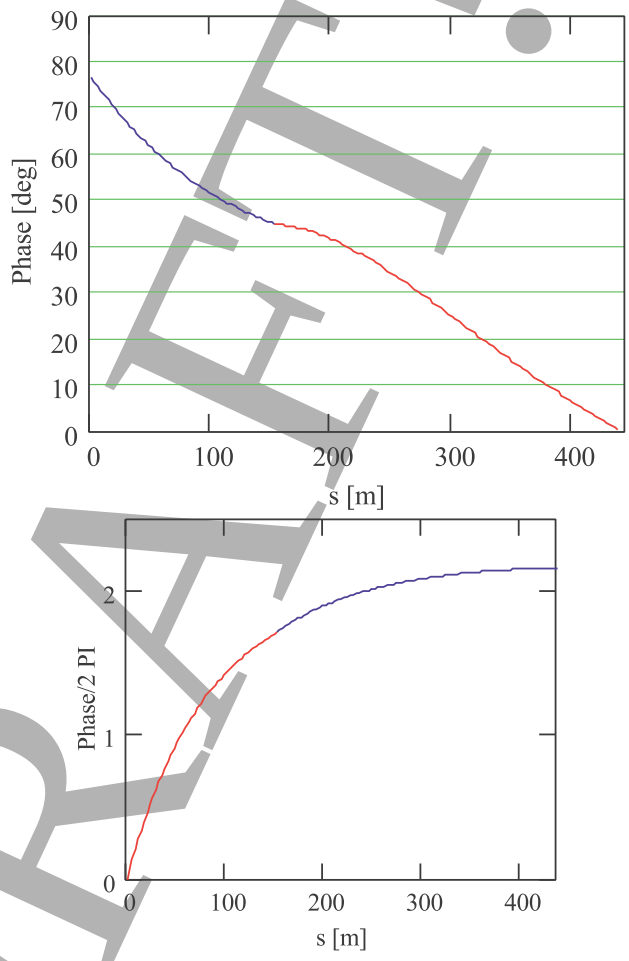

Figure 5.10: RF phase (left) and accumulated synchrotron oscillations (right) in the preaccelerator linac, as a function of the distance down the linac.

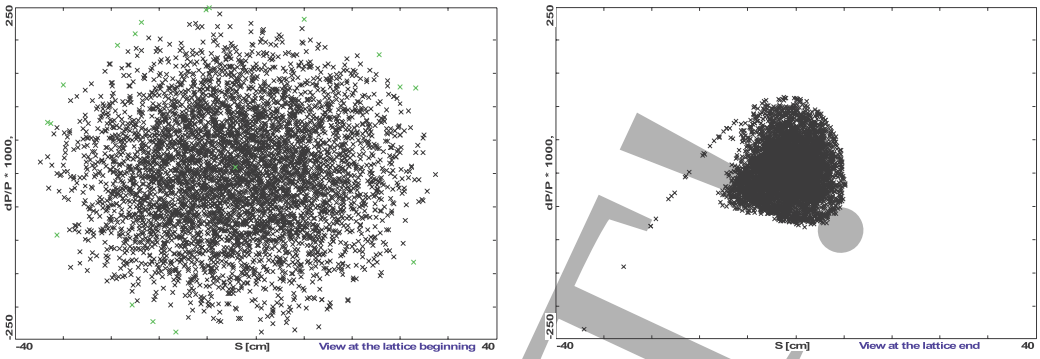

Figure 5.11: Beam distribution at entrance to preaccelerator linac (left) and at end (right). Particles marked in green in the initial distribution are lost.

5.2.4 Longitudinal Beam Dynamics

To maximize the longitudinal acceptance of the preaccelerator linac, the RF phase is initially chosen to be 75° off crest. This of course leads to a very low effective RF gradients. However, as one accelerates, the bunch will be adiabatically compressed in time, allowing the RF phase to be brought closer to crest while still not letting the bunch fall out of the RF bucket. As the bunch is accelerated, the synchrotron oscillations slow, and this adiabatic compression slows. Thus, at higher energies, due to the negligible synchrotron oscillations, there really is no "bucket," and the bunch can be accelerated on the crest of the RF. Figure 5.10 shows the RF phase and accumulated synchrotron oscillations as a function of the distance down the linac. Figure 5.11 shows the evolution of the initial distribution at the beginning of the linac to its compressed form at the end of the linac.

5.2.5 Transverse Dynamics

There is significant focusing nonlinearity, about 7% over the solenoid aperture according to 5.1, in this system. This causes fourth and sixth order resonances to become important. The large energy spread in the beam also leads to a large tune spread, which cannot be corrected in a straight beamline. The combination of these elements leads to beam loss at relatively low tunes, as shown in Figure 5.12. One would like the maximum possible tune to minimize the linear beta function as shown in Figure 5.13. Considering these two circumstances, it seems best to set the tune at about 0.175.

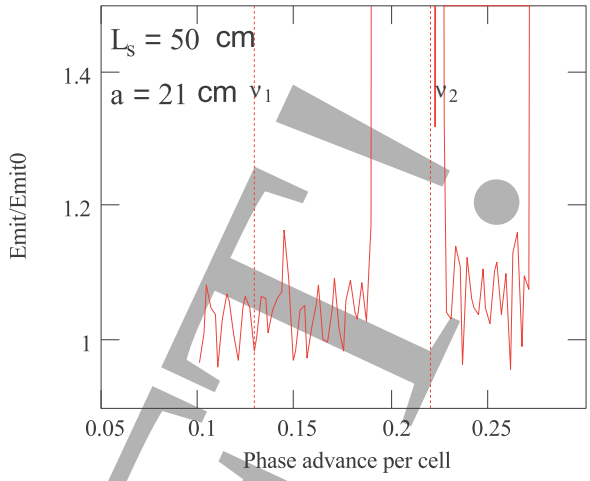

Figure 5.12: Emittance growth for 50 solenoid lenses for an initial normalized emittance of 15 mm.

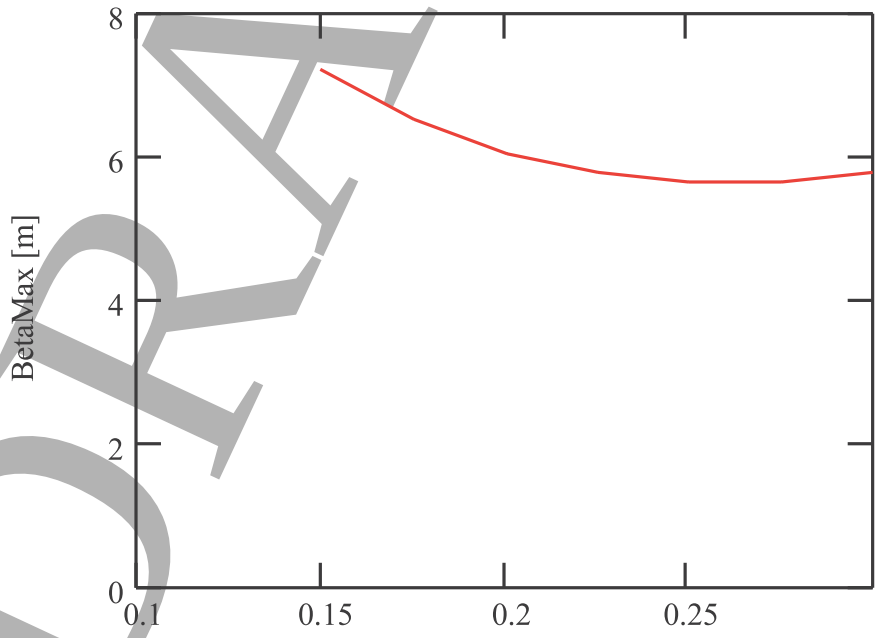

Figure 5.13: Maximum beta function for solenoid lattice as a function of tune.

Table 5.4: Parameters for the RLA.

Initial Energy	2.3918 GeV
Final Energy	20 GeV
Number of passes	4
Total initial energy acceptance	$\pm 9.2\%$
Total final energy acceptance	$\pm 1.9\%$
Initial transverse acceptance	635π mm-mrad
Initial transverse acceptance (x/y)	$157/108\pi$ mm-mrad
Total voltage per linac	2.3347 GV
Circumference	≈ 1300 m

Table 5.5: Longitudinal parameters in the RLA. $\Delta p/p$ is the full energy spread, $A_{x,y}$ are the horizontal and vertical acceptances.

	KE GeV	Phase $^\circ$	$2\Delta p/p$ %	A_x mm-mrad	A_y mm-mrad
Entrance	2.3918	0	18.4	692	660
Arc 1	4.7265	-35	11.8	390	354
Arc 2	6.6390	-23	11.6	304	264
Arc 3	8.7881	-23	9.61	252	208
Arc 4	10.937	-19	6.57	221	174
Arc 5	13.145	-15	5.86	201	151
Arc 6	15.400	-14	4.72	187	134
Arc 7	17.665	0	4.27	178	122
Exit	20.000		3.77	157	108

5.3 Recirculating Linac

5.3.1 Overall Layout

Table 5.4 shows the parameters for the RLA. A triplet focusing scheme is chosen, as opposed to a FODO scheme, since it will tend to keep the beta functions more independent of energy, and therefore minimize the mismatch in beam envelopes and consequent emittance growth.

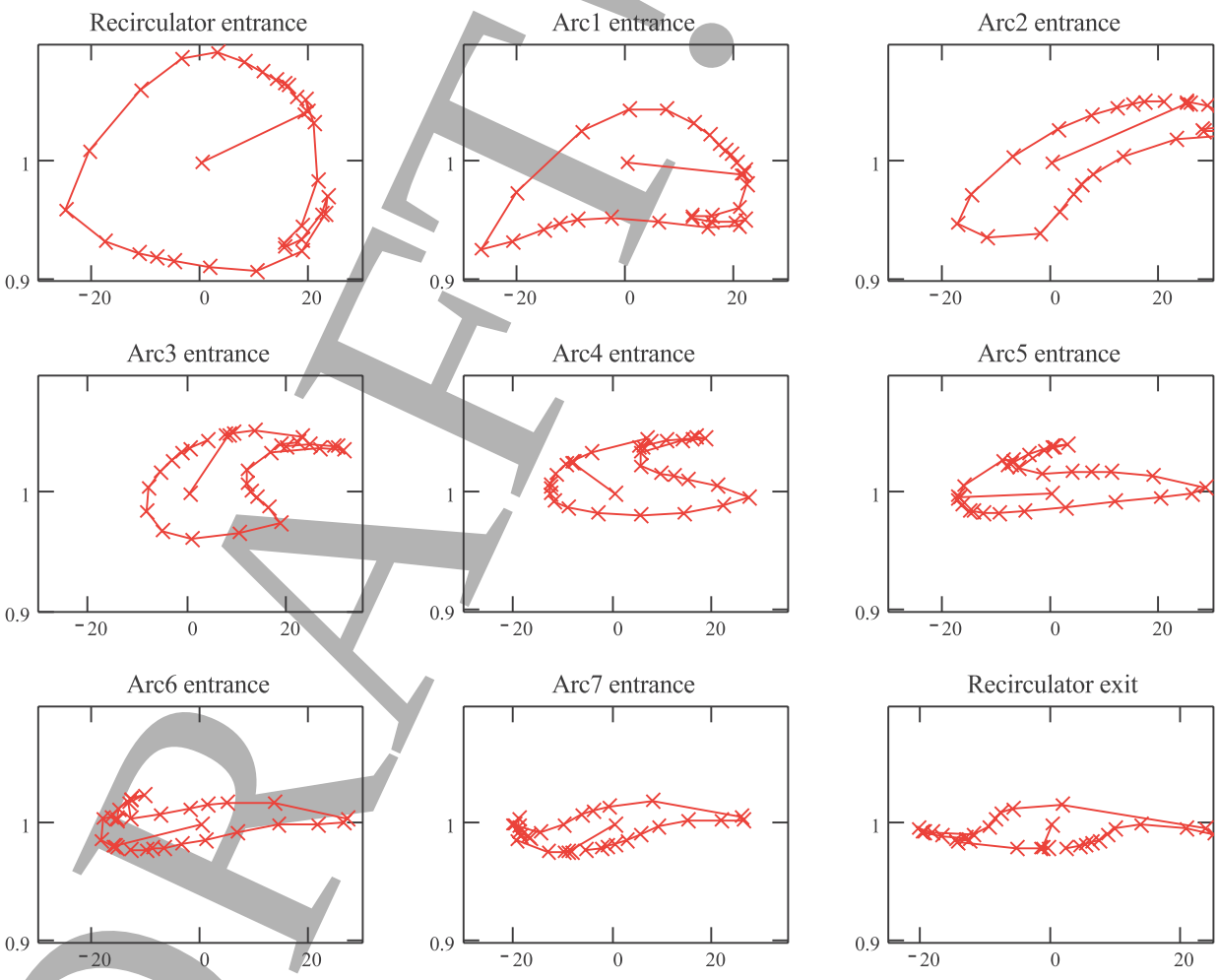

Figure 5.14: Longitudinal beam envelope in the RLA.

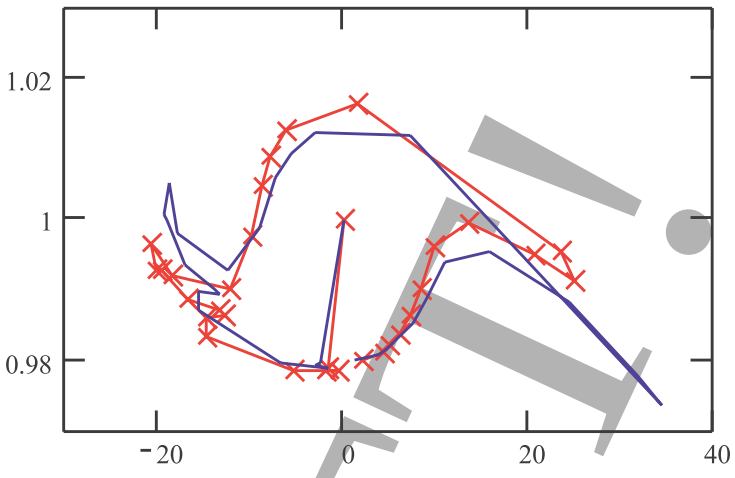

Figure 5.15: Longitudinal beam envelopes for the first (red) and last (blue) bunches in the bunch train. The total charge in the train is 3×10^{12}.

5.3.2 Longitudinal Dynamics

Table 5.5 gives the linac phases, energy spreads, and required acceptances in the RLA. Each arc has $M_{56} = 1.4$ m, and each linac has a total voltage of 2.3347 GV. The acceptances assume a horizontal emittance dilution of 9% per arc, and a vertical emittance dilution of 4% per arc. The injection chicane is also considered to add these same emittance growths. Figure 5.14 shows the evolution of the longitudinal beam envelope through the RLA.

Due to the high total current in the bunch train, the fact that the head of the train extracts energy causes the tail of the train to see a different voltage. Synchrotron oscillations partially compensate for this effect, causing the bunch to oscillate about the correct reference energy. In addition, the large stored energy in 200 MHz RF at the high gradients we are using means that the fractional energy extraction and therefore the effect on the gradient is relatively small. The result is that for our system, the effect of beam loading is relatively small. Figure 5.15 shows the longitudinal phase space envelope for the first and last bunches; it can be seen that both bunches are essentially identical when compared to the distortion caused by nonlinearity.

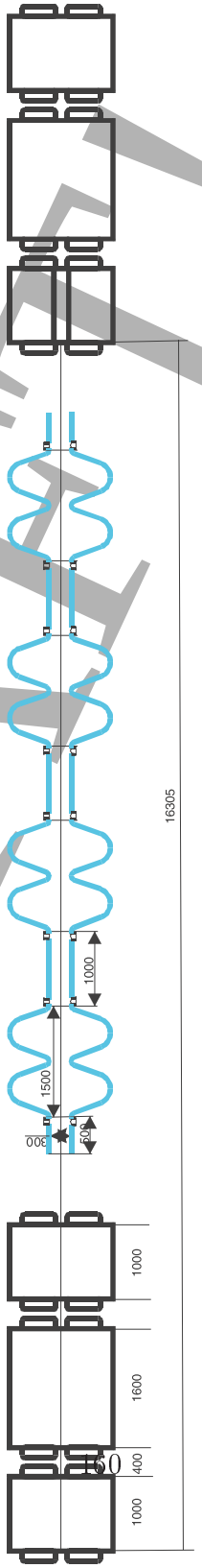

Figure 5.16: Linac cryostat.

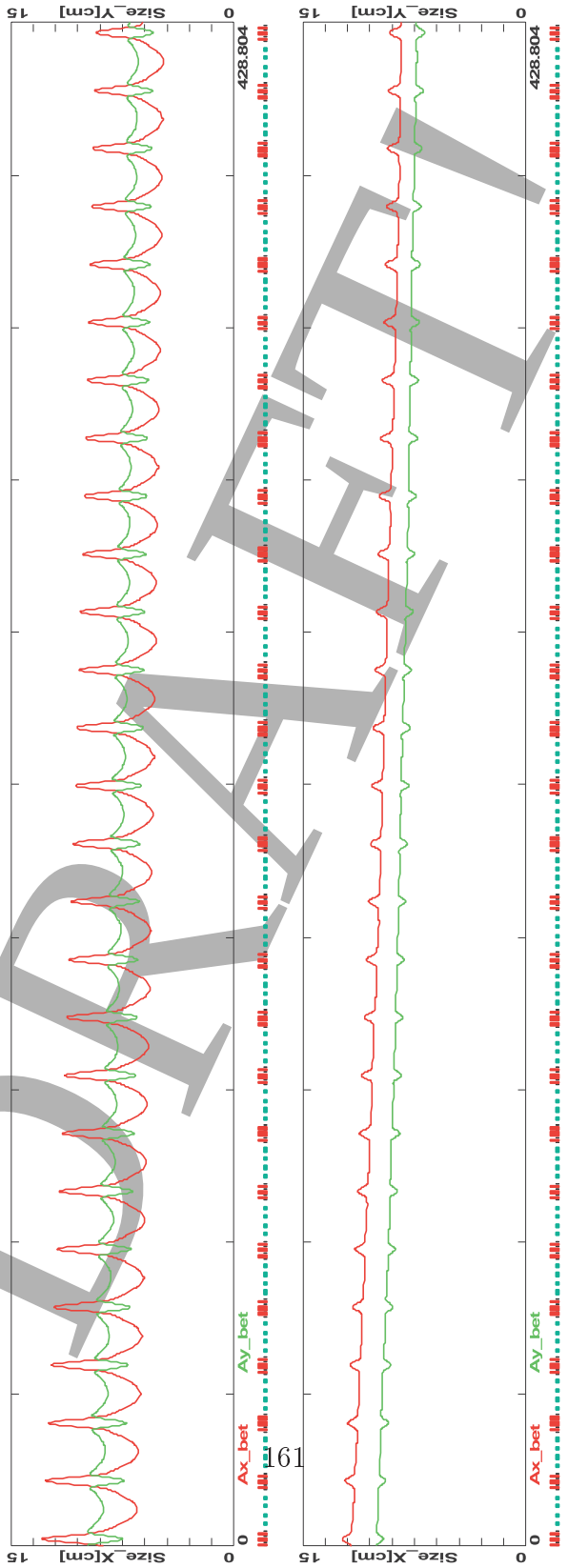

Figure 5.17: Beam size in the first pass (left) and the last pass (right) through the RLA linac.

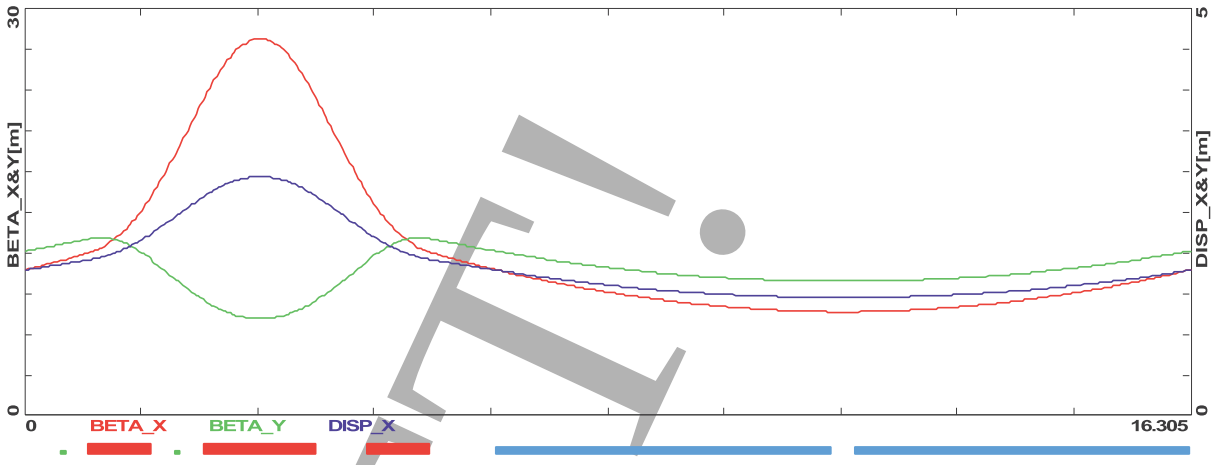

Figure 5.18: Lattice functions for an arc cell.

Table 5.6: Upper bounds on nonlinear fields of quadrupoles. Fourth order is octupole.

Order	F_n bound
4	0.018
6	0.005
10	0.03

5.3.3 Linac Cryostat Layout

Figure 5.16 shows the layout of the cryostat in the linacs of the RLA. Figure 5.17 shows the beam size in the linac on the first and last passes.

5.3.4 Arc Cell Layout

The highest energy arc uses 2T dipoles. There is not much of a point in going to higher field dipoles, since the arcs are already half the length of the linacs. There would be little to be gained in decay losses by going to higher fields. Triplet focusing with a phase advance of 90° per cell is chosen; this phase advance gives good potential for chromaticity correction.

Figure 5.18 gives the lattice functions for the arc cell. Figure 5.19 shows the lattice functions for the entire first arc, including the switchyards and a sextupole correction scheme involving three families of sextupoles. The chromatic variation of the beta functions is shown in Figure 5.20.

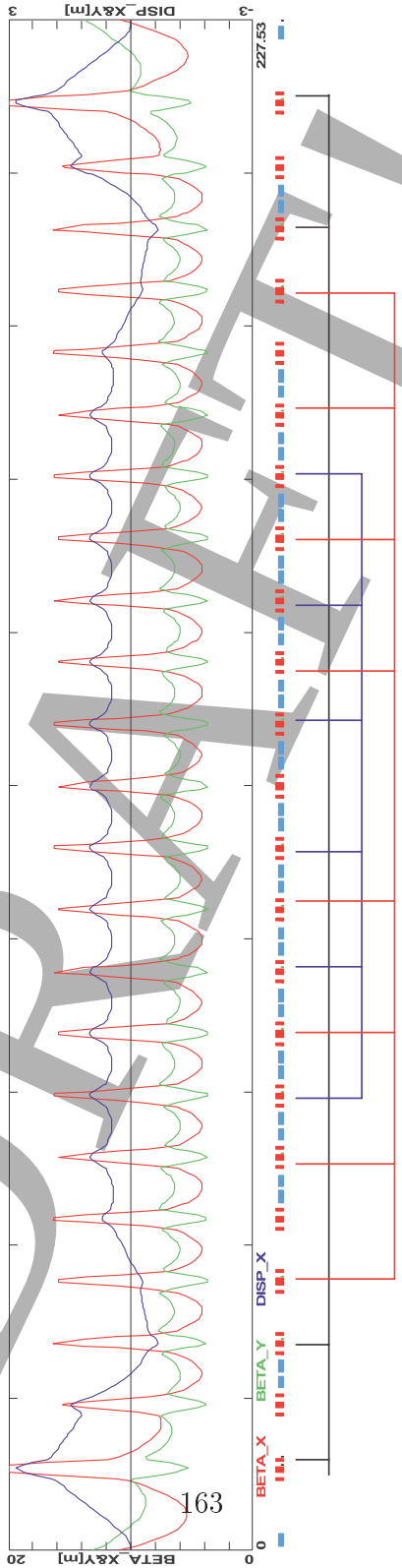

Figure 5.19: Lattice functions for the entire first arc. Sextupole correction scheme with three families of sextupoles is indicated.

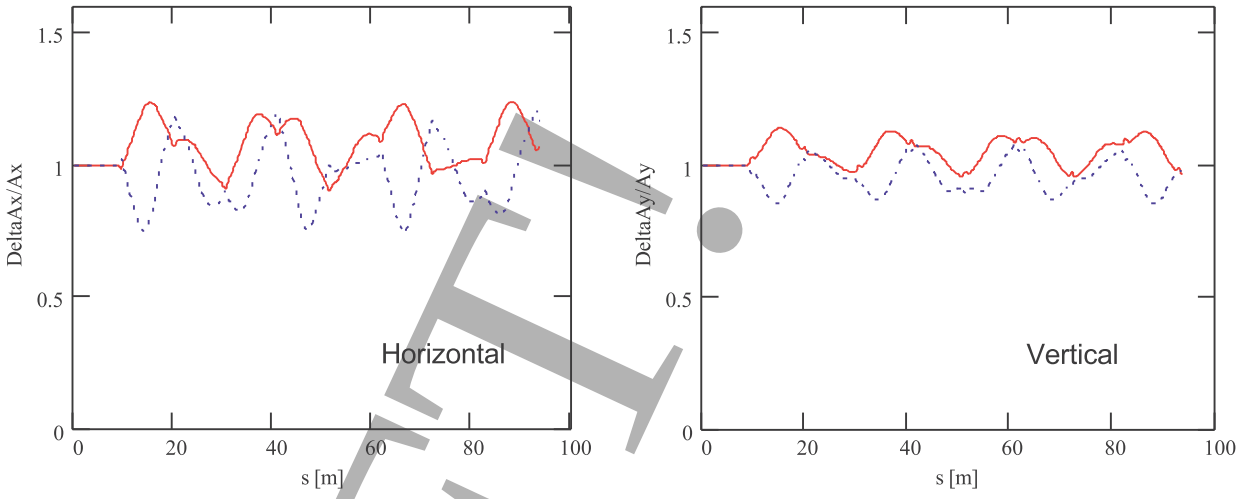

Figure 5.20: Relative variation of beta functions with energy. The two curves show the relative beta function value for ±10% relative momentum change.

The nonlinear fields in the quadrupoles must be bounded according to the values in Table 5.6, where F_n is defined to be

$$F_n = \frac{1}{Ga}\frac{a^{n-1}B_n}{n!}. \tag{5.2}$$

Figures 5.21–5.23 demonstrated the necessity of the sextupole families for correcting the dispersion and the path length. Due to the large energy spread in the beam, were it not for the sextupole correction, there would be a significant orbit offset without the chromatic correction, as well as a significant deviation in the longitudinal oscillation behavior.

5.3.5 Injection

The injection chicane is shown in Figure 5.24. Chromaticity will cause the closed orbit to fail to close over the energy spread in the beam; thus, a sextupole correction scheme is introduced. The four focusing quadrupoles have a built-in sextupole component with an integrated strength of 0.16 kG/cm each. This corresponds to a sextupole strength of 1 G/cm^2, or approximately a 5% correction in the gradient at a radius of 20 cm. The quads (and thus

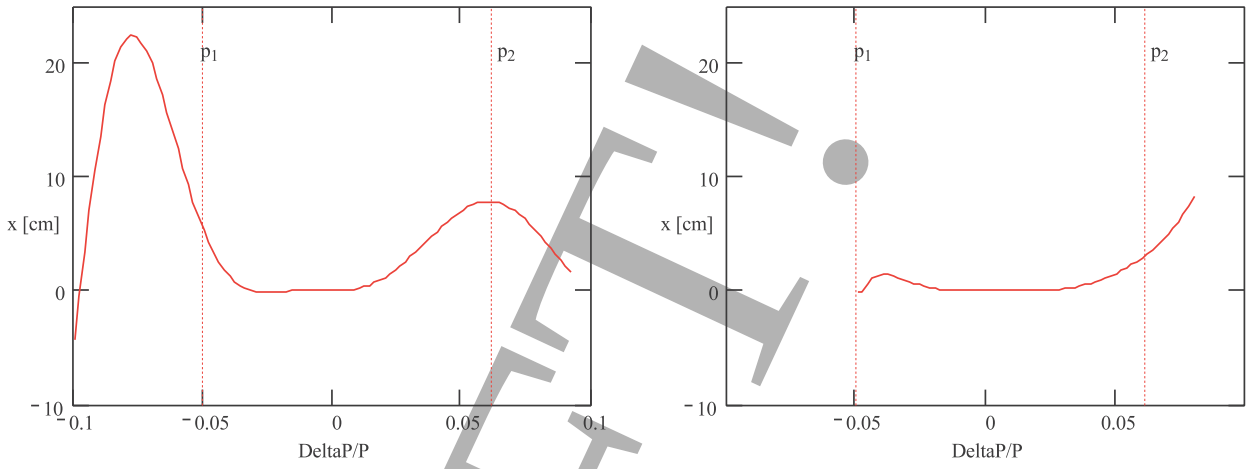

Figure 5.21: Dispersion at the arc end uncorrected (left), and corrected with sextupoles (right). Ideally, the value should be zero.

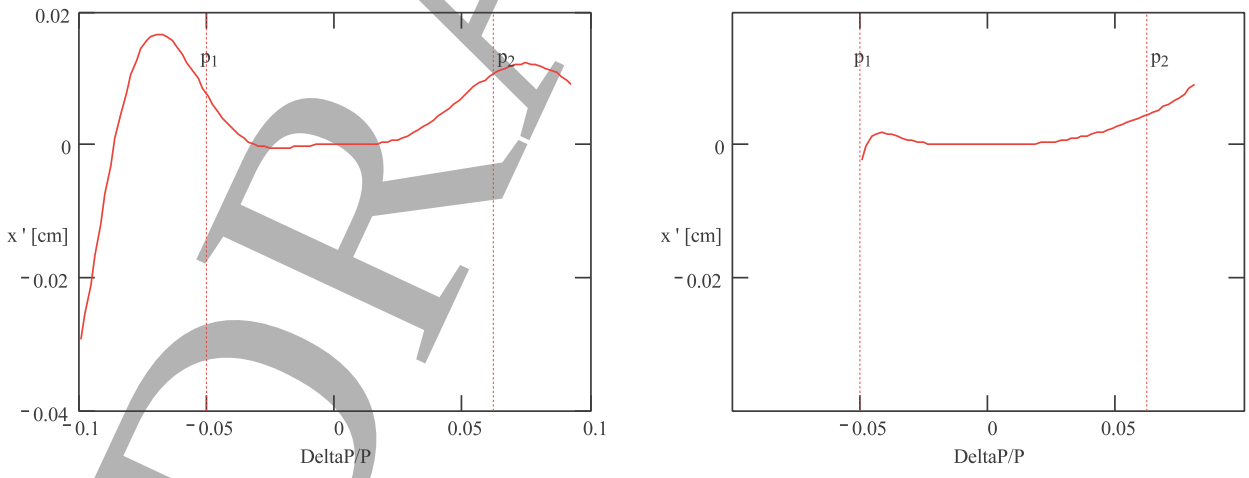

Figure 5.22: Angular dispersion at the arc end uncorrected (left), and corrected with sextupoles (right). Ideally, the value should be zero.

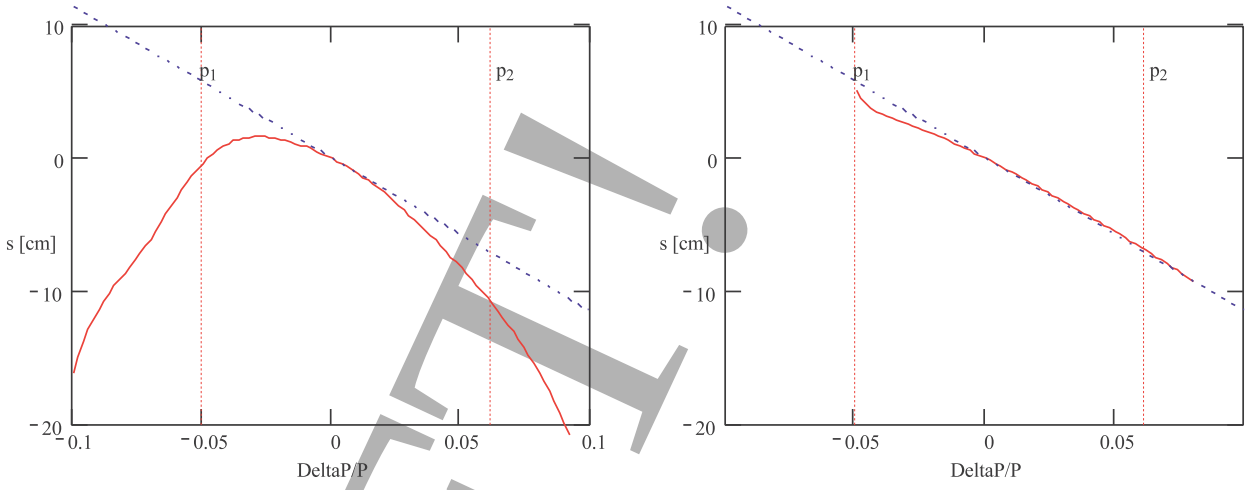

Figure 5.23: Arc path length uncorrected (left) and uncorrected (right). Ideally, the slope should be constant.

the sextupoles) are separated by $\pi/2$ in betatron phase, and so the geometric aberrations are canceled in the linear approximation. This scheme works better than 2 sextupoles shifted by π in betatron phase, which only give the cancellation for small energy spread. The sextupole gradient is chosen to minimize the total emittance growth: it does not correspond to the best possible dispersion correction. Figure 5.25 shows the result of this chromaticity compensation.

Without the chromaticity correction, there is a 28% horizontal emittance growth in the injection chicane with a 2.8% beam loss; with the correction, the horizontal emittance growth is only 15% with a beam loss of 1.4%. This comes at the cost of a vertical emittance growth of 2.5%, whereas there was none without the chromaticity correction.

5.3.6 Switchyard

Figure 5.26 shows a switchyard in the RLA.

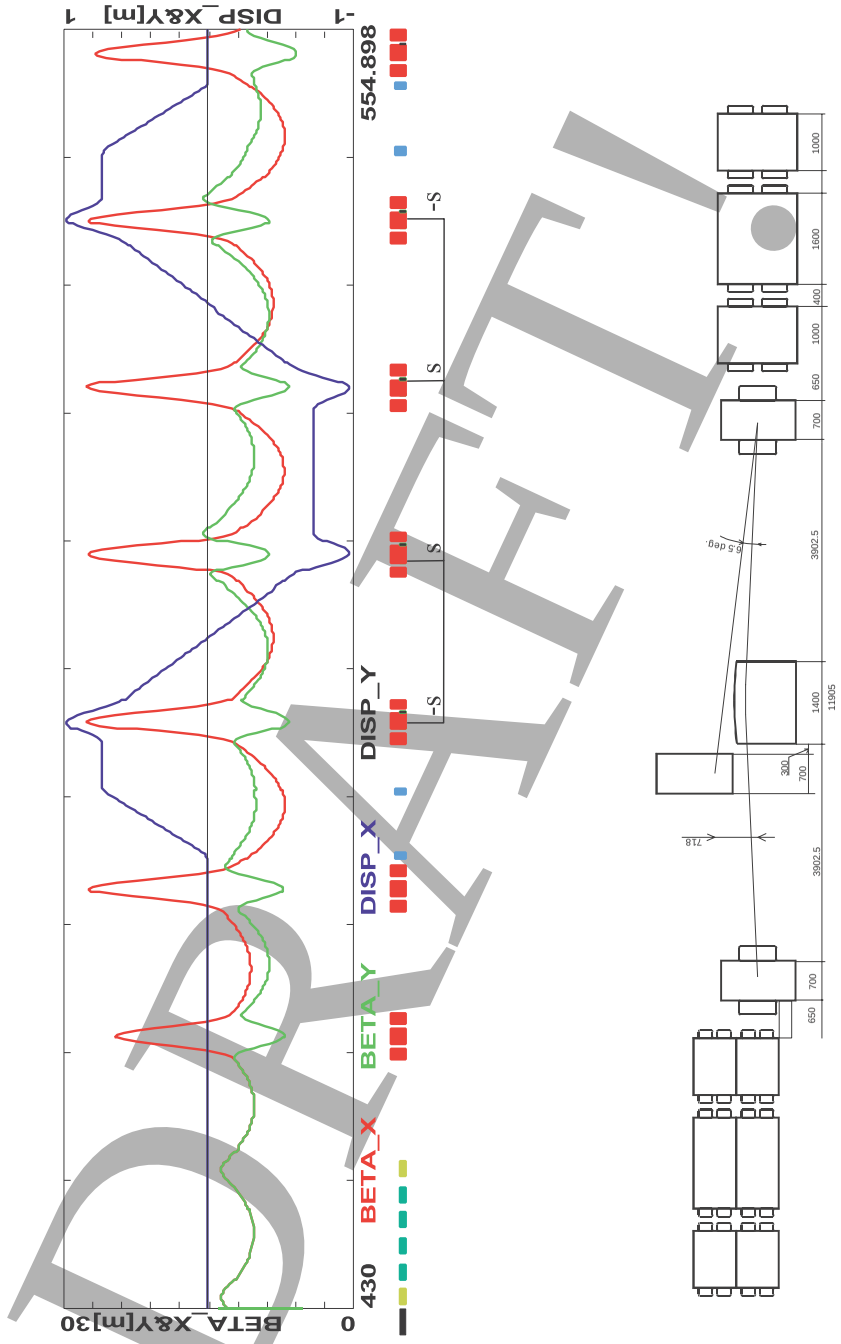

Figure 5.24: Injection chicane beta functions and dispersions, with chromaticity correction scheme indicated (left), and the layout of the last period of the injection chicane (right).

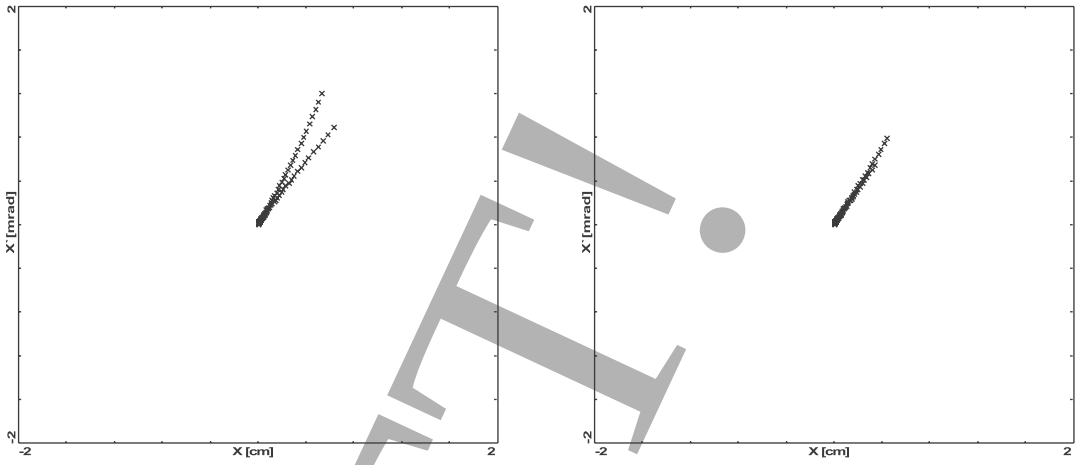

Figure 5.25: Particle displacement for uncompensated (left) and compensated (right) chromaticity.

5.3.7 Transverse Dynamics

5.3.8 Injection from Cooling

The strategy is to start with a constant phase advance per cell of $0.195 \times 2\pi$, scaling the length from one cell to the next by a factor of 1.45. This should then be optimized by varying the phase advance per cell along the line to minimize the variations in the β-function with energy at the end of the line.

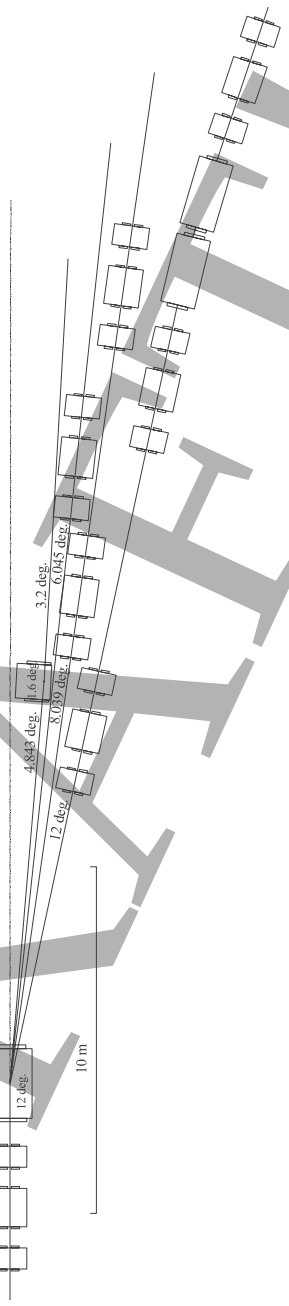

Figure 5.26: The first switchyard encountered by the beam in the RLA.

Chapter 6

Muon Storage Ring

B. Parker

This file is parkerCh16ver10.tex Except in figures colored text denotes editorial information which should be omitted from the final document.

In the Study–I report this is Section 8 but for Study–II it should be renamed Section 16. For this draft the headings from Study–I have been incorporated then modified.For comparison details please refer to Study–I.

For this first draft some of the figures were already modified to be consistent with a later optimized lattice configuration denoted mu_mf11c1 rather than the mu_mf09b lattice presented at the January 29 editors meeting. The new lattice has:

- Larger beta functions in the production straight, which which are needed to meet the experiments beam divergence goal of 0.1 normalized divergence.
- Smaller peak horizontal dispersion, which reduces the horizontal aperture requirements for $\pm 2.2\%$ in the dispersion suppressor enough to be able to use a conventional normal conducting quadrupole in the empty cell.

On advice from Scott Berg I will drop back to the mu_mf09b baseline lattice and only look to accept $\pm 1.9\%$ momentum spread, which is another way to keep the empty cell aperture requirement small. However this does not address the issue that the optics contribution from the production straight to the neutrino beam angular spread is about 30% too high. Fig. 6.2 and Fig. 6.6 will be revised accordingly. B.P.

6.0.9 Introduction

B. Parker

For Study–II the muon storage ring has a simple planar racetrack configuration as shown in Fig. 6.1. The racetrack is tilted such that the downward going straight section, denoted the production straight, is aimed at the distant neutrino detector. For a BNL site, depending on ring size, some of the racetrack will probably be above ground level due to the desire to keep the lowest part of the ring above the local water table. The aboveground region will be covered with fill material, mostly sand, and thus there is an incentive to keep the long axis of the racetrack as short as possible to reduce the required fill volume. This arrangement does make it much easier to inject beam into in the upward going return straight section than was

possible for the completely below ground placement considered in Study–I.Injecting into specially tailored reduced-beta optics in the return straight section rather than the high-beta optics needed in the production straight dramatically eases the injection system requirements compared to Study–I as will be discussed later.

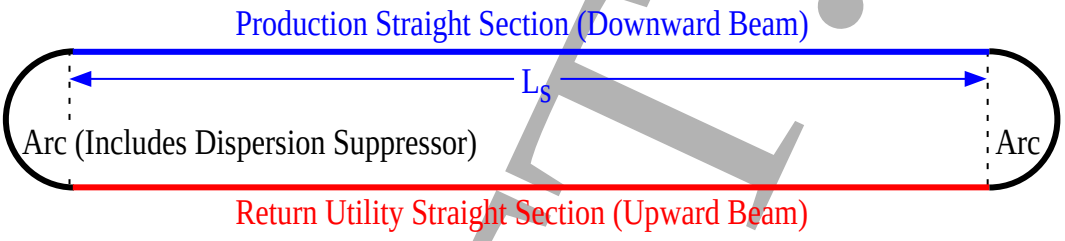

Figure 6.1: Sample Figure.

Since the fraction, f_s of muon decays which makes neutrinos which are aimed toward the detector is $f_s = L_s/C = L_s/(2L_s + L_{Arc})$, with C the ring circumference and L_{Arc} the length of one arc, it is clear that creating the shortest possible arc maximizes f_s and keeps the ring footprint as small as possible.

Because the present ring energy is 20 GeV compared to the Study–I 50 GeV, a naive expectation is that for the same f_s the Study–II ring circumference should be $\frac{2}{5}$ the Study–I circumference of 1753 m or about 700 m. In practice it is hard to achieve this scaling. Even if one takes a larger dipole field, 7 T instead of the Study–I 6 T, it is hard to make the basic separated function arc cell much shorter. As indicated in Fig. 6.2 shortening the individual magnets only serves to reduce the magnetic packing fraction since the coil ends cannot be arbitrarily shortened. In fact for a lower beam energy a larger magnet aperture is needed, assuming equal lattice functions and normalized emmitance, and thus the coil ends should be made even longer than for the Study–I magnets.

With a separated function focusing cell the only path left to make a short 20 GeV arc is to make the arc up from fewer cells than were used for Study–I and inevitably the bend angle per cell is increased. Unfortunately a larger bend angle per cell leads to larger peak dispersion which in turn implies a need for even more magnet aperture to handle the muon beam's large momentum spread.

We did find it possible to shorten the arc cell by using combined function

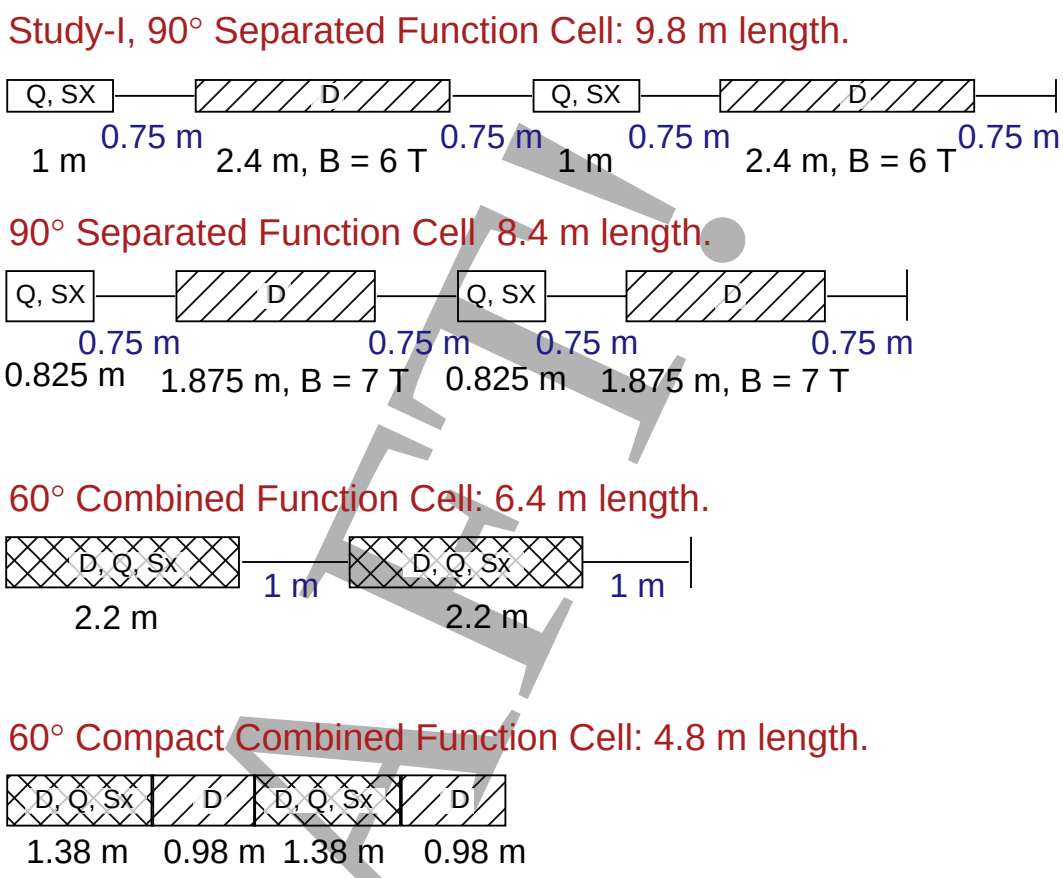

Figure 6.2: Sample Figure.

magnets. As indicated in Fig. 6.2 even with a somewhat smaller dipole guide field, reduced to accommodate the superposition of quadrupole and dipole fields at the conductor, and a more relaxed intermagnet spacing, it is feasible to shorten the basic arc cell and achieve a circumference below the naive 700 m scaling prediction.

Two possible ways to implement such a combined function field configuration, the first with $\cos n\theta$ coils and the second with flat pancake coils are show schematically in Fig 6.3. The pancake coil configuration is especially interesting because its simple bend structure enables us to use a brittle prereacted superconducting material, such as Nb_3Sn for making a high field magnet. Also an open coil structure helps to avoid energy deposition from decay electrons which are swept by the guide field to smaller bend radius in

the magnet's midplane.

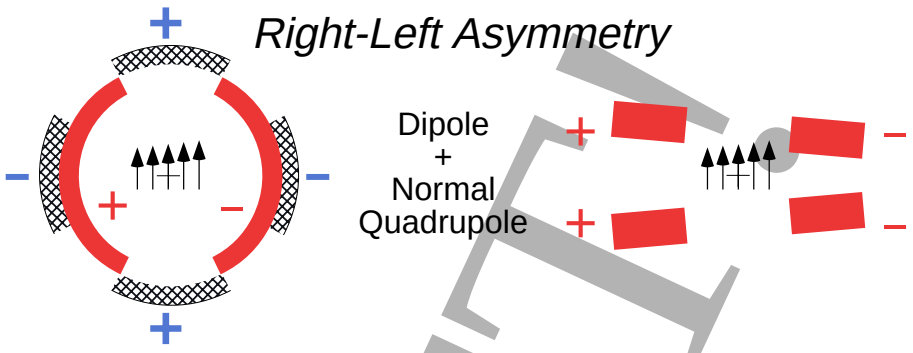

Figure 6.3: Sample Figure.

In addition to conventional upright quadrupole focusing we also investigated focusing structures using a combination of skew quadrupole and normal dipole fields. As indicated in Fig. 6.4 and Fig. 6.5 such skew quadrupole can naturally be made with various arrangements of either $\cos n\theta$ or pancake coils. The skew quadrupole gradient is independently adjustable from the dipole component in Fig. 6.4 and fixed via coil geometry in Fig. 6.5. Skew combined function focusing implies top-bottom asymmetry while upright combined function focusing come from right-left coil asymmetry.

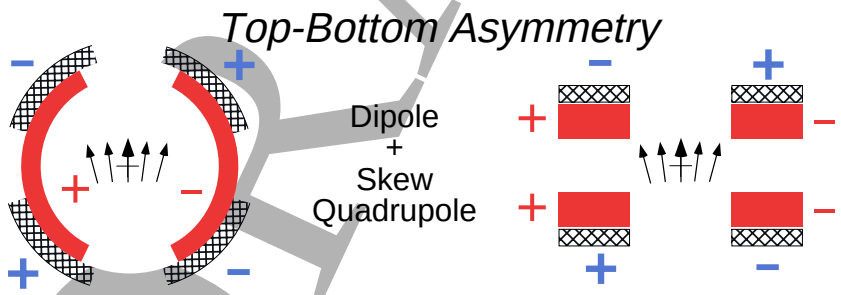

Figure 6.4: Sample Figure.

There is however one trick which only works for making skew quadrupole fields, displacing the coil ends longitudinally with respect to the dipole body field. This trick is illustrated in Fig. 6.6.

By changing the top-bottom overlap of the pancake coils, as indicated schematically in Fig. 6.6, we create double coil regions with the full dipole

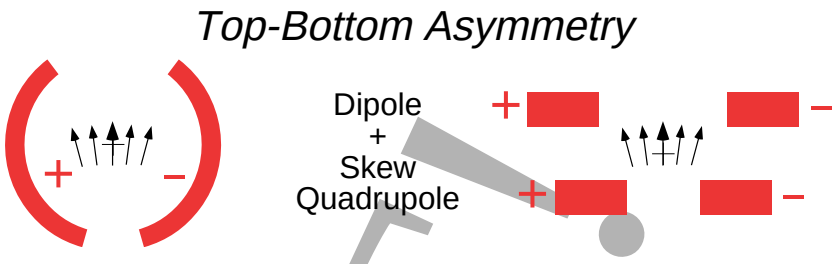

Figure 6.5: Sample Figure.

field but no skew focusing which alternate with single coil gap regions with roughly half the dipole field but full skew quadrupole focusing. The sign of the skew quadrupole focusing depends upon whether the top or bottom coil is missing in the single coil gap region. The result is a compact magnet structure with quasicontinuous bending and alternating gradient focusing. This new focusing structure can be made more compactly than is possible with a standard combined function cell because the space penalties which come from magnet coil ends are essentially avoided and therefore this compact skew focusing cell structure is the basis for the Study–II muon storage ring lattice.

6.0.10 The Lattice

B. Parker

Lattice functions for the 20 GeV muon storage ring using compact skew combined function arc cells are shown in Fig. 6.7. Here the beta functions, (β_A, β_B) are given for the 45° rotated betatron eigenplanes (A,B) shown in Fig. 6.8 but the eigenplane dispersion functions (η_A, η_B) are projected to dispersion in the normal horizontal-vertical, (β_X, β_Y), coordinate system according to the relation ships, $\eta_X = \frac{\eta_A + \eta_B}{\sqrt{2}}$ and $\eta_Y = \frac{\eta_A - \eta_B}{\sqrt{2}}$.

By construction the dispersion in the A and B eigenplanes is nearly equal so the effective vertical dispersion is much smaller than the horizontal dispersion. With this skew lattice the horizontal dispersion is nearly constant across the arc while the vertical dispersion oscillates with small amplitude about zero. Each arc contains cells without bending such that with 60° cell phase advance the dispersion is matched to zero for both eigenplanes in the straight sections.

The lattice shown in Fig. 6.7 has a 1:4 length ratio between the lengths of

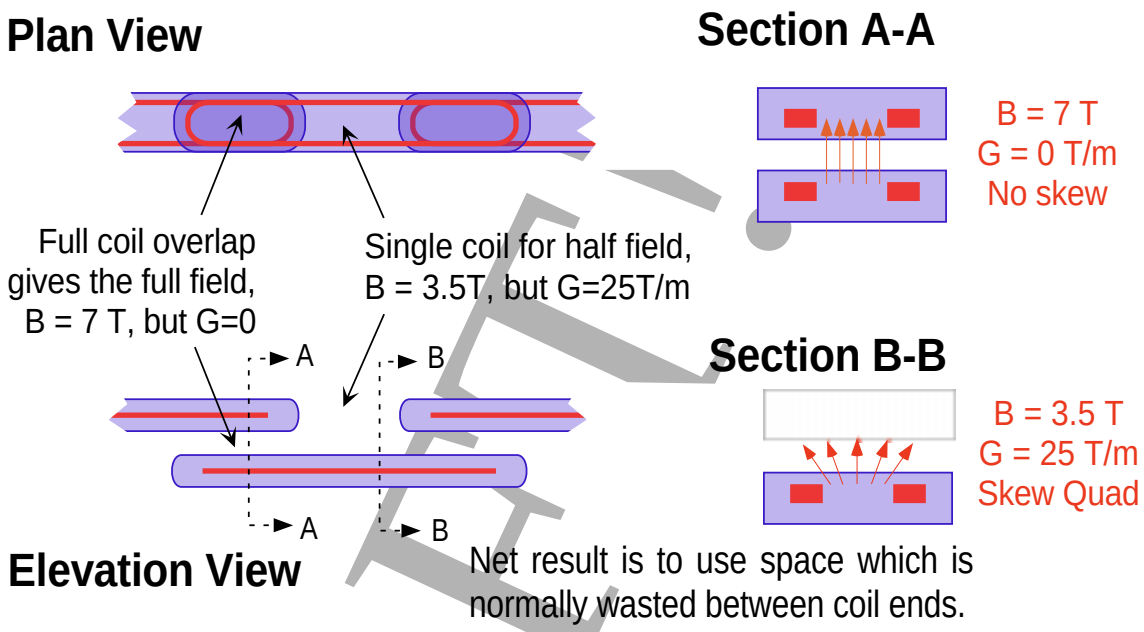

Figure 6.6: Sample Figure.

arcs and straight sections in order to have a geometric decay ratio, f_s, equal of 40%. The production straight beta functions are large in order limit the impact of the muon beam divergence on the divergence of the neutrino beam and the beta functions in the return straight are intermediate in magnitude between the values in the arcs and production straight in order to simplify injection.

Symmetry between the (A,B) betatron eigenplanes is ensured by requiring a small added normal quadrupole focusing component, with normalized strength, K_ρ, $K_\rho = -\frac{1}{2\rho^2}$ in order to partially offset the weak focusing due to a sector dipole bend of local bend radius, ρ. As discussed in a paper by Byrd, Sagen and Talman[?] if left uncompensated the weak normal focusing of a sector bend shows up as coupling between the otherwise uncoupled independent betatron motion in the (A,B) eigenplanes. The value chosen above for K_ρ is precisely the amount needed to make the weak normal focusing in the linear lattice cylindrically symmetric and thus to restore symmetry between the (A,B) eigenplanes.

In practice K_ρ of order parts per mil of the skew focusing strength, K_S, is sufficient to ensure local linear decoupling. Note that the addition of K_ρ does

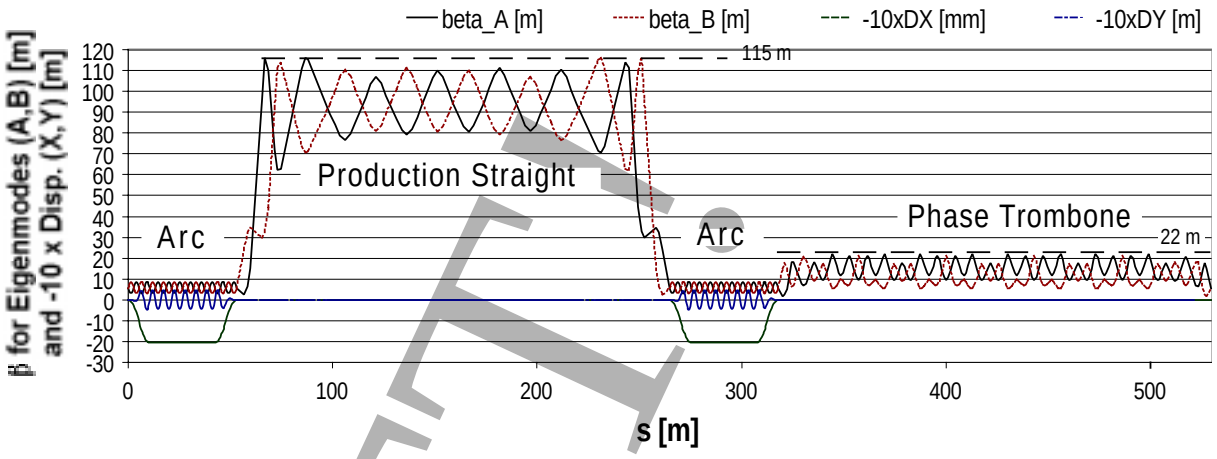

Figure 6.7: Sample Figure.

not cancel the weak sector focusing and the net focusing in an arc cell with bending is slightly different from than of a cell without bending. Accounting for this difference is important for getting a good dispersion match. Also for nonzero momentum offset, $\Delta p/p$, one has to be prepared to deal with coupling effects due to expected nonlinear edge fields.

The ring geometry is shown in Fig. 6.9. The arcs at the racetrack ends are each end are 53 m long and for $f_s = 40\%$ we have the straight sections at four times this length at 219 m for a circumference which is ten times the single arc length or 530 m. Defining the effective arc radius, $R_{eff} = L_{Arc}/\pi$ gives $R_{eff} = 16.9$ m for a total machine length of 246 m. Depending upon the location of the neutrino detector, which affects the racetrack dip angle, it may be desirable to shorten the straight sections somewhat. This strategy helps to reduce the amount of fill needed for a steep dip angle at the cost of smaller f_s.

The Arcs

B. Parker

The arc lattice is shown in more detail in Fig. 6.10. The arc contains ten 60° cells for a total phase advance across one arc of $\frac{10}{6}$ in both eigenplanes. With the chosen 60° phase advance it is possible to match to zero dispersion by omitting the dipole field component from the second and next to last arc cells. The focusing skew quadrupoles in these empty cells will be done

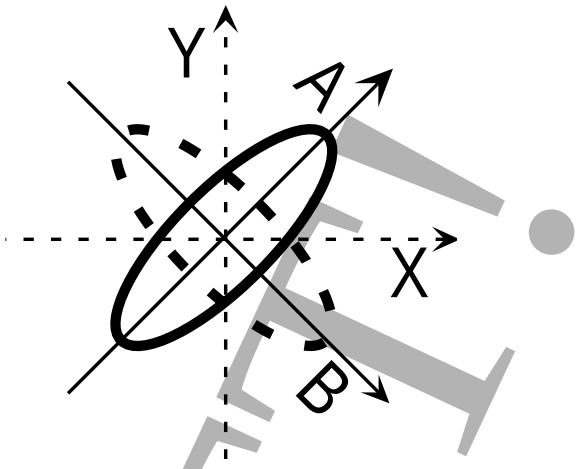

Figure 6.8: Sample Figure.

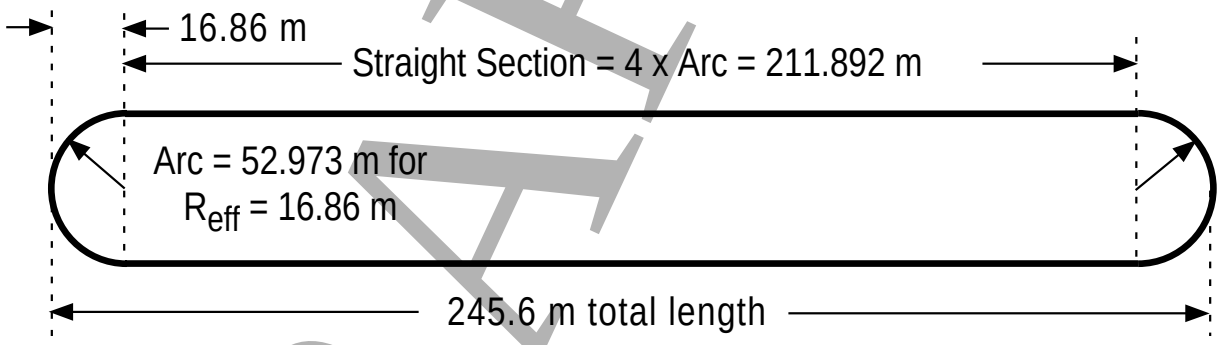

Figure 6.9: Sample Figure.

with conventional warm skew quadrupoles while the rest of the arc is made up from the regular pattern of overlapping pancake superconducting coils supported in a warm iron yokes described earlier. Magnetic field and arc cell optics parameters are listed in Table 6.1.

Beam profiles near the beginning and end of the arcs, where the beam size contribution due to dispersion is negligible, are shown at a skew defocusing location in Fig. 6.11 and a skew focusing location in Fig. 6.12.

Near the middle of the full dipole region, where there are both top and bottom coils the beam profile is round as shown in Fig. 6.13

Will include description of skew sextupole chromaticity correction scheme as well as a description of how to break the regular coil pattern at transitions

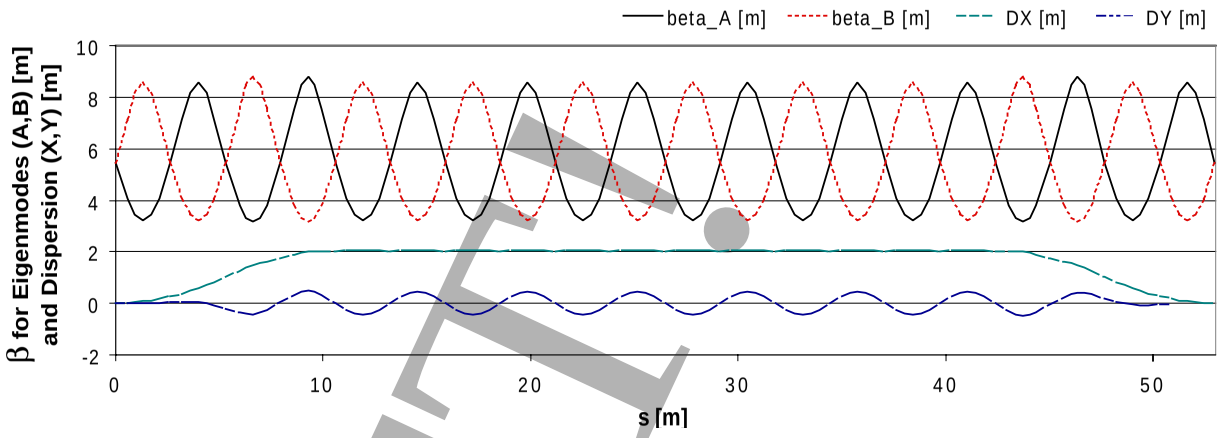

Figure 6.10: Sample Figure.

to empty cell regions and at the ends of the arc (this requires some short coils). Note that discussion of ways to make optics adjustments and beam orbit bumps (e.g. corrector magnets) is beyond the present scope of work but could reasonably be argued as needed under a heading of beam commissioning or operational scenarios. Also the design of the skew sextupoles is presently not addressed.

Magnet design details for warm and cold magnets will be given in later subsections.

Production Straight

B. Parker

Physics requirements drive large beta functions. Possible additional topics for this section include: discussion of rf system requirements and possible normal quadrupole decoupling scheme.

Return Straight

B. Parker but maybe C. Johnstone is better here?

During the editors meeting only a place holder was described for this region. It makes sense to me to outline the functional requirements for this straight section but try to avoid being too specific about the actual detailed solution as this is the only straight section left where we can introduce knobs to fix problems elsewhere. One difference with Study–I is that it does look

Table 6.1: Arc magnet and optics parameters table (blank).

AAA	BBB	CCC

reasonable to inject going up into the return straight and this should be much more favorable than trying to inject into the high beta production straight.

In conversations with Scott Berg it seems that it may not be necessary to have rf-cavities (if momentum compaction is small enough that beam does not spread out too much during a few hundred turns). Could include short section here on parameters for a minimal rf-system to keep beam from debunching. Note that if one follows Lebedev's suggestion to use a 200 MHz cryomodule of the same type as in his accelerator proposal then we will have to face up providing high quality vacuum near the superconducting cavities (presumably without the use of his isolation windows).

Ring Acceptance

B. Parker

For calculation the effective vertical betatron acceptance, β_{eff}, we have $\beta_{eff} = \frac{\beta_A+\beta_B}{2}$ and for half aperture, Δh, as shown in Fig. 6.14 we have physical acceptance, A, of $A = \frac{(\Delta h)^2}{\beta_{eff}}$ or normalized acceptance, A_n, $A_n = \gamma A$. Values are given in Table 6.2

As show schematically in Fig. 6.15 a pencil beam with momentum offset, $\Delta p/p$, moves the beam horizontally by an amount, ΔX, $\Delta X \approx \eta_X \times \Delta p/p$ and vertically by an amount, ΔY, $\Delta Y \approx \eta_Y \times \Delta p/p$. Values are given in Table 6.3

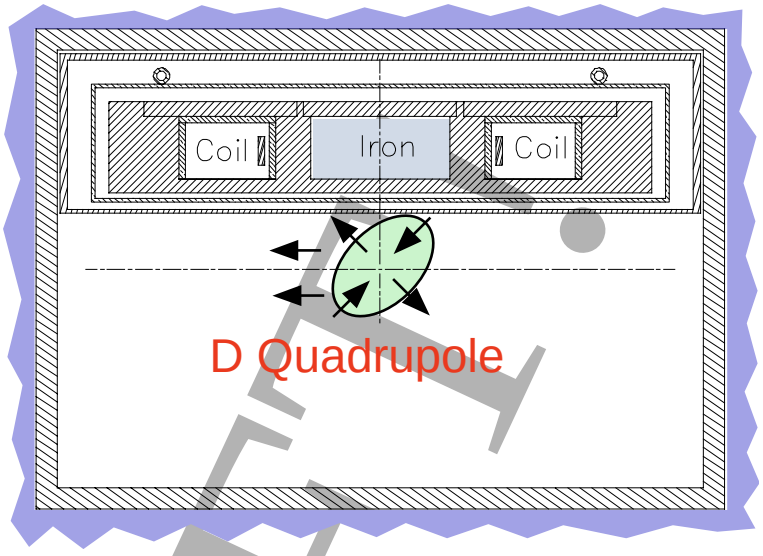

Figure 6.11: Sample Figure.

Table 6.2: Betatron acceptance in the arcs.

AAA	BBB	CCC

If we use a round beam pipe in the warm skew quadrupoles in the production straight section, as shown in Fig. 6.16, we see that the betatron acceptance can be calculated directly from the eigenplane beta functions, (β_A, β_B), as shown in Table 6.4.

It is probably desirable to use a butterfly or other shape beam pipe in some of the skew quadrupoles that the injected beam goes through off axis as this is a relatively cheap way to gain a bit of injection aperture.

Injection System

B. Parker

Without some better idea for the transfer line it is hard to be too specific here. We should be able to show a straw design for estimates of magnet

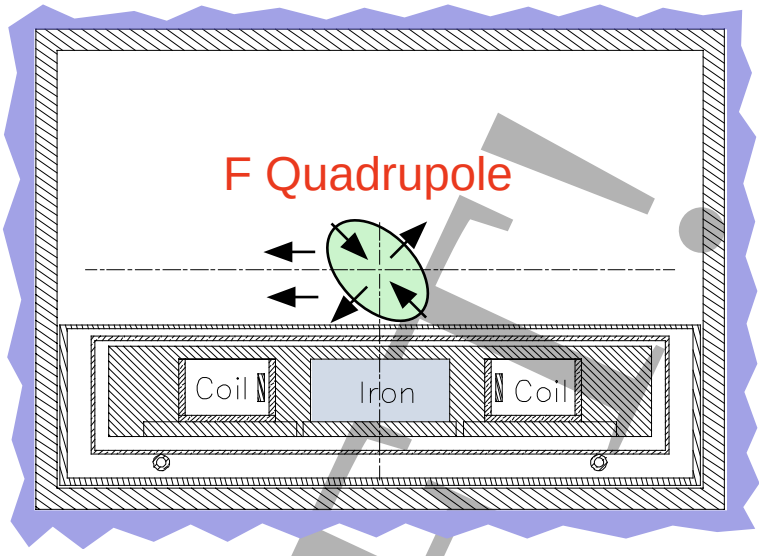

Figure 6.12: Sample Figure.

Table 6.3: Momentum acceptance in the arcs.

AAA	BBB	CCC

parameters, required apertures etc. Must decide: Should we discuss magnetic septum quadrupole and should we include a description of collimation system for protection against injection errors here?

It may make sense to postpone discussion of the beam protection components to the later energy deposition section. Nikolai?

Superconducting Magnets

?

Conventional Warm Magnets

B. Parker

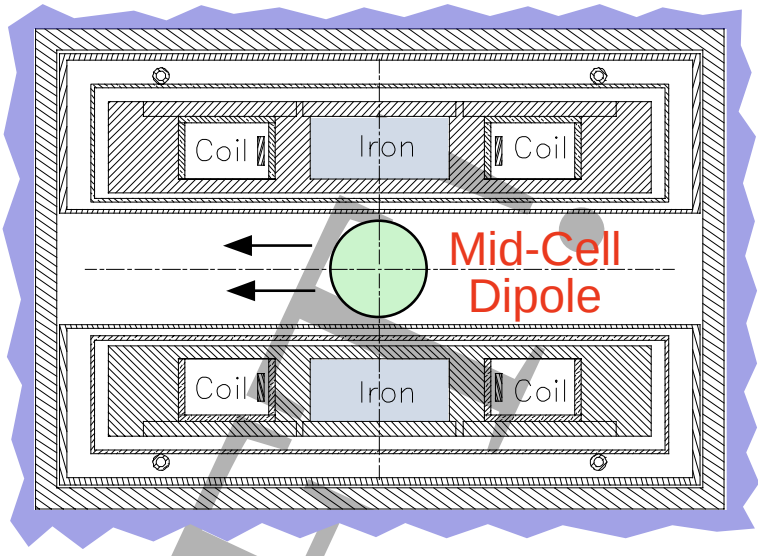

Figure 6.13: Sample Figure.

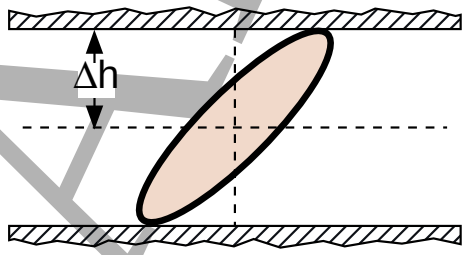

Figure 6.14: Sample Figure.

This section covers: the warm quadrupoles in the arcs, optics matching quadrupoles near ends of the straight sections and the straight section quadrupoles. If time permits we may want to include some requirements for beam orbit control corrector dipoles, ring tune and coupling control quadrupoles.

Anything else, Carol?

Instrumentation

J. Norem

The cooling ring presents some new beam instrumentation problems. In addition to the usual emittance, divergence, closed orbit, injection, extrac-

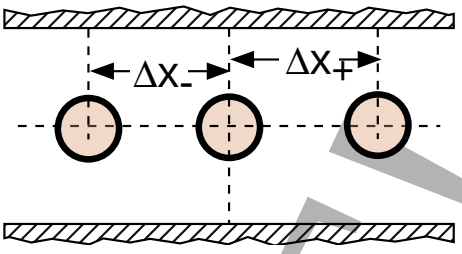

Figure 6.15: Sample Figure.

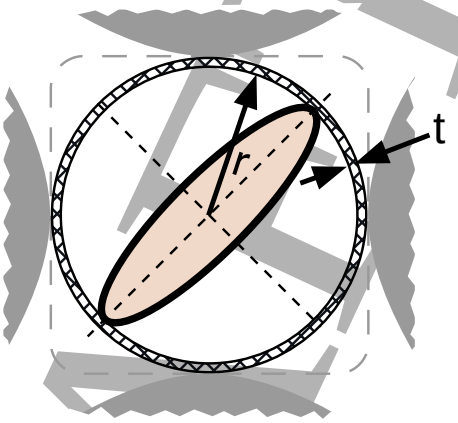

Figure 6.16: Sample Figure.

tion, beam loss and beam energy measurements, it seems desirable to measure the beam polarization, and precision measurements of beam direction in the decay straight section as a function of time, to help determine the parameters of the neutrino beam. The instrumentation issues for the muon beam in the storage ring should utilize mostly proven technology. The primary difficult would be that precision measurements can be complicated by the presence of decay electrons in the beam.

The muon decays can help determine some of the machine parameters. Semertzidis and Morse[?] have looked at using the $g-2$ frequency of the muons to determine the beam energy. They consider measurement of the synchrotron radiation from decay electrons which will give a very substantial signal.

We anticipate that the 6D "pencil" beams used to tune up the accelerator will also be useful in tuning up and operating the storage ring.

Table 6.4: Betatron acceptance in the production straight.

AAA	BBB	CCC

One issue which has been identified is the possibility of a high electron shower background at the downstream end of the two straight sections. This background would be due to muon decay electrons which were not swept from the beam. Although the fraction of primary decay electrons in the beam is $L/\gamma\tau c$, where L is a path length in the storage ring, and $\gamma\tau c \sim 126$ km, is the decay length at 20 GeV. This means the fraction of muons which will decay in the 116 m straight sections is 0.001, and the electron/muon ratio at the downstream end of the straight will be $\sim 0.001 F_s$, where F_s is a factor which depends on the probability of electrons being swept and showering in the vacuum pipe. Estimates of the electron background are underway, but it seems desirable to consider precision measurements external to the ring for determining the neutrino beam direction, profile and divergence.

We assume the most reliable measurements of the neutrino beam size and divergence would be obtained from fine grained detector consisting of Tungsten sheets interspersed with hodoscopes. These would be located in shafts downstream of the decay straight. Rates could be high, on the order of 100 events/fill for a 1 m detector. (more details coming - M. Goodman)

More detailed descriptions of polarization measurements and other neutrino measurements will be added in a later draft.

Power Supplies for the Muon Storage Ring

No name

To this point no new work done here so everything has to be TBD.

Quench Protection Dumps

No name

To this point no new work done here so everything has to be TBD.

Muon Storage Ring Quench Detection and Protection

No name

To this point no new work done here so everything has to be TBD.

6.0.11 Lattice Performance and Tracking

C. Johnstone

The issues discussed here are similar to those from Study–I but in detail things will look quite different due the novel features of the proposed skew focusing lattice.

A description of the on going work with Kyoko Makino, Martin Berz etc. belongs here. The importance of this work is such that it could point to the need for reworking the lattice. The present choice of lattice parameters represents a choice, in the absence of tracking results, to go with parameters that make the magnet parameters easier to achieve and provides increased protection from energy deposition due to showers coming from the long straight sections; however, it is entirely possible that we will have to compromise these goals somewhat in order to achieve good enough dynamic aperture.

6.0.12 Beam Induced Energy Deposition And Radiation Fields

N. Mokhov

Discussion similar to Study–I.

Arc Magnets

N. Mokhov

This section is different from Study–I to the extent that the open coil structure adopted for Study–II changes the energy deposition pattern. Some mitigation of hot spots still might be required. An important result here is the extent to which the warm cells near then ends of the arcs are useful in trapping energy coming from the long straight sections.

Straight Section Components

N. Mokhov

Estimations for energy deposition issues for warm magnets, kickers, diagnostics etc. This also may be the best pace to discuss protection against injection errors and injection tuning. If a superconducting rf system is needed then there may be issues for how to protect and isolate it. In particular it may not be possible to use windows to isolate the rf station's beam vacuum (unlike previous accelerator).

Radiation Around Arc Tunnel And Downstream Of Straight Sections

N. Mokhov

Standard discussion but takes into account BNL guidelines.

Bibliography

[1] Semertzidis and Morse paper.

[2] BST paper from the 1989 ICFA beam Dynamics Workshop.

Chapter 7

Solenoid Magnets

M. Green

Chapter 8

rf Systems: 200 and 400 MHz

R. Rimmer
H. Padamsee

18. HighPower RF systems: 201.25 and 402.5 MHz

R. Rimmer*, J. Corlett*, N. Hartman*, D. Li*, R. Macgill,* A. Moretti†, J. Reid†, H. Padamsee‡, G. Rongli‡, V. Shemelin‡

*LBNL, †*FNAL,* ‡*Cornell*

18.1 Introduction

The RF systems for the buncher and the cooler are required to match the muon beam into the longitudinal acceptance of the cooling channel and replenish the beam energy lost during ionization cooling. Since they must operate inside the strong solenoid fields they cannot be superconducting. These systems require a large number of RF cavities operating at high gradient, and a large amount of pulsed RF power. They are technically challenging and expensive and have therefore been the focus of continued development during study II. The cooling channel layout has continued to evolve since study I with emphasis on integration of realistic components into the available space along with optimization of the channel performance. The buncher and cooling channel systems must accommodate liquid hydrogen absorbers, high gradient RF cavities, windows, tuners, superconducting solenoids, diagnostics, pumping, harmonic cavities and other equipment. The system must be designed in such a way as to allow assembly and access for maintenance.

The buncher and cooling channel will be made of a large number of modules. The module layouts are described in sections 18.4.2 and 18.4.3. Each module contains two or four 201.25 MHz closedcell cavities and is powered by one or two high power klystrons. The density of equipment in the building is therefore high and the systems must be carefully laid out to allow access for installation and maintenance.

The proposed buncher and cooling channel is approximately 163 m long and requires more than 162 cavities and 73 klystrons. The total installed power is approximately 670 MW (approx. 1.3 MW average), and the installed voltage is 933 MV.

The cooling channel is followed by an acceleration section employing 300 twocell superconducting RF cavities and 26 4cell cavities at 201.25 MHz. These structures are also challenging because of the high gradient and large physical size. The power requirements of these sections are not as high as the normal conducting RF sections but the pulse length is much longer. Many cavities can be powered from a single klystron station. Several multicell RF cavities may share a common cryostat. The final energy at the end of the accelerating section is 20 GeV, compared to the 50 GeV of study I, which has reduced the size and cost of the acceleration section significantly.

18.2 NCRF Specifications for Cooling Channel and Buncher

Table 18.A shows the inventory of RF cavities contained in the study II parameter list. The cooling channel simulations have assumed ideal pillbox cavities with lengths that are determined by the space available in the chosen lattices (and zero space between cavities). The gradients and phases of these cavities have been adjusted to optimize the cooling channel performance while keeping the gradients and RF power requirements within feasible limits. Table 18.B shows the peak cavity power and klystron output power to meet these requirements and the total power for each cavity type. Both tables also show how the required voltages could be obtained using practical reentrant or "omega" shaped cavities with closed off irises of finite thickness. The loss of active length in this case is compensated by the greater efficiency of the rounded design. To be conservative the iris diameter used for the omega cell was sufficient to accommodate any reasonable beryllium foil. In practice the foils may be smaller and in any case will decrease in size towards the end of the cooling channel. Ideally the cavity shape would be optimized for each foil size. This would maximize the efficiency and minimize the cost. Note that the RF power requirements are dominated by the cooling sections 1.11.3 and 2.12.3, which have the largest number of cavities and the highest gradients.

Table 18.A

ideal pillbox dimensions from param. List 1/16/01

section	**radius**	**length**	**freq**	**#cavs**	**Epk***	**Veff**
	(m)	(m)	(MHz)		(MV/m)	(MV)
b1						
	0.570					
	0.373					
		201.25				
			196			

4

6.40

2.07

b2

0.570

0.373

201.25

8

6.00

1.94

b3

0.570

0.373

201.25

8

8.00

2.59

1.11.3

0.570

0.466

201.25

68

15.48

5.76

2.12.3

0.570

0.559

201.25

74

16.72

6.71

match?

b1 402.5 MHz

0.285

0.186

402.5

2

6.40

1.03

b2 402.5 MHz

0.285

0.186

402.5

4

8.00

1.29

Omega cavities

b1

0.607

0.405

201.25

4

7.41

2.07

200

b2

0.607

0.405

201.25

8

6.95

1.94

b3

0.607

0.405

201.25

8

9.27

2.59

1.11.3

0.607

0.405

201.25

68

201

20.62

5.76

2.12.3

0.615

0.483

201.25

74

23.06

6.71

match?

b1 402.5 MHz

0.308

202

0.288

402.5

2

6.57

1.03

b2 402.5 MHz

0.308

0.288

402.5

4

8.21

1.29

* note: Kilpatric number is about 15 MV/m at 201.25 MHz

Table 18.B

ideal pillbox dim.'s

section	**Veff**	**Rs†**	**Pc***	**Pkly****	**#cavs**	**Ptot**	**sum**

(MV)

(M)

(MW)

(MW)

(MW)

(MW)

b1

2.07

8.899

0.567

0.628

4

2.51

b2

1.94

8.899

0.499

205

0.552

8

4.42

b3

2.59

8.899

0.886

0.982

8

7.85

1.11.3

5.76

10.701

3.646

4.038

68

274.60

206

2.12.3

6.71

11.428

4.635

5.134

74

379.91

match?

669.29

b1 402.5 MHz

1.03

6.275

0.200

0.222

2

0.444

b2 402.5 MHz

1.29

6.275

0.313

0.347

4

1.387

1.831

Omega cavities

b1

2.07

10.220

0.494

0.547

4

2.19

209

b2

1.94

10.220

0.434

0.481

8

3.85

b3

2.59

10.220

0.772

0.855

8

6.84

1.11.3

5.76

10.220

3.818

4.228

68

287.54

2.12.3

6.71

11.794

4.491

4.974

74

368.09

match?

	668.50
b1 402.5 MHz	
	1.03
	8.368
	0.150
	0.166
	2
	0.333
b2 402.5 MHz	
	1.29
	8.368
	0.235
	0.260
	4
	1.040
	212

† Rs, calculated, = V2/P, * Real cavity, Qo assumed 85% of theoretical,

** Klystron forward power for 3 filling

18.3 RF Station Description

Each RF station consists of a modulator, klystron, distribution system, lowlevel RF and controls driving two or more cavities. The modulator must provide a flat top DC pulse of up to 125 μs with a recharge time of less than 20 ms. This is equivalent to a repetition rate of 50 Hz, however not every 50 Hz pulse is required. The output from the AGS appears as 6 pulses spaced at ˜20 ms followed by ˜300 ms gap. (The AGS cycles at 2.5 Hz). The "average" duty factor is ˜1.9 x 103.

The RF power source must provide approximately 10 MW of peak power to drive two cavities. The source will most likely be a multibeam klystron, which should give good reliability and a long operational lifetime.

The distribution will be via high power coaxial lines, with the power split between two or more cavities with appropriate delays to maintain the proper phase . The cavities will use coaxial feedthroughs and looptype couplers. The peak power requirements will require careful design of the components, although the average power of around 10 kW is quite modest. Provision should be made for adjusting the phase of individual cavities and for handling the reflected power during the initial part of the cavity fill time.

Each station will require a water distribution system and a rack of lowlevel RF hardware and controls.

18.3.1 RF Power Source and equipment

The ionization cooling channel requires high peak RF power sources at 201.25 MHz and 402.5 MHz to efficiently cool the muon beam. Table 18.B lists the peak RF power requirements for each section of the cooling channel. There are 162, 201.25 MHz cavities in the channel that require 668 MW of RF power for a pulse length of 125 s at 15 Hz (average) and 6, 402.5 MHz cavities that require up to 1.8 MW at 15 Hz. An examination of the requirements shows that an RF source of about 6 or 12 MW would be ideal for the 201.25 MHz cavities and a source of 500 to 750 kW for the 402.5 MHz cavities. The RF for the 201.25 MHz cavities could be supplied by existing gridded tubes at about the 5 MW level. However, the low gain and lifetime of gridded tubes make the R&D effort to develop an alternative most attractive. Preliminary calculations at SLAC have shown that a 201.25 MHz klystron could be built with a reasonable amount of R&D. The gain, efficiency, and lifetime are higher, greater than 50 dB, 50% and 50,000 hours, respectively. SLAC has examined two designs a single gun diode design, and a multibeam klystron. The multibeam klystron is the most attractive in that it reduces the overall length of the tube from 7.5 m to between 3.5 and 4.0 m. The length reduction factor of the multibeam klystron and its potential for higher efficiency make it the optimum candidate for the neutrino factory. The length of the multibeam klystron is, also, consistent with the manufacturing capabilities of current tube manufacturers. However the manufacture of a 7.5 m diode tube would be a big step and would require new and costly facility upgrades. To provide RF power overhead for dynamic regulation of the RF phase and amplitude, a 12 MW multibeam klystron has been selected as the high power RF source for the neutrino factory. This provides an RF power overhead margin of about 20 % for regulation. Table 18.C shows the cost estimate for a multibeam klystron system of 73, 12 MW klystrons for supplying the required RF to the cooling channel. The first item is the R&D costs to develop the 12 MW multibeam klystron. The design should be a fully integrated horizontal package incorporating the tube, solenoid, and high voltage terminal as pioneered at CERN for LEP. This would facilitate the replacement and installation of tubes in the facility. With a mean time between failures (MTBF) of 50,000 hours and 73 tubes, a tube, after the initial breakin period, would fail and need to be replaced every 30 days. Many of these "failures" towards the end of life are gradual and replacement can be scheduled for routine maintenance periods. Another advantage of the horizontal design besides the ease of handling is the reduced cost of the RF building because of the lower building height requirement. Because of the

large size and costs of waveguide the transmission lines from the tubes to the cavities will be large coaxial lines of 0.31 to 0.36 m diameter pressurized to 1.75 atmospheres of dry air. Power splitters would divide the RF power from each tube to supply the appropriate RF power to the cavities. Sections b1 and b2 of the buncher will require a 12 way splitting of the power; section b3 a 8 way, and sections 1.1 to 2.3 a 2 way splitting of the power. Splitters with proper built in phase delays would further divide the power to each cell or cavity section of the cooling channel.

Table 18.C. 12 MW , 201.25 MHz Klystron Cost

R&D klystron amortized over 73 Tubes

$ 125 k

Tube

525 k

Solenoid

200 k

Modulator

300 k

Transmission Line components

100 k

Water Skid

60 k

Station Relay Racks, LLRF and Control

120 k

Utilities, Safety Interlocks

100 k

Installation

120 k

Total = \$1650 k

System Costs for Spreadsheet RF requirements: 73 Klystrons = $122.3 M

The 402.5 MHz system can use currently existing 900 kW diode RF klystron amplifiers. Because of their long length, it would be advisable to fund a small R&D development of an integrated horizontal package for the tube. Again, as for the multibeam klystron, this would improve the efficiency of tube handling and provide cost saving because of reduced building height requirement. Again, coaxial transmission lines with splitters would be used to provide the RF power to the cavities. Only 3 klystron tube amplifiers are required to supply the requirements of the 402.5 MHz RF spreadsheet. The cost of system of the three 402.5 MHz klystron amplifiers system is $3.525 M or $1.175 each, a little more than half of the 201.25 MHz multibeam klystron. Figures 18.A and 18.B show a cross section and plan of a portion of the RF building gallery along a 201.25 MHz section. The RF building is approximately 170 m long and 30 m wide. With the horizontal packaging of the 201.25 and 402.5 MHz klystrons the height of the building roof line need only be 5.5 m. Because of the large footprint of the equipment, the klystrons are arranged side by side and on both sides of the gallery. Not shown in the figures are the transmission line splitters required to supply the RF power to the cavities as well as the utilities. The 402.5 MHz klystron system footprint will be much the same, but about half the size and be located in sections b1 and b2 interspersed between the 201.25 MHz equipment.

18.3.2 RF Station Controls and LLRF

The low level RF (LLRF) and controls provides the drive power for the final klystron amplifier, contains feedback loops for phase, amplitude and cavity frequency control, personnel safety and equipment protection. A frequency reference line which runs the length of the complex provides RF

phasing reference to which each cavity is locked. A microprocessor in each RF station processes error information to control the amplitude, phase and keep the cavity tuned to the reference frequency. The microprocessor communicates and accepts directions from the central control room. The system would be similar to systems currently in use at Fermilab or planned for the SNS project. Spark detection will include fast circuits to detect sparks and malfunctions and immediately inhibit the RF to protect the equipment and cavities. Other fast circuits will monitor for high RF leakage from equipment and contact with high voltage and current and activate interlocks for personnel protection. The equipment would be housed in five standard racks next to the klystron and associated equipment, figure 18.B.

18.3.3 High Voltage Modulator and Power Supply

The high voltage modulator and power supply for the 201.25 MHz will use the latest solid state design. Currently available Insulated Gate Bipolar Transistors (IGBT) modulator technology will be built by industry to provide the pulse power requirements of the klystron. The neutrino factory will use IGBT modulators similar to designs currently being built for the SNS project. They are very reliable, efficient and cost effective. A 6 beam klystron, the basis of this design, has a calculated efficiency of 50% and klystron tube perveance of 2 x 10E6. The specifications for the modulator and power supply are: high Voltage = 84 kV, peak current = 292 A, duty = 0.1875 %, average power = 46 kW and droop 0.1 %. The modulator and power supply for the 402.5 MHz are of the IGBT type with the following specification: High Voltage = 60 kV, peak current = 31 A and average power = 3.4 kW. The overall efficiency of the modulator and power supply from the AC mains is about 95%.

18.3.4 NCRF Mains Electrical Power and Water System

The mains AC power for the normal conducting RF must support 73 tubes with 46 kW average power and three tubes with 3.4 kW average power with an assumed efficiency of 95%. This comes to 3.6 MW. Solid state amplifiers and solenoid power supplies add another 1 MW. Cooling water systems and miscellaneous other loads add a further 2.3 MW. These all require a 480 V three phase supply for a total of 6.9 MW. In addition to this AC power is

required at 120 V and 208 V for racks and other miscellaneous equipment totalling approximately 0.6 MW. This gives a total of 7.5 MW at the AC mains.

The cooling water system will be sized to accomodate the average power of 7.5 MW with a proper temperature rise for safe and efficient operation of the equipment. Each klystron station requires 75 gpm of low conductivity water (LCW), for cooling the klystron and associated equipment and 20 gpm LCW to cool and maintain temperature control of the cavity. This gives a total water requirement of 6,935 gpm. This could be divided up between room temperature and higher and chilled systems for cavity control at 20 gpm per station. The header pressure being 100 psi and return of 40 psi.

FIGURE 18.A. Cross section of cooling channel equipment gallery

FIGURE 18.B. Cooling channel linac equipment gallery, plan view

18.4 NCRF Cavities at 201.25 MHz and 402.5 MHz

The 201.25 MHz normalconducting cavities in the cooling sections must operate at very high accelerating gradients. This would be impractical with conventional open iris structures because of the large size of the beam iris required. A great improvement can be made in the shunt impedance of the cavity by closing the iris with a thin conducting barrier. This barrier must use the smallest amount of material to minimize scattering of the muon beam. It is proposed to close the irises with thin beryllium foils. Other methods of closure such as grids of thinwalled tubes will be evaluated in the future. The foils must be thick enough to conduct away the heat from the RF currents and keep the temperature to a predetermined level. The foils will be prestressed in tension during manufacture in order to keep them flat. This method had been tested experimentally and works well up to the point where the thermal expansion exceeds the prestress and the foils begin to move. Foil thicknesses have been chosen for study II which should keep the temperatures below this critical level. The use of tapered foils or foils with stepped thickness can reduce the amount of material intercepted by

the core of the beam, reducing the amount of scattering significantly. Table 18.D shows the suggested minimum foil thicknesses for the various types of cavities in the buncher and cooling channel.

Table 18.D. Beryllium foil thicknesses for various cells in the buncher and cooling channel.

type						
section						
frequency						
length						
gradient						
Thickness*						
Radius*						
MHz						
m						
MV/m						
m						
cm						
end						
b1						

402.5

0.186

6.4

75

18

end

b2

402.5

0.186

6

75

18

end

b1

201.25

0.3728

6.4

10

21

221

middle

b1

201.25

0.3728

6.4

120/240

14/21

end

b2

201.25

0.3748

6

100

21

middle

b2

201.25

0.3748

222

6

105/210

14/21

end

b3

201.25

0.3748

8

180

21

middle

b3

201.25

0.3748

8

187/374

14/21

end

223

1.1

201.25

0.466

15.48

200/400

12/18

middle

1.1

201.25

0.466

15.48

700/1400

14/21

end

1.32.1

201.25

0.5592

16.72

248/495

224

12/18

middle

1.32.1

201.25

0.5592

16.72

917/1834

14/21

end

2.1

201.25

0.5592

16.72

119/239

10/15

middle

2.1

201.25

225

0.5592

16.72

495/990

12/18

* dual values imply a steppedthickness foil *note 119/239 might need to be 128/256RR*

The normalconducting cavities in the buncher can be of the same design as those in the first cooling section, though they would be operated at lower gradient. This will allow the use of thinner foils to minimize the scattering. The buncher section also contains a small number of harmonic cavities operating at 402.5 MHz. These fit into the spaces normally occupied by the hydrogen absorbers in the cooling cells. For these cavities the foils occupy most of the diameter of the end walls, but the gradients are much lower so the losses in the foils are manageable.

The normal conducting cells must have some cooling to remove the average power losses in the walls and to stabilize the frequency. The study II design has been evaluated for room temperature operation although the option of operating at reduced temperature has been kept open. This would lower the wall resistance and reduce the peak power requirements at the expense of adding a potentially large refrigeration system.

18.4.1 201.25 MHz Closed Cell Description

The cooling channel simulations have used simple pillbox cavities which have continuous, flat, conducting end walls from the center all the way to the outer radius. The cavity lengths assumed for the simulations are just the available space divided by the appropriate number of cells. In practice the cavities must be closed by assemblies of foils or grids that should be demountable from the cavities for assembly or repair. This requires a finite thickness for each iris, reducing the length available for RF and lowering the effective shunt impedance. This can be mitigated by rounding the outer walls of the cavity to improve the quality factor and restore the shunt impedance. Any practicable assembly of foils (or grids), requires some space for flanges and access. We have assumed a minimum spacing of 50mm between cavities,

as shown in figure 18.C. The dimensions of the cavities have been adjusted to fit the remaining available space. Note that the resulting cavity lengths are significantly shorter than the optimum for a particle of this velocity (beta = 0.87). In future studies this cavity length may be restored by adjusting the total cell length appropriately. The cavity shape is slightly reentrant in order to maximize the inductance, minimize the capacitance and hence get the highest shunt impedance [ref. 18.1]. Figures 18.C and 18.D show the cavities separated by a pair of foils. This would allow variable thickness foils to be used where the stepped side is not exposed to RF. Figure 18.E shows a MAFIA simulation of the electric field in two halfcells separated by a pair of foils. Some field enhancement can be seen on the noses. Alternatively a single foil of twice the thickness could be used in the center of the iris, heated from both sides (except for the end cells). Another advantage of the closed cells is that there is no RF coupling through the iris so the cavities can be individually phased for optimum performance of the cooling channel. One penalty of the omega shape is some field enhancement on the "nose", see figure 18.F. The nose is made with as large a radius as practical but still may have an enhancement factor of as much as 1.7 over the field on axis. However, the highest surface field in table 18.B is only about 1.5 times the Klipatric number for this frequency. The only good thing about this field concentration is that it is not on the foil but on the solid copper so a breakdown to this point may be less harmful. Figure 18.Fb shows the azimuthal magnetic field. The distribution on the foil and therefore the RF heating are similar to the pillbox model although there is some shielding due to the noses.

Figure 18.G shows the profile of the cavity from the downstream part of the cooling channel where only two cavities are used per cooling cell. The cavities are longer and closer to the optimum for this particle speed (although there is still room for some improvement). Figures 18.H a and b show the 2D electric and magnetic field profiles for this case.

FIGURE 18.C. Profile of cavities for buncher and first cooling section

FIGURE 18.D. Section 1 cavity **FIGURE 18.E**. MAFIA model with 2 foils

FIGURE 18.Fa. URMEL 2D Efield **FIGURE 18.Fb.** Azimuthal Hfield

FIGURE 18.G. Profile of cavities for second cooling section

FIGURE 18.Ha. URMEL Efield **FIGURE 18.Hb**. Azimuthal Hfield

18.4.2 Foil Requirements

The closedcell cavity design described above assumes that beryllium foils will be used to seal off the beam irises. Other methods, including grids of thin walled tubes, have been discussed and show promise but are not as far advanced in understanding or testing as the foils. Hence prestressed foils have been chosen as the baseline design for study II. The foils are made of thin high purity beryllium sheet bonded to a thicker ring of slightly lower grade material at Brush Wellman Corp, see figure 18.I. The exact details of this process are proprietary but the combination of materials used results in a small but significant difference in the thermal expansion of the foil relative to the ring assembly. This produces a tensile prestress on cool down from the joining operation, which helps to keep the foil flat.

When the foils are heated by RF and only cooled by conduction to the edges they assume an approximately parabolic temperature profile, see figure 18.J. This has been simulated in ANSYS and tested experimentally by heating foils in a low power test cavity with a halogen lamp [ref. 18.2]. The actual RF induced profile is slightly flatter than parabolic and can be used in ANSYS as a load set for the stress calculations. Figure 18.K shows an example of the temperature distribution in a thin foil from such an analysis.

The foils remain flat until the thermal expansion exceeds the tensile prestress. At this point compressive stress is generated in the foil, and it starts to deflect by buckling into a gently bowed shape, see figure 18.L. The maximum allowed temperature difference is about 35C and is approximately independent of the radius and thickness. Of course a thicker foil can take more power before reaching the buckling temperature, as shown in figure 18.M. A set of foils has been determined for the set of cavities used in table 18.A, which keep the temperatures below the critical point. For the larger irises the foils become quite thick and the scattering of the muon beam becomes significant. One way to reduce this is to make the windows thinner in the middle, where the core of the beam passes, and thicker towards the outside where there are fewer particles, see figure 18.N. It is thus possible to reduce the scattering while maintaining the same temperature rise in the foil. Figure 18.O shows the temperature profile for a thin window of uniform thickness and for windows with thicker profiles starting at different radii. As can be seen from the figure adding material at large radius has a significant effect on the temperature profile up to about one third of the way in. Beyond this point there is a diminishing return and much past half way there is little to be gained by adding more material. Simulations have shown that such a stepped window reduces the multiple scattering significantly compared to a

uniform foil for the same temperature. Going to multiple steps in thickness or a continuous taper should yield further small improvements in scattering but the simulations do not show a significant improvement in transmission through the cooling channel.

FIGURE 18.I. Layout of beryllium test window (all dimensions in mm)

FIGURE 18.J. Actual temperature profile for RF heating and parabolic approximation from halogen lamp tests.

FIGURE 18.K. ANSYS calculated temperature profile for thin window with 60W loading

FIGURE 18.L. ANSYS model showing example of buckling displacement (dimensions in m).

The prestressed foil properties have been investigated experimentally in a lowpower test cavity at 805 MHz using a halogen lamp as a heat source. These experiments used small (160 mm diameter) foils and the results have been extrapolated to larger foils. We have assumed that the same prestress can be achieved in the larger foils, but this must be validated experimentally as part of the future R&D program. It should be straightforward to attain the desired prestress by adjusting the combination of materials in the outer ring but some experimentation may be required to find the optimum combination.

FIGURE 18.M. ANSYS calculated displacement vs. power for larger windows

FIGURE 18.N. Stepped window design

FIGURE 18.O. Temperature profile of uniform thin window and windows with steps to thicker outer region at various radii.

One concern with the closediris structures is the possibility of multipactoring due to the high secondary yield of beryllium or aluminum (foils or tubes) This could cause outgassing and possibly breakdown in the cavity, which might damage the delicate structures. Persistent multipactor discharge may also heat the surfaces involved. Unlike copper the secondary yield of aluminum does not reduce with RF conditioning because of a stable surface oxide layer. It is expected that beryllium may behave similarly, although the handbook values for beryllium oxide are lower than those for aluminum oxide. It is proposed to suppress this problem by the application of low secondary emission coatings such as titanium nitride (TiN). This problem will be investigated experimentally in a high power cavity as part of the ongoing muon collaboration 805 MHz R&D program. The cavity is designed to use demountable foils or copper blankoff plates and can be conditioned to very high gradient using the high power klystron test stand in the lab G facility at FNAL. The foils will be coated on one side with TiN and conditioning tests can be run with all copper surfaces, uncoated beryllium windows, coated beryllium windows or combinations of these. Windows of various thickness and with stepped profiles will be tested and the conditioning can be attempted with a wide range of magnetic fields from the existing superconducting solenoid.

18.4.2 2.75 m lattice implementation

The cooling channel lattice is a tightly packed assembly of equipment including liquid hydrogen absorbers, superconducting solenoids, high gradient RF cavities, instrumentation, vacuum equipment etc.. Initial studies show that it is possible to integrate all these components into the available cell length. Several iterations have been performed on this layout to try to make the most efficient use of the space. Constraints include the size of the RF cavities, which is dictated by the frequency, the size of the absorbers which is determined by the beam size, and the cell length, which has been fixed for this study at 2.75 m for the buncher and first cooling section and 1.65 m for the second part. This dimension can and should be reevaluated for subsequent studies. The size of the coil packs and cryostats have been chosen to allow practical current densities and the coil diameters have been kept as small as possible to minimize the amount of superconductor required and therefore the cost. The largest coil is the central one that must go around the RF cavities. The inner diameter of this coil has been left large enough to allow the cavity structures to pass through during assembly. The RF feeds must come out through the wall of the cryostat and may be angled to give clearance to other hardware. Pumping ports should be short and wide to give good conductance and may also penetrate the cryostat. Clearance is also required at the end of each cooling cell to allow for installation or removal of one absorber/RF module from the channel. This is achieved by using a collapsible flange in the outer cryostat wall, which is reinforced after it is made up in order to handle the possible magnetic forces. RF shields should be used to keep beaminduced signals from escaping into the outer cryostat and vacuum system.

Figure 18.P shows a possible cooling channel layout for the first lattice type including all major components except the beam instrumentation package, which may occupy the clearance opening at the end of each cell or the space between the RF cavities and the hydrogen absorber. The space in the cryostat outside of the cavities may be evacuated to minimize the load on the RF structures or to provide insulation if they are operated below room temperature. This would also obviate the need for UHV connections between each cavity and between the cavities and the hydrogen absorbers. The flanges would merely be required to provide RF continuity (for screening) and to separate the UHV of the RF system from the guard vacuum of the cryostat.

FIGURE 18.P. Cooling channel section 1, four cavities per cell

18.4.3 1.65 m Lattice Implementation

The 1.65m lattice for the downstream part of the cooling channel will use a similar layout to the upstream part but with smaller hydrogen absorbers and only two RF cavities per cell. The density of equipment is similarly high. The cavity lengths are closer to the optimum for this particle speed but could be improved in future studies if the cell length can be increased slightly. Figure 18.Q shows a possible cooling channel layout for the second lattice type including all major components except the instrumentation package, which may occupy the clearance opening at the end of each cell or the space between the RF cavities and the hydrogen absorber.

FIGURE 18.Q. Cooling channel section 2, two cavities per cell

18.4.4 402.5 MHz Buncher Cavity

The buncher harmonic cavities, figure 18.U, are smaller simpler versions of the 201.25 MHz cavities. They are rounded pillboxes and are closed by similar foils (or grids) that are smaller and thinner than the large cavities. There is adequate space for the cavities to be the optimal length for this particle speed. The power requirements are modest but cooling water should be used to stabilize the frequency and remove the small amount of average power dissipated in the walls. The harmonic cavities are installed in some of the buncher cells in the location where the hydrogen absorbers are placed in the cooling sections, i.e. inside the bore of the smaller solenoid coils. If required due to radial space constraints, the diameter of the cavity could be reduced slightly at the cost of a little more power and somewhat thicker foils.

FIGURE 18.U. 402.5 MHz buncher harmonic cavity

18.4.5 Tuning Requirements

Since there is negligible beam loading the tuning requirements for the cavities are simply to compensate for temperature variations due to water supply and RF heating. If we assume bulk water temperature fluctuations are of the order of 1C or less and a thermal expansion coefficient of copper of approximately 17 ppm/C then the frequency variation would be about 3.4 kHz. Since the average power is modest it should be easy to limit the temperature rise due to RF heating to 10C or less. A worst case cold start with the cavities around 0C and a normal operating temperature of 40C would produce a frequency detuning of about 136 kHz. Simple 2D calculations show that if the length of the cavity is varied about the nominal value the frequency sensitivity is about 236 kHz/mm so a small range of motion would be adequate to achieve the required tuning range. A tuning scheme similar to that used for the superconducting cavities where the cavity is mechanically stretched or compressed within elastic limits could easily achieve this range of motion. Alternatively a moving plunger tuner could be used to tune the cavity inductively but this would require an additional aperture in the cavity and may be harder to package within the confines of the cryostat.

It would also be possible to tune the cavities over a limited range by controlling the water temperature but the water stability would have to be a fraction of a degree to keep the frequency stable to within the bandwidth of the cavity (3.3 kHz unloaded, 6.6 kHz critically coupled). Each cavity would require an independent water circuit and controller, which may be impractical and expensive.

Depending on the elastic range of motion of the cavities it may be desirable to have some kind of "fixed" tuning after assembly to account for manufacturing tolerances (analogous to the "dimpling" of linac cavities). This could be a specific part of the cavity which is designated to be deformed or the cavity as a whole could be designed such that it can be stretched or compressed beyond the elastic limit to achieve a permanent tuning. If detailed

analysis shows that the cavity has a sufficiently large elastic tuning range it may be possible to relax the requirement of keeping the foils flat and allow some movement to take place. Precurving of the foils would ensure that this happens in a predictable manner. This would allow thinner foils to be used and the scattering to be reduced.

In the event that vibrations of the foils or other parts of the system should produce troublesome fluctuations in the RF fields the superconducting type tuner could be augmented with a fast piezoelectric actuator allowing feedback at audio frequencies. This has been demonstrated to reduce the effect of microphonics in superconducting cavities.

18.4.6 Vacuum Requirements

The operating vacuum in the high gradient cavities should be in the 108 Torr range or better. Operating much above this range is likely to produce more frequent arcing and would require significantly longer time to condition the cavities initially and after any vent. The reliability of the RF window is also strongly influenced by the vacuum level. The frequency of window arcs and the lifetime of antimultipactor coatings on the ceramic are both degraded by operating at pressures above about 107 Torr. These conditions will require strong pumping and good conductance to the RF cavities. Because of the presence of strong magnetic fields ion pumps may not be used in close proximity to the cavity during operation, though they may be useful during initial conditioning with solenoids off. Cryopumps or Titanium sublimation pumps may be useful close to the cavities with magnetic fields on. It may be advantageous to pump the cavities through the RF coupler if there proves to be sufficient conductance, since this will ensure the best possible vacuum at the window. A large diameter coaxial feed with a short distance to the pump may have sufficient conductance by itself. If not it may be supplemented by an additional pumping port on the cavity body. A thorough bakeout to above 150 C would be advantageous but may be incompatible with the superconducting solenoids in the same assembly. In that case the individual components may be baked separately before final assembly into the cryostat.

18.5 SCRF Specifications for Acceleration

Note this section will be updated due to changes in the SCRF layoutR.R.

Based on the high real estate gradient desired to minimize muon loss, superconducting cavities are selected to provide an active gradient of 15 MV/m, and a real estate gradient of 10 MV/m. At such high gradients, the peak RF power demand for copper cavities would become prohibitively expensive (15 MW per cell). By virtue of low losses, SC cavities can be filled slowly (rise time 2 3 mS) reducing the peak power demand to roughly half MW per cell for 3 mS rise time.

As a result of experience at LEP, CEBAF, TTF, Cornell, KEK and CEASaclay, the science and technology of superconducting cavities and associated technologies are highly developed. In all, SRF systems totaling one km in active length have been installed in a variety of accelerators and routinely operated to provide a total of 5 GV. The largest installation is for LEPII where 500 m of niobium coated copper cavities provide more than 3 GV of acceleration.

Although sheet metal Nb cavites used for TESLA are capable of providing gradients of the order of 15 MV/m and higher, we have chosen Nb/Cu technology developed at CERN for LEPII for several reasons:

1) Because of the lower RF frequency 201.25 MHz, and the accompanying thicker wall (e.g. 6 mm), the cost of raw sheet niobium becomes prohibitive (¿ 100 M$ at $500/kg) for the roughly 700 cells needed for Nufact.

2) High thermal conductivity copper provides better stability against quenching of superconducting cavities over sheet Nb. This is especially beneficial at 201.25 MHz because of the high stored energy per cell (roughly one kJ per cell at 15 MV/m).

3) The wall thickness of large size 201.25 MHz cavities may need to be greater than 6 mm for mechanical stability against atmospheric load and for reducing, Lorentz force detuning and microphonic effects from external vibrations.

4) A coated copper cavity allows the use of pipe cooling instead of the more usual bath cooling. Pipe cooling saves liquid helium inventory (estimated at 100,000 Liters for standard bath cooling of 700 cells). It also opens additional avenues for improving the mechanical stability for large scale cavities.

Recent results from CERN on 400 MHz Nb/Cu cavities (figure H1) reached accelerating gradients of 15 MV/m at 2.5 K at a Q of 2 x 109. Because of

the lower frequency for Nufact, we can expect the Q to be four times higher. We have chosen an operating temperature of 2.5 K and a Q value of 6x109. LEP results at 4.5 K when scaled for the lower frequency will imply a much lower Q ¡ 2x109. And LEP cavities have never reached Eacc = 15 MV/m at 4.5 K.

Modeling the Q vs. E obtained for LHC 400 MHz cavities (figure H1) and incorporating the Q increase for 201.25 MHz, ANSYS studies conclude that it will not be possible to reach Eacc = 15 MV/m at a Q of 6 x109, unless the operating temperature is reduced to 2.5 K, see figure H2.

FIGURE H1. Qo vs. gradient for Nb/Cu CERN cavity.

FIGURE H2. Qo vs. gradient expected for 201.25 MHz cavity.

Accelerator physics studies show that an aperture of 300 mm (diameter) is acceptable for the neutrino factory except for the first 700 MeV (?) of the preaccelerator linac, where an aperture of 460 mm has been chosen. Because of the higher peak fields arising from the larger aperture the gradient for the first section of the preaccelerator has been reduced to 10 MV/m.

In selecting the RF pulse length (Trf), a tradeoff must be made between peak RF power on the one hand with refrigerator load, tolerance to microphonics and to Lorentz force (LF) detuning on the other hand. Increasing Trf will lower the peak power, but increase the average RF power and the refrigeration load. Increasing Trf will also drive QL toward higher values, decreasing the cavity bandwidth and thereby increasing its sensitivity to LF detuning and microphonics. The peak RF power (Ppk) needed to establish the fields depends on the stored energy (U), cavity time constant () and the amount of detuning expected from Lorentz force and microphonics as follows:

Once the fill time and detuning tolerance are selected, the loaded Q of the cavity can be found to minimize the peak power required. A conservative estimate for detuning tolerance in these large 201.25 MHz structures is 40 Hz. Cavities at TTF and CEBAF show microphonic excitation of ¡ 10 Hz. For a fill time of 3 ms, the optimum QL is 1x106 (bandwidth = 200 Hz) and the required peak power is 395 kW per cell for the small aperture case. Coaxial couplers developed for the KEKB factory have delivered 380 kW CW to one amp beams. In pulsed mode, higher power performance can be expected. For a wall thickness of 8 mm, the Lorentz force detuning at 15 MV/m is 100 Hz. Most of this can be taken care of with feedforward techniques developed at TTF for TESLA.

Future R&D on structure stiffening, feed forward, and active tuning to compensate LF detuning and microphonics could lower the required peak power by reducing the detuning tolerance. For example if the detuning tolerance can be lowered to 20 Hz, the input power drops to 350 kW per cell and optimum QL rises to 1.5 x106. Going further in this direction and adopting a 4 ms fill time would decrease input power to 270 kW per cell at best QL = 1.5 x106

18.5.1 SCRF Structures at 201.25 MHz

To improve the realestate gradient it is important to have a large filling factor of cavities in the cryomodule. This pushes structures towards multicell cavities. On the other hand, because of the low frequency and high gradient, the coupler power and stored energy per structure increases with number of cells. Tradingoff between these factors, 2cell units at 15 MV/m are chosen for most of the neutrino factory. In the first 700 MeV of the preaccelerator linac, where gradients are lowered to 10 MV/m, 4cell units are selected. The input coupler power is kept at the 400 kW level by providing one coupler at each end for both 2cell and 4cell units.

Figure H3. Twocell geometry Figure H4. 4cell geometry

The performance of a superconducting cavity depends on the peak surface fields. Minimizing Epk is important to avoid field emission that lowers the cavity Q and increases heat load. Minimizing Hpk is also important, since the Q of Nb/Cu cavities falls with surface magnetic field, one of the characteristic

features of Nb/Cu cavities (figure H1). In the CERN 400 MHz LHC cavity which reached Eacc = 15 MV/m, the corresponding peak surface fields were Epk = 33 MV/m and Hpk = 750 Oersted. Because of the relatively smaller beam pipe of the 201.25 MHz, 2cell cavity it is possible to optimize the neutrino factory cavity geometry (see figure H3) to reduce the peak fields by 30% below LHCcavity values. Relative to CERN cavity performance there is adequate safety margin through improved structure choice. Table H1 lists the properties of the 2cell unit and Table H2 for the 4cell units. Figure H3 shows the 2cell geometry and figure H4 shows the 4cell geometry.

Table H1cell cavity parameters

RF freq	MHz	201.25
No. of cells per cavity		2
active cavity length	m	1.5
number of cavities		300

linac

92

RLA

208

aperture diameter

mm

300

Eacc

MV/m

15

Energy gain per cavity

MV

22.5

240

stored energy per cavity

Joule

1563

R/Q

Ohm/cavity

258

Ep/Eacc

1.43

Hp/Eacc

Oersted/MV/m

38

Epk at 15 MV/m

MV/m

21.5

Hpk at 15 MV/m

241

	Oe
	570
Q0	
	6x109
Bandwidth	
	Hz
	200
Input power per cavity	
	kW
	800
RF ontime	
	ms
	3
RF duty factor	
	%
	242

4.5

Dynamic heat load per cavity

watt

14.7

Operating temperature

K

2.5

QL

106

Microphonics Detuning tolerable

Hz

40

Wall thickness

mm

8

243

Lorentz force detuning at 15 MV/m	
	Hz
	100

Table H2. 4cell cavity Parameters

RF freq	
	MHz
	201.25
No. of cells per cavity	
	4
active cavity length	
	m
	3
number of cavities	
	26

aperture dimater

mm

460

Eacc

MV/m

10

Energy gain per cavity

MV

30

stored energy per cavity

Joule

1584

R/Q

Ohm/cavity

452

Ep/Eacc

1.94

Hp/Eacc

Oersted/MV/m

46

Epk at 10 MV/m

MV/m

19

Hpk at 10 MV/m

Oe

460

Q0

6x109

Bandwidth

Hz

200

Input power per cavity

kW

800

RF ontime

ms

3

RF duty factor

%

4.5

Dynamic heat load per cavity

watt

14.9

Operating temperature

K

247

2.5

QL

106

Microphonics Detuning tolerable

Hz

40

Input Power Coupler

The antenna type coaxial design will be chosen based on the successful experiences of CERN (LEPII), DESY (HERA and TTF) and especially the success of the KEK input coupler for KEKB. Figure H6 shows the dimensions of the KEK, 508 MHz coupler, which will be scaled proportionately to 201.25 MHz. The lengths of the various sections will be adjusted to fit the final cavity and cryostat designs adopted. The waveguidetocoaxial transition is of the doorknob variety. As in all high power applications, the main window will be at room temperature and remote from the cavity. At KEKB, it is a disk shaped, water cooled, 95% pure alumina ceramic with a central hole for the inner conductor. Figure *(no figure yetBob)* shows the window in more detail. A teflon coaxial centering disk between the window and doorknob serves to limit the flow of air to the cavity in the unlikely event of a ceramic

window break. The inner conductor is made of OFHC copper pipe and is water cooled. The outer conductor is made of copper plated (30m) stainless steel and has fins cooled by a 4.5 K stream from the refrigerator (Fig.). This reduces both the dynamic and static coupler associated heat leaks.

Benefitting from simulation codes recently available for calculating and avoiding multipacting, the dimensions of the inner and outer conductor will be chosen so that multipacting will not be a serious problem. The coaxial design also permits application of a DC bias voltage between the two conductors to curtail any possible multipacting that may develop near the window or other sensitive regions.

The coupler will be equipped with standard diagnostics for vacuum, gas species, temperature and light monitoring. Vacuum and light levels can be used to trip the RF in case of an arc.

The Q_{ext} value of the input coupler can be fixed after initial adjustment of the position of the inner conductor by the use of appropriate spacing washers during final assembly. From experience at KEK we expect that the Q_{ext} for the nonaccelerating modes of the fundamental pass band will be of the same order as the Q_{ext} for the accelerating mode, i.e. a few x105.

The design of the input coupler will be finalised during the prototyping stage and will be based on the KEKB coupler.

Figure H6. KEK 508 MHz coupler

Higher Order Mode (HOM) Couplers

The function of the HOM couplers is to damp the higher order modes to Q_{ext} values of 10^4 10^5 to prevent resonant build up of beam induced fields that may make the beam unstable or increase the HOM power. The HOM couplers extract beam induced HOM power from the cavity and deposit it at room temperature loads. Because of large muon bunch length we do not expect HOM's to be a serious issue.

Two couplers are needed with a relative azimuthal angle of about 90 degrees to ensure damping of both polarizations of dipole modes. One coupler is attached to each end of the cavity. The HOM couplers must reject the accelerating mode by means of a filter.

Detailed calculations will be carried out during the prototyping stage for the HOM spectra, possible trapped modes, and expected HOM power. Codes exist and procedures have been well established for electron applications.

A possible candidate is loop type coupler (figure H7) because it is demountable, compact, has relaxed mechanical tolerances, and demonstrated performance in mode damping. The plane of the loop is orthogonal to the beam axis. The loop couples mainly to the magnetic field of dipole modes and mainly to the electric field of longitudinal modes. The rejection filter is formed by the inductance of the loop and the capacity between the loop end and the outer conductor. A capacitive coupling links the loop to the external load via a type N connector. The loop is cooled by conduction through an upper stub. Final tuning of the filter can be carried out outside the clean room once the coupler is attached and the cavity sealed. Q_{ext} values are typically 103 to 105 for high impedance modes in a 9cell TELSA cavity. These Q's will be even lower for the neutrino factory 2cell and 4cell cavities.

Power tests carried out under CW operating conditions showed good thermal behavior up to an accelerating field of 21 MV/m in TESLA cavities.

The design of the HOM couplers will be finalized during the prototyping stage and will be based on successful HOM coupler designs for the TESLA test facility (TTF).

Figure H7. TESLAtype HOM coupler

Tuner

The function of the tuner is to match the cavity resonance frequency with the desired accelerator operating frequency. If the cavity is not being used for acceleration, the tuner must detune the cavity frequency a few bandwidths away from resonance, so that the beam will not excite the fundamental mode. During accelerator operation the tuner must correct for slow changes in the cavity frequency due to changes in the liquid helium bath pressure, or in the lengths of the cavity and He vessel support system. Tuning is achieved by varying the total length of the cavity so that the field flatness is preserved. The tuning coefficient of 2cell cavity is of the order of 50 Hz/m. Plunger tuners are not advisable in superconducting cavities because of moving parts and the danger of dust introduction.

If a mechanical tuner is adopted, the length of the cavity will be controlled by an electromechanical system acting differentially with respect to the cavity body. If each cavity is enclosed in its own helium vessel the latter must have some flexibility built in.

A mechanical tuning system is generally composed of a stepping motor, gear box, a screw and nut assembly, and a lever arm with a flex mechanism attached. A piezo electric element can be added for fine tuning, controlling Lorentz force detuning, figure H5, as well as reducing microphonics. Figures H12 and H13 show the vibrational modes of the twocell and 4cell cavities that could be excited by vibrations. The stiffness will be increased to raise the frequencies of these modes.

Figure H5. Lorentz force detuning

Figure H12. Vibrational mode of 2cell cavity

Figure H13. Vibrational modes of fourcell cavity

Alternatively a thermal tuner will be considered modeled after the LEP system. This uses three Ni tubes as tuner bars located in the cryomodule insulation vacuum. The tuner rib cage can also help raise mechanical resonant frequency of cavity longitudinal modes. For slow tuning in one direction (constriction) the temperature of the tubes is lowered by flowing cold helium gas For tuning in the opposite direction the temperature is raised by centrally located electric heaters. The typical tuning speed is 10 Hz/sec. Heat losses are minimized by counter flow cold He gas through the tuner tubes. For fast tuning coils can be wound around the Ni tubes to produce a magnetic field which changes the length of the tubes by the magnetostrictive effect. Rapid (ms) tuning ranges of kHz are possible.

Tuners are an active part of the complete RF control system, which stabilizes the frequency, amplitude and phase variations induced by sources such as the RF drive, beam current variations, Lorentz force detuning, and microphonics.

The design of the tuner will be finalized during the prototyping stage and will be based on several successful tuner designs in operation for CEBAF and TTF.

18.5.2 Cryogenics for SCRF

Figure H8 shows a 3D cad model of the long cryomodule with four, 2cell units and Figure H9 shows a short cryomodule with one, 4cell unit. Each cavity has two input couplers, one on each end, and two HOM couplers, also one on each end. Mature cryomodule designs (see figure H10), available at CERN for LEPII and LHC will be adapted to the neutrino factory needs during the prototyping stage. Thin beryllium windows will be placed on the beam line at each end of the cryomodule to protect the cavity vacuum and to keep the cavity surfaces clean during installation into the beam line. Tables H3 and H4 give some cryomodule parameters.

Figure H8. Long cryomodule

Figure H9. Short cryomodule

Figure H10. LEP cryomodule

Table H3. Short Cryomodule Parameters

No. of cryomodules	

No. of cavities in one cryomodule	

One 4cell

No. of input couplers

2

Overall length

6 m

Active length

3 m

Cavity dynamic heat load @2.5 K

15 W

Couper dynamic heat load @2.5 K

1 W

Coupler static heat load @ 2.5 K, 5 8 K, 40 80K

2 W, 4 W, 40 W

Cryomodule static heat load @ 2.5 K, 5 8 K, 40 80 K

2 W, 30 W, 300 W

Total 26 cryomodule heat load @ 2,5, 58 K, 40 80 K

520, 880, 9000 W

Table H4. Long Cryomodule Parameters

No. of cryomodules

75

No. of cavities in one cryomodule

Four 2cells

No. of input couplers

8

Overall length

12.5 m

Active length

6 m

Cavity dynamic heat load@2.5 K

4x 15 = 60 W

Couper dynamic heat load @2.5

8 x 0.5 = 4 W

Coupler static heat load @2.5, 58, 40 80 K

8, 16, 160 W

Cryomodule static heat load @ 2. 5K, 5 8, 40 80 K

5, 60, 600 W

Total 75 cryomodule heat load @ 2.5, 5 8 , 40 80 K

5800, 5700, 57,000 W

Hasan

The structure of this section could resemble the same section in feasibility study I, except for modification of heat load tables.

The refrigeration section needs to be modifed to reflect a 2.5 K system. The 4.5 K system will not meet gradient and Q specs. The heat load tables need to be modified according to the cryomodule heat loads given above.

The total cryomodule heat load is 6.3 kW at 2.5 K, 6.6 kW at 5 8 K, and 66 kW at 40 80 K. Each of these numbers needs to be multiplied by a safety factor. Usually refrigeration system designers chose a safety factor of 1.5.

For SRF the refrigerator plant needed is 9 kW at 2.5K, 10 kW at 5 8 K, 100 kW at 40 80 K.

Assuming refrigerator inefficiencies of 600, 250, and 20 at 2.5, 6 and 60 K, the total AC power equivalent for SRF refrigeration is 10 MW

18.5.3 RF Power Source for SCRF

Al

The superconducting linac and recirculating linear accelerator (RLA) designs employ a total of 288 cavities. The linac contains 120 cavities running at a gradient of 17 MV/m. The early part of the linac operates at a gradient of 15 MV/m. The remaining cavities all run at a gradient of 17 MV/m. The RF pulse length is 3 ms and the average repetition rate is 15 Hz, although the recovery time between pulses is only 20ms. Each cavity is driven by two 500 kW couplers. With a 20% RF power overhead, this works out to 1.2 MW per cavity and a total RF requirement of 346 MW.

An examination of the average power requirement demonstrates that a very high efficiency source is required. The best candidate for the required source again is a multibeam klystron (MBK). This could be the same basic design as that used for the NCRF but with increased thermal capacity to handle the increased average power. However DESY has developed a 7 beam MBK with an efficiency near 70%. Scaling this design to 201.25 MHz would produce a 5 MW, 25 beam MBK with each beam having a perveance of 5×10^{5}. The tube with gun and collector would be about 5.7 m in length and could be manufactured by industry after some initial R&D.

Each tube will drive four cavities through 8way power splitters. The specifications for the modulator, an IGBTtype like the NCRF, are 50 kV at 142 A and average power of 320 kW. To save costs the modulator will be

designed to operate two 5 MW tubes requiring twice the current and average power rating. A total 72 tubes and 36 modulated are required to supply the RF power requirements.

The multibeam klystron may be designed with a vaporcooled collector to save on the cooling water requirement. Such a system is at least 10 times more efficient than conventional water cooling. With vapor cooling each tube will require 120 gpm of near room temperature cooling water with total installed capacity of 8,640 gpm. Assuming an efficiency of 95% each modulator station will require 675 kW of installed AC power for a total of 24.3 MW.

The cost of a 25beam MBK with shared modulator would be about 18 % higher than that for the NCRF system, or about $1.95 M for each klystron and $140.4 M total.

18.6 Conclusion

The normal conducting and superconducting systems have continued to evolve since study I. Both cavity designs have been studied in some detail and feasible solutions have been developed for the required cooling channel and acceleration parameters. Ongoing R&D programs are addressing the practical aspects of cavity fabrication and conditioning. No fundamental "showstopping" problems have arisen. The cooling channel layout, though densely packed has shown the feasibility of assembling all of the vital components. There is room for further optimization of the cooling channel, notably by adjusting the total cell length, to reduce the RF power requirements and minimize the superconducting magnet costs. The superconducting RF accelerating section has been developed using design choices that are consistent with the state of the art at various laboratories around the world.

An ongoing R&D program is in place to demonstrate the practical implementation of these NCRF and SCRF technologies at 201.25 MHz.

18.7 References

18.1. R.A. Rimmer, N. Hartman, D. Li, Al. Moretti, T. Jurgens
"ClosedCell 201.25 MHz RF Structures for a Muon Cooling Channel",
Submitted to PAC 2001

18.2. N. Hartman, D. Li, J. Corlett, "Thin Beryllium Windows Analysis and Design Status", MUCOOL 180

Cost estimate?

Bob, Al, Hasan

It will cost a lot...

Appendix: RF options

NCRF R&D

Nitrogen cooling

Grids vs Foils vs precurved thin foils vs?

RF for single flip channel?

Alternative power sources?

SCRF R&D

The history of SRF development for LEP, CEBAF, CESR, KEKB and TTF (TESLA) shows that it takes many years to design, prototype and test structures in order to be ready for production. The lowest frequency at which SRF cavities have been made for accelerating velocity of light particles is 350 MHz. Therefore R&D and prototyping for a neutrino factory at 201.25 MHz should be started at least five years in advance.

At present SRF R&D is in progress to address the following issues

Achieve 15 MV/m at Q of 6 x109 in a single cell 201.25 MHz cavity

Stiffen the 2cell and 4cell cavity design to reduce Lorentz force detuning and microphonics sensitivity

Explore pipe cooling to reduce liquid He inventory and stiffen multicell structures

Reduce structure cost

A collaboration has been set up with CERN to produce a onecell Nb/Cu cavity at 201.25 MHz. CERN will provide the copper cavity, coat it with 1 2 micron thick niobium film by their standard DC magnetron sputtering technique, and send it to Cornell for testing after high pressure rinsing and evacuation. To test the cavity Cornell is upgrading its facilities. Figure H11 shows a 3D cad model of the CERN cavity inside the test dewar. A test pit 2.5 m diameter by 5 meter deep is under excavation to accommodate the test dewar, which has been ordered. A 201.25 MHz low power (2 kW) RF test system is under construction. The clean room and high pressure rinsing system are being upgraded to accomodate the large cavity.

ANSYS calculations have started on the 2cell and 4cell cavities to determine the mechanical resonant modes and frequencies. The resonant frequencies are low (See figures H12 and H13). Exploration has started on stiffening schemes with and without pipe cooling.

At 201.25 MHz, structure costs will be substantial. Multicell cavities are usually fabricated in parts that have to be machined, cleaned and electron beam welded. This is an expensive, labor intensive process. We are collaborating with INFN in Italy to spin monolithic copper cells out of a single tube. INFN has experience at 1300 MHz. As a first step they will spin a

single cell 500 MHz cavity. In a future stage, the procedure will be extended to 201.25 MHz and multicell cavities.

Figure H11. Vertical dewar test

R&D and Protoyping

The goal would be to design, construct and high power test a cryomodule with the first single cell 201.25 MHz cavity, equipped with couplers and tuners. To prepare this test continuing R&D, design and prototyping are necessary in the following areas:

high power input coupler
higher order mode coupler
mechanical/thermal tuner
piezo /magnetostrictive tuner
cryomodule
system integration
high power test

Chapter 9

Cryogenic Systems (7 pages in studyI)

Chapter 10

Power Supplies

Chapter 11

Instrumentation

J. Norem
STUDY II Instrumentation for the Neutrino Source

11.1 Introduction

We discuss unique features not included in subsystem instrumentation, i.e. Vrf, ?rf etc.

11.1.1 Target monitoring issues

- Beam on target

  Beam measurements Target measurements

- Magnet structure (Gohar)

  1. Radiation damage failure modes
  2. Monitoring issues

- Magnet coolant (Bartels/Cline)

  1. Corrosion rates determined by ionization in the water
  2. Mitigation methods suggested
  3. Measurement

11.1.2 Phase Rotation / Bunching Line

11.1.3 Cooling line (jn, Solomey, et. al.)

Constraints: Most of the new problems are involved with the cooling line Profile monitors with intensity measurements should be sufficient jn, ns Limited variables require a somewhat minimal instrumentation set Don?t try to measure emittance at each section Emittance measurements are difficult and imprecise Measurements of ?T and ?L by profile ? phase advance - profile Emittance matching will be a problem Mismatches (beta functions) Breathing modes etc. (LANL data) Paul Lebrun Alignment Pencil beams

11.1.4 Special diagnostic sections jn

Beam profile is required Angular momentum measurements may be necessary How do we tune L=0 at the end? Chun-xi Background measurements are required Backgrounds are not a major problem X ray / Dark Current Backgrounds (old and new data) High energy particles need numbers from Mokhov, Simone Norem Intensity measurements are hard, need not be high precision Loss monitors are hard (lost particles don?t splash) range/mom Timing is very useful for measuring ?L and bucket filling Tune up and running instrumentation may be different Muon cooling demonstration has tougher instrumentation problems Weaker signals The same backgrounds Space and access are very limited and close to rf (sketch) Rf induced backgrounds are severe Strong B field Components should be removable from beam, and vacuum chamber Black Components are large and require big valves Component heating by the beam is significant How do we measure polarization? Tough at these very low energies ?

11.1.5 Instrumentation Options

Faraday cup / SEM systems jn, ns Properties and constraints Geometries and options, exp data Rigid structures Onel Scintillators Solomey Properties Ion chambers Mayda Transition radiation? Solomey Measurements in LH2Bolometers Oreglia, Cerenkov options Summers, Blondel Timing techniques Bross, Semiconductor arrays Plicidi

11.2 Accelerator issues (Lebedev, Berg)

Tuning with large beams, use of pencil beams Transfer functions, loss monitors

11.3 Storage ring issues (Parker, Goodman)

Measurement of beam intensity with high precision Synchrotron mesurements of muon intensity (. Morse)

11.4 Costs

Total types, numbers, costs for the facility the cooling line: instrumentation in the rest of the facility Cost Algorithm

11.5 Required R & D

Concerns with cooling line instrumentation: Radiation damage from x-ray / dark currents Lifetime of components in the Beam Heating of compononts

A possible way of introducing instrumentation.

Chapter 12

Conventional Facilities (10 pages in studyI)

Chapter 13

Environment, Safety and Health Considerations (10 pages in studyI)

Chapter 14

R & D Plans

M. Zisman

Chapter 15

Detectors

E. O'Brien

15.0.1 Introduction

The Neutrino Factory will open up a regime of neutrino physics which is inaccessable at existing facilities. When combined with a multi-kton detector located at a large distance, the proposed accelerator will allow the study of a number of unexplored neutrino oscillation parameters. A factory plus long-baseline detector will have a physics program that meshes well with ongoing and near-future neutrino oscillation experiments, and will potentially enable physicists to determine values for all remaining unknown physical constants associated with current neutrino oscillations theory.

The features of the facility that allows these challenging oscillation measurements are a high neutrino intensity, well-focused beam, precise understanding of beam composition and spectra, and optimized energy. In addition, detector facilities located in experimental areas near the neutrino source will have access to integrated neutrino luminosities 10^4 - 10^5 times larger than previously available (10^{20} neutrinos/year vs 10^{15} - 10^{16}). Standard neutrino physics at this facility could include physics topics such as precision $\sin^2\theta_W$, structure functions, high precision neutrino total CC cross sections at low $\sqrt{s}$ (a few GeV), nuclear effects (shadowing at low x, anti-shadowing...), pQCD, and neutrino magnetic moments. These topics have relevance for standard model physics, nuclear physics, astrophysics and physics beyond the standard model. Finally, the Neutrino Factory will serve as a test accelerator for a high intensity muon accelerator and so is an R&D facility that is absolutely necessary if there is to be a muon collider in the future.

15.0.2 Beam Parameters

The neutrino beams produced at the Neutrino Factory is either (ν_μ,$\bar{\nu}_e$) or ($\bar{\nu}_\mu$,ν_e) depending on whether the machine is running μ^- or μ^+. The characteristics of the machine design guarantee that the beam is pure, with no contamination from anti-particles of the same neutrino flavor. The design luminosity is L = 10^{20} μ decays/year where a year is defined at 10^7 seconds. The angular dispersion of the ν-beam is 5.3 mradians with a momentum spread of 30% RMS. The two long-baseline target sites considered in this report are the Waste Isolation Pilot Plant (WIPP) located in Carlsbad, New Mexico and Soudan, Minnesota. WIPP is located 2900 km from Brookhaven National Lab and requires a 13.1° dip angle in the muon storage ring, while Soudan is 1700 km from BNL and requires a 7.7° dip angle.

Based on design parameters in this report, the expected event rates at the two possible sites are:

E_μ (GeV) Muon Ring	Baseline (km)	E_{ν_μ}	E_{ν_e}	N(ν_μ CC) (per kt-year)	N(ν_e CC) (per kt-year)
$10_{BNL-SOU}$	1700	7.5	6.5	260	120
$20_{BNL-SOU}$	1700	15	13	2150	960
$20_{BNL-WIPP}$	2900	15	13	740	330

15.0.3 Physics Signals

Neutrino mixing can be described by the lepton CKM matrix:

$$U = U_{23}U_{13}U_{12} = \begin{pmatrix} 1 & 0 & 0 \\ 0 & c_{23} & s_{23} \\ 0 & -s_{23} & c_{23} \end{pmatrix} \begin{pmatrix} c_{13} & 0 & s_{13}\exp^{i\delta} \\ 0 & 1 & 0 \\ -s_{13}\exp^{-i\delta} & 0 & c_{13} \end{pmatrix} \begin{pmatrix} c_{12} & s_{12} & 0 \\ -s_{12} & c_{12} & 0 \\ 0 & 0 & 1 \end{pmatrix}$$

The possibility of light sterile neutrinos is not considered here. Three-flavor neutrino oscillations can be described by seven parameters, three ${\Delta m_{ij}}^2$ terms, three mixing angles θ_{ij}, and a CP violating term δ. The mass parameters are related by the simple identity ${\Delta m_{12}}^2+{\Delta m_{23}}^2+{\Delta m_{31}}^2=0$. SuperKamiokande has measured what appears to be non-zero values for ${\Delta m_{23}}^2$ and θ_{23} in atmospheric neutrinos. Over the next few years both K2K and MINOS will try to confirm the SuperK observation with accelerator based experiments and obtain accurate values for ${\Delta m_{23}}^2$ and θ_{23}. The ν-oscillation parameters ${\Delta m_{12}}^2$ and θ_{12} are the province of solar and reactor based experiments either now running or planned for the next several years. The values of these parameters hopefully will be measured over the next 5-10 years. A long baseline experiment at the neutrino factory will be able to measure θ_{13}, the sign of ${\Delta m_{23}}^2$ and possibly the CP violation term δ, providing θ_{13} is large enough. Depending on the values of the various neutrino parameters it is conceivable that the neutrino factory will be in a position to measure all the remaining outstanding neutrino mixing parameters. Additionally, a long baseline neutrino detector should be able to make the first direct measurement of the neutrino-matter oscillation effect (MSW). It would study MSW and could make a model independant measurement of the matter parameter A, where $A = \sqrt{2}G_F n_e$. Measurements of A with 10% accuracy are possible and may even be of interest to geophysicists.

15.0.4 The Long Baseline Oscillation Experiment

The characteristics of a Neutrino Factory beam, $\nu_\mu, \bar{\nu}_e$ with no $\bar{\nu}_\mu, \nu_e$ contamination, naturally lend themselves to a neutrino appearance experiment. Since a μ^- beam at the neutrino factory will not result in any initial production of $\bar{\nu}_\mu$, a $\bar{\nu}_\mu$ signal will be due to $\bar{\nu}_e \rightarrow \bar{\nu}_\mu$ oscillations. An experiment designed to look for $\bar{\nu}_\mu$ CC events measures $P(\bar{\nu}_e \rightarrow \bar{\nu}_\mu)$

$$\text{Where:} \qquad P(\bar{\nu}_e \rightarrow \bar{\nu}_\mu) = \sin^2 2\theta_{13} \sin^2 \theta_{23} \sin^2(\Delta {m^2}_{13} L/4E)$$

A program to study both $P(\bar{\nu}_e \rightarrow \bar{\nu}_\mu)$ and $P(\nu_e \rightarrow \nu_\mu)$ not only gives us access to θ_{13} but also tells us the sign of the $\Delta {m_{23}}^2$ and allows us to measure the matter parameter A (fig. 15.1).

It is interesting to note that the matter parameter becomes accessable only when the beam has passed through a significant amount of material. Calculation show that the BNL-WIPP distance of 2900 km is far enough for the MSW effect to be measureable.

As stated earlier, if both the CP violating term δ and θ_{13} are large enough they maybe disentangled in these measurements. In addition, a spectral scan on the oscillation probabilities would potentially improve the precision of the $\Delta {m_{23}}^2$ and θ_{23} measurements by nearly an order of magnitude [**?**].

The experiment's concept is to look for a $\nu_\mu(\nu_\mu)$ appearance at the distant detector in a beam that initially has no $\nu_\mu(\nu_\mu)$. Measuring $P(\nu_e \rightarrow \nu_\mu)$ and $P(\bar{\nu}_e \rightarrow \bar{\nu}_\mu)/P(\nu_e \rightarrow \nu_\mu)$ gives one access to the oscillation parameters described above.

One typically does a $\bar{\nu}_\mu$ appearance experiment by looking for the leading μ^+ from the $\bar{\nu}_\mu$ CC reaction in the detector. The challenge in a search for $\bar{\nu}_\mu$ events is primarily threefold. One must distinguish μ^+ from the μ^- coming from the non-oscillating ν_μ's, separate μ^+'s from π^+ punchthru's and reject μ^+'s coming from hadronic decay's. Another potential background which depends on the detector's environment is accidentals from either cosmics or some background radiation.

There are a number hadronic decay backgrounds for the μ^+ signal. They are:

- ν_μ CC where the primary μ^- is missed and one see the μ^+ from hadronic decay of the π^+, K^+ or D^+.

- ν_e CC where the primary e^+ is missed and one sees the μ^+ from hadronic decay of the π^+ or K^+. The D^+ is not a significant concern here.

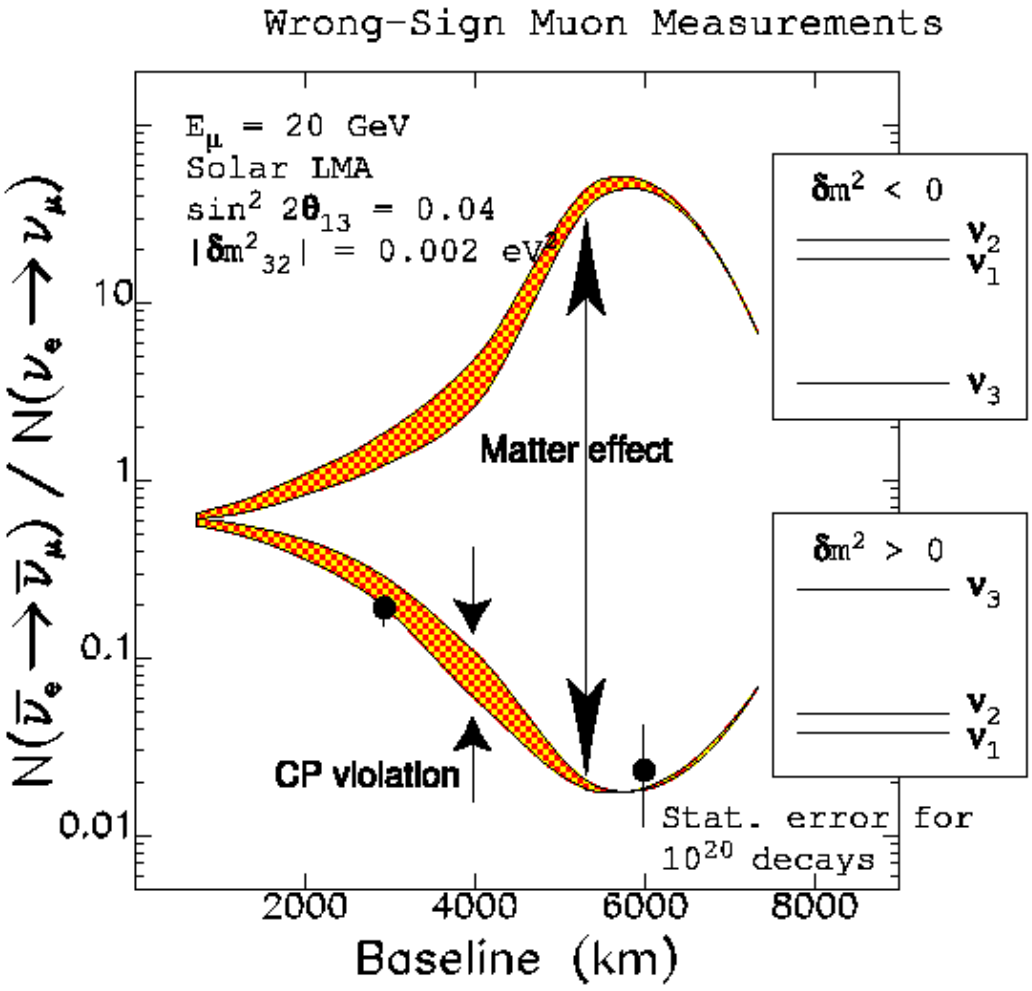

Figure 15.1: Measuring the ratio of $P(\bar{\nu}_e \rightarrow \bar{\nu}_\mu)$ to $P(\nu_e \rightarrow \nu_\mu)$ enables one to measure the sign of $\Delta {m_{23}}^2$ and the value of the matter parameter A.

- ν_μ,ν_e NC where π^+ and K^+ again causes problems.

The requirements to measure both the signal and reject the background determine a number the detector's characteristics. The measurement of the sign of the muon is critical to the experiment which means the detector must contain a magnetic field. Obtaining the muon spectrum is also important and can be done either through bending in the spectrometer or range using using dE/dx. Separation of μ's from π's is accomplished through range-out in many interaction lengths of material. Rejection of hadronic backgrounds requires a combination of momentum, p_t and isolation cuts. A detailed investigation of these background was carried out in Study I [**?**]. It was determined that to make the background managable a detector will require both momentum resolution and transverse segmentation (See figures 15.2, 15.3, 15.4). Rejection of accidental backgrounds can be handled by a detector with moderate timing resolution. Timing resolutions on the order of 100 nsec would allow the experiment to only take events in phase with the machine spill structure, and so reject accidentals by a factor of 200. A timing resolution of 10 nsec gains an additional factor of two background reject by allowing a direction cut. Finally, the neutrino event rates seen in Table 1 indicate the need for the detector to be multiple Ktons.

15.0.5 Detector Options

The specifications for the long baseline neutrino factory detector are rather typical for an accelerator-based neutrino experiment. However, because of the need to maintain a reasonable neutrino rate at these long distances the detector proposed are between 3 and 10 times more massive than those in current neutrino experiments.

Large mass detector designs are driven primarily by cost of the absorbers. Limiting the detector's cost drives us to two basic options: steel-based and water-based designs. The two detector options considered for the WIPP site in this study are a 50 kTon Steel/Scintillator/Proportion Drift Tube(PDT) detector and a Water Cerenkov Detector. The detector considered for the Soudan site, a 15 kTon Steel/Scin./PDT detector is discussed in an appendix to this document.

The Steel/Scin./PDT detector would resemble MINOS. The steel absorber plates would be between 10 - 20 cm thick, magnetized with a toroidal field to 1 - 1.5 T. A combination of PDT's and Scintillator slats would be

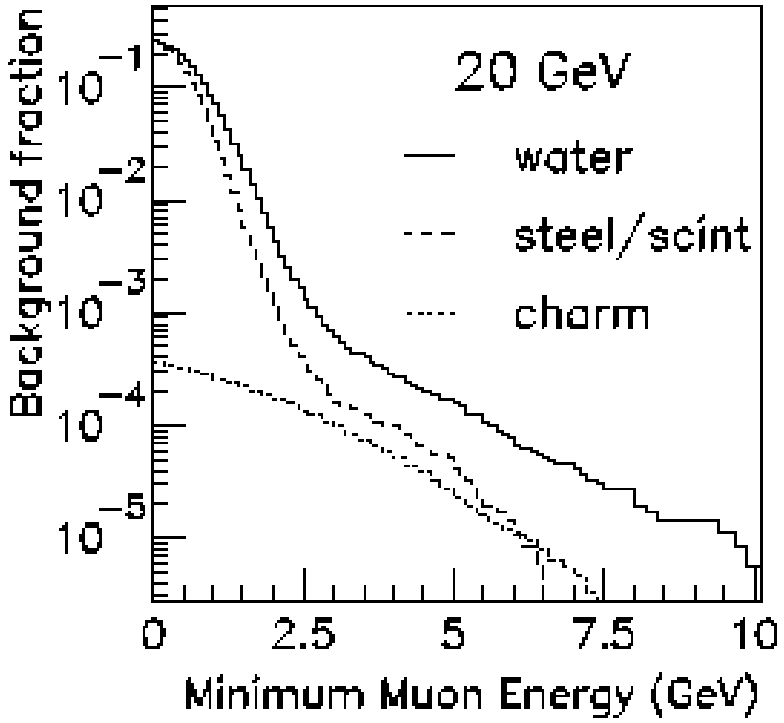

Figure 15.2: Fraction of neutrino events that produce a background signal as a function of minimum muon energy. Background sources as π and K decays, π punchthru and Charm decays.

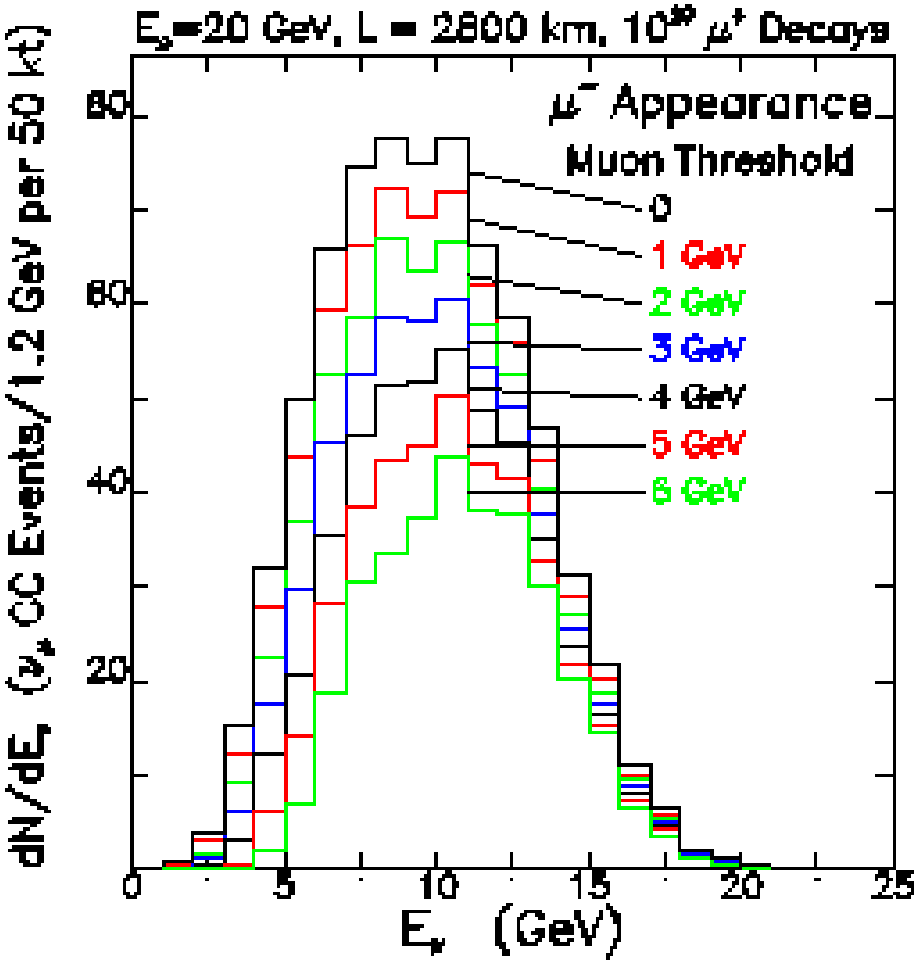

Figure 15.3: Reconstructed neutrino energy distribution for several different minimum muon energy cuts. Note that a minimum muon cut at 4 GeV reduces the signal by 30-35%.

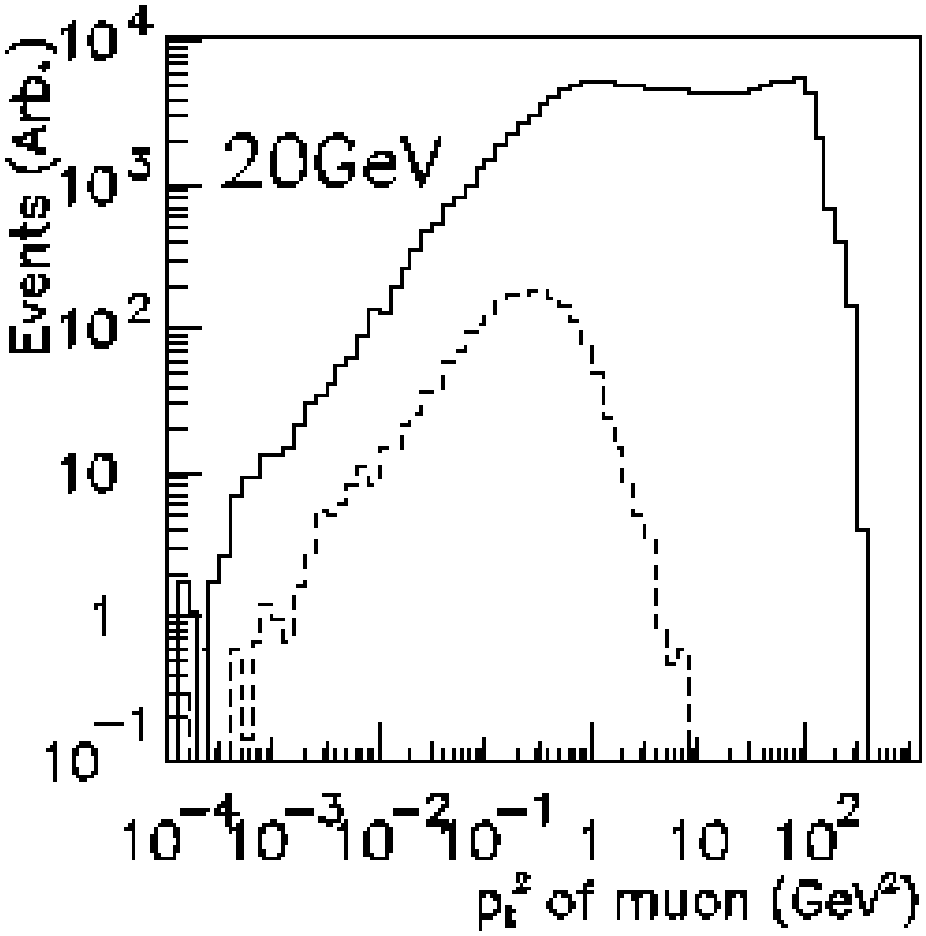

Figure 15.4: Distributions of the square of the muon momentum component transverse to the hadronic shower p_t^2 direction for ν_μ CC events (solid line) and background muons (dashed line). The effectiveness of a transverse cut can be seen.

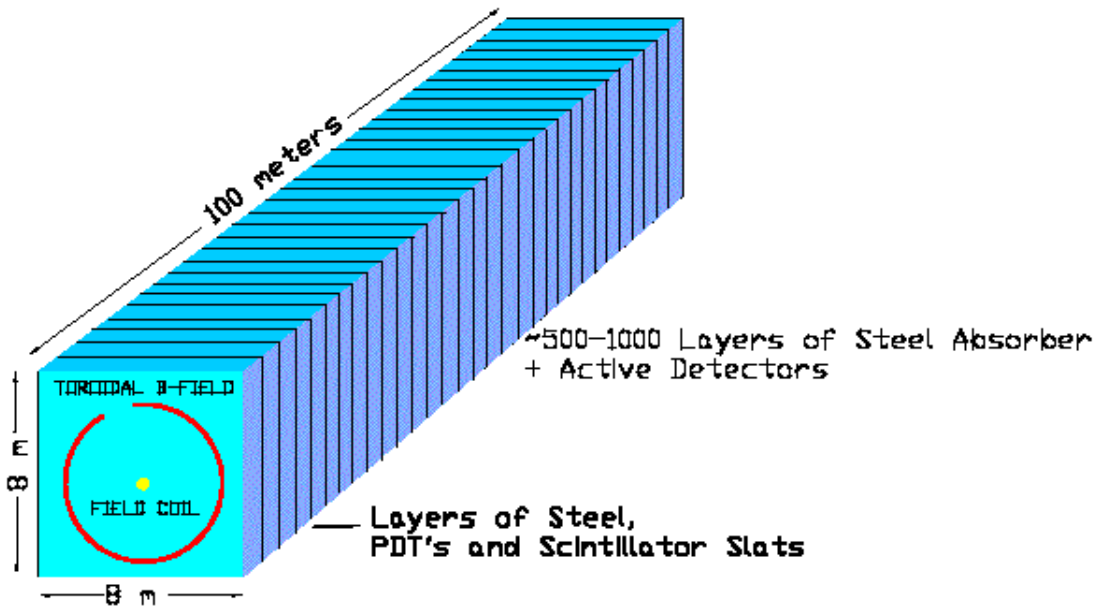

Figure 15.5: A possible 50 kTon Steel/Scintillator/PDT at WIPP.

interleaved with the absorber to provide longitudnal and transverse position resolution and course timing. In addition, the scintillator layers provide the experiment with its trigger. The thickness of the steel absorber and the ratio of PDT to scintillator slats would be optimized for momentum resolution and background rejection. The estimated electronics channel count would be of the order $1 - 5\times10^5$. With a neutrino event rate of a few mHz the electronics could be highly multiplexed to reduce cost and complexity. Phototube magnetic shielding in these detector geometries have been solved by both MINOS and predecessor experiments, and so should not be an issue. Figure 15.5 shows a 50 kton detector with dimension 8 m x 8 m x 100m. This geometry would be convenient for access and services, though designs that maximize fiducial volume to edge ratios are as possible. A detector of this size would record upto 4×10^4 ν_μ events/year.

A large water Cerenkov counter would be similar to SuperK but with

either a magnetized water volume or toriods separating smaller water tanks. The detector could be the large water cerenkov UNO detector, currently proposed to study both proton decay and cosmic neutrinos. UNO would be a 650 kton water cerenkov detector segmented into a minimum of three tanks (fig. 15.6). The gaps between the tanks may contain toroidal magents, or perhaps large gap dipoles to provide the B-field needed to identify the charge of the leading muon (fig. 15.7). The detector provides sufficient muon/hadron separation and muon containment up to 30 GeV/c. A water cerenkov detector would have backgroud rejection of the same order as a Steel/Scin/PDT detector, though results from Study I (fig. 15.2) suggest muon pt cuts would need to be 1.0-1.5 GeV/c higher in a water cerenkov counter to obtain the same rejection levels. UNO would be readout with 70k phototubes, a combination of the 20" SuperK tubes and 8"tubes. The timing provided by the PMT's would allow UNO to gate events in-time with the Neutrino Factory's spill structure. This enables UNO to work simultaneously as both a long baseline neutrino experiment and a proton decay experiment. The multifaceted nature of the UNO physics program is an appealing aspect of this detector option. The geometry of the water tanks do not provide a straightforward way to contain the spectrometer magnets fringe field so magnetic shielding of the PMT's could be a technical challlenge. UNO's active volume is large, 60 m x 60 m x 180 m (w x h x l), which implies a experiment hall of significant dimensions. To provide reasonable access the hall would need to be a least 100 m x 80 m x 300 m , and perhaps more. The detector would have an active fiducial mass of 440 ktons and would record up to 3×10^5 ν_μ events/year form the Neutrino Factory beam.

15.0.6 The Site

The WIPP facility is the US Department of Energy's Waste Isolation Pilot Plant located in Carlsbad, New Mexico. It is a large, underground depository for the storage of low level radioactive waste and has been in operation since 1999 (fig. 15.8).

The WIPP site is approximately 2900 km from the Brookhaven National Lab. The active depository is located 650 m underground in a deep salt formation. Space is potentially available for a large underground physics facility at depths of 740-1100m and discussions are underway between DOE and the UNO project on the possible development of such a facility. Infrastructure, such as elevator access and electricity is currently available at the

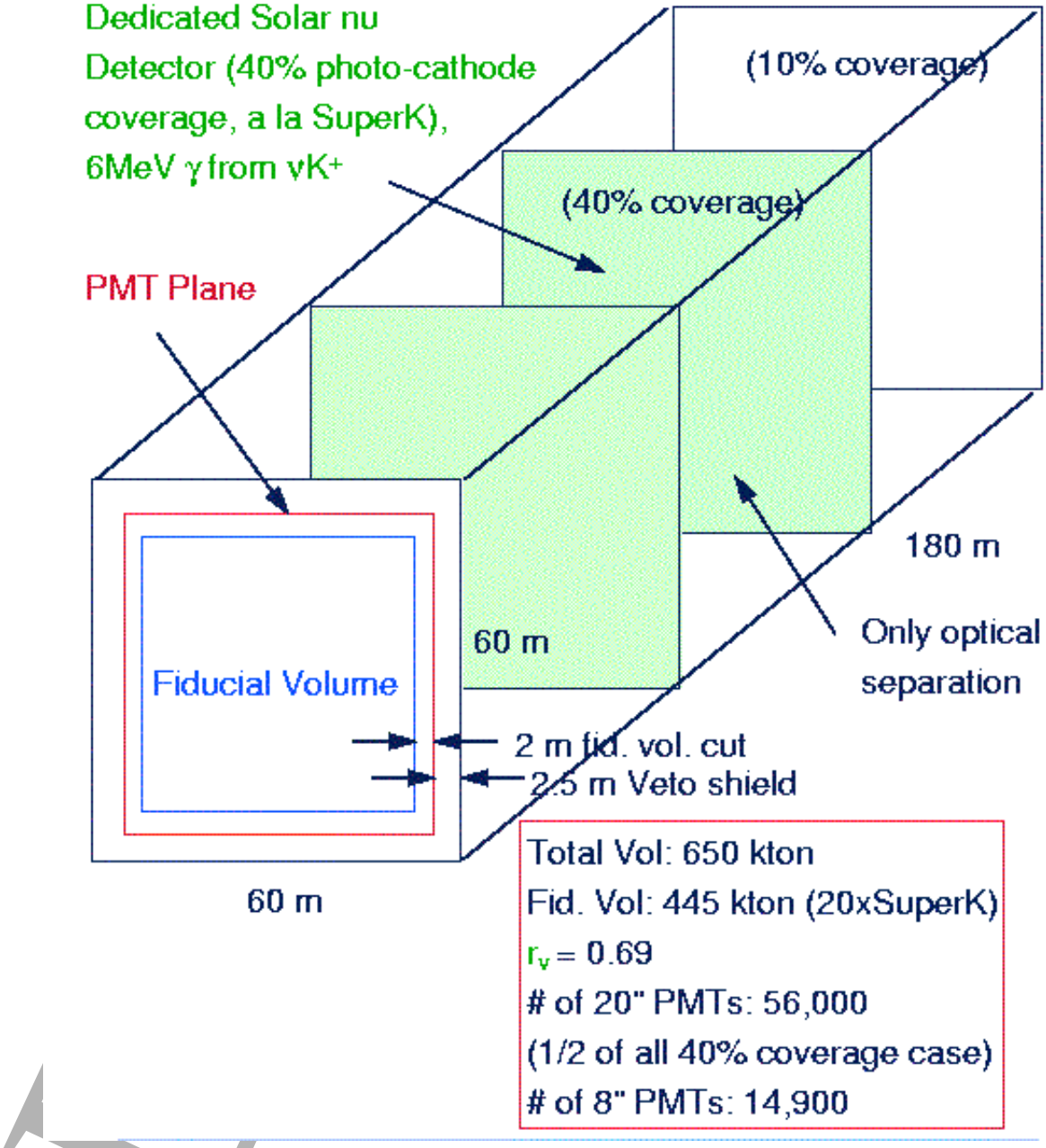

Figure 15.6: Block schematic of UNO Detector including initial design parameters.

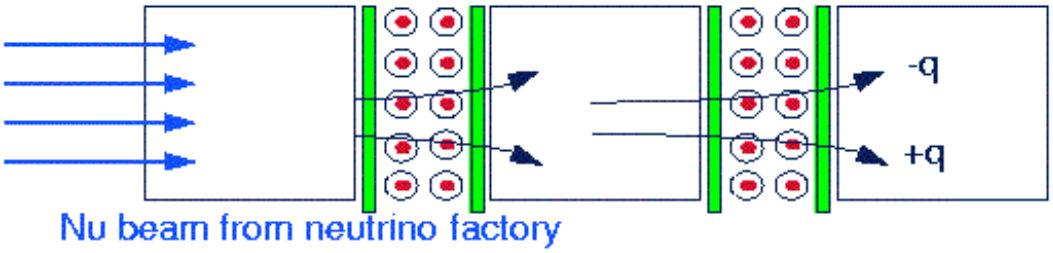

Figure 15.7: Concept of multi-water tank Cerekov counter with magnetic field included.

waste storage levels but new excavation and infrastructure installation would need to take place for the creation of an underground physics facility. The area should be considered a green field, albeit a very salty one.

The Soudan Site is located in the Soudan Mine State Park, Minnesota. It has been the location of an underground neutrino facility since 1984 and is currently being prepared for the installation of the MINOS experiment which is schedule to start taking data in 2004. There are two excavated halls available for physics experiments: the MINOS hall and a neighboring hall in which Soudan II was located. The experimental areas are 714 m underground and 1700 km from BNL (fig. 15.9). Services such as elevator access, electricity, water and cranes are available in both halls but would presumably need to be upgraded if a larger experiment were to be installed. This site is discussed further in the appendix.

Do these experiments need to be underground and as deep underground as proposed? The effort and expense to build an experiment 700+ m underground adds significantly to the challenge of the experiment. Certainly for the UNO detector option the experiment must be deep underground. A proton decay experiment which is searching for events with maximum rates of a few/year can tolerate little cosmic ray background. The ν interaction rate in a 50 kton steel-based detector is a few mHz at beam design luminosities.

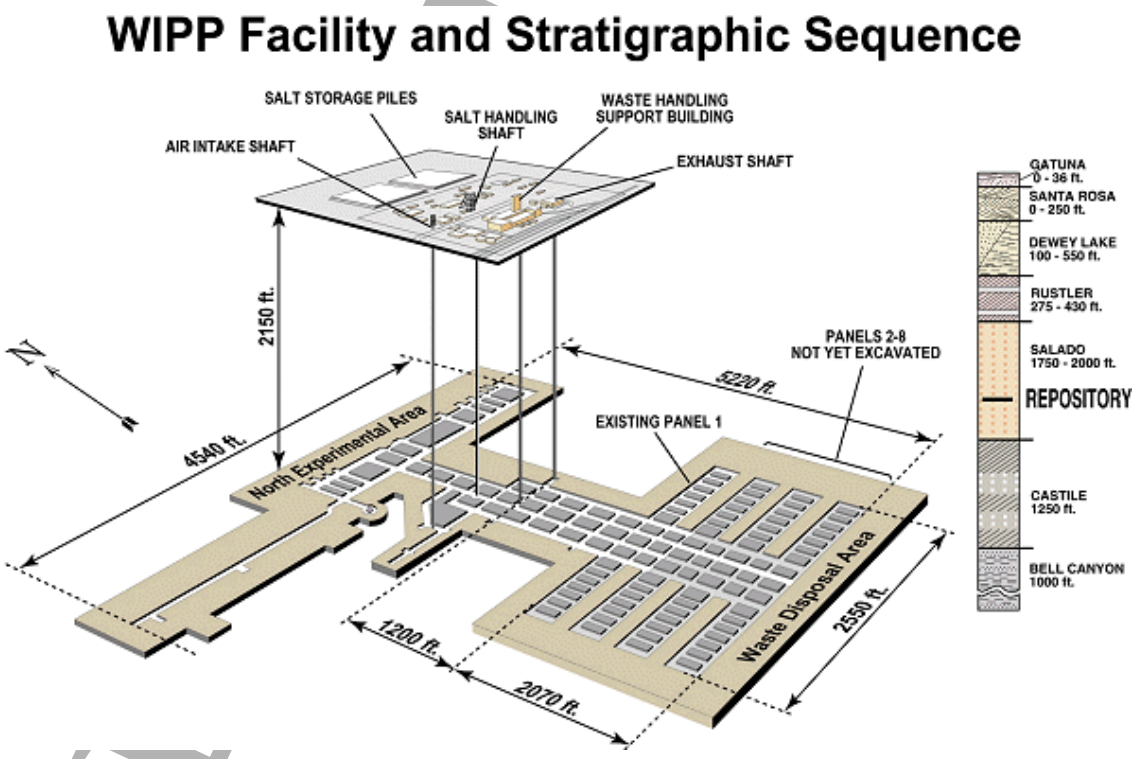

Figure 15.8: The WIPP area.

At the surface cosmic ray interaction rates in the 50 kton detector is a few $\times 10^5$. These event rates would not provide significant data loading to the Data Aquisition System from either a bandwidth or archiving perspective. The main issue is the S/N ratio of $10^{-7} - 10^{-8}$, which would be improved by gating with the Neutrino Factory spill structure and providing a veto array around the detector. These techniques should allow the S/N to be improved to $10^{-3} - 10^{-2}$. Higher level software triggers could further reduce backgrounds by cutting on event topology. A Monte Carlo study would be necessary to determine whether the remaining cosmic ray background events could be removed through data analysis.

15.0.7 Summary

The Neutrino Factory combined with a long baseline detector will allow a number of neutrino oscillation parameters to be measured (θ_{13}, sign of $\Delta {m_{23}}^2$, δ, A), some for the first time. There is the potential that by the time the factory comes online, the long-baseline experiment would be able measure all the outstanding neutrino oscillation parameters. Two experiment sites are considered in this study, WIPP and Soudan, both of which have space available 700+ Meters underground with some associated infrastructure. Either site can be targeted from a BNL-based Neutrino Factory. Detector options for the experiment include a steel/scintillator/PDT detector similar to MINOS and its progenetors, and weighing 10's of kTons. The proposed 650 kton water cerenkov detector, UNO, is also an option. Both choices are technically feasible though the water cerenkov has a number of outstanding technical questions. Conventional neutrino physics is also accessable at the Neutrino Factory with ν beam luminosities many orders of magnitude higher than previously available at accelerator facilities.

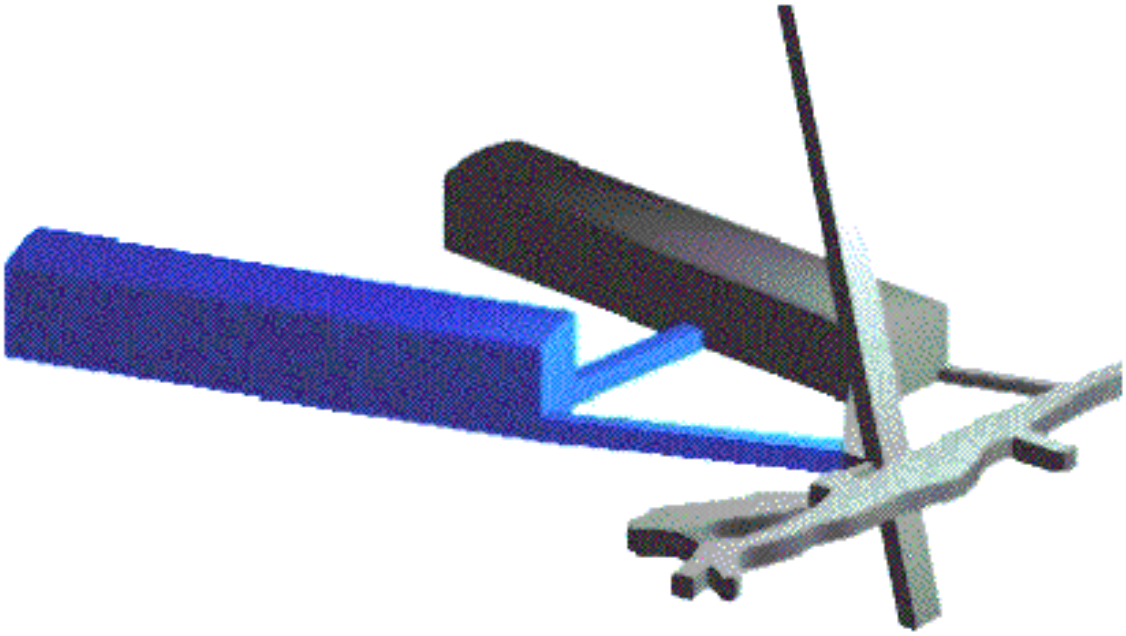

Figure 15.9: The Soudan Site. The two underground experimental halls are located at 714 m below the surface. The MINOS hall is on the left and the Soudan II hall is on the right.

Bibliography

[1] C. Albright et al., Physics at the Neutrino Factory, Fermilab-FN-692, 2000

[2] A. Cervera et al., Golden measurements at a neutrino factory, CERN-TH/2000-40

Chapter 16

Appendix-A: Cost Estimates

M. Zisman

16.1 Cost Reduction

16.2 Introduction

There are two types of cost reduction that we will consider:

- Changes in technology or design that, given some R&D, could reduce costs without effecting performance.
- Changes that do reduce performance, but which could be remedied later. Using these changes can be considered as a phasing of the construction, with an entry level phase that could be followed by an upgrade to full performance.

We will not consider changes that would not allow a later upgrade to full performance.

16.3 Proton Driver

16.3.1 No superconducting linac

If the superconducting linac were not initially available, then the AGS could be filled using the present booster. There would then be an additional 330 msec added to the 400 msec cycle time, as the ring is filled with 6 the bunches at 15 Hz. The performance loss would be 45 % for a cost saving of ***, giving a saving of *** per % of performance.

16.3.2 Lower energy SC linac

A reduction in the SC linac energy could be considered. This might not reduce the power, but it would be less conservative and could lead to greater losses.

16.3.3 No buncher ring

If the bunch compressor ring were not initially built, some bunch compression could be achieved in the AGS itself. The minimum bunch length achievable would be set by the longitudinal emittance of the bunches and by the momentum acceptance of the AGS. An rms bunch length of 9 ns seems a reasonable expectation.

Table 16.1: Efficiency vs. proton bunch length

rms bunch length ns	μ/p tot	15 mm	9.75
1	.249	0.204	.168
3	.234	0.20	.164
6	.204	0.167	.138
9	.178	.144	.117

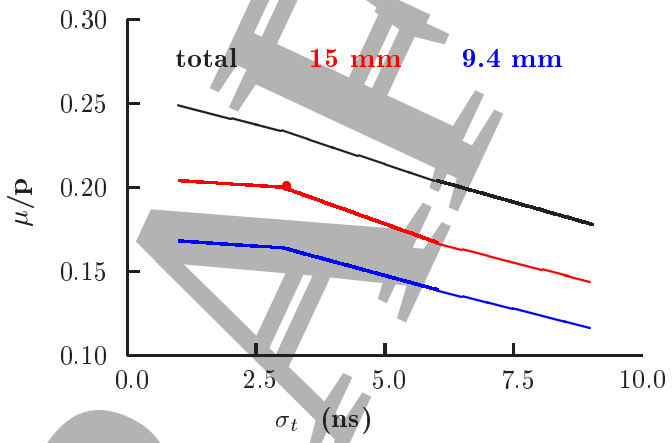

Figure 16.1: Efficiency vs. Proton Bunch Length

In a simulation study in which the proton rms bunch length was changed, without re optimization, the final muons per proton obtained are given in table 16.1 and figure 16.1. It is seen that there is relatively little gain for pulse lengths less than 3 ns (the specified value). For a 6 nsec bunch the efficiency has dropped by 16.5%, and for 9 nsec, which should certainly be attainable in the AGS, the efficiency has dropped by 28%. The cost saving would be ***, giving a saving per % of ***.

16.4 Capture Solenoid

16.4.1 Reduced capture field

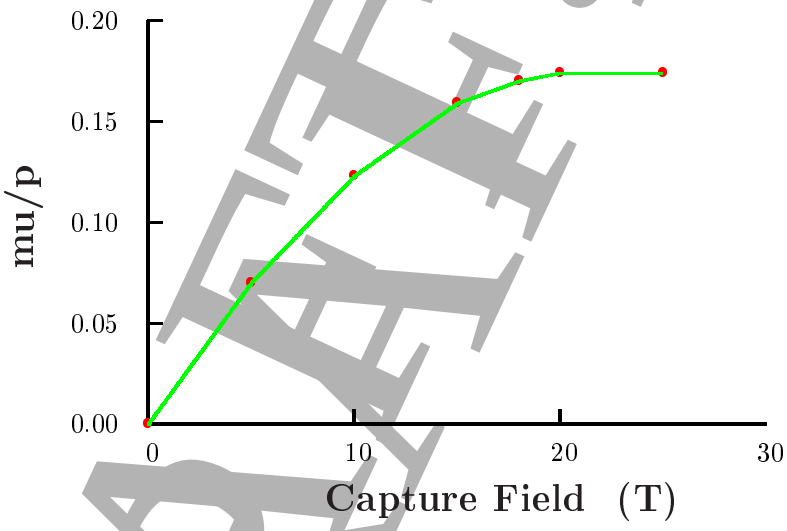

Figure 16.2: Efficiency vs. Capture Field

Figure 16.2 shows the efficiency for muon production vs. the axial peak field of the capture magnet. Maximum performance is achieved with the baseline value of 20 T, but the drop in efficiency is small for moderate reductions in this field. A drop from 20 T to 18 T would have an almost insignificant effect (2%) and even a reduction to 15 T only 9 % reduction. The savings with 18 T would be about *** M$, giving ***$ per %. With 15 T would be ***, giving ***$ per %.

16.4.2 Use of wrapped insulation

Figure 16.3 shows the field vs. power consumption for three different incert coil technologies. The lowest curve is for the baseline design using MgO

Figure 16.3: Efficiency of 3 types of inserts in 20 T magnet.

insulated hollow conductor giving 6T with 12 MW. The dotted line above is for a wrapped ceramic insulation as being developed at MIT Ref***. With this conductor, the field of the superconducting coil can be lowered from 14 T to 12.4 T for a saving of approximately ***. There would be no penalty in performance.

16.4.3 Use of Bitter magnet

The upper dashed line in figure 16.3 is for a Bitter magnet. This technology, which has a very high fraction of its volume available to carry current, is more efficient than either hollow conductor technology. It is not proposed for a baseline because of concerns for its lifetime. Bitter coils have water insulation between turns, and in a high radiation environment may rapidly corrode. R&D is needed to establish if this is a real concern. If a bitter coil could be used, the wall power could be reduced to 6 MW with the superconducting coil still providing 12.4 T

16.5 Phase Rotation

16.5.1 Combining Induction Linacs 2 and 3

In the baseline design there are 3 induction Linacs. The first linac must be separate from the other two in order to achieve a non distorting phase rotation, but the second and third linacs were separate only in order that they be each unipolar. A single second linac with a bipolar pulse approximately equal to the sum of the two opposite polarity pulses would be equally good. This, although slightly less standard appears possible and would be cheaper. The same two unipolar power supplies would be employed, both feeding a single induction linac. R&D is required to confirm this possibility. The cost saving, with no loss of performance, is estimated to be about $***.

16.5.2 Fewer Induction Linacs

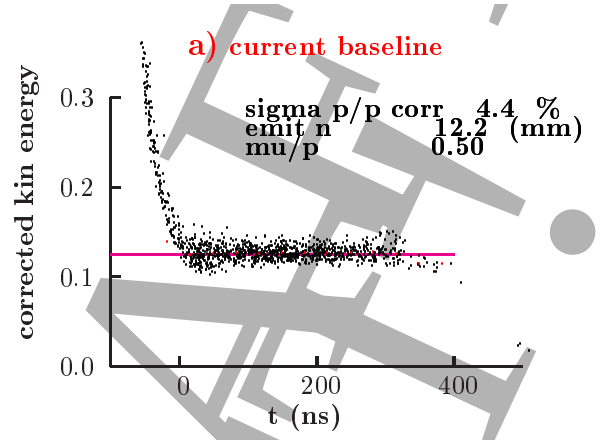
a) current baseline
sigma p/p corr 4.4 %
emit n 12.2 (mm)
mu/p 0.50
corrected kin energy
0.0
0.1
0.2
0.3
0
200
400
t (ns)

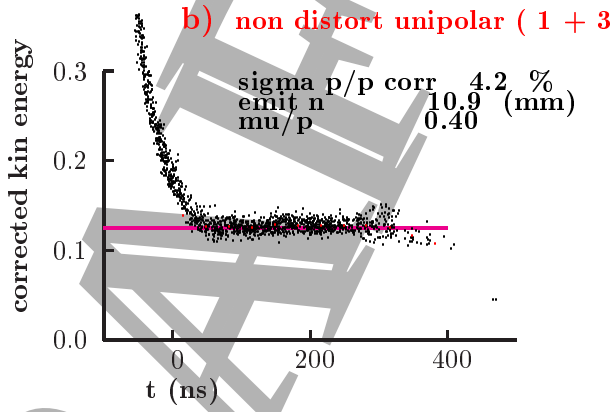
b) non distort unipolar (1 + 3
sigma p/p corr 4.2 %
emit n 10.9 (mm)
mu/p 0.40
corrected kin energy
0.0
0.1
0.2
0.3
0
200
400
t (ns)

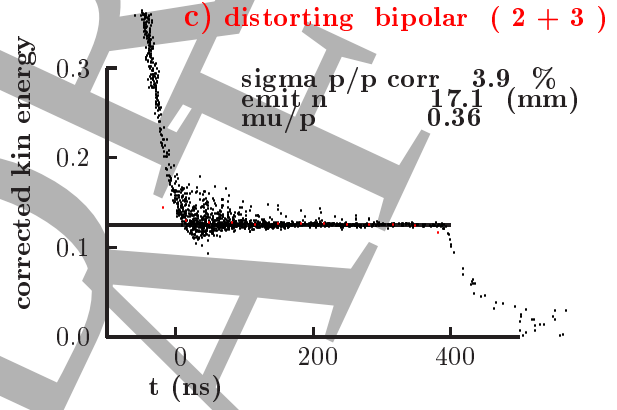
c) distorting bipolar (2 + 3)
sigma p/p corr 3.9 %
emit n 17.1 (mm)
mu/p 0.36
corrected kin energy
0.0
0.1
0.2
0.3
0
200
400
t (ns)

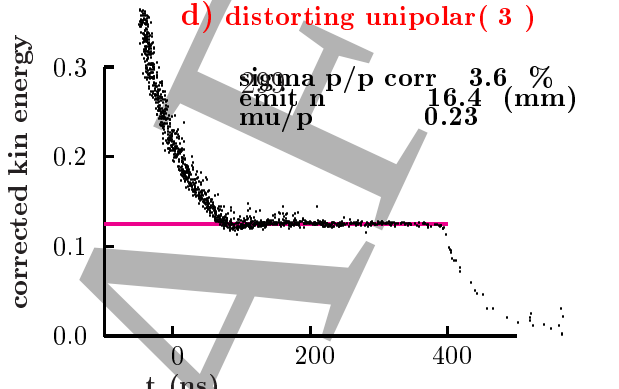
d) distorting unipolar(3)
sigma p/p corr 3.6 %
emit n 16.4 (mm)
mu/p 0.23
corrected kin energy
0.0
0.1
0.2
0.3
0
200
400
t (ns)

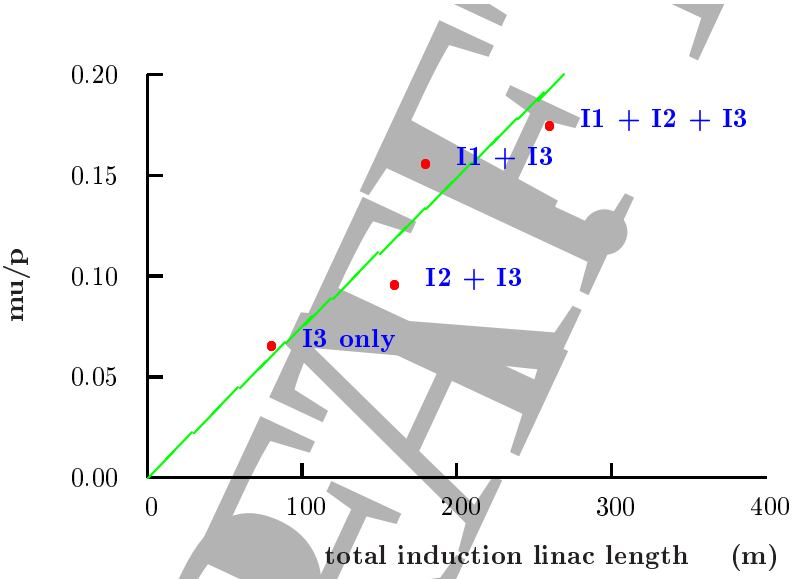

Figure 16.5: Efficiency vs. Length of Induction Linacs

Further cost savings are achieved if one or more of the linacs is eliminated and the remaining linacs re optimized. Figure 16.4 shows 3 such cases, together with the baseline design. Figure 16.5 shows the muon production efficiency for the four cases, plotted against the sum of the lengths of the remaining linacs. The losses in efficiency are large when the first linac is eliminated, but less severe if only the second linac is removed. This would save approximately 60 M$ for a loss of efficiency of 11%, i.e. 5.4 M$ per %.

16.6 Cooling

16.6.1 Less cooling

Figure 16.6 shows the muon production into the defined accelerator acceptance as a function of length. Table 16.2 shows the values for 3 cooling lengths:

Table 16.2: Efficiency for three cooling lengths

cooling length m	μ/p	loss %	savings M$
108	.174	0	0
88	.168	3.4	
68	.150	13.8	
48	.124	29	

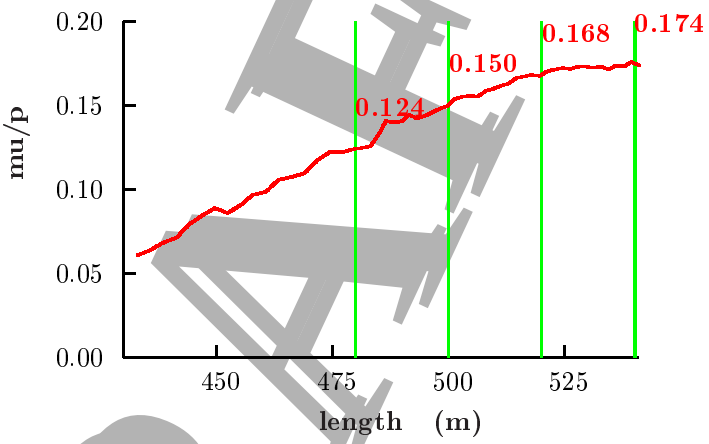

Figure 16.6: Efficiency vs. length of cooling

16.6.2 Single lattice

The baseline design employs two different lattices, the first with a cell length of 2.75 m and relatively low axial fields (3 T), the second with 1.65 m cells and higher fields (rising to nearly 5 T), and a matching section between them. A savings of $*** would result if the entire cooling is done with the 2.75 m lattice. The loss of efficiency is ***.

16.7 Acceleration

16.7.1 Dog Bone Configuration

*** from Scott

16.7.2 FFAG

*** from Scott

16.8 Summary

16.9 Storage Ring

16.9.1 Lower Field Arcs

Table 16.3: rf windows: Grid of gas cooled Al pipes

sec	r	t	cover	layers
	cm	μm	%	
1,1-1,3	30	25	50	2
2,1-2,3	25	25	50	2

16.10 Possible Improvements

16.10.1 Proton Driver

Increased proton power

It appears possible to raise the average proton power to 2 or 4 MW. *** insert from Tom Roser.

reduced bunch length

16.10.2 Phase Rotation

Use of wiggler

Bunched beam rotation

correlation matching

polaraization

16.10.3 Cooling

Grid of tubes

Gain=15%

There are known field problems if the pipes have large diameters, but these must be reduced as their diameters are reduced and their numbers increase. A second advantage of many small tubes is that, for a given pressure, their wall thicknesses can be reduced. One would like ≤ 1 cm diameter pipes, spaced on centers $= 2 \times$ their diameter, with wall thicknesses of $\leq$ 1 mill (25 μm). With 1 atmosphere of gas in the pipes, the tension in the walls would be 3000 psi which should be ok.

The grid is simulated by foils with thickness equal to the average thickness of the pipes: 80 microns.

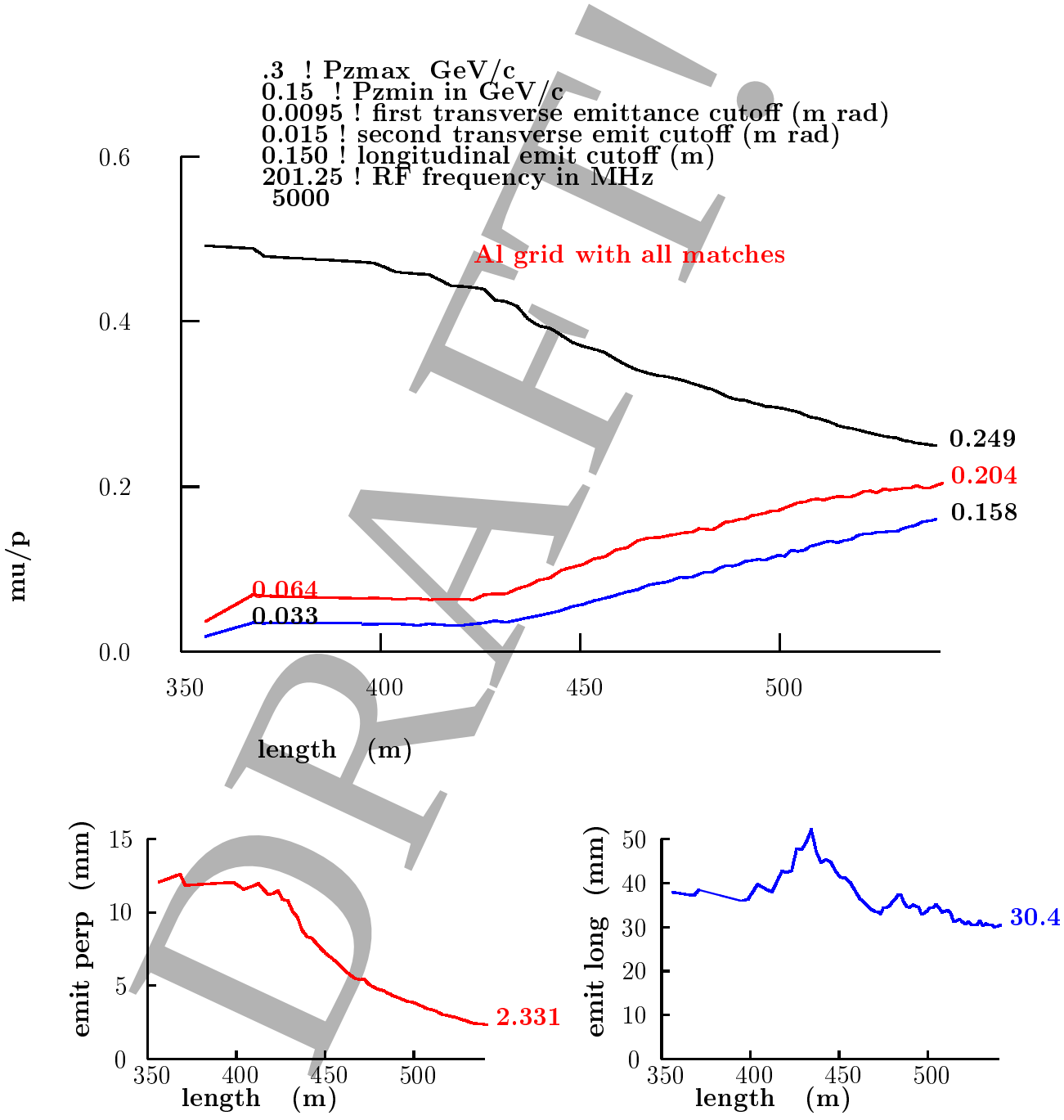

RF cavity aperture

In this study only the largest RF windows' apertures and thicknesses were changed. The 25 mm apertures were chosen, and are given in the specifications above.

maximum aperture	thickness	μ/p		
cm	μm	tot	15 mm	9.75
30	500	.253	0.21	.175
25	250	.249	0.204	.168
21	125	.224	0.189	.160

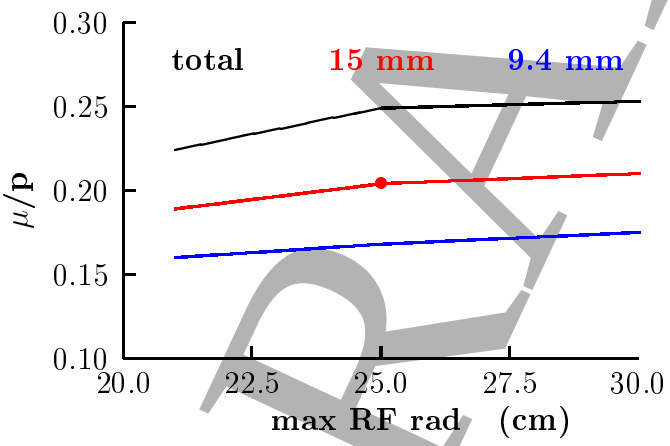

emittance exchange

Chapter 17

Appendix-B: Phased Approach

B. Palmer

Chapter 18

Appendix-C: Alternatives

18.1 Alternative Target Solenoid: Bitter Magnet

B. Weggel

18.2 Alternative Targets: Carbon Target and Rotating Band

B. King

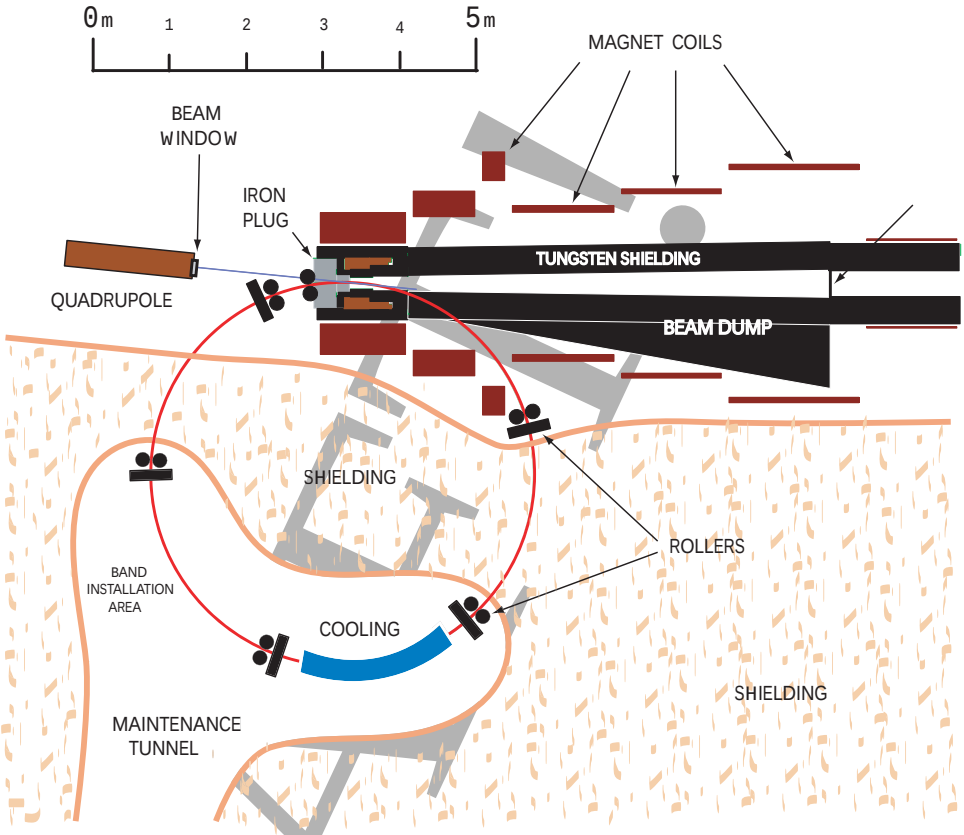

Figure 18.1: A conceptual illustration of the targetry setup.

18.2.1 Rotating Inconel Band Option for the Pion Production Target

Introduction and Overview

As a back-up scenario to the base-line mercury jet target design, this appendix presents a solid-target option that is based around an Inconel Alloy 718 target in a rotating band geometry. Similar conceptual designs for rotating band targets have been presented previously [?, ?, ?], for use at both muon colliders and neutrino factories, and a more detailed description of this particular conceptual design can be found in reference [?].

A plan view of the targetry setup for the band target option is shown in figure 18.1. An inconel target band threads through the solenoidal magnetic

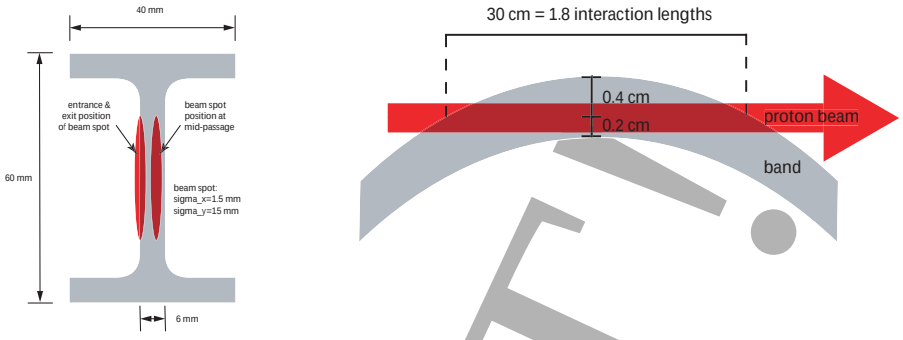

Figure 18.2: Passage of the proton beam through the target band shown in cross-sectional (left) and plan (right) views. The horizontal position of the beam spot in the band webbing varies along the interaction region due to the curvature of the band. The plan view shown in the right plot has a very distorted 10:1 aspect ratio.

capture channel to tangentially intercept the proton beam. The circulating band is cooled by passage through a water tank located in a radiation-shielded maintenance enclosure.

Inconel 718 is a niobium-modified nickel-chromium-iron superalloy that is widely used in nuclear reactors and particle accelerator applications because of its high strength, outstanding weldability, resistance to creep-rupture due to radiation damage and to corrosion from air and water. The inconel target band has an I-beam cross section. The band dimensions and positioning relative to the proton beam are shown in figure 18.2. The proton pulse structure and bunch charges were assumed to be identical to the base-line scenario with a mercury jet target. A tabulation of geometrical parameters for the inconel target, and of the assumed parameters for the incident proton beam, is provided in table 18.1.

Mechanical Design Considerations

As is evident from figure 18.1, the threading of the target band through the pion capture channel represents only a slight variation on the channel design for the base-line mercury jet target option. The band entry port need only traverse the iron plug in the upstream end of the capture solenoid while the downstream port traverses the tungsten shielding and then passes between the solenoidal magnet coil blocks and out of the pion decay channel. Two

Table 18.1: Specifications of the inconel target band and assumed proton beam parameters.

target band radius (R)	2.5 m
band thickness (t)	6 mm
band webbing height (h)	60 mm
full width of band flanges	40 mm
beam path length in band (L)	30 cm
proton interaction lengths (λ)	1.81
band rotation velocity (v)	1 m/s
proton energy	24 GeV
protons/bunch	1.7×10^{13}
bunches/fill	6
time between extracted bunches	20 ms
repetition rate for fills	2.5 Hz
horizontal beam-channel angle (α)	100 mrad
rms beam spot size at target	1.5 mm (horizontal)
	15.0 mm (vertical)

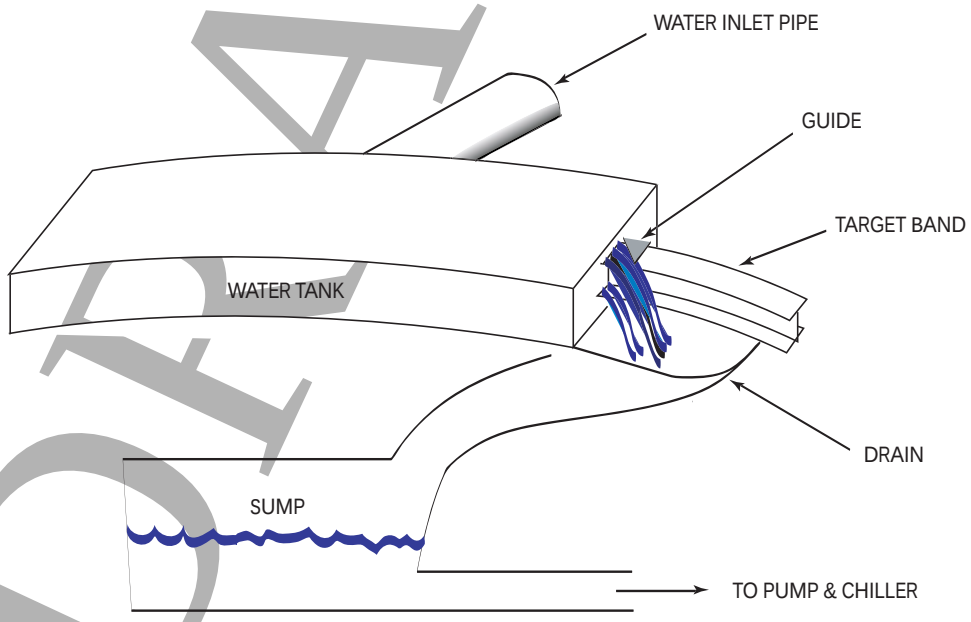

Figure 18.3: A conceptual illustration of the target cooling setup.

plausible options for incorporating the exit port into the magnet cryostat are discussed in reference [?]. The third coil block downstream from the upstream end had to be moved outwards by approximately 10 centimeters to provide adequate space for the band to exit the channel. A modest re-optimization of the coil currents was required to restore the magnetic field map in this region to the base-line specifications.

No detailed consideration has yet been given to the design of the beam dump. As is clear from figure 18.1, the target band exit port is far enough upstream from the beam dump for it to be not a relevant factor in the beam dump design.

The band is guided and driven by several sets of rollers located around its circumference, as is shown in figure 18.1. A few hundred watts of drive power [?] should be required to overcome the eddy current forces from the band entering and exiting the 20 tesla solenoid. and the smaller drag forces from the water in the cooling tank. Following the lead of the BNL g-minus-2 target design, the roller assemblies will all incorporate self-lubricating graphalloy [?] bushings that are compatible with high radiation environments.

The pion production region of the target and its surrounds are in an air environment, with beam window positions shown in figure 18.1. Activated air and gases from the target and interaction region are continuously diluted and then vented from the target hall into the outside atmosphere following the procedure adopted for the BNL g–2 target.

The heated portion of the band rotates through a 2 meter long cooling tank [?] whose conceptual design is shown in figure 18.3. The band entrance and exit ports in the ends of the tank also serve as the water outlets. Both the heat transfer rates and water flow rates are found [?] to be relatively modest and the water flows due to gravitational pressure alone with no anticipated need for forced convection.

The number of incident proton bunches on any particular section of the rotating band, and hence the localized radiation damage, is reduced by a factor of approximately 50 relative to a fixed target geometry. Hence, each target band may last for several years [?] before requiring replacement.

The heavily irradiated used bands will be remotely extracted in pieces by progressively clamping then shearing off 1 meter lengths and dropping them into a hot box. After removal of the hot box, the band maintenance area can then be accessed and the new band progressively installed by welding together, in situ, eight 1.96 meter long chords of target band that have been

previously cast (or otherwise prepared) into the correct I-beam cross section and circumferential curvature. Beam-induced stresses on the welds are minimized by welding on the flanges of the I-beam rather than on the central webbing that is exposed to the proton beam and to much larger energy depositions.

Simulations of Pion Yields and Beam-Induced Stresses

Full MARS [?] tracking and showering Monte Carlo simulations were conducted [?] for 24 GeV protons incident on the target, returning predictions for the pion yield and energy deposition densities.

The yield per proton for pions-plus-kaons-plus-muons at 70 cm downstream from the central intersection of the beam with the target was determined [?] to be 0.715 (positive) and 0.636 (negative) for the momentum range $0.05 < p < 0.80$ GeV/c, and 0.304 (positive) and 0.288 (negative) for the kinetic energy range $32 < E_{kin} < 232$ MeV that approximates the capture acceptance of the entire cooling channel. This is slightly lower than the yield from a mercury target; for the identical geometry, hypothetically replacing inconel with mercury was found to increase the yield by 15%.

Approximately 7% of the proton beam energy is deposited in the target as heat, with a maximum instanteous heat rise of approximately 30 degrees centigrade from a single proton bunch. Detailed 3-dimensional maps of energy deposition densities were generated for input to dynamic target stress calculations [?] using the commercial ANSYS finite element analysis code.

The ANSYS simulations conservatively assumed the deposited energy to all be converted to an instantaneous local temperature rise. The von Mises stress (i.e. the deviation from the hydrostatic state of stress) was found to be initially zero but to develop and fluctuate over time as the directional stresses relax or reflect from material boundaries. The predicted 200 MPa peak value for the von Mises stress from a single proton bunch is approximately a factor of six below the yield strength for inconel 718 and well below its fatigue strength.

The band rotation speed, 1 m/s, advances the band by 40 cm between successive beam fills. This presents a fresh 30 cm chord of target band for each beam fill but the energy depositions from the 6 bunches within the fills are largely superimposed. However, the pile-up of stresses is not considered serious since any significant level of von Mises stress is expected to die out well within the 20 millisecond time span between successive bunches, leaving only

the relatively benign hydrostatic stresses. This prediction could not be fully verified due to computational limitations but the general trend of reduction in von Mises stresses was tentatively confirmed in ANSYS calculations that simulated a time span of only several microseconds.

Conclusions

In summary, the inconel rotating band target design appears to be a promising back-up option to the base-line mercury jet target. The pion yield appears slightly lower than the mercury base-line, although this has yet to be fully optimized. The engineering design looks manageable and initial simulations of target stresses are encouraging.

Bibliography

[1] *A Cupronickel Rotating Band Pion Production Target for Muon Colliders*, B.J. King *et al.*, Proc. PAC'99, IEEE, pp. 3041-3.

[2] *Rotating Band Pion Production Targets for Muon Colliders and Neutrino Factories*, B.J. King, NIM A 451 (2000) pp. 335-343, Proc. ICFA/ECFA Workshop "Neutrino Factories based on Muon Storage Rings (nuFACT'99)", physics/0005007.

[3] *Some thoughts on a high-power, radiation cooled, rotating toroidal target for neutrino production*, J.R.J. Bennett, NIM A 451 (2000) pp. 344-348, Proc. ICFA/ECFA Workshop "Neutrino Factories based on Muon Storage Rings (nuFACT'99)".

[4] Muon Collider Note in preparation.

[5] Graphalloys are manufactured from molded graphite impregnated with metal. Graphalloy is a registered trademark of the Graphite Metallizing Corporation.

[6] N.V. Mokhov, "The MARS Code System User's Guide", Fermilab-FN-628 (1995). N.V. Mokhov and O.E. Krivosheev, "MARS Code Status", Fermilab-Conf-00/181 (2000). http://www-ap.fnal.gov/MARS/ .

18.3 Alternative Phase Rotation

L. Reginato

18.4 Alternative Cooling Scenario

V. Balbekov

V. Balbekov[1], E. Black[2],V.D. Elvira[1]
P. Lebrun[1], D. Neuffer[1], J.M. Rey[1], P. Spentzouris[1]
[1]Fermilab, Batavia, IL 60510, USA
[2]ITT, Chicago, IL, USA

A 220 m long ionization cooling system consisting of three solenoids with two field-flip sections, is proposed as an alternative cooling channel for the neutrino factory. The reduction of transverse emittance is achieved using 87 Liquid hydrogen absorbers (30-40 cm long), and 87 (2 m long) 201 MHz Linacs. The first flip is performed at relatively small magnetic field, B = 3 T, to keep the longitudinal motion under control. The field is then increased adiabaticaly up to 7 T and a second field flip performed. The cooler is studied both theoretically and through a detailed simulation using GEANT4. Preceeded by a 16 GeV proton driver, a carbon target, a minicooler and a buncher, the system provides about 0.1 muons per incident proton. Transmission and emittance predictions at the end of the channel are presented.

18.4.1 INTRODUCTION

Unlike the baseline sFOFO channel, the Double Flip channel has a very simple lattice (see Fig. 18.4): the cooling sections use continuous focusing from long solenoids, with the absorbers placed inside the magnets.

Such a configuration provides simple transverse optics: for a matched beam there is no modulation of the beam envelope in the channel. The field of the long solenoid is reversed twice in the lattice in order to displace the Larmor centers toward the beam axis, and achieve a canonical phase ellipsoid on exit. Special matching sections ire used at these points, both to minimize the length of the region affected by the polarity change, and to mitigate particle losses due to the excitation of synchrotron oscillations. These oscillations arise from the longitudinal-transverse phase-space correlations that develop due to the dependence of the time of flight on the transverse amplitude of the particles in a solenoid. The transverse momentum and thus the transverse amplitude changes at the field reversals; this change has to occur in a spatial region smaller than the Larmor wavelength of the beam in order to control these effects. Fig. 18.5 illustrates the cooling principle of the double-flip channel.

The first section cools the transverse momenta of the muons using a relatively low solenoidal field (3 T on axis), to first order without affecting the transverse size of the beam (to second order the beam grows slightly due to

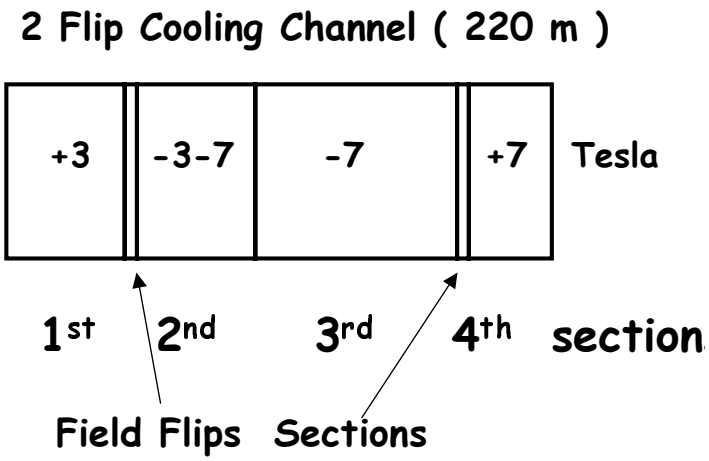

Figure 18.4: sketch of the double-flip channel.

multiple scattering). (For an infinitely long channel, neglecting scattering, the muon helices would shrink to lines.) In the matching section between sections 1 and 2, the centers of the Larmor orbits are displaced such that in channel 2 the muons to first order execute Larmor motion about the solenoid axis. Then the field is increased adiabatically up to -7 T in order to reduce the β-function for final cooling of both the beam size and the transverse momenta. The second field flip is therefore performed at -7 T without a significant perturbation of the longitudinal motion because the beam radius has reached a small enough value at this point. The section lengths are appropriatelly chosen to obtain a canonical beam without parasitic correlations at the end of the channel. The beam is slowly accelerated to compensate for longitudinal emittance growth and particle losses. The full length of the cooling channel is approximatelly 220 m.

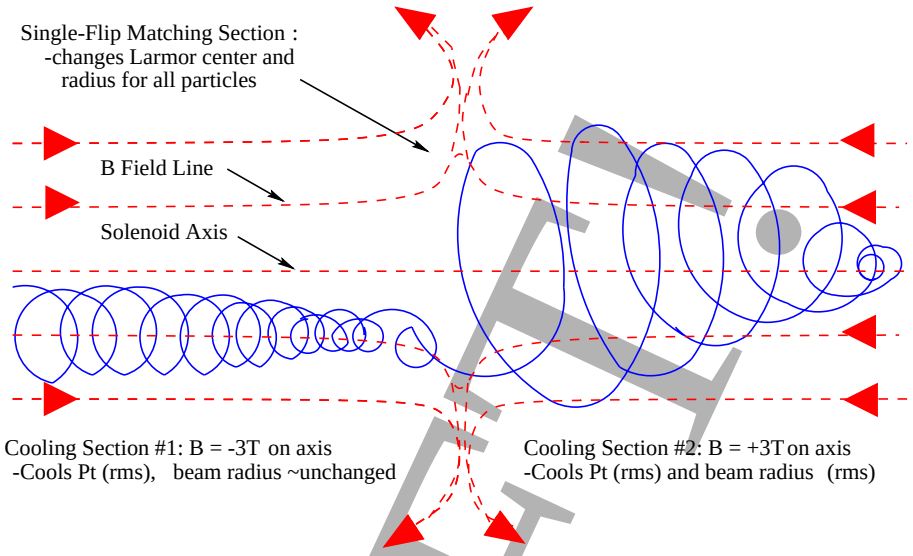

Figure 18.5: Illustration of the particle motion before and after the first flip region.

18.4.2 INITIAL CONSTRAINTS AND THE INPUT BEAM

The optimization of any cooling channel is strongly coupled to the front-end design. The design of the double-flip channel is optimized to maximize the transmission and the cooling performance for the input beam produced at the end of the buncher. The front-end, and therefore the input beam for the double-flip channel, are different from the baseline designs described in the previous chapters. They follow the design proposed in Ref.[?] which we briefly describe in the following paragraph.

The front-end system consists of:

- *A 16 GeV proton beam and a 9 m target station.* The proton beam size is $\sigma_x = \sigma_x = 2.14$ mm, σ_t=3 ns. The solid carbon target is 0.8 m long and it is placed in a 20 T magnet.

- *A decay channel.* It is a uniform solenoid 41 m long, with a radius of 30 cm and a field of 1.25 T on axis.

- *A 4 m long matching section.* It provides a matching between the

decay channel and the induction linac. The magnetic field increases from 1.25 T to 3 T, and the solenoid radius from 30 cm to 20 cm.

- *A 100 long induction linac.* It develops a voltage from -50 MV to 150 MV in a pulse. The accelerating voltage in the gaps is adjusted to accept muons in the energy interval 230 MeV $< E_{tot} <$ 330 MeV.

- *A minicooling and matching section.* Minicooling is accomplished by a 2.6 m long liquid hydrogen (LH_2) absorber inside a 3 T solenoid with a radius of 40 cm. It produces some transverse cooling and decreases the energy of the most populated part of the beam from 280 MeV to 200 MeV, which is optimal for bunching.

- *A buncher*, which includes 3 accelarating stations and 3 drift spaces inside a r =71 cm, 3 T solenoid. Each station consists of six ν =201 MHz $\pi/2$ cavities 32 cm long. The full voltage of the 3 stations is 15, 19.5 and 24 MV respectivelly. The synchronous phase is zero at the total reference energy of 200 MeV.

The performance of the channel was tested using the beam at the end of the buncher (see Table 18.2). In addition, the channel was also tested using a gaussian beam with parameters (lab. frame): $\sigma_x = 5.46$ cm, $\beta_f = 38.03$ cm, $\sigma_{ct} = 10$ cm, $\langle E \rangle = 200$ MeV, $\sigma_E = 20$ MeV. The E-p_T correlations present in the beam at the end of the buncher are also modelled in the gaussian beam (for a clockwise Larmor motion):

$$p_x = p_x + \frac{y \times 1.55 MeV/c/cm}{2}$$

$$p_y = p_y - \frac{x \times 1.55 MeV/c/cm}{2}$$

18.4.3 TECHNICAL DESCRIPTION OF THE CHANNEL

This cooling lattice consists of four sections: the first contains 20 cooling cells, 2.51 m long, in an almost-constant magnetic field of 3 T on axis. Between the first and the second sections there is a 1.02 m long matching section in which the field changes polarity. The second section consists of 20 cells,

Table 18.2: Parameters of the beam after bunching (input to the cooling channel).

σ_x	σ_{px}	$\sigma_x\sigma_x/mc$	ε_x	μ/p	μ/p
(mm)	**(MeV/c)**	**(mm)**	**(mm)**	**E < 300 MeV**	**(in bucket)**
5.46	24.4	12.6	11.1	0.191	0.135

2.51 m long, at a field on axis which adiabatically (and linearly) grows from -3 T to -7 T on axis. It is followed by a third section containing 32 cells, 2.51 m long, at a field of -7 T on axis. The second field flip region is 1.26 m long and is followed by the fourth section with 15 cells, 2.51 m long, at a field of 7 T on axis. Gaps in the solenoids are required for rf power feeds and absorber cooling equipment and are included in the simulation. There are therefore four short coils, 47.45 cm long, and four gaps, 15.3 cm wide, in a unit cooling cell. Although this is the model incorporated in the simulation, we show a new engineering design in Fig 18.6 which avoids most of the gaps by using flexible rf power feeds which all go through just one 20 cm wide gap. To accomodate these new feeders, the coils inner radii are increased from 74 cm to 80 cm. The coils would be of NbTi superconductor material with aluminum, cooled to 4.2K and locally to 1.8K in the high field regions. The performance should not depend on the design change, since the field will not vary significantly in the beam region. Figs. 18.7, 18.8 illustrate how the magnetic field is constructed in the simulation. The coil blocks are modelled with a set of infinitelly thin current sheets which share the total coil current. Fig. 18.9 shows the field B_z on axis as a function of z.

The specifications of the cooling sections are given in Table 18.3.

Each cooling section contains one liquid-hydrogen absorber and one linac consisting of 6 $\pi/2$ TM010-mode pillbox cavities. Our preliminary design for the cooling solenoids (the one used in the simulation) specifies 3-cm-thick coils for the 3 T field at a density of 105.7 A/mm^2, and 6-cm-thick coils for the 7 T field at a density of 123.4 A/mm^2. This current densities exceed the conservative limit. One possibility to reduce hoop stresses is to use thicker coils at lower current density. The alternative followed in the new design is to remove the gaps to allow a lower current density for a given coil thickness.

The absorber length vary from 30 cm in the first two sections of the channel. The synchronous phase of the r.f. cavities was tuned to produce the

desired reference energy dependence on the cell number. The reference energy is the average energy of a particle in the beam. The "reference particle", if it existed, would have a longitudinal velocity equal to the propagation velocity of the r.f. wave. A particle with an energy of 200 MeV would loose about 10 MeV per absorber in the first section and gain ≈12.5 MeV per linac at synchronous phase $\phi \approx 25.7°$. This slow acceleration allows to to increase the size of the rf bucket and compensate for the increase of the rms energy spread through the channel. The goal of increasing the bucket size is to avoid particle loss due to this longitudinal phase-space dilution. The reference energy in the double flip channel is therefore set to increase linearly from 200 MeV to 250 MeV in the first section (see Fig 18.10). At the flip regions, the beam gains transverse momentum and its average longitudinal velocity decreases. The reference energy is therefore decreased by 15 MeV at the flip regions to allow the bucket to accomodate to the changing shape of the beam. The same average net acceleration, 2.5 MeV/cell, is performed to the beam in the second section, and then decreased to ≈0.85 MeV/cell in the last two sections. The reference energy at the end of the fourth section is 326 MeV. To compensate for the smaller dE/dx values as the energy increases, and keep approximatelly the same synchronous phase throughout the channel for an effective voltage of 15 MV/m, the absorber length is increased to 39 cm in the third (starting from the third cell) and fourth sections. Fig. 18.11 shows the absorber (in grey) inside the solenoidal coils (in blue) in a unit cell, including the aluminum windows (in light grey). The window radius and thickness are 20 cm and 200μm in the first two sections, and 10 cm and 100μm in the last two sections (where the beam size is smaller). Figs. 18.12, 18.13 show the 6 cavities associated to a linac in a unit cell (in red). The beryllium windows, with a radius of 20 cm and a thickness of 125 μm, are shown in green.

The most sensitive parameter of the cooling channel is the gradient of the magnetic field in the field-flip regions. This gradient must be maximized in order to stabilize the longitudinal motion. The two matching sections are illustrated in Fig. 18.14, 18.15. The 1.02 m long first flip region consists of the two outer coils separated by 20 cm and two 42 cm long inner coils separated by 2 cm from each other. The current density for both is 89 A/mm^2 and their radii 74 cm and 21 cm, respectivelly. The 1.26 m long second flip region consists of the two outer coils separated by 20 cm, two 15 cm long central coils separated by 80 cm, and two 22 cm long inner coils separated by 2 cm. The current densities and radii are 108, 108, 104 A/mm^2 and 74, 41, 11 cm, respectivelly. The coil thickness in the flip regions is a matter

of discussion. For now, the simulation is performed using 3 cm thick coils in the first matching section, and 6-8 cm thick coils in the second matching section. The magnetic fields on axis, B_z, associated to the matching sections are shown in Figs. 18.16, 18.17. The matching section is the most technically challenging component of this cooling channel.

18.4.4 PERFORMANCE

The performance of the channel, given the parameters described in Tables 18.2, 18.3 is summarized in Fig. 18.18 for the gaussian beam (based on 1000 particles). The transverse cooling factor is 7, from 12.6 cm to 1.8 cm. The channel heats longitudinally by a factor of 2. As seen in the figure, the first section of the double flip channel reduces the rms transverse momentum of the beam by a factor of two without changing the size of the beam envelope. The change of field polarity in the matching section causes σ_{px} to grow by a factor of 3. Due to the displacement of the Larmor orbits, the second section cools both σ_x and σ_{px}, to final values of 13.2 mm and 21.2 MeV/c, respectively. The second, third, and fourth sections recover from the emittance growth in the field-flip regions, cool the transverse size of the beam, and restores angular momentum such that the beam is canonical when it exits the cooling section. Fractional transmission through this channel is approximately 75%.

Fig. 18.19 illustrates the performance of the double flip channel for the realistic beam (1000 particles). The bunch fills the 201.25-MHz rf bucket from the start. About half of the lost particles are muons that are not captured into the bucket; these are lost in the first few meters of the cooling channel. The remaining particle loss is due to the excitation of longitudinal motion in the first field-flip region. Low-momentum muons are lost at the maximum of this synchrotron oscillation, a few meters after the matching section. Thus the second section of the channel scrapes longitudinally. Final transverse and longitudinal emittance are 1.8 mm and 80 mm, respectivelly. The longitudinal emittance increases by a factor of 1.6 between the end of the first section and the end of the channel. Both σ_x and σ_{px} are cooled from initial values of 57 mm and 25.5 MeV/c to final values of 14 mm and 21 MeV/c, respectively. The transmission predicted by the GEANT4 simulation, refered to the total number of particles in the initial beam (with a E<300 MeV cut), is 40%, against the 52in Ref.[?]. This poorer performance, coming from a stronger perturbation to the longitudinal motion in the first section (given

that we have a full bucket), may be understood from the known differences in the two simulations. While we have used Pill Box cavities in the GEANT4 simulation, which include realistic dimensions and flying time considerations, the study in Ref. [?] uses ideal thin cavities. The size of the unit cells are also different: 2.51 m in all sections in the GEANT4 simulation, and 2.42 m in the first two sections (2.51 m in the other two) in the Ref. [?] simulation. These differences deserve to be further investigated to allow an optimization of the channel parameters.

Given the parameters of the front-end system described above, the number of muons/proton at the end of the cooling channel is approximatelly 0.08-0.1 (this number does not include the acceptance cut of the accelerator system downstream).

18.4.5 Summary

We have studied double-flip cooling channel using GEANT4. The channel offers greater mechanical simplicity, since it has only two field reversals. The 0.08-0.1 muons/protons at the end of the double flip channel are computed for a 16 GeV proton driver and a carbon target. If we upgraded the design to a 24 GeV proton driver and a liquid mercury target (as in the study II proposal) the number of muons per proton would almost triplicate to 0.23-0.28. (this number does not include the acceptance cut of the accelerator system downstream). To confirm this statement, it may be necessary to re-visit the front-end simulation. The current GEANT4 simulation has to be updated with the new magnet engineering design and more realistic r.f. window thicknesess (slightly thicker). Moreover, the geometry and field parameters have to be optimized to mininize the perturbation to the longitudinal motion, and maximize transmission. The optimization of the magnetic field values and section lengths, based on a cost/benefit equation, is also an issue.

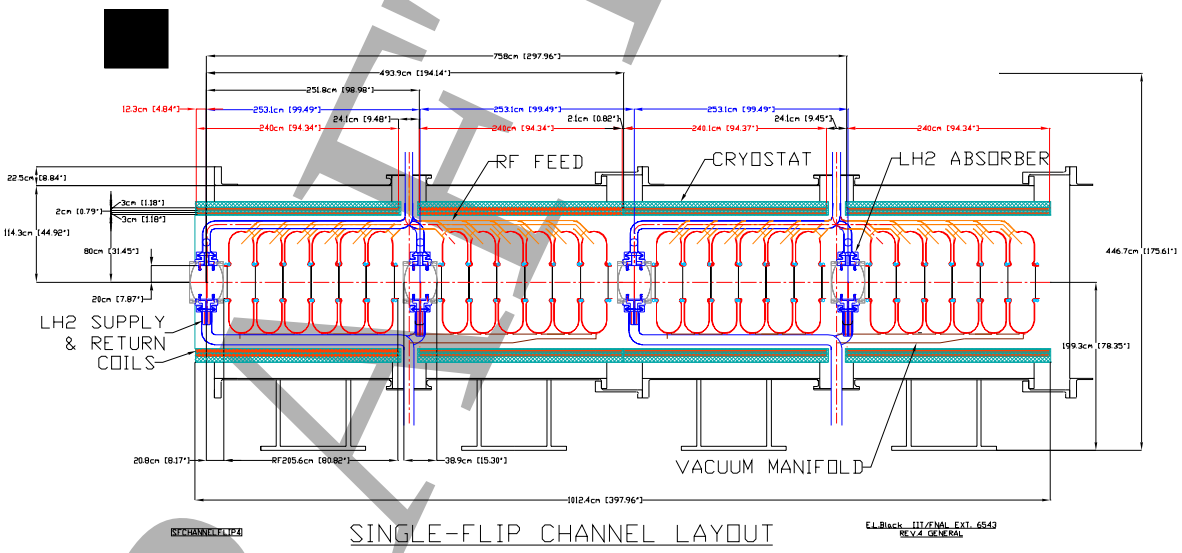

Figure 18.6: Engineering drawing of a cooling channel unit cell. Remember this is the new design which was still not incorporated in the simulation. The performance should not depend on the design change, since the field will not vary significantly in the beam region.

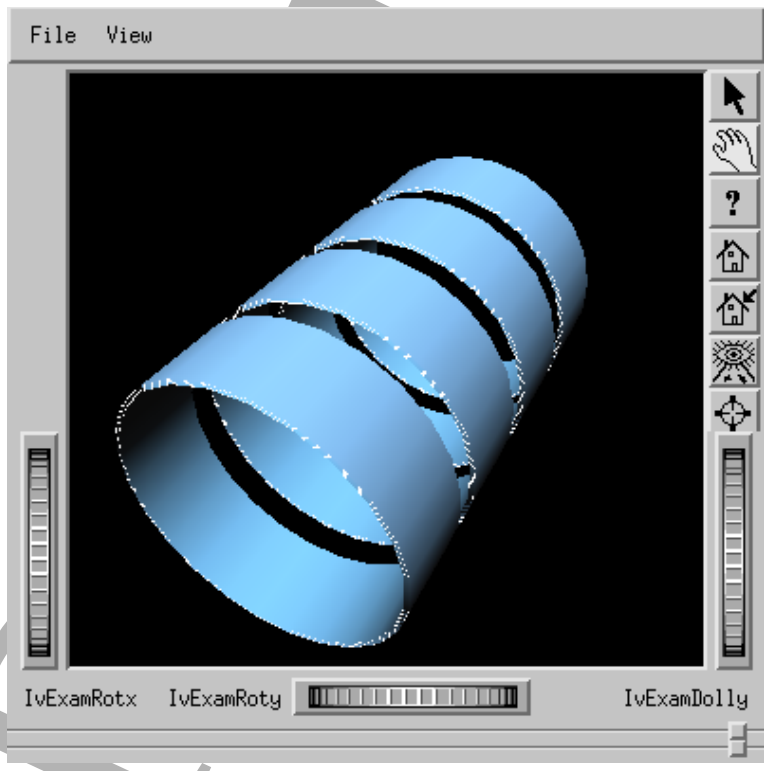

Figure 18.7: Four coils associated with a cooling unit cell.

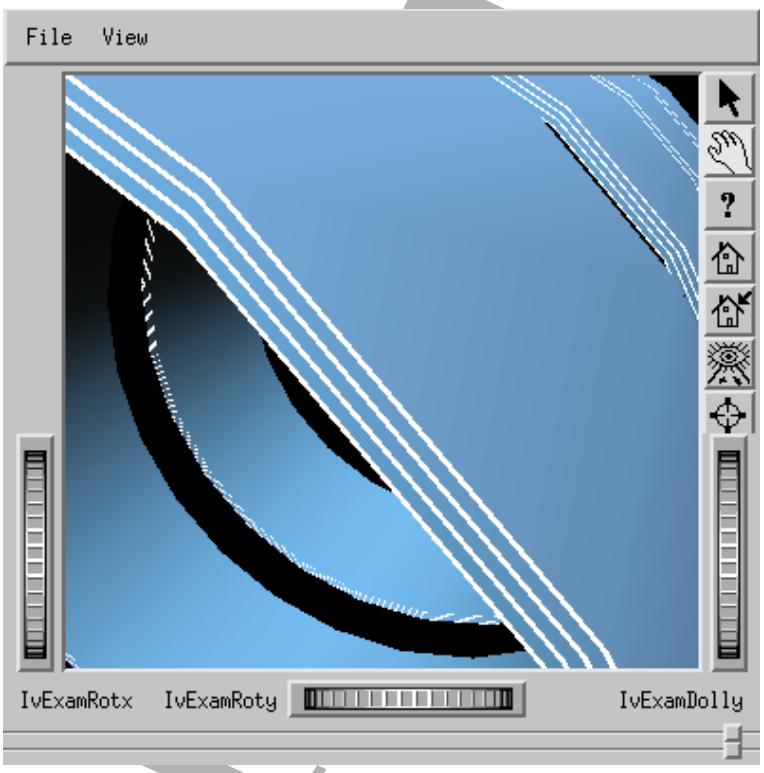

Figure 18.8: The coil blocks are models with infinitelly thin current sheets.

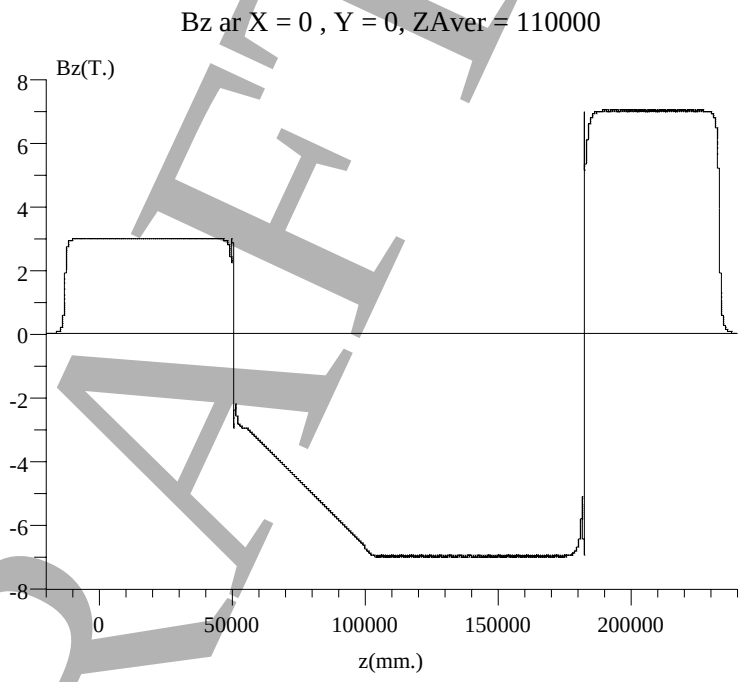

Figure 18.9: B_z on axis as a function of z.

Table 18.3: List of parameters associated to the double-flip cooling channel.

PARAMETER	**VALUE**
Global	-
Length of a section, ΔL	2.51 cm
Magnetic field on axis, ΔL	$3 \rightarrow 7$ T
Magnetic field at the coil	8 T maximum
Field variation	0.2%
Current densities	88-125 A/mm^2
Coil thickness	3-8 cm
Coil radius	74 cm
Number of sections	4
Number of cells/section	20, 20, 32, 15
Number of flip sections	2
Absorber	-
Length of hydrogen (LH2) absorber	30-39 cm
Density of LH2	0.0708 g/cm^2
Thickness of absorber windows	$200 \rightarrow 100$ μ
Material absorber windows	Aluminum
Energy loss per cell	$\approx$10 MeV
Radial aperture, in LH2	20 cm
Linac	-
Length of linac (per cell)	1.925 m
Number of r.f. cells	6
Frequency	201.25 MHz
Effective voltage	15 MV/m
Synchronous phase	$24 - 26$degrees
Beryllium-window thickness	125 μm
Radial aperture, linac	20 cm

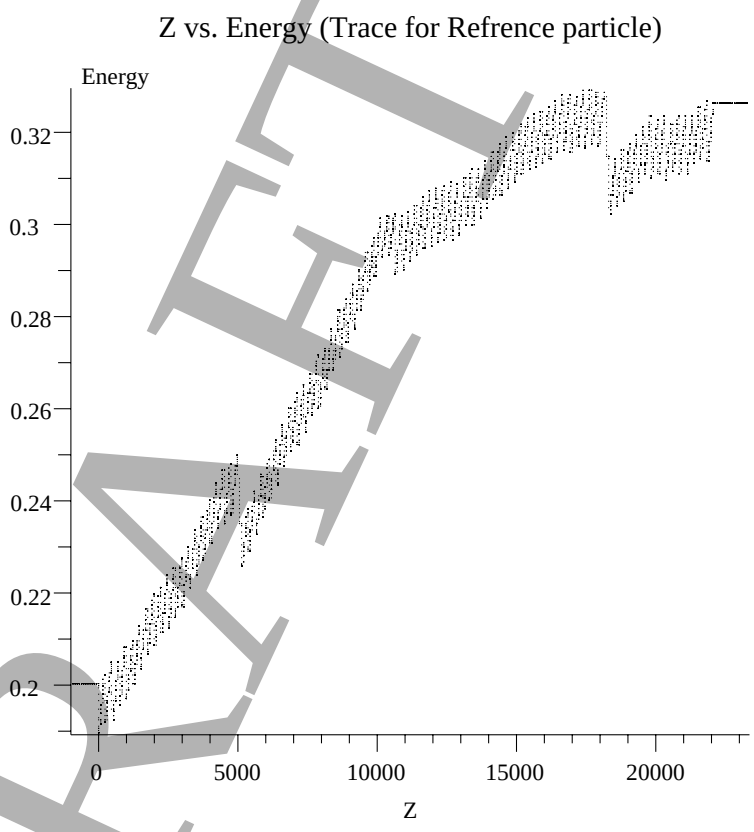

Figure 18.10: Reference energy versus Z. The reference energy increases from 200 MeV to 326 MeV from the begining to the end of the channel.

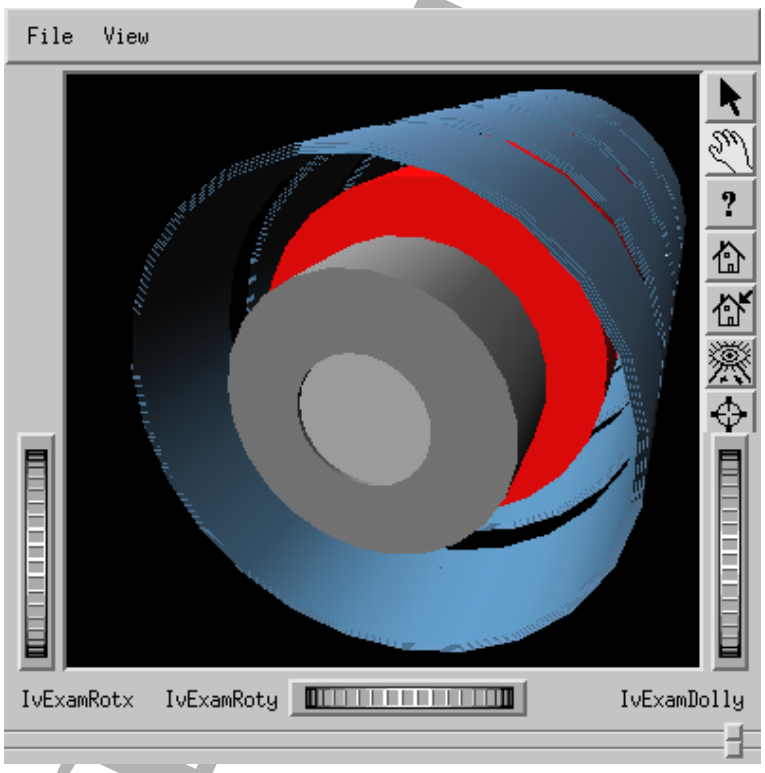

Figure 18.11: The absorber (in grey) is placed inside the solenoidal coils (in blue) in a unit cell. The aluminum windows are shown in light grey .

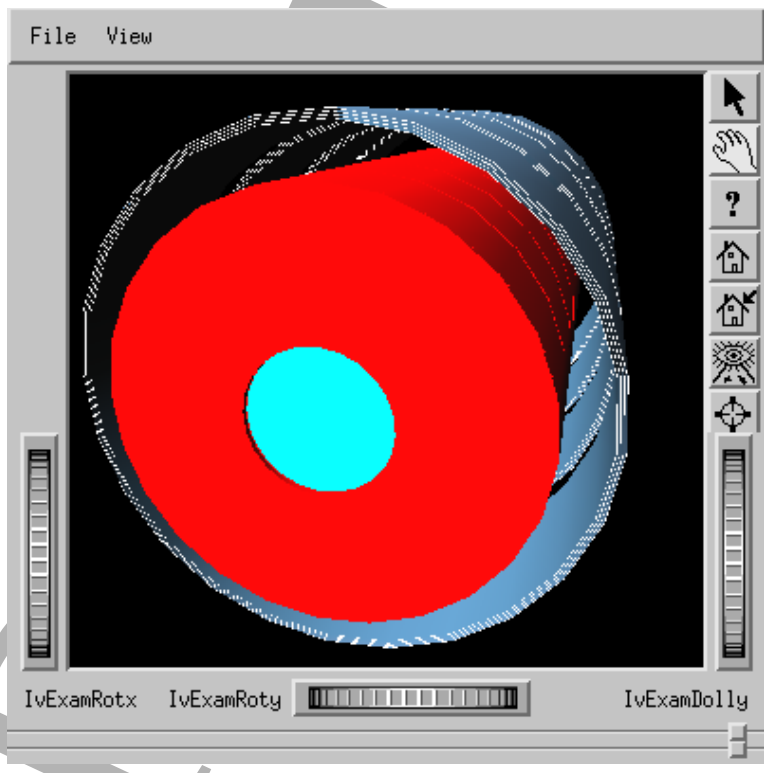

Figure 18.12: The six r.f. cavities forming the linac (in red).

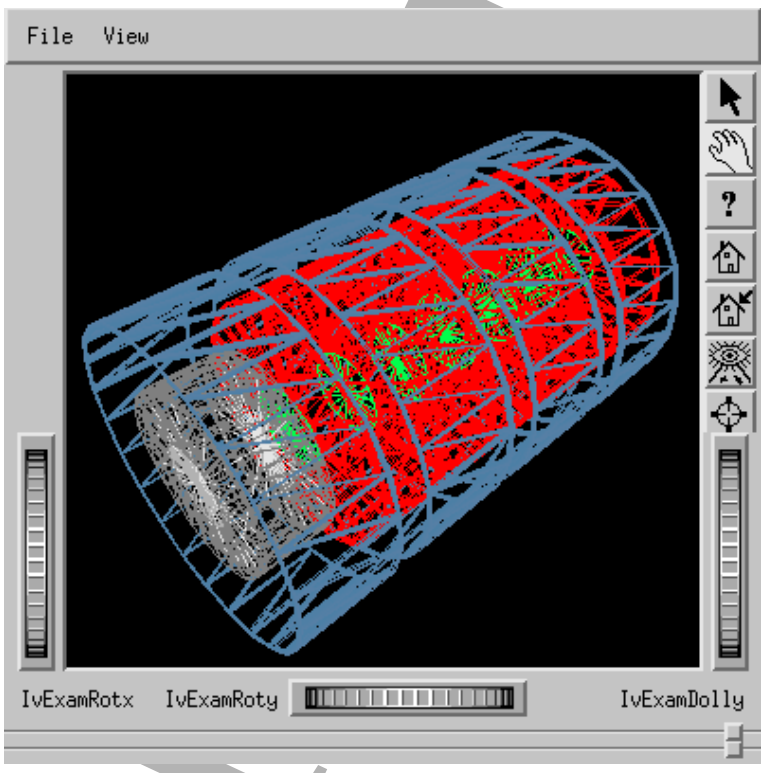

Figure 18.13: The six r.f. cavities (red) and their berylium windows (green).

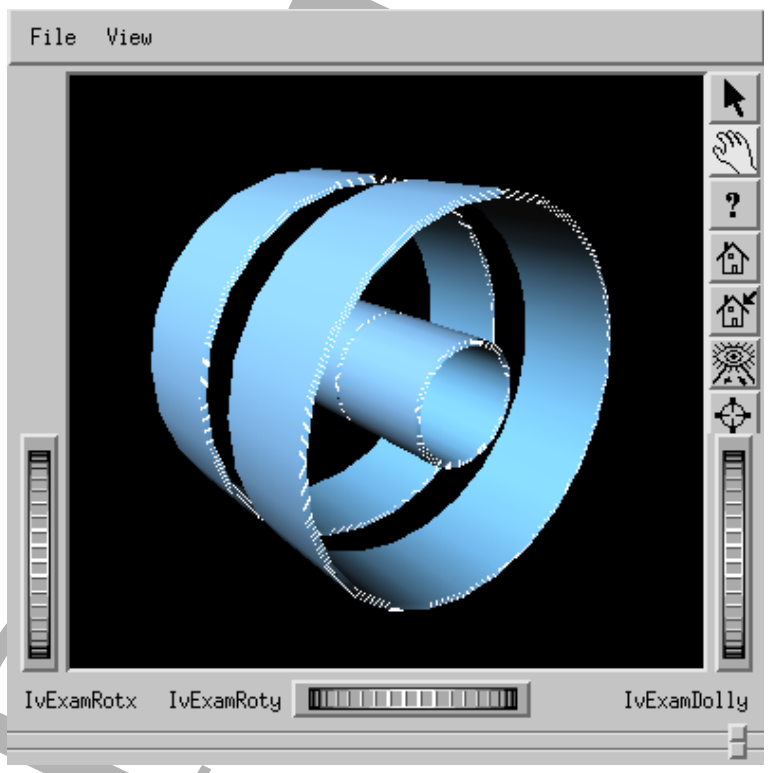

Figure 18.14: The first matching section.

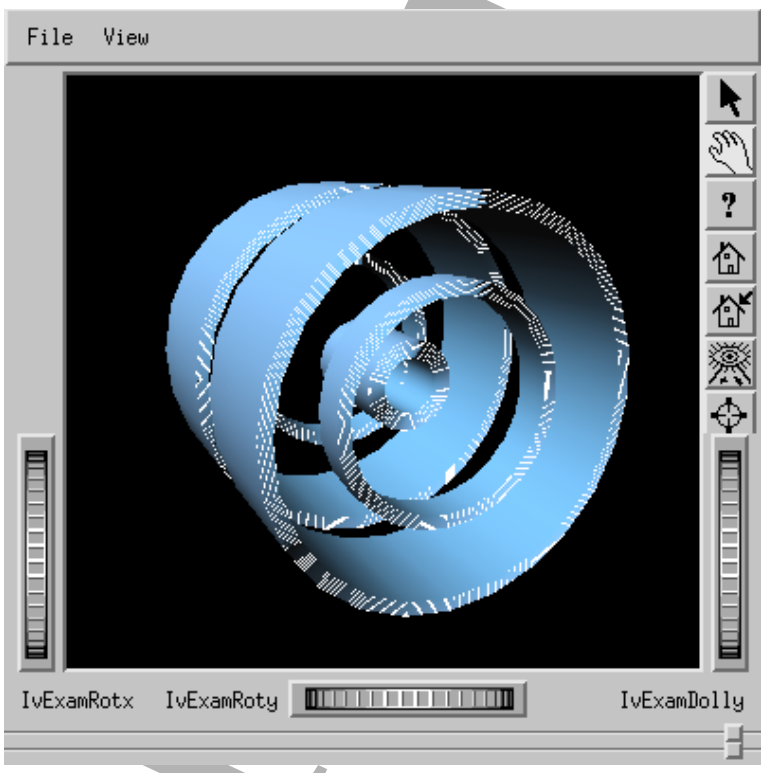

Figure 18.15: The second matching section.

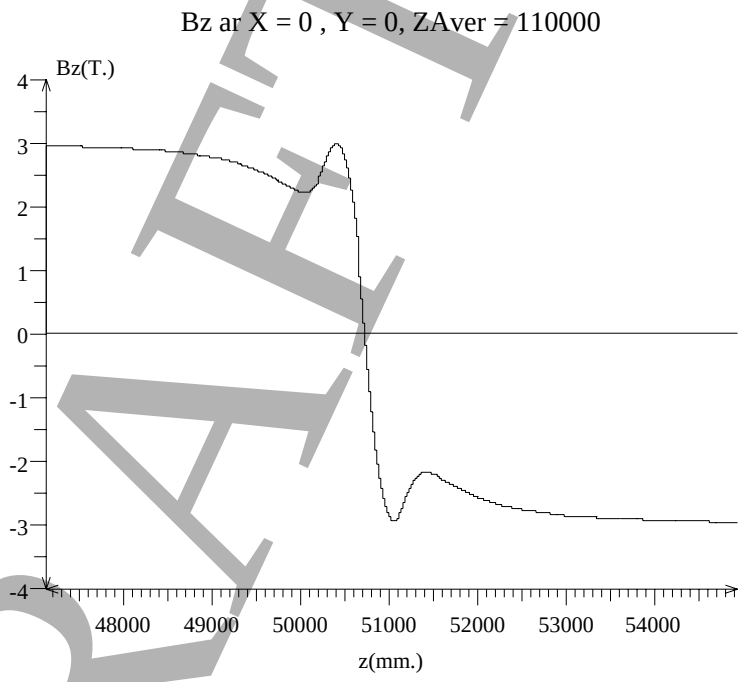

Figure 18.16: The magnetic field on axis, B_z, assiciated to the first field flip region.

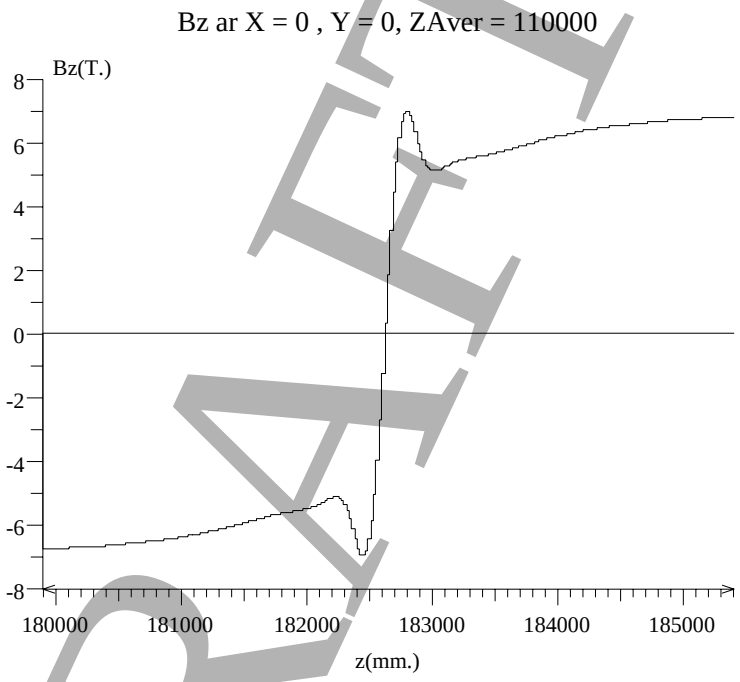

Figure 18.17: The magnetic field on axis, B_z, assiciated to the second field flip region.

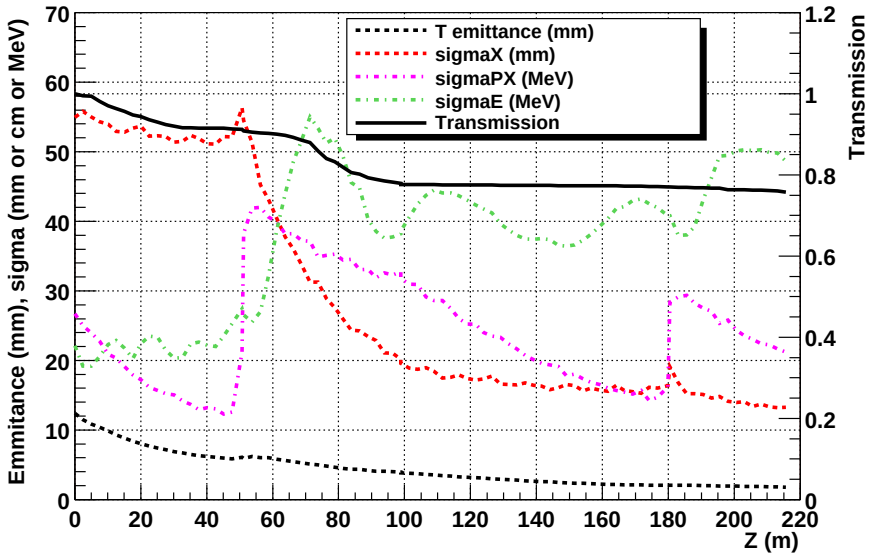

Figure 18.18: Performance of the double flip cooling channel given a gaussian beam.

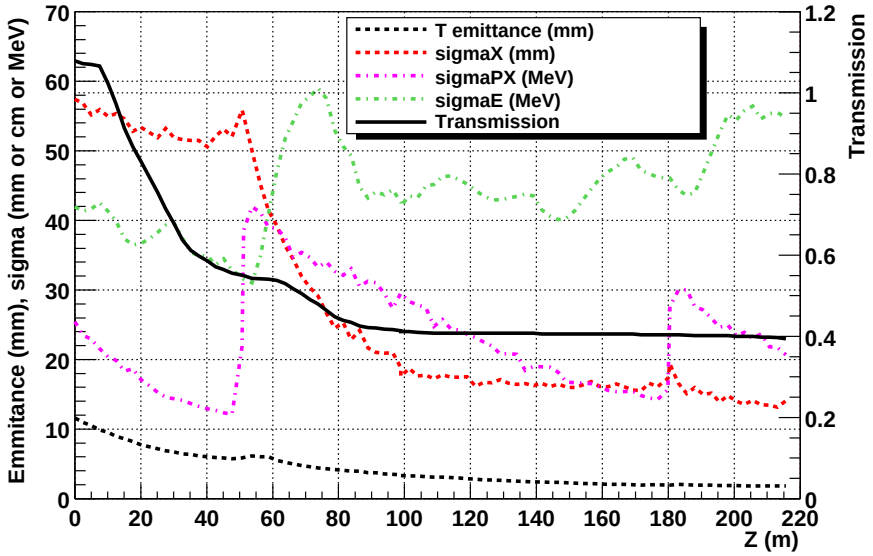

Figure 18.19: Performance of the double flip cooling channel given a reallistic beam.

Bibliography

[1] V. Balbekov, "Double Field Flip Cooling Channel for Neutrino Factory (front-end simulation)".

18.5 Alternative Acceleration

S. Berg

18.6 Alternative Detector

E. O'Brien

Bibliography

[1] N. Holtkamp, D. Finley,Editors, *A Feasibility Study of a Neutrino Factory Based on a Muon Storage Ring*,Aug., 2000

`http://www.fnal.gov/projects/muon_collider/nu-factory/fermi_study_after_april1st/`

.